

**SPECTRAL INTERFEROMETRY: A STUDY OF THE
DEGREE OF COHERENCE IN THE SPACE-
FREQUENCY DOMAIN AND THE APPLICATIONS**

**THESIS SUBMITTED FOR THE DEGREE OF
DOCTOR OF PHILOSOPHY**

**BY
V. NIRMAL KUMAR**



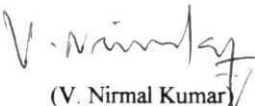
**SCHOOL OF PHYSICS
UNIVERSITY OF HYDERABAD
HYDERABAD - 500 046
INDIA
JANUARY 1997**

DECLARATION

I hereby declare that the matter embodied in this thesis is the result of investigations carried out by me in the School of Physics, University of Hyderabad, Hyderabad, India, under the supervision of Dr. D. Narayana Rao.

Place: Hyderabad

Date: 15/1/97


(V. Nirmal Kumar)

CERTIFICATE

This is to certify that the research work described in this thesis entitled "**Spectral interferometry: A study of the degree of coherence in the space-frequency domain and the applications**", has been carried out by **Mr. V. Nirmal Kumar** under my direct supervision and the same has not been submitted for the award of research degree of any university.

Place: Hyderabad, India / Boston, USA

Date: 15-1-97



(Thesis Supervisor)

(D. Narayana Rao)



Dean

School of Physics.

DEAN,
SCHOOL OF PHYSICS,
UNIVERSITY OF HYDERABAD.

ACKNOWLEDGMENTS

It is a pleasure to thank everybody who have helped me at different stages of my research carrier and my stay at the University of Hyderabad

First of all, I should thank my supervisor **Dr D. Narayana Rao** for his guidance and constant encouragement. His dedication and developmental skills have inspired me beyond words.

I thank the **Dean**, School of Physics, for providing the necessary facilities.

This gives me an opportunity to thank all the faculty members of the school for their motivating research atmosphere and the non-teaching staff for their cooperation.

Financial assistance during my research tenure from the **University Grants Commission**, India is greatly acknowledged.

I must acknowledge the help of **Mr. C.S. Murthy, CIL** for his help in building some electronic circuits and **R.K. Swamy, M/S Welltech Engineers** for the development of optical hardware essential for the experiments.

My lab mates and colleagues **Venu**, **Siva**, **Ram Mohan**, **Chandrasekar**, **Raji** and **Geeta** have always helped me at all stages of my work, sometimes even sparing their working hours.

Friends like **Gautam**, **Ashoka**, **Chandan**, **Harsha**, **Sarief**, **Satish**, **Jolly**, **Soma** and lots of others have been of support at all times. Old pals, **Drs P.K. Rajan**, **S. Arun Kumar**, **M. Ramachandran** have really made my stay a memorable one. Their acquaintance have made me feel that there is always a lot to learn.

It feels great to have people like **Prof. M. Ramanan** and his family to keep ones niceties intact.

Special thanks to **Dr. N. Ramesh** and **Sripriya** for inspiring me into a research career and **Mr. Ramakrishna**, **U Mass.**, **Boston**, for the crucial help during final stages of thesis writing.

With a deep sense of gratitude I must acknowledge my family. Without the support and encouragement from my parents and brother, this dream of mine would have remained so. I should thank also my in-laws for their cordiality. And **finally**, the patience, understanding and care my wife, Kavita could download from thousands of miles is simply my **asset**

CONTENTS

List of Publications.....	(0)
CHAPTER 1: Introduction.....	1-10
1.1 A brief overview of optical interferometry.....	1
1.2 Spectral interferometry.....	2
1.3 Organization of the thesis.....	4
References.....	8
CHAPTER 2: Theory.....	11-41
2.1 Introduction.....	11
2.2 Some elementary concepts and definitions.....	13
2.3 The laws of interference and the second order correlation phenomenon.....	21
2.4 Partial coherence in the space-frequency domain.....	23
2.4.1 Second order correlation in the space-frequency domain.....	24
2.5 Quasi-homogeneous source and the degree of spectral coherence.....	30
2.6 Spectral impurity of beams.....	36
2.7 Complete coherence in the space-frequency domain.....	38
References.....	40
CHAPTER 3: Coherence time measurement and interference in complementary domains.....	42-64
3.1 Introduction.....	42
3.2 Construction and characterization of dye laser.....	43
3.2.1 Dye cell design.....	44
3.2.2 Performance of the dye laser.....	45
3.2.3 Dye amplifier.....	47
3.3 Time delayed degenerate fourwave mixing using incoherent light.....	48

3.3.1 Theory.....	49
3.3.2 Experimental measurement of the coherence time.....	52
3.4 Interference in complementary domains.....	54
3.4.1 Theoretical formulation.....	55
3.4.2 Experimental demonstration.....	58
References.....	62

CHAPTER 4: Measurement of the degree of spectral coherence.....65-94

4.1 Introduction.....	65
4.2 Overview of the degree of coherence measurement.....	66
4.3 Effect of the degree of coherence on the radiated spectrum.....	70
4.4 Determination of the degree of coherence from spectral measurements in a Michelson interferometer.....	74
4.4.1 Theoretical details.....	75
4.4.2 Experimental.....	78
4.4.3 Results and discussion.....	79
4.5 Measurement of the effect of spectral correlation using the Young's double slit experiment.....	83
4.5.1 Theoretical details.....	84
4.5.2 Experimental.....	86
4.5.3 Results and discussion.....	87
4.6 Space-frequency equivalence and some applications.....	89
References.....	91

CHAPTER 5: Measurement of linear displacements using spectral interferometry.....95-112

5.1 Introduction.....	95
5.2 Spectral modulations in the Mach-Zehnder interferometer.....	96
5.2.1 Theoretical formulation.....	98
5.2.2 Experimental measurement of linear displacement using abroad band laser source.....	102

5.3 Effect of vibrational stabilization on the spectral interferogram.....	105
5.3.1 Analysis of vibrations.....	106
References.....	110

CHAPTER 6: Spectrally resolved white light interferometry for simultaneous measurement of the refractive index and thickness.....113-134

6.1 Introduction.....	113
6.2 Experimental details.....	115
6.2.1 White light source.....	115
6.2.2 Interferometer.....	116
6.2.3 Samples.....	116
6.3 Theoretical background.....	119
6.4 Results and discussion.....	123
6.4.1 Normal dispersive materials.....	123
6.4.2 Absorbing materials.....	128
References.....	131

CHAPTER 7: Measurement of the instrument function of a spectrometer.....135-158

7.1 Introduction.....	135
7.2 Measurement techniques.....	137
7.3 Sinusoidally modulated spectra.....	139
7.3.1 Fabry-Perot interferometer.....	139
7.3.2 Michelson interferometer.....	140
7.4 Grating spectrometer.....	142
7.5 Modulation transfer function of the spectrometer.....	144
7.6 Results and discussion.....	150
7.6.1 Variation with path delay.....	150
7.6.2 Variation with the slit widths.....	153
References.....	157

List of Publications

(1) Experimental demonstration of spectral modification in a **Mach-Zehnder** interferometer.

- J. Mod. Opt. 41, 1757, (1994).

(2) Using interference in the frequency domain for precise determination of thickness and refractive indices of normal dispersive materials.

- J. Opt. Soc. Am. B, 12, 1559, (1995).

(3) Measurement of optical constants of thin polymer films using spectrally resolved white light **interferometry**.

- **Pramana**, 47, 163, (1996).

(4) A compact interferometric system for simultaneous measurement of refractive index and thickness.

- submitted for publication.

(5) Determination of the instrument **function** of a grating spectrometer using white light interferometry.

- submitted for publication.

(6) Measurement of the degree of spectral coherence using a Michelson interferometer and Young's double slit experiment.

- to be communicated.

(7) Absorption and emission spectral studies of Sm^{3+} and Dy^{3+} ions in **Pbo-PbF₂** glasses.

- submitted for publication.

Conference proceedings:

(1) Picosecond and sub-picosecond relaxation studies in liquids with **an** incoherent nanosecond source.

- **Proc. National laser symposium**, p-243, (1993).

(2) Stimulated Raman scattering in gases and fabrication of laser Raman shifter.

- **Proc. National laser symposium**, p-122, (1994).

- (3) Interference in **frequency** domain to determine the **refractive** index of materials.
- **Proc. National laser symposium, p-142, (1995).**
- (4) Measurement of **n** and **t** of thin films using spectral interference technique.
- National symposium on Optics and opto-electronics, **(1996).**
- (5) Spectrometer slit width effects on resolution of the spectra.
- National symposium on Optics and opto-electronics, (1996).
- (6) Spectral **interferometry**: A study of the degree of coherence in the space-frequency domain and the applications.
- accepted for Thesis presentation in National laser symposium, Feb. 1997.

CHAPTER 1

INTRODUCTION

1.1 A brief overview of optical interferometry

Optical interferometers are instruments used for the production and observation of interference between two or more light beams to obtain a wide variety of information based on either the path traversed by the light beam or the nature of the light emitted by the source. The simplest form of interference occurs when light from a source is divided into two beams which, after traversing two different paths fall overlapped on an observing surface. The departure of the resultant intensity from the sum of the individual intensities from the two separate paths, giving rise to bright and dark bands of light are a manifestation of the interference phenomenon and this resultant **variation** in the intensity are called the interference fringes. Based on this, a wide variety of **metrological** measurements can be performed using the interferometers right from study of the surface quality of the optical components with an accuracy of few tenth of a nanometer ($1 \text{ nm} = 10^{-9} \text{ m}$) [1], to the measurement of separation of binary stars which are millions of miles apart, to the measurement of the refractive indices of materials to range finding and velocimetry [2], and so on. In spectroscopic applications, interferometers have practical advantage over the other methods in determining the spectra of sources and the hyperfine structure of spectral lines with a very high spectral resolution [3]. Large number of books and review articles are dedicated to the discussions on the general introduction to interferometry, details of different instruments, different applications and more recent developments [4-8]. The different classification of the interferometers, the quantities that are measured and some of the relevant applications are briefly summarized in the Table 1.1.

With the development of intense and coherent laser light sources, increasing use of computers for data processing and the availability of very low noise single-mode optical fibres, the optical interferometry has undergone a complete transformation with

Measurement		Applications
Direct	Derived	
Fringe position	Mean phase difference	Length standard and wavelengths
		Length comparisons and machine control
		Refractometry
		Velocity of light
	Phase variations	Interference microscopy
		Microtopography
		Optical testing
Fringe visibility	Spectrum of source	Profiles of symmetrical spectral lines
	Spatial distribution of source	Stellar diameters
Complete intensity distribution (position and visibility)	Spectrum of source	Direct interference microscopy
		Fourier spectroscopy
	Spatial distribution of source	Optical transfer function
		Radio astronomy
		Holograms
Spectral fringes t	Periodicity of fringes	Absolute distance
		Dispersion relation
		Thickness and profilometry
	Fringe visibility	Spectral degree of coherence
		Modulation transfer function
		Absorption

Table 1.1

Fields of interferometry and their applications [5] t denotes the applications of the field of spectral interferometry developed and demonstrated in this thesis.

remarkably wide range of applications [8,9]. Some of the applications take advantage of the single **frequency** stabilized output from lasers for length and rotation measurements. Interference or Fourier transform spectroscopy with a Fabry-Perot or Michelson interferometer is used for the direct observation of spectrum at a high resolution. Digital **interferometry** for high precision tests of optical elements, fibre-optic interferometry for sophisticated detection techniques and nonlinear interferometry with very high light intensity from pulsed lasers are some of the other areas which are filled with the advantages of the interferometric measurements. Further, the holographic and speckle interferometers are very **useful** in the measurement of the deformation, vibrations and contour measurements of diffuse objects [10-12]. Even without much sophistication involved in some of the methods mentioned above, interferometers have been used to demonstrate the geometric phase [13] generated by a cyclic change in the polarization state of a beam of light.

1.2 Spectral interferometry

The advantages of the different interferometric techniques using monochromatic light source, mentioned in the last section however has its own limitations in some of the applications. For example, the interferometric surface profilers using monochromatic light suffers from the phase ambiguity problem which limits the test surface height measurement to not more than half the wavelength of the source [14]. The usual time domain interferometry has the difficulty that the interference signal recorded as a function of the time delay using a scanning Michelson interferometer oscillates very fast with the period of the mean wavelength of the source. Also, large number of points and large number of **fringes** must be scanned to obtain high spectral resolution. This limitation however, can be overcome by using Shannon principle. As most of the measurements are made from the fringe visibility, the vibration instability of the interferometer greatly affects the reliability of the data and an accurate knowledge of the optical path usually requires a reference laser **beam** through the interferometer.

Spectral interferometry with a broad bandwidth white light source is a potential technique to overcome most of the difficulties discussed **above**. First of **all**, the white light sources are cheap, efficient and can give an illumination which is free of speckle noise. White light interferometers have virtually unlimited unambiguous range. The phase storage and retrieval from optical systems based on achromatic interference effects [15,16] or the channeled spectrum [17] has potential application in the optical information processing. The main advantage of spectral interferometry is that the whole spectrogram can be recorded in a single shot using a dispersing element like a prism or a grating and a CCD array detector. Small vibrations does not invalidate the information that can be obtained from the spectrogram as most of the information is stored in the periodicity of the fringes and not in their contrast. Spectral interferometry has been applied to the measurement of the spectral phase introduced by optical fibers [18], differential refractive index of liquid samples [19], **multimode** reflectometers for ultra high spatial resolution [20], real time measurement of dispersion curves [21], polarization mode dispersion in optical fibers [22], group delay of dielectric laser mirrors [23], absolute distance [24], simultaneous measurement of the refractive index and thickness of transparent materials [25], high resolution profilometry [26] etc.

Since the prediction of coherence-induced spectral changes by Wolf [27], there has been increased interest in the theoretical studies and experimental demonstrations explaining the phenomenon of the spectral changes and the formation of spectral interference fringes in the framework of optical coherence theory [28]. The state of coherence can affect the spectrum of the interfering fields to the effect of shift in the peak to the observation of modulations in the spectrum depending on the bandwidth of the light source and the change in the degree of spectral coherence between the interfering fields. These spectral changes have been used to study the path difference between the interfering beams [29], estimate the field cross-correlation and hence the angular separation of sources [30], intensity distribution across the source [31], size of the source [32], etc.

1.3 Organization of the thesis

A complete theoretical background necessary to interpret the results obtained in the different experiments of spectral interferometry are discussed in detail in the chapter 2. All the relevant basic concepts and definitions necessary for describing the interference phenomenon in both the space-time and the space-frequency domains **are** given first. We have also presented a brief derivation and discussion of interference law and the second order correlation phenomenon in the time domain to emphasize the significance of the new treatment. Spectroscopy of partially coherent sources can be discussed more elegantly using the recently developed space-frequency description. Using the concept of second order correlation in this **domain**, the spectral interference law for the interference between two fluctuating optical fields is derived. The degree of spectral coherence which plays the central role in discussing the spectral interference **phenomenon**, has been derived for a statistically quasi-homogeneous source and is found to be identical with the far-zone form of the van **Cittert-Zernike** theorem. Two special types of fields produced by the planar, secondary, quasi-homogeneous sources and the limiting conditions under which they can be called spectrally impure beams and fully coherent light beams are also highlighted using the space-frequency description.

Interference phenomenon predicted in the complementary time and frequency domains, depending on the delay introduced between the interfering beams have been experimentally demonstrated using a home built broad band dye laser. The chapter 3 begins with a detailed description of the dye laser design and its performance with different cavity elements to decide on the suitable bandwidth for our experimental investigations. The coherence time (τ_c) of the laser source, is a very important parameter in observing the transition of interference effects from one domain to the other. This is measured using the time delayed degenerate four wave mixing experiment. A simple demonstration of the interference phenomenon in the complementary domains is illustrated using a dispersion compensated Michelson interferometer along with the derivation of theoretical equations with the appropriate conditions necessary to understand the physical process involved. The interference

fringes in the spectral domain are then characterized by measuring the fringe modulations and the number of fringes over the entire source spectrum and the spectral intensity of the fringes at a particular wavelength as a **function** of the delay introduced between the two interfering beams of a Michelson interferometer.

The quantity that plays pivotal role in understanding the interference phenomenon in the space-frequency domain is the degree of spectral coherence. We have **demonstrated** two experimental schemes to measure the modulus and the real part of the complex degree of spectral coherence using the Michelson and Young's double slit interferometers respectively in the chapter 4. The degree of spectral coherence is found to change the spectrum radiated from a white light source drastically because of the field correlation effects. Theoretically derived equations are used to fit the experimental data to get a quantitative estimate of the effect of different experimental parameters like the path delay and the source size in the Michelson interferometer, slit widths of the spectrometer, width of the secondary source and the separation between the double slits in the Young's interference experiment, affecting the spectrum of the interfering light beams. The demonstration of the principle of space-frequency equivalence from the measurement of the degree of spectral coherence has found applications in the radio astronomy, aperture synthesis imaging, etc.

Chapter 5 deals with one of the applications of the interference phenomenon in the space-frequency domain. Spectral interferometry as it is called, has been used in the measurement of linear displacement from the periodicity of the spectral interference fringes. Use of the broad band dye laser constructed for the purpose of demonstrating the complementary nature of the interference phenomenon, was further extended to observing the effects of partial correlation between the interfering **beams**. We compare the absolute value of the displacement calculated from the theoretical fitting in our method [29] with the already established Fourier transform technique to substantiate the claim on the accuracy of our results. The Mach-Zehnder interferometer used for this purpose is prone to the effects of vibrations and other disturbances which spoil the modulation depth of the interference fringes and hence the quality of information that

can be obtained. We have tried different interferometer **configurations** to study the effect of various experimental parameters affecting the fringe contrast and to improve the stability of the interferometer against disturbances and hence getting spectral interference **fringes** with better fringe contrast.

In the process, we found out that more information can be obtained from spectral fringes obtained with **an** increased source bandwidth. Chapter 6 discusses a potential application of the spectrally resolved white light **interferometry** in determining simultaneously the refractive index over the entire visible region and the thickness of any transparent material placed in one of the arms of a Michelson interferometer [25]. Compared to other available techniques for the measurement of the refractive index and thickness, we have demonstrated the superiority of our method by measuring the optical constants of glass and polymer materials of different refractive index and thickness to a high accuracy of the order of 10^{-5} . Single shot, real time, non-destructive measurement of the dispersion curve over the entire spectrum of the source is the highlight of the experiment. The versatility of the technique lies in its simplicity and the unlimited dynamic measurement range. Spectral phase and the appearance of stationary phase point are some of the other results discussed. The real and imaginary parts of the refractive index because of either a normal dispersive material or an absorbing sample can also be obtained from the frequency or amplitude modulated spectral fringes **respectively**

The sinusoidally modulated spectral fringes with the flexibility over their periodicity obtained using a white light source and a Michelson interferometer can also be used to exactly **quantify** the optical characteristics of a dispersing spectrometer as demonstrated in the chapter 7 To exactly measure the line profiles of spectral sources, it is important to know the behavior of the instrument **function** of a **spectrometer** The modulation transfer **function** (MTF) which is the Fourier transform of the instrument function, specifies the quality of the instrument and is experimentally measured for different slit widths of the spectrometer and at different resolution levels. The effect of these parameters of the spectrometer is found to affect the contrast or the MTF of the spectral **fringes** observed at the output. From their behavior, the instrument function

can be calculated by taking its inverse Fourier transform [33]. **In** the process, we have also measured the spectral slit width and hence the limit of the grating spectrometer under different experimental conditions.

References

- [1] J.C. Wyant, Laser focus world, September, **131**, (1993)
- [2] A. Chebbour, C. Gorecki and G. Tribillon, **Opt Commun.** **111**, 1, (1994).
- [3] R.J Bell, Introductory Fourier transform spectroscopy, (Academic press, NY, 1972).
- [4] S. Tolansky, An introduction to interferometry, (Longmans, **London**, 1955).
- [5] W.H. Steel, Two beam interferometry, in Progress in optics, Edited by E. Wolf, (North-Holland, **1966**), vol. 5; Interferometry, (Cambridge University press, 1967).
- [6] M. Francon, Optical interferometry, (Academic press, NY, **1966**).
- [7] K.M. Baird and G.R. Hanes, Interferometers, in Applied optics and optical engineering, Edited by R. Kingslake (Academic press, NY, **1967**), vol. 4.
- [8] P Hariharan, Optical interferometry, (Academic press, Australia, 1985), Interferometry with lasers, in Progress in optics, Edited by E. Wolf, (North-Holland, 1987), vol. 24.
- [9] Optics source book, Edited by S.P. Parker, (McGraw Hill, NY, 1988).
- [10] P. Hariharan, Optical holography: **Theory**, techniques and applications, (Cambridge university press, 1984).
- [11] A.E Ennos, Speckle interferometry, in Progress in **optics**, Edited by E. Wolf, (North-Holland, 1978), vol. 16.
- [12] I. Yamaguchi, Fringe formations in deformation and vibration measurements using laser light, in Progress in optics, Edited by E. Wolf, (North-Holland, 1985), vol. 22.

- [13] P. Hariharan and D. Narayana Rao, Curr. Sci. 65, 483, (1993).
- [14] **K. Creath**, Phase measurement interferometry techniques, in Progress in optics, Edited by E. Wolf, (North-Holland, **1988**), vol. **26**
- [15] E.N. Leith and J. Upatnieks, J. Opt. **Soc. Am.** 57, 975, (1967).
- [16] B **J** Chang, R. **Alferness** and E.N. Leith, **Appl. Opt.** 14, 1592, (1975).
- [17] A. Lacourt, J.Ch. Vienot and J P. Goedgebuer, Opt. **Commun.** 19, 68, (1976).
- [18] J. Piasecki, B. Colombeau, **M** Vampouille, C. Froehly and J A. Arnaud, **Appl. Opt.** 19,3749,(1980).
- [19] **C** Sainz, **J E** Calatroni and **G** Tribillon, Meas. Sci. Technol. 1, 356, (1990); A **L** Guerrero, C. **Sainz**, H. **Perrin**, **R.** Castell and J. Calatroni, Opt. laser Technol. 24, 333, (1992).
- [20] N. Tan-no **T** Ichimura, **T** Funaba, N Anndo and Y. Odagiri, Opt. **Lett** 19, 587,(1994).
- [21] C. Sainz, P. Jourdain, R. Escalona and **J** Calatroni, Opt. **Commun** **110**, 381,(1994).
- [22] **X.D** Cao and D **D** Meyerhofer, Opt. Lett. 19, 1837, (1994).
- [23] A **P** Kovacs, **K** Osvay, **Zs** Bor and **R** Scipocs, Opt. **Lett** 20, 788, (1995).
- [24] U. Schnell, E **Zimmermann** and R. Dandliker, J. Pure **Appl** Opt. 4, 643, (1995).
- [25] **V** Nirmal Kumar and D. Narayana Rao, J. Opt. **Soc Am B** 12, 1559, (1995); V. Nirmal Kumar, Y. Chandrasekhar and D, Narayana Rao, **Pramana**, 47, 163, (1996); V. Nirmal Kumar and D. Narayana Rao, submitted for publication.

- [26] **P. Sandoz**, G. Tribillon **and** H. **Perrin**, J. Mod. Opt. 43, 701, (1996).
- [27] E. Wolf, Phys. Rev. Lett. 58, 2646, (1987).
- [28] L. Mandel and E. Wolf, in Optical coherence and Quantum optics, (Cambridge press, **1995**), chapter 5; **E** Wolf, in Recent developments in quantum optics, Edited by R. **Ingua**, (Plenum, NY, **1993**), 369.
- [29] D. Narayana Rao and V. Nirmal Kumar, J. Mod. Opt. 41, 1757, (1994).
- [30] **H.C.** Kandpal, K. Saxena, D.S. Mehta, J.S. Vaishya and K **C** Joshi, J. Mod. Opt 42,447,(1995).
- [31] **H.C** Kandpal, **J S** Vaishya, K. Saxena, D.S. Mehta and **K.C** Joshi, J. Mod. Opt. 42,445, (1995).
- [32] S. Vicalvi, G.S. Spagnolo and M. Santarsiero, Opt. Commun. **130**, 241, (1996).
- [33] V. Nirmal Kumar and D. Narayana Rao, submitted for Publication.

CHAPTER 2

THEORY

2.1 Introduction

The field produced by all optical sources fluctuate in time with highly complicated and irregular waveforms. Though these fluctuations are much too rapid to observe directly, their existence can be deduced from appropriate experiments which provide information about the correlation that exist between the fluctuations at two or more space-time points [1,2]. In this process, information about the waveform remains unknown as the detectors used measure only the intensity, **time** averaged over the entire waveform. The mathematical model of classical coherence theory is very **successful** in describing the effects of unknown waveform based on the observed measurement of the time averaged intensity [3-5]. In a broad sense, the optical coherence theory is concerned with the statistical description of the fluctuations and the coherence phenomena are the manifestation of correlation between them. Interference effects, which arise when two beams that are derived from the same source are superposed are the simplest phenomena that reveals the correlation between optical **fields** [1]. The outcome of the investigations of coherence was the introduction of a precise measure of the correlation between the fluctuating field variables at two space-time points and the formulation of dynamical laws which the correlation functions obey [2]. In the second order theory, the correlation functions are in general a set of second rank tensors written in terms of the electric and magnetic fields. Though a study of the higher order correlation effects in optical fields have been done [1], the second order theory provides a unified, simple treatment of all the well known coherence, interference and polarization phenomena of traditional optics.

In this chapter, the basic theoretical background necessary to interpret the experimental results obtained in both the space-time and space-frequency domains are discussed. In the first part of the chapter, a short discussion about some basic

concepts and definitions regarding different field and coherence parameters and the temporal and spatial coherence useful in the discussion of simple correlation experiments are presented [6]. The second order correlation phenomenon in the usual space-time domain is briefly explained using the two beam **Young's** interference experiment and is used to derive the mutual coherence function $\Gamma(\mathbf{r}_1, \mathbf{r}_2, \tau)$ and the complex degree of coherence $\gamma(\mathbf{r}_1, \mathbf{r}_2, \tau)$. In the second part of the chapter, a detailed derivation cum discussion on the second order correlation phenomenon in the space-frequency domain for partially coherent light beams is given. From which, the significance of the cross-spectral density $\mathbf{W}(\mathbf{r}_1, \mathbf{r}_2, \nu)$ and the complex degree of spectral coherence $\mu(\mathbf{r}_1, \mathbf{r}_2, \nu)$ are explained. Quasi-homogeneous sources are more realistic physical sources taking into account the finite size of the source and the slow variation of intensity distribution across the source plane. Utilizing the concept of statistical quasi-homogeneity, the field correlation equations are derived. The reciprocity theorem derived is found to be formally identical with the far-zone form of the van Cittert-Zernike theorem for the field correlation at two points in the field generated by a spatially incoherent, quasi-monochromatic, planar source. A comparison between the two gives the explicit form for the complex degree of spectral coherence. When two spectrally impure beams are made to interfere, the interference fringes show detailed periodic coloring. A theoretical estimation of the spectral impurity of the beams is essential in analyzing the effect of the degree of spectral coherence on the superposed spectrum of the beams. The concept of cross-spectral purity of light beams is used to analyze the behavior of the spectral changes in the interference fringes. A short note on the conditions for complete coherence of the interfering light beams in the space-frequency domain is also presented. A complete coherence in the space-frequency domain implies certain functional form for the cross-spectral density $\mathbf{W}(\mathbf{r}_1, \mathbf{r}_2, \nu)$ and the spectral degree of coherence $\mu(\mathbf{r}_1, \mathbf{r}_2, \nu)$. At the upper limit of unity for $\mu(\mathbf{r}_1, \mathbf{r}_2, \nu)$, interference fringes of maximum visibility can be produced using a suitable experiment.

2.2 Some elementary concepts and definitions

(i) Analytic signal representation: In classical coherence theory, it is advantageous to represent the electromagnetic field by a complex quantity because of its mathematical simplicity and also because it serves to emphasize the fact that coherence theory deals with phenomena that are sensitive to the envelope or to the average intensity of the field [7]. The complex representation of real polychromatic field is a natural generalization of the well known complex representation of the monochromatic fields used in the classical optics. The real part of the field amplitude for a typical monochromatic component of the field is given by

$$\varepsilon^{(r)}(\mathbf{r}, \nu) = \varepsilon_0(\mathbf{r}) \cos[\phi(\mathbf{r}) - 2\pi\nu t] \quad (2.1)$$

where $\varepsilon_0(\mathbf{r})$ is the magnitude of the field and $\phi(\mathbf{r})$ is the phase. For the ease of manipulation, it is conventional to work with the complex field amplitude of the type

$$\varepsilon(\mathbf{r}, \nu) = \varepsilon_0(\mathbf{r}) \exp[i\phi(\mathbf{r})] \quad (2.2)$$

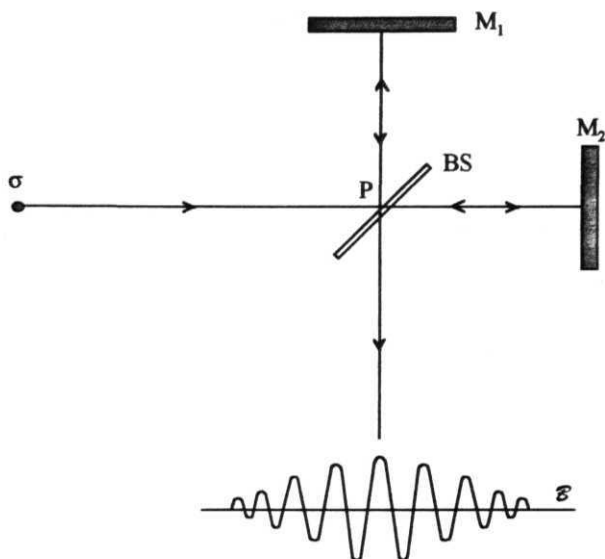
A time dependent complex analytic signal is usually defined as the Fourier transform of this, i.e.,

$$\varepsilon(\mathbf{r}, t) = \int_0^\infty \varepsilon(\mathbf{r}, \nu) \exp(-2\pi i \nu t) d\nu \quad (2.3)$$

The integration in the above equation is only from zero to infinity because of the Hermitian symmetry of the complex field amplitude about the origin, i.e., $\varepsilon(-\mathbf{r}, \nu) = \varepsilon^*(\mathbf{r}, \nu)$. By taking the real part of the analytic signal, we get the actual field component.

(ii) Temporal coherence and coherence time, τ_c : Consider light beam from a point source a, divided into two beams in a Michelson interferometer (Figure 2.1 (a)). The two beams are then **recombined** at the same beamsplitter after introducing a path delay $\Delta = c\tau$ (c is the velocity of light in vacuum) between them. The light is assumed quasi-

(a)



(b)

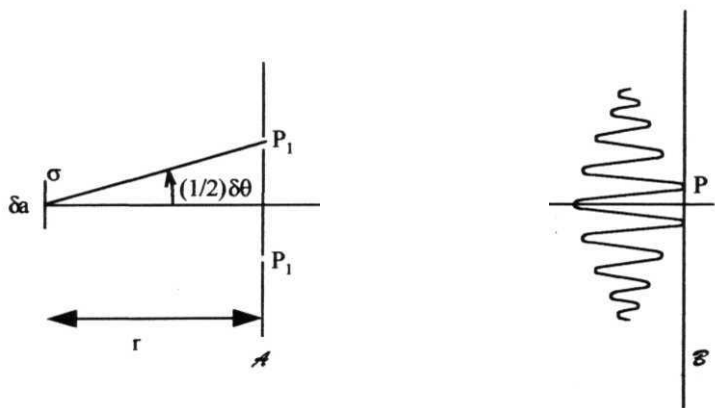


Figure 2.1

(a) Temporal coherence illustrated using a Michelson interferometer.
 (b) Spatial coherence illustrated by means of Young's interference experiment. σ = source, BS = Beamsplitter, M_1 , M_2 = Mirrors, \mathcal{B} = Plane of observation, \mathcal{A} = Plane of double slit.

monochromatic, which means its bandwidth $\delta\nu$ is small compared to mid frequency ν_0 , i.e.,

$$\delta\nu \ll \nu_0 \text{ or } \delta\nu/\nu_0 \ll 1 \quad (2.4)$$

As usually, the averaging time interval to make an observation is much longer than the mean period and correlation time of the fluctuations, the light beam can be assumed to be macroscopically steady. For a sufficiently small path difference A , interference fringes are formed in the observation plane \mathcal{B} . These fringes are a manifestation of the *temporal coherence* between the two interfering beams. The ability of the two beams to form fringes can be explained using the concept of correlation that exist between the fluctuations of the two beams reaching \mathcal{B} as a function of the time delay T introduced between them [8]. Interference fringes will be observed only if

$$\tau_c \delta\nu \leq 1 \quad (2.5)$$

and hence the limiting time delay given by $\tau_c \approx 1/\delta\nu$ is known as the coherence time of the light and the corresponding path

$$l_c = c \tau_c = c/\delta\nu \quad (2.6)$$

is called the coherence length or more precisely termed as the longitudinal coherence length. With $\nu = c/\lambda$, where λ is the wavelength and $\delta\nu \approx c\delta\lambda/\lambda_0^2$ and the coherence length may be written as $l_c \approx (\lambda_0/\delta\lambda)\lambda_0$ where λ_0 is the mean wavelength.

The formation or absence of the interference fringes in the observation plane can also be considered to arise from the addition of spatially periodic distributions, each of them being formed by a frequency component present in the spectrum of light. Two examples of the light sources used in this study are given to illustrate the order of magnitude of the coherence time (τ_c) and coherence length (l_c) in typical cases. For the quasi-monochromatic broad band dye laser ($\delta\nu/\nu_0 = 0.015$), the band width is $\delta\lambda = 8.7 \text{ nm}$ or $\delta\nu \approx 7.77 \times 10^{12} \text{ Hz}$. The corresponding coherence time is 0.129 psec and the coherence length is $39 \text{ }\mu\text{m}$. Whereas for the white light source (tungsten filament lamp

for which $\delta v/v_0 = 0.36$), the bandwidth $\delta\lambda = 194.4 \text{ nm}$ or $5v = 2.038 \times 10^{14} \text{ Hz}$ so that the coherence time is **4.91** fsec and the coherence length is **1.47** urn.

(iii) Spatial coherence and coherence area, 6A: Consider the Young's interference experiment with a quasi-monochromatic and quasi-thermal light from an extended source σ (Figure 2 1 (b)). A symmetrical experimental arrangement is considered for simplicity. For the source with square sides $5a$ and the pinholes P_1 and P_2 sufficiently close to the symmetry axis, interference fringes are observed on the screen \mathcal{B} near the axial point P . The appearance of these **fringes** is a manifestation of the *spatial coherence* existing between the beams reaching the screen \mathcal{B} from P_1 and P_2 , since their visibility depends on the spatial separation of the pinholes and can be explained as arising from the correlation that exists between them. Interference fringes are generally observable only if

$$(\delta\theta)(\delta a) < \lambda_0 \quad (2.7)$$

where 58 is the angle that the distance P_1P_2 of separation between the pinholes subtends at the source and $\lambda_0 = c/v_0$ is the mean wavelength of the light. If ' r ' is the distance between the source plane and the plane containing the pinholes, to observe the fringes near P , the pinholes must be situated within an area around their midpoint of size

$$\delta A \approx (r \delta\theta)^2 \approx (r \lambda_0 / \delta a)^2 \quad (2.8)$$

This region is called the coherence area of the light in the plane of the pinholes around their midpoint and the square root of the coherence area is also known as the transverse coherence length.

Formation of the interference fringes at the observation plane \mathcal{B} can be explained as due to the addition of the intensities of the individual interference patterns produced by different mutually independent point sources. A deeper understanding of this phenomenon is possible in terms of the concept of correlation [8], which sums up to the fact that even statistically independent sources will give rise to correlation in the fields that are generated in the process of propagation and superposition. An

elementary analysis of the spatial coherence is illustrated by considering the examples of the sources used in our study. For the broad band dye laser oscillating in the **TEM₀₀** mode, the expanded laser beam gives rise to interference fringes with constant visibility for **different slit separations** spanning the entire beam **cross-section**, concluding that the laser beam is fully spatially coherent. For the tungsten filament lamp illuminating a slit of linear dimension $5a = 0.1$ mm and of mean wavelength $\lambda_0 = 533.5$ nm kept at a distance of 50 cm from the Young's double **slit**, the coherence area δA in the plane of the double slit is about $7 \mu\text{m}^2$ and the transverse coherence **length**, given by its square root is ≈ 2.65 mm.

(iv) Mutual coherence function, $\Gamma(\mathbf{r}_1, \mathbf{r}_2, \tau)$: The cross-correlation function $\Gamma(\mathbf{r}_1, \mathbf{r}_2, t_1, t_2)$ between the light vibrations at two space-time points (\mathbf{r}_1, t_1) and (\mathbf{r}_2, t_2) known as the mutual coherence **function** [1], is the central quantity of importance in the elementary theory of optical coherence. This mutual coherence function is defined by

$$\Gamma(\mathbf{r}_1, \mathbf{r}_2, \tau) = \lim_{T \rightarrow \infty} \frac{1}{2T} \int_{-T}^{+T} \varepsilon^*(\mathbf{r}_1, t) \varepsilon(\mathbf{r}_2, t + \tau) dt \quad (2.9)$$

where the correlation function depends on the two time arguments only through their difference $\tau = t_2 - t_1$ and $\varepsilon(\mathbf{r}, t)$ is the complex analytic time dependent signal at some point ' \mathbf{r} ' and time ' t ' defined in eqn.(2.3). It was assumed in the above definition that the field $s(\mathbf{r}, t)$ is *stationary* in time i.e., all the ensemble averages are independent of the origin of time and moreover for an *ergodic* field, the ensemble averages become time independent and may be replaced by the corresponding time averages. In such a case the above equation could be replaced by

$$\Gamma_{12}(\tau) = \langle \varepsilon^*(\mathbf{r}_1, t) \varepsilon(\mathbf{r}_2, t + \tau) \rangle \quad (2.10)$$

where the sharp brackets denote the ensemble average.

(v) Intensity, $I(\mathbf{r}, t)$: In coherence theory, intensity is usually considered an observable **quantity**. It is defined as the time averaged square magnitude of the analytic signal

given by eqn.(2.9) which is **also** the trace of the mutual coherence function defined by eqn. (2.10) i.e.,

$$I(r, t) = \lim_{T \rightarrow \infty} \frac{1}{2T} \int_{-T}^{+T} \varepsilon^*(r, t) \varepsilon(r, t) dt = \Gamma_{11}(0) \quad (2.11)$$

This quantity is always real. For an analytic signal which is assumed to be an ergodic random process, the above equation can also be written in terms of ensemble averages **of the** form

$$I(r, t) = \langle \varepsilon^*(r, t) \varepsilon(r, t) \rangle \quad (2.12)$$

This averaged **field** intensity at a point '**r**' is useful in normalizing the mutual coherence function as defined in eqn.(2.10).

(vi) Complex degree of **coherence**, $\gamma(r_1, r_2, \tau)$: A function that depends only on the coherence properties of the light field is more useful and is obtained by normalizing the mutual coherence function by setting

$$\gamma_{12}(\tau) = \frac{\langle \varepsilon^*(r_1, t) \varepsilon(r_2, t + \tau) \rangle}{\sqrt{\langle \varepsilon^*(r_1, t) \varepsilon(r_1, t) \rangle \langle \varepsilon^*(r_2, t) \varepsilon(r_2, t) \rangle}} \quad (2.13)$$

$$\gamma_{12}(\tau) = \frac{\Gamma_{12}(\tau)}{\sqrt{\Gamma_{11}(0) \Gamma_{22}(0)}} = \frac{\Gamma_{12}(\tau)}{\sqrt{\langle I(r_1, t) \rangle \langle I(r_2, t) \rangle}}$$

where $\langle I(r, t) \rangle$ is the ensemble averaged intensity of the light at the point '**r**' and time '**t**'. The quantity $\gamma_{12}(\tau)$ defined by eqn. (2.13) is called the complex degree of coherence. It is a properly normalized function such that $\gamma_{11}(0) = \gamma_{22}(0) = 1$, i.e., the field at a point in space must always be perfectly coherent with itself. All other values **of** $\gamma_{12}(\tau)$ are generally complex and has amplitude values less than 1, which means that the fields at two different points or at the same point after a time delay **T**, are generally less than perfectly coherent with each other. The magnitude of this complex degree of coherence is a measure of the mutual coherence between the fields at the two space-time points and should **satisfy** the inequality

$$0 \leq |\gamma(\mathbf{r}_1, \mathbf{r}_2, \tau)| \leq 1 \quad (2.14)$$

for **all** values of the arguments $\mathbf{r}_1, \mathbf{r}_2$ and τ of γ

(vii) Cross-spectral density function, $\mathbf{W}(\mathbf{r}_1, \mathbf{r}_2, \nu)$: The cross-spectral density or the cross-power spectrum is the ensemble averaged correlation function between typical monochromatic components of the field disturbance at a point \mathbf{r}_1 with the complex conjugate of the same component at some other point \mathbf{r}_2 at frequency ν and is defined by the equation

$$\langle \epsilon^*(\mathbf{r}_1, \nu) \epsilon(\mathbf{r}_2, \nu') \rangle = W(\mathbf{r}_1, \mathbf{r}_2, \nu) \delta(\nu - \nu') \quad (2.15)$$

where the ensemble average is taken over the different realizations of the field and δ is the Dirac delta function. The field amplitude $\epsilon(\mathbf{r}, \nu)$ is taken to be a random variable of arbitrary coherence. According to the generalized **Wiener-Khinchine** theorem, the two correlation functions, the mutual coherence function and **cross-spectral** density function form a Fourier transform pair i.e.,

$$\begin{aligned} \Gamma(\mathbf{r}_1, \mathbf{r}_2, \tau) &= \int_{-\infty}^{\infty} W(\mathbf{r}_1, \mathbf{r}_2, \nu) \exp(-2\pi i \nu \tau) d\nu \\ W(\mathbf{r}_1, \mathbf{r}_2, \nu) &= \int_{-\infty}^{\infty} \Gamma(\mathbf{r}_1, \mathbf{r}_2, \tau) \exp(2\pi i \nu \tau) d\tau \end{aligned} \quad (2.16)$$

The cross-spectral density function is **Hermitian** in the sense that $W(\mathbf{r}_2, \mathbf{r}_1, \nu) = W^*(\mathbf{r}_1, \mathbf{r}_2, \nu)$ and is non-negative and definite.

(viii) Spectrum, $S(\mathbf{r}, \nu)$ and normalized spectrum, $s(\mathbf{r}, \nu)$: In the special case when the two points \mathbf{r}_1 and \mathbf{r}_2 coincide, the cross-spectral density function given by eqn.(2.15) reduces to a function which depends only on the location of one point ' \mathbf{r} ' and on the frequency ν . This function is known as the spectral density or the power spectrum of light which is the trace of the cross-spectral density function and is defined as

$$S(\mathbf{r}, \nu) = \langle \epsilon^*(\mathbf{r}, \nu) \epsilon(\mathbf{r}, \nu) \rangle = W(\mathbf{r}, \mathbf{r}, \nu) \quad (2.17)$$

The power spectrum can be normalized according to the equation

$$s(r, \nu) = \frac{S(r, \nu)}{\int_0^{\infty} S(r, \nu) d\nu} \quad (2.18)$$

and the normalized spectrum has the property $\int_0^{\infty} s(r, \nu) d\nu = 1$, which is independent of the total intensity. However, the intensity of the spectrum is equivalent to the intensity of a single monochromatic component of the field defined by eqn.(2.12). Since different monochromatic components of the field are mutually incoherent and can not interfere, the intensity of the total field is calculated as the sum of intensities of all the monochromatic components, i.e.,

$$I(r, \nu) = \int_0^{\infty} S(r, \nu) d\nu \quad (2.19)$$

(ix) Complex **degree** of spectral coherence, $\mu(r_1, r_2, \nu)$: The cross-spectral density **function** contains information about both the spectrum and the coherence of the field. As it is always useful to have a **function** which depends on the coherence properties of the field only, we define a new **function** known as the complex degree of spectral coherence [9] as

$$\mu(r_1, r_2, \nu) = \frac{W(r_1, r_2, \nu)}{\sqrt{W(r_1, r_1, \nu)W(r_2, r_2, \nu)}} = \frac{W(r_1, r_2, \nu)}{\sqrt{S(r_1, \nu)S(r_2, \nu)}} \quad (2.20)$$

where $S(r, \nu)$ is the spectral density or the power spectrum of the light. $\mu(r_1, r_2, \nu)$ is referred to as the spectral degree of coherence at frequency ν , of the light at the point r_1 and r_2 . It is also known as the complex degree of spatial (or spectral) coherence at frequency ν [10-11]. It should satisfy the inequality

$$0 \leq |\mu(r_1, r_2, \nu)| \leq 1 \quad (2.21)$$

for all values of the arguments n , r_2 , ν . If the magnitude of this function is zero, it means complete incoherence between the field amplitudes at the two points and a value

of unity indicates that the monochromatic field components of frequency ν are perfectly coherent between the points. If magnitude of this **function** is less than unity, it **indicates** less than perfect coherence. As can be seen this **function** depends only on the positions of the points and the single frequency ν that the field components at the two points **share**. Field components of different frequency are always uncorrelated, even at the same point.

(x) Measurement of coherence: Second order coherence is usually measured using some form of interferometer that samples light from two space-time points $(\mathbf{r}_1, \mathbf{t}_1)$ and $(\mathbf{r}_2, \mathbf{t}_2)$ [12,13]. The field intensity of the interference pattern which is measured as a function of the time delay τ between the two beams has the general form

$$\langle I(\mathbf{r}, \tau) \rangle = \langle I^{(1)}(\mathbf{r}, t) \rangle + \langle I^{(2)}(\mathbf{r}, t) \rangle + 2 \left[\sqrt{\langle I^{(1)}(\mathbf{r}, t) \rangle \langle I^{(2)}(\mathbf{r}, t) \rangle} \right] \text{Re} \{ \gamma(\mathbf{r}_1, \mathbf{r}_2, \tau) \} \quad (2.22)$$

Thus, by measuring the average intensities, the real part of the complex degree of coherence can be **determined** [8]. Instead if the spectrum of the interfering beams is monitored, the following expression for the spectral density of light at a point 'r' in the plane of observation is obtained

$$S(\mathbf{r}, \nu) = S^{(1)}(\mathbf{r}, \nu) + S^{(2)}(\mathbf{r}, \nu) + 2 \left[\sqrt{S^{(1)}(\mathbf{r}, \nu) S^{(2)}(\mathbf{r}, \nu)} \right] \times \text{Re} \{ \mu(\mathbf{r}_1, \mathbf{r}_2, \nu) \exp(-2\pi i \nu \tau) \} \quad (2.23)$$

From which the complex degree of spectral coherence can be measured. It is important to note that though the mutual coherence function $\Gamma(\mathbf{r}_1, \mathbf{r}_2, \tau)$ and the cross-spectral density function $\mathbf{W}(\mathbf{r}_1, \mathbf{r}_2, \nu)$ form a Fourier transform pair, the corresponding complex degree of coherence $\gamma(\mathbf{r}_1, \mathbf{r}_2, \tau)$ and the degree of spectral coherence $\mu(\mathbf{r}_1, \mathbf{r}_2, \nu)$ are in general *not* Fourier transforms of each other.

2.3 The laws of interference and the second order correlation phenomenon

Second order coherence effects are due to the correlation that exist between the light vibrations at two space-time points. A precise measure of this correlation can be analyzed using a simple two beam interference experiment where the measurement is made on the average intensity of the interfering beams [2]. Let $\epsilon(\mathbf{r}_1, \mathbf{t})$ and $\epsilon(\mathbf{r}_2, \mathbf{t})$ be the analytic signal representation of the quasi-monochromatic, statistically stationary and ergodic light oscillations at two points \mathbf{P}_1 and \mathbf{P}_2 specified by the position vectors \mathbf{r}_1 and \mathbf{r}_2 respectively at time ' \mathbf{t} '. The light vibrations from the two slit sources on an opaque screen fl interfere at a point $P(\mathbf{r})$ on the screen (B and the resulting intensity distribution of the superposition is measured (Figure 2.2). Assuming the distance ' \mathbf{R} ' between the two sources and screen is large compared to the optical wavelengths, the instantaneous field at the point $P(\mathbf{r})$ is, to a good approximation given by

$$e(\mathbf{r}, \mathbf{t}) = \mathbf{K}_1 \epsilon(\mathbf{r}_1, \mathbf{t} - \mathbf{t}_1) + \mathbf{K}_2 \epsilon(\mathbf{r}_2, \mathbf{t} - \mathbf{t}_2) \quad (2.24)$$

where $\mathbf{t}_1 = \mathbf{R}_1/c$ and $\mathbf{t}_2 = \mathbf{R}_2/c$ are the time of travel from \mathbf{P}_1 and \mathbf{P}_2 respectively to P , \mathbf{K}_1 and \mathbf{K}_2 are constants that depend on the dimensions of the slits and its geometry as $i(\Delta A)/\lambda_0 \mathbf{R}$, (ΔA is the area of each slit, λ_0 is the mean wavelength and R is the average distance $\mathbf{P}_1 P \approx \mathbf{P}_2 P$). The instantaneous intensity at the point $P(\mathbf{r})$ and at time ' \mathbf{t} ' defined by the formula

$$I(\mathbf{r}, \mathbf{t}) = \langle \epsilon^*(\mathbf{r}, \mathbf{t}) \epsilon(\mathbf{r}, \mathbf{t}) \rangle \quad (2.25)$$

under the usual experimental conditions is simplified to

$$I(\mathbf{r}) = I^{(1)}(\mathbf{r}) + I^{(2)}(\mathbf{r}) + 2 \left[\sqrt{I^{(1)}(\mathbf{r}) I^{(2)}(\mathbf{r})} \right] \text{Re} \{ \gamma(\mathbf{r}_1, \mathbf{r}_2, \tau) \} \quad (2.26)$$

where $T = (\mathbf{R}_1 - \mathbf{R}_2)/c$ is the time difference for the light to reach the observation point P from \mathbf{P}_1 and \mathbf{P}_2 and $I^{(1)}(\mathbf{r})$ and $I^{(2)}(\mathbf{r})$ are the average intensities of the light reaching the point P when only one of the slits is open. $\gamma(\mathbf{r}_1, \mathbf{r}_2, \tau)$ is the complex degree of coherence of the light vibrations at the points $\mathbf{P}_1(\mathbf{r}_1)$ and $\mathbf{P}_2(\mathbf{r}_2)$ and is determined from

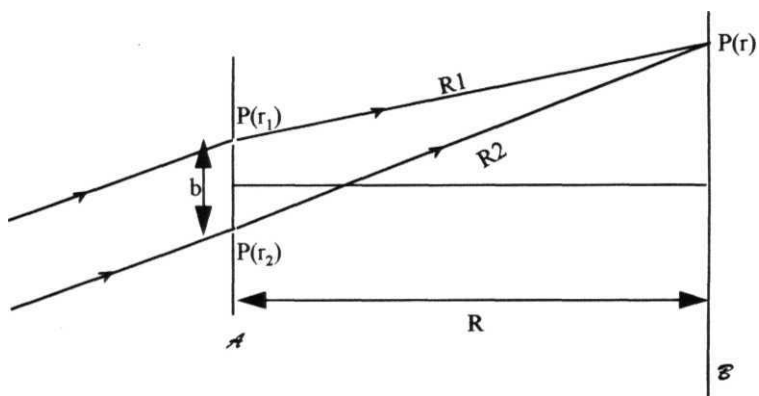


Figure 2.2

Notation **relating** to the Young's double slit experiment used to determine the second order correlation functions of light beams.

the measurement of the averaged intensities using the above equation and 'Re' is its real part.

To verify the fact that it is the absolute value of the complex degree of coherence γ rather than its real part which is the true measure of the *sharpness* of the interference fringes, let

$$\gamma(r_1, r_2, \tau) = |\gamma(r_1, r_2, \tau)| \exp\{i[\alpha(r_1, r_2, \tau)] - 2\pi\nu_0\tau\} \quad (2.27)$$

$$\text{where, } \alpha(r_1, r_2, \tau) = \arg[\gamma(r_1, r_2, \tau)] + 2\pi\nu_0\tau \quad (2.28)$$

Substituting from the above equations in eqn.(2.26), the expression for the averaged intensity becomes

$$\begin{aligned} I(r) &= I^{(1)}(r) + I^{(2)}(r) + 2 \left[\sqrt{I^{(1)}(r) I^{(2)}(r)} \right] |\gamma(r_1, r_2, \tau)| \\ &\times \cos[\alpha(r_1, r_2, \tau) - (2\pi\nu_0\tau)] \end{aligned} \quad (2.29)$$

Using the properties of the envelope representation for the quasi-monochromatic light, the changes in $|y|$ and a due to the changes in the argument T may be neglected provided the change in the distance $(R_1 - R_2)$ is small compared to the coherence length ($l_c = c \tau_c$) of the light. From the above equation it is clear that, over a sufficiently small portion in the plane of observation \mathcal{B} , the averaged intensity will vary nearly sinusoidally with position provided $|y| \neq 0$. The usual measure of the sharpness of the interference fringes is known as the visibility, introduced by Michelson [14]. The visibility of the fringes at the point $P(r)$ in the interference pattern on the screen \mathcal{B} is defined by the formula

$$V(r) = \frac{I_{\max}(r) - I_{\min}(r)}{I_{\max}(r) + I_{\min}(r)}$$

where $I_{\max}(r)$ and $I_{\min}(r)$ are the maximum and minimum values of the averaged intensity in the immediate neighborhood of P . Substituting the corresponding values from eqn.(2.29) in eqn. (2.30), it can be easily deduced that for beams of equal intensities i.e., for $I^{(1)}(r) = I^{(2)}(r)$, the visibility is

$$V(r) = |\gamma(r_1, r_2, \tau)| \quad (2.31)$$

As is well **known**, $0 < |y| < 1$ for all possible values of the arguments of y and the phase of y , given by eqn. (2.28) can be measured from the location of the fringe maxima.

2.4 Partial coherence in the space-frequency domain

Coherence phenomena are customarily described by the space-time correlation functions such as the mutual coherence function $\Gamma(r_1, r_2, \tau)$ or its normalized form, the degree of coherence $\gamma(r_1, r_2, \tau)$. Though this is adequate for the analysis of all the elementary interference and diffraction phenomena with light of any state of coherence, the problem becomes mathematically unwieldy in the treatment of the interaction of light with **matter**. The reason for this is that the interaction of an incident **field** with matter is described more naturally by the frequency response functions like the dielectric constant, refractive **index**, magnetic susceptibility etc. The single frequency description of some of the situation involving the statistical features of the medium becomes inappropriate to analyze using space-time correlation functions of the optical fields. Thus, it is more convenient and also many physical situations involving the coherence properties of light are more appropriately characterized by the space-frequency correlation functions [9]. The space-frequency formulation of coherence theory by Wolf [15], has found many useful applications. For example, in the study of radiation from sources of different states of coherence [16,17], in studies of propagation of partially coherent light beams in dispersive and absorptive media [18], in investigations concerning the effects of spatial coherence on reflection and transmission [19,20], in researches regarding the influence of source correlations on the spectra of the emitted radiation [21], to mention a few.

2.4.1 Second order correlation in the space-frequency domain

Let $e(r,t)$ be the analytic signal representing the fluctuating optical field assumed to be stationary and ergodic at the space-time point (r,t) . This scalar function can be expressed as a generalized Fourier integral with respect to the time variable as

$$e(r,t) = \int_0^{\infty} e(r, \nu) \exp(-2\pi i \nu t) d\nu \quad (2.32)$$

$$e(r, \nu) = \int_{-\infty}^{\infty} e(r, t) \exp(2\pi i \nu t) dt \quad (2.33)$$

Considering the field at two different points r_1 and r_2 at two different frequencies ν and ν' , the product $e^*(r_1, \nu) e(r_2, \nu')$ averaged over the ensembles is written as

$$\langle e^*(r_1, \nu) e(r_2, \nu') \rangle = \iint_{\mathcal{D}} \langle e^*(r_1, t) e(r_2, t') \rangle \exp[2\pi i (\nu' t' - \nu t)] dt dt' \quad (2.34)$$

where, ' \mathcal{D} ' is the domain of the integral which goes from $-x$ to $+x$. Substituting a change of variables $t' = t + \tau$, the above equation can be written as

$$\langle e^*(r_1, \nu) e(r_2, \nu') \rangle = \iint_{\mathcal{D}} \langle e^*(r_1, t) e(r_2, t + \tau) \rangle \exp[2\pi i (\nu' - \nu)t] \exp(2\pi i \nu' \tau) dt d\tau \quad (2.35)$$

In the above expression, $\langle e^*(r_1, t) e(r_2, t + \tau) \rangle$ in the integrand is the mutual coherence function $\Gamma(r_1, r_2, \tau)$ defined by eqn.(2.10) which is independent of time ' t ' for a stationary optical field. The integration with respect to ' t ' yields

$$\int_{-\infty}^{\infty} \exp[-2\pi i (\nu - \nu')t] dt = \delta(\nu - \nu') \quad (2.36)$$

$$\int_{-\infty}^{\infty} \Gamma(r_1, r_2, \tau) \exp(2\pi i \nu \tau) d\tau = W(r_1, r_2, \nu) \quad (2.37)$$

is the **cross-spectral** density function of the optical fields at the points $\mathbf{P}_1(\mathbf{r}_1)$ and $\mathbf{P}_2(\mathbf{r}_2)$. $\mathbf{W}(\mathbf{r}_1, \mathbf{r}_2, \nu) = 0$ for $\nu < 0$ as a result of the analytic signal nature of $\Gamma(\mathbf{r}_1, \mathbf{r}_2, \tau)$. Substituting the above two equations in eqn.(2.35) yields

$$\langle \mathbf{E}^*(\mathbf{r}_1, \nu) \mathbf{E}(\mathbf{r}_2, \nu') \rangle = \delta(\nu - \nu') \mathbf{W}(\mathbf{r}_1, \mathbf{r}_2, \nu) \quad (2.38)$$

It is clear from the above equation that the cross-spectral density function is a measure of the correlation between the spectral fields of any particular frequency component of light vibrations at the points \mathbf{r}_1 and \mathbf{r}_2 . In other words, the above equation implies that the Fourier components of different frequencies ν and ν' are uncorrelated while the strength of the correlation of Fourier components of the same frequency is characterized by the non singular part of the right hand side of eqn.(2.38) i.e., by the cross-spectral density function $\mathbf{W}(\mathbf{r}_1, \mathbf{r}_2, \nu)$. It was shown [22] that the **cross-spectral** density may be expressed in the form of Mercer type series:

$$\mathbf{W}(\mathbf{r}_1, \mathbf{r}_2, \nu) = \sum_n \chi_n(\nu) \psi_n^*(\mathbf{r}_1, \nu) \psi_n(\mathbf{r}_2, \nu) \quad (2.39)$$

where the $\psi_n(\mathbf{r}, \nu)$ are the eigen functions and the $\chi_n(\nu)$ are the eigen values of the equation

$$\int_D \mathbf{W}(\mathbf{r}_1, \mathbf{r}_2, \nu) \psi_n(\mathbf{r}_1, \nu) d^3 r_1 = \chi_n(\nu) \psi_n(\mathbf{r}_2, \nu) \quad (2.40)$$

and the kernel of this integral equation (**cross-spectral** density) is **Hermitian**, i.e.,

$$\mathbf{W}(\mathbf{r}_2, \mathbf{r}_1, \nu) = \mathbf{W}^*(\mathbf{r}_1, \mathbf{r}_2, \nu) \quad (2.41)$$

and the eigen values are real and positive i.e., $\chi_n(\nu) > 0$. The **cross-spectral** density is a non-negative definite, continuous matrix [15], in the sense that, for any positive frequency ν , any set of N position vectors $\mathbf{r}_1, \mathbf{r}_2, \dots, \mathbf{r}_N$, (n being an arbitrary positive integer) and for any set of N complex numbers a_1, a_2, \dots, a_N ,

$$\sum_{j=1}^N \sum_{k=1}^N a_j^* a_k \mathbf{W}(\mathbf{r}_j, \mathbf{r}_k, \nu) \geq 0 \quad (2.42)$$

For $N = 1$, $W(r, r, v) = S(r, v) > 0$, i.e., the spectral density or the power spectrum $S(r, v)$ at any point in the field is non-negative. With the choice $N = 2$, the **eqn.(2.42)** gives an additional condition

$$W(r_1, r_1, v)W(r_2, r_2, v) - W(r_1, r_2, v)W(r_2, r_1, v) \geq 0 \quad (2.43)$$

Making use of this inequality and the Hermiticity relation (eqn.(2.41)), the normalized **cross-spectral** density function is given by

$$\mu(r_1, r_2, v) = \frac{W(r_1, r_2, v)}{\sqrt{W(r_1, r_1, v)W(r_2, r_2, v)}} = \frac{W(r_1, r_2, v)}{\sqrt{S(r_1, v)S(r_2, v)}}$$

In view of the inequality relation (eqn.(2.43)), the normalized cross-spectral density function for all possible values of the arguments r_1, r_2 , and v satisfies the inequality

$$0 \leq |\mu(r_1, r_2, v)| \leq 1 \quad (2.45)$$

As the cross-spectral density function $W(r_1, r_2, v)$ characterizes the field correlation in the space-frequency **domain**, its normalized function **defined** by **eqn.(2.44)**, is known as the complex degree of spectral coherence of the optical field at points $P_1(r_1)$ and $P_2(r_2)$. It is also known as the spectral correlation coefficient at frequency v or complex degree of spatial (or spectral) coherence at frequency v . This quantity plays a similar role in connection with the spectral structure of the fringes obtained when the light from $P_1(r_1)$ and $P_2(r_2)$ are allowed to interfere, as does $\gamma(r_1, r_2, \tau)$ for the distribution of average light intensity $I(r)$ in the interference pattern. The two complex degree of coherence $\gamma(r_1, r_2, \tau)$ and $\mu(r_1, r_2, v)$ which define the field correlation in the **space-time** and space-frequency domains respectively are measures of **different** characteristics of the field. For partially coherent optical fields, the following is the relationship between the two degree of coherence [23]:

$$\gamma(r_1, r_2, \tau) = \int_0^\infty \sqrt{S(r_1, v)S(r_2, v)} \mu(r_1, r_2, v) \exp(-2\pi i v \tau) dv \quad (2.46)$$

The basic interference law given by eqn.(2.29) for partially coherent light beams does not provide any information about the spectral composition of the light forming the interference pattern. The interference law in the **space-frequency** domain that provides spectral information of the interfering beams is derived by considering the two beam interference experiment discussed previously (section 2.3) and illustrated in Figure 2.2. The light fields from the two slits $\mathbf{P}_1(\mathbf{r}_1)$ and $\mathbf{P}_2(\mathbf{r}_2)$ because of **diffraction** and interference reach the point $\mathbf{P}(\mathbf{r})$ in the plane of observation \mathcal{B} . Considering one frequency component of the interference pattern at a time, the Fourier amplitude at $\mathbf{P}(\mathbf{r})$ because of the dispersive effects associated with diffraction is given by the **Kirchhoff** diffraction formula [2] to be

$$\epsilon(\mathbf{r}, \nu) = \mathbf{K}_1(\mathbf{r}_1, \mathbf{r}, \nu) \exp(2\pi i \nu \mathbf{t}_1) \epsilon(\mathbf{r}_1, \nu) + \mathbf{K}_2(\mathbf{r}_2, \mathbf{r}, \nu) \exp(2\pi i \nu \mathbf{t}_2) \epsilon(\mathbf{r}_2, \nu) \quad (2.47)$$

where $\mathbf{K}_1, \mathbf{K}_2$ are complex numbers that depend on the position of the points $\mathbf{P}_1, \mathbf{P}_2, \mathbf{P}$, on the physical dimensions of the slit and on the frequency (explicit form of which is given in section 2.3) and are slowly varying **functions** of position and frequency, $\mathbf{t}_1 = \mathbf{R}_1/c$ and $\mathbf{t}_2 = \mathbf{R}_2/c$ are the time the two interfering beams take to reach from the points \mathbf{P}_1 and \mathbf{P}_2 respectively to the point \mathbf{P} on the screen. The ensemble average of the product $\epsilon^*(\mathbf{r}, \nu) \epsilon(\mathbf{r}, \nu')$ for two different frequencies ν and ν' of the eqn.(2.47) and making use of the **eqn.(2.38)** gives the following expression for the spectral density of the interfering beams in the plane of observation

$$\begin{aligned} \mathbf{W}(\mathbf{r}, \nu) &= |\mathbf{K}_1|^2 \mathbf{W}(\mathbf{r}_1, \nu) + |\mathbf{K}_2|^2 \mathbf{W}(\mathbf{r}_2, \nu) \\ &+ \mathbf{K}_1^* \mathbf{K}_2 \exp[-2\pi i \nu (\mathbf{t}_1 - \mathbf{t}_2)] \mathbf{W}(\mathbf{r}_1, \mathbf{r}_2, \nu) + \mathbf{K}_1 \mathbf{K}_2^* \exp[2\pi i \nu (\mathbf{t}_1 - \mathbf{t}_2)] \mathbf{W}(\mathbf{r}_2, \mathbf{r}_1, \nu) \end{aligned}$$

The **first** term on the right hand side of the above equation

$$|\mathbf{K}_1|^2 \mathbf{W}(\mathbf{r}_1, \nu) \equiv \mathbf{W}^{(1)}(\mathbf{r}, \nu) \equiv \mathbf{S}^{(1)}(\mathbf{r}, \nu) \quad (2.49a)$$

is the spectral density at frequency ν of the light that reaches the point $\mathbf{P}(\mathbf{r})$ from the slit $\mathbf{P}_1(\mathbf{r}_1)$ only, with the other slit kept closed. Similarly, the second term on the right hand side of the eqn (2 48),

$$|K_2|^2 W(r_2, r_2, \nu) \equiv W^{(2)}(r, \nu) \equiv S^{(2)}(r, \nu) \quad (2.49b)$$

represents the spectral density of the light reaching the point P(r) from the slit $P_2(r_2)$ only. The third term of the eqn.(2.48) can be expressed in terms of $S^{(1)}$, $S^{(2)}$ and μ as

$$\begin{aligned} & K_1^* K_2 W(r_1, r_2, \nu) \exp[-2\pi i \nu(t_1 - t_2)] \\ &= \sqrt{S^{(1)}(r, \nu) S^{(2)}(r, \nu)} \mu(r_1, r_2, \nu) \exp[i\alpha - 2\pi i \nu(t_1 - t_2)] \end{aligned} \quad (2.50)$$

and a similar equation for the fourth term also, which is the complex conjugate. In deriving this, the eqns.(2.44) and (2.49) are made use of and α is the phase of $K_1^*(r_1, r, \nu) K_2(r_2, r, \nu)$ which is real to a first approximation and depends on the position and frequency only weakly. Substituting the eqns.(2.49) and (2.50) into the eqn.(2.48) and making use of the Hermiticity relation for the cross-spectral density (eqn.(2.41)), gives the following expression for the spectral density of the light at the point P(r) in the plane of observation \mathcal{O} ,

$$\begin{aligned} S(r, \nu) &= S^{(1)}(r, \nu) + S^{(2)}(r, \nu) \\ &+ 2\sqrt{S^{(1)}(r, \nu) S^{(2)}(r, \nu)} \operatorname{Re}\{\mu(r_1, r_2, \nu) \exp[i\alpha - 2\pi i \nu \tau]\} \end{aligned}$$

where $\tau = (t_1 - t_2)$ and 'Re*' is the real part. This equation is known as the *spectral interference law* [9] for partially coherent beams. It is clear from the equation that the spectral density $S(r, \nu)$ of the light reaching the observation point P(r) is not just the sum of the spectral densities $S^{(1)}(r, \nu)$ and $S^{(2)}(r, \nu)$ of the two beams reaching the point from the two slits, but differs from it depending on the complex degree of spectral coherence $\mu(r_1, r_2, \nu)$ of the light at the two slits. The spectral interference law (eqn.(2.51)) may also be considered as expressing the energy distribution as a function of frequency in the interference pattern obtained by superposition of the light from the two slits.

The spectral visibility, which is a measure of the sharpness of the interference fringe pattern depends on the absolute value of the complex degree of spectral coherence. This can be derived by writing the complex degree of spectral coherence in the following form:

$$\mu(\mathbf{r}_1, \mathbf{r}_2, \nu) = |\mu(\mathbf{r}_1, \mathbf{r}_2, \nu)| \exp[i\beta(\mathbf{r}_1, \mathbf{r}_2, \nu)] \quad (2.52)$$

Substituting eqn.(2.52) into **eqn.(2.51)**,

$$\begin{aligned} S(\mathbf{r}, \nu) &= S^{(1)}(\mathbf{r}, \nu) + S^{(2)}(\mathbf{r}, \nu) \\ &+ 2\sqrt{S^{(1)}(\mathbf{r}, \nu)S^{(2)}(\mathbf{r}, \nu)} |\mu(\mathbf{r}_1, \mathbf{r}_2, \nu)| \cos[\beta(\mathbf{r}_1, \mathbf{r}_2, \nu) - (2\pi\nu\tau - \alpha)] \end{aligned} \quad (2.53)$$

The cosine term within the bracket depends on the positions $\mathbf{r}_1, \mathbf{r}_2$, \mathbf{r} and on the frequency ν and denotes the phase difference introduced between the light from the two slits by their passage from the slits to the point P. Assuming that the plane of observation \mathcal{B} is far away from the plane \mathcal{A} of the two slits, the spectral densities $S^{(1)}(\mathbf{r}, \nu)$, $S^{(2)}(\mathbf{r}, \nu)$ and μ will vary slowly with the position of the point P(\mathbf{r}). Hence the sinusoidal variations in the spectral density at the point P(\mathbf{r}) is possible provided $\mu(\mathbf{r}_1, \mathbf{r}_2, \nu) \neq 0$. Even when the two interfering beams have the same spectral densities and equal to the source **spectrum**, i.e., $S^{(1)}(\mathbf{r}, \nu) = S^{(2)}(\mathbf{r}, \nu) = S_0(\mathbf{r}, \nu)$, the spectral distribution of the superposed light beams will in general be different. With this **condition**, the eqn.(2.53) simplifies to

$$S(\mathbf{r}, \nu) = 2S_0(\mathbf{r}, \nu) \left\{ 1 + |\mu_{12}(\nu)| \cos[\beta_{12}(\nu) - (2\pi\nu\tau - \alpha)] \right\} \quad (2.54)$$

where the explicit dependence on the positions \mathbf{r}_1 and \mathbf{r}_2 are incorporated in the suffixes of the appropriate quantities. The maximum and minimum values of the above equation given for the values of the cosine term equal to either '0' or ' π ' are respectively

$$S_{\max}(\mathbf{r}, \nu) = 2S_0(\mathbf{r}, \nu) \left\{ 1 + |\mu_{12}(\nu)| \right\} \quad (2.55a)$$

$$\text{and } S_{\min}(\mathbf{r}, \nu) = 2S_0(\mathbf{r}, \nu) \left\{ 1 - |\mu_{12}(\nu)| \right\} \quad (2.55b)$$

By analogy with the definition (2.30) for the visibility of the interference fringes, the spectral visibility $V(\mathbf{r}, \nu)$ at frequency ν at a point P(\mathbf{r}) in the spectral fringe pattern is defined by the formula

$$V(r, v) = \frac{S_{\max}(r, v) - S_{\min}(r, v)}{S_{\max}(r, v) + S_{\min}(r, v)} \quad (256)$$

Substituting the maximum and minimum spectral densities from the eqn.(2 55), the eqn.(2.56) reduces to

$$V(r, v) = |\mu_{12}(v)| \quad (2.57)$$

i.e., the spectral visibility of the fringes is equal to the absolute value of the complex degree of spectral coherence. The phase $\beta_{12}(v)$ of $\mu_{12}(v)$ is also related to the distribution of the spectral density of the light in the plane of observation. The maxima of the spectral density are to a good approximation located at points for which

$$\arg[\mu_{12}(v)] \equiv \beta_{12}(v) = (2\pi v\tau - \alpha) + 2\pi m, m = 0, \pm 1, \pm 2, \dots \quad (2.59)$$

From the measurement of the position of the fringe **maxima**, the argument of the complex degree of spectral coherence or the phase difference $\beta_{12}(v)$ between the light beams at the slits $P_1(r_1)$ and $P_2(r_2)$ can be obtained.

2.5 Quasi-homogeneous source and the degree of spectral coherence

Real physical sources having **finite** size are treated more elegantly by assuming them to belong to the class of statistically quasi-homogeneous (QH) sources [24]. The light intensity distribution across this kind of sources vary slowly with **position**, remaining constant over distances of the order of the correlation length of the light vibrations in the source plane. The degree of spectral coherence in the far field of the QH sources is equal to the normalized two dimensional spatial Fourier transform of the intensity distribution across the source. This reciprocity theorem is identical with the far-zone form of the classic theorem by the **van-Cittert** and Zernike [2], that gives the degree of **coherence** of light from a spatially incoherent source.

For a statistically stationary light distribution in some plane $z = 0$, the **cross-spectral density function** of the light at some frequency ν at two points \mathbf{P}_1 and \mathbf{P}_2 in that plane specified by the position vectors \mathbf{r}_1 and \mathbf{r}_2 is given in terms of the spectral density $S(r)$ of the light at the point $P(r)$ and the complex degree of spectral coherence $\mu(\mathbf{r}_1, \mathbf{r}_2, \nu)$ by eqn.(2.44)

$$W(\mathbf{r}_1, \mathbf{r}_2, \nu) = \sqrt{S(\mathbf{r}_1, \nu)S(\mathbf{r}_2, \nu)}\mu(\mathbf{r}_1, \mathbf{r}_2, \nu) \quad (2.59)$$

Based on the requirement that the degree of spectral coherence depends on the position vectors \mathbf{r}_1 and \mathbf{r}_2 only through their difference $\mathbf{r}' = (\mathbf{r}_1 - \mathbf{r}_2)$ and the condition that for sources of finite extent, the spectral density considered as a function of $r = \mathbf{r}_1 + \mathbf{r}_2$ varies slowly across the source, the above eqn.(2.59) can be written in a simpler form

$$W(\mathbf{r}_1, \mathbf{r}_2, \nu) = S(r/2, \nu)g(\mathbf{r}', \nu) \quad (2.60)$$

When the cross-spectral density function of the light across the source can be expressed in the above **form**, the source is said to be quasi-homogeneous. The function $S(r)$ is a *slow* function of r and $g(\mathbf{r}')$ is said to be a *fast* function of \mathbf{r}' . The treatment is based on the assumption that the sources are considered QH as long as the conditions on $S(r)$ and $g(\mathbf{r}')$ are satisfied elsewhere in the source area and the departure from true **quasi-homogeneity** is negligible at the **boundaries** of the source.

To derive the far zone behavior of the field generated by a QH source, located at $z = 0$ and radiating into the **half-space** $z > 0$ (Figure 2.3), consider the cross-spectral density function $W(\mathbf{r}_1, \mathbf{r}_2, \nu)$ given by eqn.(2.38) as the ensemble average of the light fields at two points \mathbf{P}_1 and \mathbf{P}_2 specified by their position vectors

$$\mathbf{r}_1 = r_1 \mathbf{a}_1 \text{ and } \mathbf{r}_2 = r_2 \mathbf{a}_2 \quad (2.61)$$

where \mathbf{a}_1 and \mathbf{a}_2 are the unit vectors pointing from the origin 'O' to the points \mathbf{P}_1 and \mathbf{P}_2 respectively. The light field ensemble in the half-space $z > 0$, can be represented in the form of an angular spectrum of plane waves [25], i.e.,

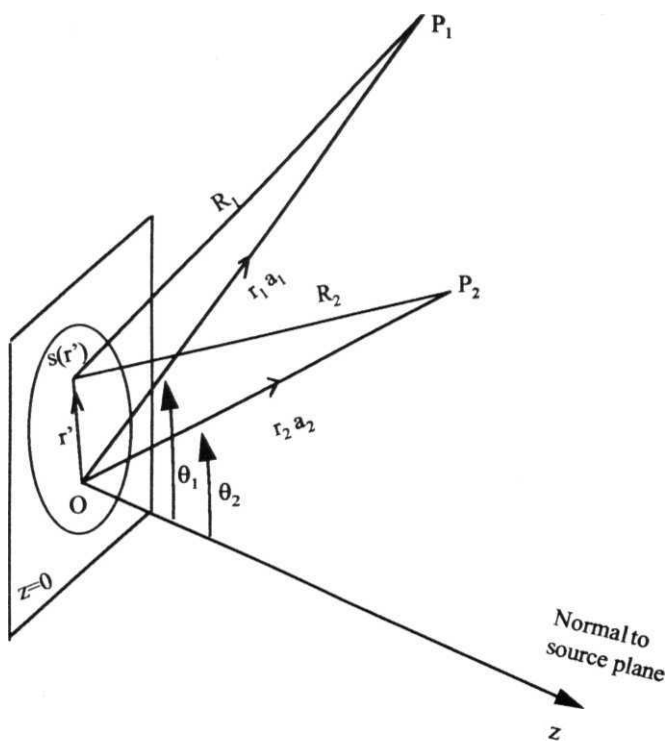


Figure 2.3

Illustration of notation relating to the far-zone behavior of the **field** generated by the source.

$$\mathbf{e}(\mathbf{r}, \nu) = \int \zeta(\mathbf{a}_\perp, \nu) \exp\left(i\mathbf{k} \cdot \hat{\mathbf{a}} \cdot \mathbf{r}\right) d^2 \mathbf{a}_\perp \quad (2.62)$$

where $\hat{\mathbf{a}} \equiv (\mathbf{a}_x, \mathbf{a}_y, \mathbf{a}_z)$, $\mathbf{a}_\perp \equiv (\mathbf{a}_x, \mathbf{a}_y, 0)$

$\mathbf{a}_z = (1 - \mathbf{a}_x^2 - \mathbf{a}_y^2)^{1/2}$, if $\mathbf{a}_x^2 + \mathbf{a}_y^2 \leq 1$ for homogeneous plane waves,

$\mathbf{a}_z = i(\mathbf{a}_x^2 - \mathbf{a}_y^2 - 1)^{1/2}$, if $\mathbf{a}_x^2 + \mathbf{a}_y^2 > 1$ for evanescent plane waves

and $k = 2\pi\nu/c$

The suffixes x, y, z label the components with respect to the fixed Cartesian rectangular coordinate system. Eqn (2.62) expresses the field $\mathbf{e}(\mathbf{r}, \nu)$ as a superposition of homogeneous and evanescent plane waves decaying exponentially in amplitude with increasing distance from the $z = 0$ plane. The **cross-spectral density function** (eqn.(2.38)) can be expressed in terms of the angular spectrum of plane waves [26] by substituting eqn.(2.62) in (2.38). Interchanging the order of integration and averaging, the equation is simplified to

$$\mathbf{W}(\mathbf{r}_1, \mathbf{r}_2, \nu) = \iint Z(\mathbf{a}_{1\perp}, \mathbf{a}_{2\perp}, \nu) \exp\left[i\mathbf{k}(\mathbf{a}_{1\perp}^* \cdot \mathbf{r}_1 - \mathbf{a}_{2\perp} \cdot \mathbf{r}_2)\right] d^2 \mathbf{a}_{1\perp} d^2 \mathbf{a}_{2\perp} \quad (2.63)$$

$\mathbf{a}_{1\perp}$ and $\mathbf{a}_{2\perp}$ are the projections of \mathbf{a}_1 and \mathbf{a}_2 onto the source plane. The angular correlation function [25] is defined by the formula

$$Z(\mathbf{a}_{1\perp}, \mathbf{a}_{2\perp}, \nu) \delta(\nu - \nu') = \langle \zeta^*(\mathbf{a}_{1\perp}, \nu) \zeta(\mathbf{a}_{2\perp}, \nu) \rangle \quad (2.64)$$

which represents the correlation between the two plane waves of the field, denoted by the two dimensional vectors $\mathbf{a}_{1\perp}$ and $\mathbf{a}_{2\perp}$. The angular correlation function may be expressed in terms of the cross-spectral density function of the field at pairs of points $\rho_1 = (x_1, y_1, 0)$ and $\rho_2 = (x_2, y_2, 0)$ in the source plane. This is derived by letting $\mathbf{r}_1 \rightarrow \rho_1$ and $\mathbf{r}_2 \rightarrow \rho_2$ in the eqn.(2.63) and taking the Fourier inverse of the resulting formula, which gives, after change of variables and integration

$$Z(\mathbf{a}_{1\perp}, \mathbf{a}_{2\perp}, \nu) = k^4 \tilde{\mathbf{W}}^{(0)}(\mathbf{k}\mathbf{a}_{1\perp}, -\mathbf{k}\mathbf{a}_{2\perp}, \nu) \quad (2.65)$$

where $W^{(0)}$ is the four dimensional Fourier inverse of $W^{(0)}$. Equation (2.65) gives the angular correlation function and applies to the field generated by any planar, statistically stationary, secondary source.

The far-zone behavior of this field or the asymptotic behavior of the cross-spectral density function is determined by letting the distances of the two points $P_1(r_1)$ and $P_2(r_2)$ to infinity, i.e., $kr_1 = kr_2 \rightarrow \infty$. This asymptotic limit denoted by $W^{(\infty)}(r_1, r_2, v)$ may be expressed in terms of the four-dimensional spatial Fourier inverse $W^{(0)}$ of $W^{(0)}$ by the formula

$$W^{(\infty)}(r_1, r_2, v) = (2\pi k)^2 \cos\theta_1 \cos\theta_2 \tilde{W}^{(0)}(ka_{1\perp}, -ka_{2\perp}, v) \frac{\exp[ik(r_1 - r_2)]}{r_1 r_2} \quad (2.66)$$

θ_1 and θ_2 are the angles the unit vectors \hat{a}_1 and \hat{a}_2 make with the normal to the source plane, $\cos\theta_1 = z_1/r_1$ and $\cos\theta_2 = z_2/r_2$. For a QH light source at the source plane ($z = 0$), according to eqn.(2.60)

$$\tilde{W}^{(0)}(ka_{1\perp}, -ka_{2\perp}, v) = g \left[\frac{1}{2} k(a_{1\perp} + a_{2\perp}) \right] \tilde{S}^{(0)}[k(a_{1\perp} - a_{2\perp})] \quad (2.67)$$

Substituting the eqn.(2.67) into (2.66), the following expression for the cross-spectral density function of the light in the far-zone of a QH source is obtained to be

$$W^{(\infty)}(r_1, r_2, v) = (2\pi k)^2 \cos\theta_1 \cos\theta_2 g \left[\frac{1}{2} k(a_{1\perp} + a_{2\perp}) \right] \times \tilde{S}^{(0)}[k(a_{1\perp} - a_{2\perp})] \frac{\exp[ik(r_1 - r_2)]}{r_1 r_2} \quad (2.68)$$

Using the above equation, the spectral density $S^{(\infty)}(r, v)$ at a typical point in the far-zone is given by

$$S^{(\infty)}(r, v) = W^{(\infty)}(r, r, v) = (2\pi k)^2 \tilde{S}^{(0)}(0) g^2(ka_{\perp}) \frac{\cos^2 \theta}{r^2} \quad (2.69)$$

The complex degree of spectral coherence of the light in the far zone is defined by the equation

$$\mu^{(\infty)}(r_1, r_2, \nu) \equiv \frac{W^{(\infty)}(r_1, r_2, \nu)}{\sqrt{S^{(\infty)}(r_1, \nu) S^{(\infty)}(r_2, \nu)}} \quad (2.70)$$

Substituting from the eqns.(2.68) and (2.69) on the right hand side of the above equation

$$\mu^{(\infty)}(r_1, r_2, \nu) = \frac{\tilde{S}^{(v)} \left[k(a_{1\perp} - a_{2\perp}) \right]}{\tilde{S}^{(0)}} \tilde{G}^{(0)}(ka_{1\perp}, ka_{2\perp}) \exp[ik(r_1 - r_2)] \quad (2.71)$$

$$\text{where, } \tilde{G}^{(0)}(ka_{1\perp}, ka_{2\perp}) = \frac{\tilde{g}^{(0)} \left[\frac{1}{2} k(a_{1\perp} + a_{2\perp}) \right]}{\sqrt{\tilde{g}^{(0)}(ka_{1\perp}) \tilde{g}^{(0)}(ka_{2\perp})}} \quad (2.72)$$

In view of the reciprocity inequality [24] involving the effective width of the Fourier

transform pairs for a QH source, $\tilde{g}^{(0)}(f)$ is considered a slow function of 'f' compared

to the $\tilde{S}^{(0)}(f)$ which is a fast function of f and also $\tilde{g}^{(0)}(ka_{1\perp}, ka_{2\perp}) \approx \tilde{g}^{(0)}(ka_{2\perp}, ka_{1\perp}) = 1$ Using this, the complex degree of spectral

coherence of the light in the far-zone of a QH planar source is given by

$$\mu^{(\infty)}(r_1, r_2, \nu) = \frac{\tilde{S}^{(0)} \left[k(a_{1\perp} - a_{2\perp}) \right]}{\tilde{S}^{(0)}} \exp[ik(r_1 - r_2)] \quad (2.73)$$

as a product of a simple phase factor and the normalized Fourier transform of the distribution of optical spectral intensity across the source (eqn.(2.73)).

This result is compared to be identical with the far-zone form of the van Cittert and Zernike theorem for the spatially incoherent light. The result is illustrated for a **QH source with the** assumption that the **source** size is large compared to the

wavelength i.e., $(\delta a)_\sigma \gg X$. In the asymptotic limit when the distances \mathbf{r}_1 and \mathbf{r}_2 are sufficiently large,

$$\mathbf{r}_1 \ll \mathbf{R}_1 - \mathbf{a}, \cdot \mathbf{r}', \mathbf{r}_2 \approx \mathbf{R}_2 - \mathbf{a}_2 - \mathbf{r}' \quad (2.74)$$

where \mathbf{R}_1 and \mathbf{R}_2 are the distances from the point $\mathbf{s}(\mathbf{r}')$ on the source to the points $\mathbf{P}_1(\mathbf{r}_1)$ and $\mathbf{P}_2(\mathbf{r}_2)$, respectively (Fig.(2.3)). Substituting eqn.(2.74) into eqn.(2.73) and integrating over the entire radiating surface of the planar secondary QH source a , on simplification leads to

$$\mu^{(\infty)}(\mathbf{R}_1, \mathbf{R}_2, \nu) = \exp[ik(\mathbf{R}_1 - \mathbf{R}_2)] \frac{\int_\sigma S(\mathbf{r}') \exp[ik(\mathbf{a}_2 - \mathbf{a}_1) \cdot \mathbf{r}'] d^2 r'}{\int_\sigma S(\mathbf{r}') d^2 r'} \quad (2.75)$$

For a QH source, the intensity across the source varies slowly with position or remains a constant over the correlation length of the light from the source plane. Thus, integral of $S(\mathbf{r}')$ over the source area remains a constant. Assuming that the points $\mathbf{P}_1(\mathbf{r}_1)$ and $\mathbf{P}_2(\mathbf{r}_2)$ are situated at equal distance from the origin \mathbf{O} of the source i.e., $\mathbf{r}_1 = \mathbf{r}_2 = \mathbf{r}$, the eqn.(2.75) reduces to

$$\mu(\mathbf{R}_1, \mathbf{R}_2, \nu) = \int_{\mathbf{r}' \in a} \exp[-ik(\mathbf{a}_1 - \mathbf{a}_2) \cdot \mathbf{r}'] d^2 r' \quad (2.76)$$

This integral is similar in form to the Fraunhofer diffraction integral [2]. The source is considered to be a rectangular aperture of sides $2a$ and $2b$ with the origin at the centre of the rectangle and with axes $\mathbf{O}\xi$ and $\mathbf{O}\eta$ parallel to the sides. The points $\mathbf{P}_1(\mathbf{R}_1)$ and $\mathbf{P}_2(\mathbf{R}_2)$ with coordinates (X_1, Y_1) and (X_2, Y_2) are considered in the plane parallel to the source in the far field. With $\mathbf{a}_{1\perp} = (X_1, Y_1, 0)$ and $\mathbf{a}_{2\perp} = (X_2, Y_2, 0)$ and approximating the distances so that $(X_1 - X_2)/R = p$ and $(Y_1 - Y_2)/R = q$, the above integral can be simplified

to

$$\mu(\mathbf{R}_1, \mathbf{R}_2, \nu) = \int_{-a-b}^{+a+b} \int_{-a-b}^{+a+b} \exp[-ik(p\xi + q\eta)] d\xi d\eta = \left(\frac{\sin(kpa)}{(kpa)} \right) \left(\frac{\sin(kpb)}{(kpb)} \right)$$

which gives the explicit form of the complex degree of spectral **coherence** for a planar, secondary, quasi-homogeneous source in terms of the source dimensions, the separation between the points in the plane of observation and the frequency range of the source.

2.6 Spectral impurity of beams

In the two beam interference experiment considered so far, let the two light beams emerging from the slits \mathbf{P}_1 and \mathbf{P}_2 have the same spectral distribution. Now, if the spectrum of the superposed light at the screen \mathcal{B} far from the plane containing the two slits is examined, it is in general found to have different spectral composition at different points on the screen. From an analysis of the spectral composition of the superposed light beams, the spectral purity of the interfering beams can be known. Two light beams of same normalized spectral density are referred to as *spectrally pure*, when their superposition (with path difference $T \ll 1/5\nu$) reproduces the same spectral distribution [27]. Conversely, the beams are called *spectrally impure* if they do not have this property.

To examine the spectral purity of the light **distribution**, resulting from the superposition of the two light beams from \mathbf{P}_1 and \mathbf{P}_2 , consider the interference equation (eqn. 2.48) in terms of the spectral density function $W(r, r, \nu)$. For the ease of analysis, this equation is written in a simplified form as

$$W(\nu) = |\mathbf{K}_1|^2 W_{11}(\nu) + |\mathbf{K}_2|^2 W_{22}(\nu) + 2\mathbf{K}_1^* \mathbf{K}_2 W_{12}(\nu) \exp(-2\pi i \nu \tau) \quad (2.78)$$

Using the normalized spectral density function given by eqn.(2.44), the above equation can be rewritten in terms of the degree of spectral coherence

$$W(\nu) = |\mathbf{K}_1|^2 S(r_1, \nu) \mu_{11}(\nu) + |\mathbf{K}_2|^2 S(r_2, \nu) \mu_{22}(\nu) + 2\mathbf{K}_1^* \mathbf{K}_2 \sqrt{S(r_1, \nu) S(r_2, \nu)} \mu_{12}(\nu) \exp(-2\pi i \nu \tau) \quad (2.79)$$

The above equation is known as the auto-power spectrum of the interfering beams. The normalized auto-power spectrum on simplification can be written as

$$\mu(\nu) = \frac{W(\nu)}{W^{(0)}(\nu)} = \frac{\mu_{11}(\nu) + \operatorname{Re}[K_{12}\mu_{12}(\nu)\exp(-2\pi i\nu\tau)]}{\mu_{11}(\nu) + \operatorname{Re}[K_{12}\mu_{12}(\nu)]} \quad (2.80)$$

$$\text{Where } K_{12} = \frac{2K_1^* K_2 \sqrt{S(r_1, \nu)S(r_2, \nu)}}{|K_1|^2 S(r_1, \nu) + |K_2|^2 S(r_2, \nu)} \quad (2.81)$$

Equation (2.80) can be rewritten as

$$\mu(\nu) = \frac{1 + \operatorname{Re}\{K_{12}\mu_{12}(\nu)\exp(-2\pi i\nu\tau)\}}{1 + \operatorname{Re}[K_{12}\mu_{12}(\nu)]}$$

with $\mu_{11}(\nu) = 1$, for the spectral coherence between self similar points. Examination of this equation makes it clear that the spectral densities of the input and output light beams can not be equal for all possible values of x . Since, for values of path **difference** $\tau \ll 1/5\nu$, the spectral changes are not very appreciable, the beams forming the interference are considered spectrally pure with the validity of the reduction formula [27]. However, for large path differences between the interfering **beams**, the term within the bracket oscillates with increasing τ . Thus it is clear that for partially coherent light, the original spectral distribution corresponding to $u(\nu) = 1$ can not be recovered in an interference experiment with large path differences, when the cosine modulation of the spectrum starts appearing. Such beams are called spectrally impure. Let the exponential term within the bracket equals $B(\nu)$, which represents the departure of the beams from the condition for cross-spectral purity. This quantity, integrated over all frequencies is a **useful** criterion for the measurement of the departure from cross-spectral purity. Though the assumption is been made that $B(\nu)$ is a finite quantity, there are certain frequencies ν_k ($k = 1, 2, \dots$) within the bandwidth 6ν for which $B(\nu)$ is zero. The frequencies ν for which the spectra coincide depend on the x values and is given by

$$2\pi\nu\tau = \left(n + \frac{1}{2}\right)\pi, \quad n = 0, \pm 1, \pm 2, \dots \quad (2.83)$$

The difference between the spectrally pure and spectrally impure beams can be made clear by considering the interference of partially coherent beams. The correlation

between the interfering beams leads to both intensity and spectral modulations and both are periodic with the path **difference**. In the Young's double slit experiment with white light, the interference **fringes** have detailed periodic coloring as the spectral composition of the **each** single **fringe** is different. Then the beams are said to be spectrally impure. However in the Michelson interferometer with white light when the path difference is close to zero, the fringes appear colored and the gradual change of color over a range of several fringes is not periodic. The interfering beams are of high cross-spectral purity as the spectra of the individual colored fringe remain the same as the input beam. However as the path difference is increased to more than the coherence length of the source, the beam becomes cross-spectrally impure.

2.7 Complete coherence in space-frequency domain

When the absolute value of the complex degree of spectral coherence $\mu(\mathbf{r}_1, \mathbf{r}_2, \mathbf{v})$ given by eqns.(2.45) and (2.57), equals the upper limit of unity, the spectral fringes will have the maximum visibility and this limiting case represents the complete second-order coherence [28]. The functional form of the cross-spectral density $\mathbf{W}(\mathbf{r}_1, \mathbf{r}_2, \mathbf{v})$ and the spectral degree of coherence $\mu(\mathbf{r}_1, \mathbf{r}_2, \mathbf{v})$ for the case of complete coherence can be derived as follows. According to the non-negative **definiteness** condition for the **cross-spectral density** given by eqn.(2.42) and its relation to the degree of spectral coherence (eqn.(2.44), the complex degree of spectral coherence should also satisfy the inequality

$$\sum_{j=1}^N \sum_{k=1}^N \mathbf{a}_j^* \mathbf{a}_k \mu(\mathbf{r}_j, \mathbf{r}_k, \mathbf{v}) \geq 0 \quad (2.84)$$

for all positive integers N , any set of points $\mathbf{n}, \mathbf{r}_2, \dots, \mathbf{r}_N$, and set of real or complex numbers $\mathbf{a}_1, \mathbf{a}_2, \dots, \mathbf{a}_N$. The properties of the degree of spectral coherence function $\mu(\mathbf{r}_1, \mathbf{r}_2, \mathbf{v})$ that are used here are, its **Hermiticity**, the degree of spectral coherence between same points is unity and its modulus is unity for spatially fully coherent **field** at some fixed **frequency** $\mathbf{v}_0 (> 0)$ and are expressed as

$$\begin{aligned}
\mu_{kj} &= \mu_{jk}^* \\
\mu_{jj} &= 1 \\
|\mu(r_1, r_2, v_0)| &= 1
\end{aligned} \tag{2.85}$$

Using these conditions, the inequality (eqn.(2.84)) reduces to

$$\operatorname{Re}[\mu_{12}\mu_{23}\mu_{13}^*] \geq 1 \tag{2.86}$$

and applying the last condition of eqn.(2.85), μ_{jk} may be expressed in the form

$$\mu_{jk} = \exp(i\phi_{jk}) \tag{2.87}$$

where ϕ_{jk} is real, Hermitian and satisfies the inequality

$$\cos(\phi_{12} - \phi_{32} + \phi_{31}) \geq 1 \tag{2.88}$$

with a maximum value of unity when its argument is equal to $2\pi m$. Considering the origin to be at an arbitrary point, the spectral degree of coherence can be written as

$$\mu(r_1, r_2, v) = \exp[-i\beta(r_1, v_0) + i\beta(r_2, v_0)] \tag{2.89}$$

where $\beta(r, v_0) = \phi(0, r, v_0)$. Thus, for a fully spatially coherent field at some particular frequency v_0 given by the last of the eqn.(2.85), the degree of spectral coherence has the form given by eqn.(2.89), with $\beta(r, v_0)$ a real function of position. Recalling the definition of the degree of spectral coherence (eqn.(2.44)), the cross-spectral density function at frequency v_0 can be expressed in the factored form

$$\begin{aligned}
W(r_1, r_2, v_0) &= \varphi^*(r_1, v_0)\varphi(r_2, v_0) \\
\text{where, } \varphi(r, v_0) &= \sqrt{S(r, v_0)} \exp[i\beta(r, v_0)]
\end{aligned} \tag{2.90}$$

with $S(r, v_0)$ representing the spectral density at frequency v_0 at a point 'r' and $\beta(r, v_0)$ is the phase factor.

References

- [1] **L Mandel and E. Wolf**, Rev. Mod. Phys. 37, **231**, (1965).
- [2] M. Born and E. **Wolf**, Principles of optics, (**Pergamon**, Oxford, **1980**).
- [3] **J. Perina**, Coherence of light, (Van **Nostrand**, **London**, **1971**).
- [4] A.S. Marathay, Elements of optical coherence theory, (Wiley, NY, 1982).
- [5] **J.W. Goodman**, Statistical optics, (Wiley, NY, 1985).
- [6] W.H. Carter, in **J Opt. Soc. Am. Handbook of optics**, Edited by M. Bass, (**McGraw Hill**, NY, 1995).
- [7] **L. Mandel**, J. Opt. Soc. Am. 57, 613, (1967).
- [8] **L. Mandel and E. Wolf**, in Optical coherence and Quantum optics, (Cambridge Press, **1995**), Chapters 4 and 5.
- [9] **L. Mandel and E. Wolf**, J. Opt. Soc. Am. 66, 529, (1976).
- [10] E. Wolf and W.H. Carter, Opt. **Commun.** 16, 297, (1976).
- [11] **M.J. Bastiaans**, Opt. Acta 24, **261**, (1977).
- [12] **B J Thompson and E. Wolf**, J. Opt. Soc. Am. 47, 895, (1957).
- [13] W.H. Carter, **Appl. Opt.** 16, 558, (1977).
- [14] A.A. **Michelson**, Phil. Mag. 30, 1, (1890).
- [15] E. Wolf, J. Opt. Soc. Am. 72, 343, (1982); J. Opt. Soc. Am. A 3, 76, (1986).
- [16] E. Collett and E. Wolf, Opt. Lett. 2, 27, (1978).
- [17] F. **Gori**, Opt. Commun. 46, 149, (1983).
- [18] W. Wang and E. Wolf, J. Mod. Opt. 32, 2007, (1992).
- [19] W. Wang and E. Wolf, Opt. Commun. 79, **131**, (1990).

- [20] W. **Wang, R.** Simon and E. **Wolf, J** Opt. Soc. Am. A 9, 287, (1992).
- [21] E. **Wolf**, in International trends in **optics**, Edited by J.W. **Goodmann**, (Academic Press, 1991).
- [22] E. Wolf, Opt. **Commun.** 38, 3, (1981).
- [23] **A.T Friberg and** E. Wolf, Opt. Lett. 20, 623, (1995).
- [24] W.H. Carter and E. **Wolf, J** Opt. Soc. Am. 67, 785, (1977).
- [25] E.W. Marchand and E. Wolf, J. Opt. Soc. Am. 62, 379, (1972).
- [26] E. Wolf and W.H. Carter, Opt. Commun. 50, **131**, (1984).
- [27] **L** Mandel, J. Opt. Soc. Am. 51, 1342, (1961).
- [28] L. Mandel and E. Wolf, Opt. Commun. 36, 247, (1981).

CHAPTER 3

COHERENCE TIME MEASUREMENT AND INTERFERENCE IN COMPLEMENTARY DOMAINS.

3.1 *Introduction*

The main idea of discussing the interference phenomenon in the complementary spaces [1] is to demonstrate and get maximum information from the frequency domain when the corresponding interference is lost in the complementary time domain. In classical optics it is known for many years that interference between light beams manifest themselves as spatial or spectral variations depending on the path difference between the interfering beams [2-7]. Recently there has been considerable amount of work done on the effect of the state of coherence on the emitted spectrum of light sources. The effect appears pronounced in the case of two beam interference and is shown as a shift in the central frequency for narrow bandwidth spectra [8-10] or as cosinusoidal modulations of broad bandwidth spectra [11-13]. This spectral interference phenomenon can be applied to the synthetic aperture imaging technique [14], utilizing the space-frequency equivalence theorem [15]. Similar phenomenon has been observed in the other areas of physics also. By proper postselection procedure, spectral interference fringes are observed for spatial phase shifts larger than the coherence length of the interfering beams in neutron interferometry [16,17]. Rauch has also demonstrated the interference in complementary spaces for matter waves using neutron interferometry [18,19]. Mandel and coworkers have demonstrated quantum interference effects in the space-frequency domain by mixing two down converted signal photons from similar nonlinear LiIO_3 crystals pumped by a single laser source [20].

In this chapter, we demonstrate the optical interference phenomenon in the complementary time and frequency domains by using a home built broad band dye

laser. Different cavity elements are initially tried to look for a suitable bandwidth for the dye laser which will enable us to experimentally observe both spatial and spectral interference fringes using a single source. A broad band **dye** laser, though gives a spatially coherent output, is temporally incoherent because of the short coherence time of the laser ($\tau_c \approx 1/5\nu$). The use of the dye laser with a broad band reflector is mainly to have a small and measurable coherence time (τ_c) which can be used to observe the transition of the interference effects from the **space-time** to space-frequency domain as the path delay is increased from zero to more than the coherence length ($l_c = c \tau_c$) of the source. After discussing in detail, the construction and the spectral characteristics of the home built dye laser with different cavity elements, the coherence time τ_c of the broad band source is measured using the time delayed degenerate four wave mixing (TDFWM) experiment. Working in the phase-conjugate geometry, the coherence time of the source is determined from the behavior of the **phase-conjugate** signal with one of the delays. A simple theoretical insight is given into the role the coherence time plays in observing the transition of the interference effects from the time to frequency domain. This is confirmed experimentally and the spectral fringes are further characterized for different time delays larger than τ_c . The technique of utilizing the spectral interference fringes so obtained, known as spectral **interferometry** has been used for varied applications, some of them are demonstrated and discussed in later chapters of this thesis.

3.2 Construction and characterization of dye laser

The versatility and utility of organic dye lasers in science and technology continue to increase even long after the inception of the dye laser [21]. High average power [22] and narrow pulse width [23] dye lasers are developed for communications, atmospheric propagation studies, isotope separation and many other applications. New laser dyes are also being developed which provide high **efficiency** and chemical stability for dye lasers at wavelengths ranging from the near infrared to the ultraviolet [24]. Construction and operation of organic dye lasers depend on the photophysical

and chemical properties of the dye solutions, which are used as the lasing medium [25]. The structural and spectroscopic properties of efficient laser dyes and detailed information on their lasing properties are listed in the data sheets of dye manufacturers [26]. The most important criteria in selecting components for the dye laser system are the chemical inertness and the construction materials [27]. The safest materials that can be used are glass or **quartz**, stainless steel and Teflon.

3.2.1 Dye cell design

The dye cell is one of the most crucial element in the dye laser and involves some difficult machining. The cell must allow easy entry of the pumping light and easy exit of the dye laser radiation. A complete schematic of the dye cell design is given in the Figure 3.1. The dye is allowed to flow through a 3 mm / **15** mm quartz tube to facilitate transverse pumping. The dye solution is made to flow through the dye cell to continuously replace the heated and photodissociated dye molecules from the region of excitation. The cavities of the stainless steel dye cell through which the dye laser beam **exits**, are machined at an angle of about **10°** to avoid the reflection of laser light from the solvent-glass and glass-air interfaces which can cause undesired stimulated emission from the excited dye molecules. The flow tube and the entrance and exit quartz windows are fixed to the dye cell using Neoprene O-rings. The solvent evaporation and the resulting change of dye concentration are nearly eliminated by tightly fixing tubes and the windows.

In organic dye lasers, the upper laser level has a lifetime of 4 to 8 ns. The laser medium thus, cannot store energy for more than a few nanoseconds and consequently the single pass gain is approximately proportional to the instantaneous intensity of the exciting pump. For this reason, the generation of gain sufficient for dye laser oscillation requires pump light which is of high intensity rather than high energy. The pump light source that has been used for the excitation of pulsed dye laser is the second harmonic (532 nm) of the **Q-switched Nd: YAG** laser (CONTINUUM, USA **660B-10**). The laser pulse peak power is typically 20 MW and is of 6 ns duration with

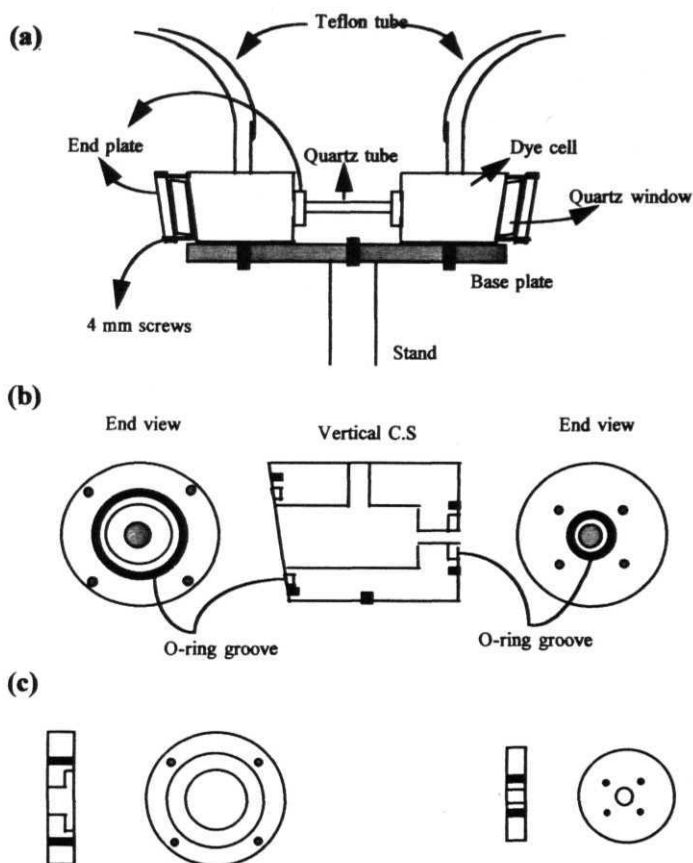


Figure 3.1

Design of the dye cell (a) Full view, (b) Vertical cross-section and end views, (c) End plates

a repetition rate of 10 Hz. 8% of the laser pulse power, divided by a glass plate from the main beam is used to pump the oscillator of the dye laser and the remaining power is **used** for the amplifier. Schematic of the dye laser with different cavity elements **and** a single stage **amplifier**, pumped by the frequency doubled YAG laser is shown in Figure 3.2.

The dye laser is pumped in the transverse pumping arrangement. The pump beam is expanded using a **plano-concave** lens ($f = 50$ mm) and is focused to a nearly rectangular cross section (0.3 mm / 15 mm) using a cylindrical lens ($f = 50$ mm). The focusing is adjusted so that the excited region of the dye solution forms a pencil shaped volume with a nearly circular cross section on the inner wall, parallel to the axis of the dye laser resonator. Since, only a thin layer near the inner wall of the dye cell is excited by the pump light, diffraction usually causes a substantial angular spread of the dye fluorescence, which emerges from the cell in the direction of the dye laser axis.

The most important attribute of dye lasers is the wide selection of dye molecules that are available and can be used in laser devices. Rhodamine 6G (Rh 6G), which was among the **first** to be discovered [28], is still one of the best dyes available for laser applications. Some of the important parameters of this dye and Rhodamine B (Rh B) which are used in our dye laser are given in the **Ref.** [24]. The optimum oscillator concentration for the Rh 6G dye dissolved in methanol is 302×10^{-6} mole/lit. The dye flow system consists of a pump, a reservoir and the dye cell. Filters are provided to remove particulate matter and air bubbles which cause losses to the laser system by scattering of the laser emission.

3.2.2 Performance **of** the dye laser

The dye laser is tuned by providing feedback at the desired wavelength to the pumped dye molecules using a grating [29] or a prism-mirror combination depending on the required peak wavelength and bandwidth of the output laser. The grating used in our configuration is a reflection type holographic grating (Bausch & Lomb) with 600 **grooves/mm** and blazed at 54° . It has five orders of diffraction and is oriented in

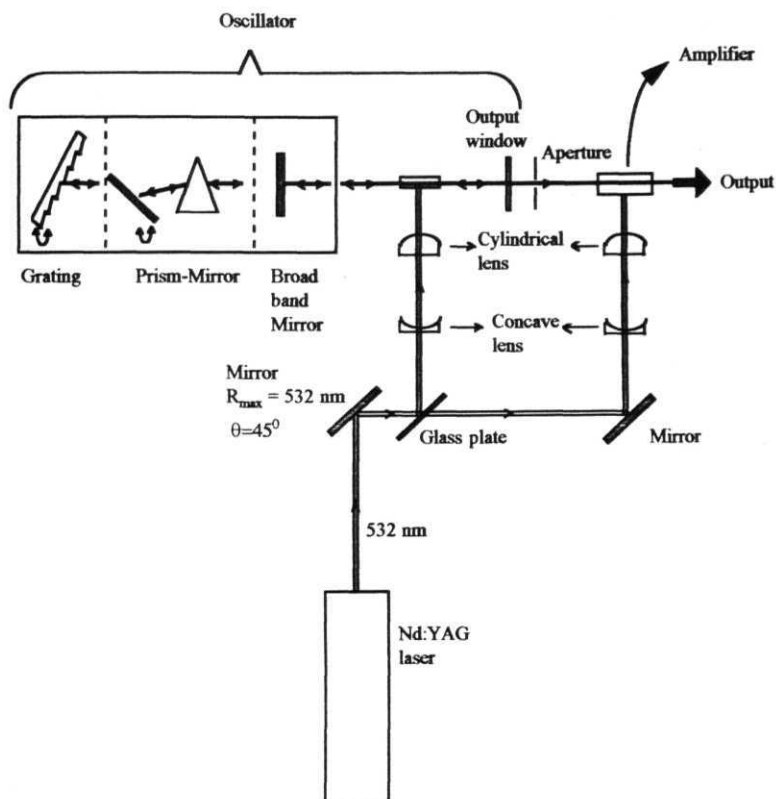


Figure 3.2

Schematic of the dye laser setup with different cavity elements for the oscillator and a single stage **amplifier**.

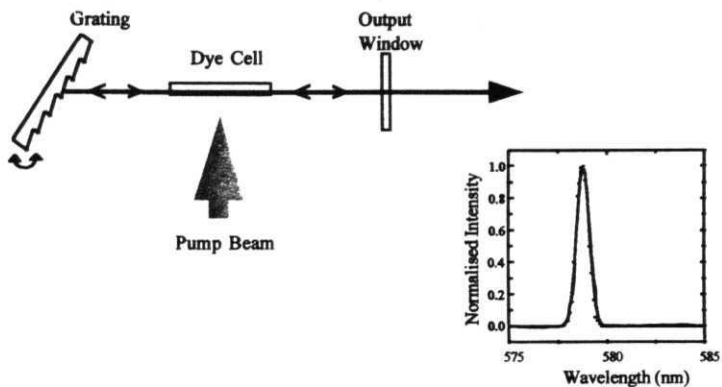
the Littrow position [30], for which the incident light and the diffracted light of a given wavelength lie along the same direction (Figure 3.3 (a)). The wavelength across the dye spectrum can be continuously tuned by rotating the grating with respect to a vertical axis. The spectral line narrowing in the nanosecond (ns) pulse is avoided by using a glass plate (4% **reflectivity**) as the output coupler, which also limits the number of light passes in the cavity during the short excitation time (6 ns) of the laser. A spectroscopic analysis, using a 50 cm grating monochromator (**Jobin-Yvon**, HRS 2) of the output pulses showed them to have any wavelength maximum (λ_0) within the emission spectrum of the dye and a full width at half maximum (**FWHM**), $\delta\lambda$ between **0.1** and **2 nm** depending on the order of the grating used and its distance from the dye cell. A typical spectral recording of the dye laser from 575 to 585 nm with the grating in the 5th order, kept at a distance **of** ~ 20 cm from the dye cell is shown in the inset of Figure 3.3 (a). As the small diameter of the laser **beam**, of the order of a few millimeter, covers only a small area at the surface of the **grating**, there is a reduction in the spectral resolution or an increase in the bandwidth of the output spectrum. The spectrum is fitted using standard least-square fitting procedure to a Gaussian distribution of the form

$$S(\lambda) = \left(\frac{A}{\delta\lambda\sqrt{\pi/2}} \right) \exp \left[\frac{-2(\lambda - \lambda_0)^2}{(\delta\lambda)^2} \right] + Y_0 \quad (3.1)$$

where $A = 0.79$ and $Y_0 = -2.9E-4$ are constants and the fitted values for the maximum wavelength and the bandwidth of the dye laser with the errors are $\lambda_0 = 578.8 \pm 0.11$ **nm**, $\delta\lambda = 0.63 \pm 0.023$ nm.

When a prism-mirror combination of lower spectral resolution than the grating is used as the tuning element, the bandwidth of the output laser increases. The crown glass prism ($n = 1.5793$) is positioned at very high angle of incidence ($\approx 80^\circ$). Through the prism, the beam is dispersed with a simultaneous reduction in the beam divergence. This light is sent back into the laser cavity by a high reflectivity ($R = 99\%$) aluminium coated mirror. Wavelength selection within the bandwidth of the dye emission spectrum is achieved by rotating the tuning mirror with respect to a vertical

(a)



(b)

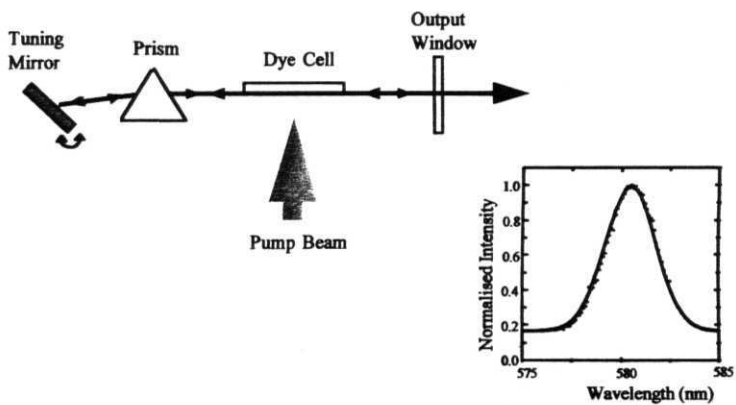


Figure 3.3

Home built dye laser with (a) Grating and (b) **Prism-Mirror** as tuning elements and the corresponding **spectra**.

axis. The experimental setup and a typical recording of the output spectrum (570 - 590 nm) are shown in the Figure 3.3 (b). The fitted values for a Gaussian spectrum (eqn. (3.1)) are $\lambda_0 = 580.5 \pm 0.03 \text{ nm}$ and $\delta\lambda = 2.6 \pm 0.028 \text{ nm}$. As both the dispersive elements, discussed above are used in the low wavelength discrimination modes, the output peak power is low and needs amplification.

3.2.3 Dye amplifier

The dye cell design for the dye amplifier is the same as the oscillator. The amplifier is also transversely pumped for high amplifications, with the remaining pump power after the oscillator [31]. The dye laser oscillator beam enters one end of the active region of the amplifier and exits the opposite end. The dimension of the quartz flow tube in the dye amplifier is 5 mm diameter and 20 mm length. The gain medium is designed to be longer and bigger for the laser emission to be amplified upto saturation intensities. The single pass traveling light amplifier is the simplest and gives an accurate reproduction of the input signal [32]. The high gain and wide bandwidth makes the dye solutions **useful** for such applications. Strongly excited dye solutions of appropriate concentration are proved to have large gain coefficient. The optimised concentration for Rh 6G dye in methanol that has been used in the amplifier is $128 \times 10^{-6} \text{ mole/lit}$. The large amplified stimulated emission (ASE), owing to high value of stimulated emission cross section produced in one stage is reduced from reaching the next stage by using pinhole spatial filters. Equal amplification over the entire circular cross-section of the input beam is achieved by, (i) adjusting the amplifier cell position so that the input light beam from the oscillator goes through the maximum amplification region without getting obstructed on the cell walls, (ii) properly adjusting the distances of the concave and cylindrical lenses ($f = 50 \text{ mm}$ for both) and hence the width of the excited volume in the amplifier cell for maximum amplification.

A sufficiently broad band (high $\delta\lambda$), temporally incoherent (low τ_c) laser light is achieved by replacing the frequency selective element (grating or prism) in the dye laser cavity by a broad band mirror, which makes the dye to oscillate over a broader

emission region with sufficient gain. The plane mirror used is dielectric coated for a maximum reflectivity (99%) over the wavelength region of 400 to 680 nm. With both the high reflectivity mirror and the output coupler window being plane parallel, the resonator cavity is barely stable, according to the stability condition for the laser resonator [33]. Hence the laser cavity alignment has to be made very carefully to avoid spurious feedback and intensity fluctuations. The shot to shot stability of the laser pulses is ascertained with the help of averaging for every 10 pulses using a 400 MHz oscilloscope (Tektronix, 2465 B) and a digitising camera (Tektronix, C 1002). Care is also taken to avoid mechanisms leading to the formation of cavity modes, which leads to undesirable structure in the laser spectrum. The spectrum recorded from 570 nm to 590 nm is smooth without any mode structure and is fitted to a gaussian profile (eqn. (3.1)) giving a peak wavelength $\lambda_0 = 579.5 \pm 0.08$ nm and a FWHM width of, $\delta\lambda = 5.8 \pm 0.17$ nm (Figure 3.4).

3.3 Time delayed degenerate fourwave mixing using incoherent light

Excitation pulses from a broad band laser light can be regarded as a train of incoherently phased noise spikes [34]. Though the phase of each noise spike is random, when the output from a single laser is divided, delayed and recombined, the correlated noise spike pair will have the same relative phase, contributing to the overall output signal. The correlated noise spike pairs first act together to setup accumulated grating [35] in the sample and then these are interrogated by a third uncorrelated field, also derived from the same laser and get diffracted to generate the time delayed four wave mixing (TDFWM) signal in a direction satisfying the phase matching condition of the wavevectors [36]. Satisfying certain inequalities (eqn. (3.5)), a correlation experiment of this kind gives a measure of the autocorrelation function $g(x)$ and the correlation time τ_c of the light field [37]. The correlation time is an important parameter to characterize the temporal coherence of the incoherent light beams. The most important criterion for selecting a proper sample for such measurement is that the

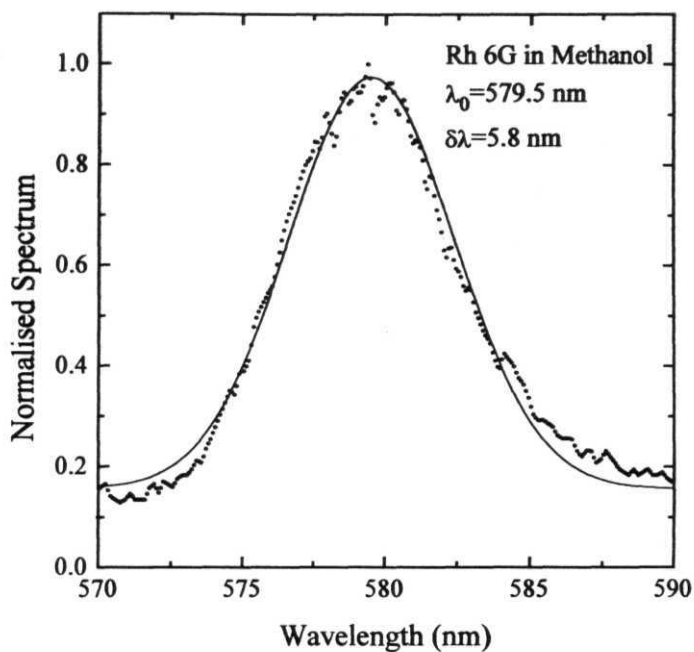


Figure 3.4

Dye laser spectrum with broad band mirror and glass plate as cavity elements. Dots are experimental points and continuous line is Gaussian fit

phase relaxation time (T_2) of the sample should be shorter than the correlation time. If $T_2 > \tau_c$, one may generally end up measuring the dephasing time of the excited sample [38]. Correlation of broad band ($\delta\nu \approx 1/\tau_c$) excitation pulses of length t_p and correlation time τ_c when interacts resonantly with such a sample, leads to the formation of phase grating in the sample. In other words, the atoms or molecules in the sample of resonant frequency ν_0 interact predominantly with the Fourier components within the bandwidth $\delta\nu$ centered at ν_0 . The interactions outside the bandwidth average out and can be neglected in its contribution to the laser induced material grating. Thus, to a first approximation the sample behaves as if it interacted only with a coherent narrow band light pulse [34].

The field correlation can also be determined using either an interferometer where the absolute fringe position is measured or by heterodyne detection [39]. The interferometric method is similar to the dispersive Fourier spectroscopy used in the infrared region [40]. But in these methods the delay between the pump pulse and the reference pulse has to be controlled to within less than an optical period. This leads to unnecessary complications of the experimental setup when the investigated signal varies on time scales much larger than the optical period, especially in the visible region, where this period is only a few femtoseconds. Thus, noninterferometric optical grating methods have been developed for autocorrelation function measurements [41]. We have used one such technique to write an illumination grating produced by interference between two pulses in a dye solution (Rh B in methanol). The visibility of the fringes is then measured by diffraction of a third beam (probe pulse) with a suitable time delay. The diffracted light intensity is directly related to the visibility and is measured as a **function** of the delay T between the writing pulses to measure the correlation time τ_c of the beams producing the grating.

3.3.1 Theory

Nonlinear optical techniques for pulse measurements do not provide a direct display of the pulse shape but instead give measurement of the correlation functions. It

is therefore important to consider in some detail the theoretical relationship between the output signal and its correlation **function**.

The instantaneous electric **field** vector of a broad band light pulse with central frequency $\omega_0 = 2\pi\nu_0$ at a spatial point given by vector 'r' and at time 't' is given by

$$E(\mathbf{r}, t) = \varepsilon(0, t) \exp[i(2\pi\nu_0 t - \mathbf{k}_1 \cdot \mathbf{r})] + c.c \quad (3.2)$$

where, $\varepsilon(0, t)$ is the field envelope and varies slowly with respect to the optical frequency $2\pi/\omega$, ' \mathbf{k}_1 ' is the field wave vector and c.c. is the complex conjugate.

For a broad band field, the envelope $\varepsilon(0, t)$ is a complex random function and can be expressed as

$$\varepsilon(0, t) = \varepsilon_0(t) u(t) \quad (3.3)$$

where $\varepsilon_0(t)$ varies on the time scale of the pump pulse width t_p and $u(t)$ is a stationary Gaussian random process. The relationship satisfied by $u(t)$ are

$$\begin{aligned} \langle u(t) \rangle &= 0, \\ \langle u(t) u(t + \tau) \rangle &= 0 \\ \langle u^*(t) u(t + T) \rangle &= g(T) \end{aligned} \quad (3.4)$$

The angled brackets $\langle \rangle$ is for statistical average. The autocorrelation function $g(\tau)$ is normalized by $g(0) = 1$ and its width is the correlation time τ_c .

The laser pulse is assumed to be long and broad band in the sense that the following inequalities are satisfied:

$$1/\nu \ll \tau_c \ll t_p \quad (3.5)$$

The longest time parameter is the laser pulse width t_p (6 nsec), is much longer than the coherence time τ_c , which is much larger than the optical period (few fsec). The idea of getting a measure of τ_c of the light and not its pulse duration t_p lies in taking advantage of the broad nature of the radiation. This is achieved by measuring the field correlation between the pump pulse and a reference pulse which is the time delayed replica of the

pump pulse, as a function of the variable delay x of the reference pulse. The electric field of the reference pulse is

$$E_R(r, t) = \epsilon(0, t + \tau) \exp[i(2\pi\nu_0 t - k_z \cdot r)] + c.c \quad (3.6)$$

with $\epsilon(0, t + \tau) = \epsilon_0(t)u(t + \tau)$, for Gaussian random process. T is the delay between the pump pulse and the reference pulse at the observation point ' r ' and ' k_z ' is its wavevector. The field cross-correlation between the pump pulse and the reference pulse is the ensemble average $\langle C(\tau) \rangle$, where $C(\tau)$ is given by

$$C(\tau) = \int_{-\infty}^{\infty} dt \epsilon^*(0, t) \epsilon(0, t + \tau) \quad (3.7)$$

The square of this cross correlation function is

$$\langle C(\tau) \rangle^2 = \left| \int_{-\infty}^{\infty} dt \epsilon_0^2(t) \right|^2 \left| \int_{-\infty}^{\infty} d\tau \langle u^*(t) u(t + \tau) \rangle \right|^2 \propto \left| \int_{-\infty}^{\infty} d\tau g(\tau) \right|^2 \quad (3.8)$$

where, the autocorrelation function $g(x)$ plays the role of the pulse envelope in the short pulse experiment. Thus it is clear that the time resolution of the field cross-correlation analysis is the coherence time τ_c of the light, which is much shorter than the pulse duration t_p [42].

The field correlation is measured by splitting a single broad band pulse into a pump pulse, reference pulse and a probe pulse. The reference pulse and the probe pulse go through variable optical delay lines. For the measurement of the square of the field cross-correlation function, the pump pulse and the reference pulses are made to interfere in an absorbing dye medium. The light power $I(r)$ in the interference region is given by [41]

$$I(r) \propto \int_{-\infty}^{\infty} dt |E(r, t) + E_R(r, t)|^2 \quad (3.9)$$

$$= \int_{-\infty}^{+\infty} dt \left\{ |\epsilon(0, t)|^2 + |\epsilon(0, t + \tau)|^2 + \epsilon^*(0, t) \epsilon(0, t + \tau) \exp[i(k_1 - k_2) \cdot r] + c.c \right\} \quad (3.10)$$

From this equation, the spatial intensity maximum I_{\max} and minimum I_{\min} can be determined to get the visibility of the fringes. The temporal coherence function or the autocorrelation function of the light pulse is determined by measuring the visibility of the interference fringes as a function of the time delay τ between the two beams. The light power absorbed in the sample cell, produces a spatial modulation of the optical constants described by a complex refractive index. The spatial amplitude $\Delta n(t, x)$ of the refractive index is given by the light power absorbed upto the time t . The excited state relaxation of the Rh B dye molecules is 20 fs (very fast) [38] and is neglected. Δn is then given by

$$\Delta n(t, \tau) \equiv \left| \int_{-\infty}^t dt \epsilon^*(t) \epsilon(t + \tau) \right| \quad (311)$$

This change in the refractive index which is a measure of the correlation of between the two exciting pulses is measured by diffraction of the probe beam incident on the grating with a suitable time delay after excitation. The delay time of the probe pulse is selected such that there is no correlation between this and either the pump or the reference pulse.

3.3.2 Experimental measurement of the coherence time

The experimental setup used for the measurement of the coherence time of broad band incoherent dye laser pulses is shown in the Figure 3.5. As discussed before, the temporally incoherent light is produced by pumping Rh 6G dye oscillator consisting of a broad band coated cavity mirror and a glass plate as cavity elements and a single stage amplifier, using the second harmonic of a Q-switched NdYAG laser. The main beam is divided into two parts to pump both the oscillator and the amplifier simultaneously. The peak wavelength of the dye laser is 579.5 nm and the width

(FWHM) of the spectrum is 5.8 nm. The effective bandwidth of the Gaussian shaped spectrum, calculated for a stationary Gaussian random process is [43]

$$\delta\lambda_{eff} = \sqrt{\pi / 2 \ln 2} \delta\lambda \approx 1.5 \delta\lambda = 8.7 \text{ nm} \quad (3.12)$$

A broad band laser is preferred as the incoherent light source because, the TDFWM experiments require light beams with sufficient intensity, directivity and temporal incoherence. The home built dye laser satisfies these conditions and hence is used in our experiments.

In the phase-conjugate geometry used for the τ_c measurement [44], the dye laser beam of pulse width $t_p = 6$ ns is first split into three beams of intensities I_1 , I_2 and I_3 by beam splitters. The first beam splitter has a reflection to transmission (R/T) ratio of 30/70 and the second one is a 50/50 beam splitter. This is to make the intensities of all the three interacting beams almost equal. The beam splitters are front surface coated with AR coating on the back side. Beams 2 and 3 go through variable delay lines, the lengths of which can be adjusted with the help of a translational stage of movement accuracy ± 5 μ m. Corner cube retroreflectors are used in the beams 2 and 3 to make the alignment of the beams easier. The beam after passing through the retroreflector leaves at the same angle as the incident beam but from a point an equal distance on the opposite side of the reflection centre with respect to the point of incidence. The mirrors used to deflect the beams are dielectric coated for maximum reflectivity at $\theta = 45^\circ$ in the wavelength range 560 - 640 nm.

All the three beams of 3 mm diameter are focused onto the sample (Rh B in methanol) using biconvex lenses of focal length 200 mm. This is to make sure that the spot size of the beams and hence the interaction region inside the sample is the same for all the three beams, which maximizes the signal efficiency. The effective diameter of the focused spot ($d_o = 2fVD$) in the sample is about 80 μ m of peak intensity 300 MW/cm^2 at the focal point. In our measurements, the counter-propagating probe beam I_2 is delayed by a fixed 0.2 ns with respect to the other two beams I_1 and I_3 . Thus, it has no correlation with the pump beams as the correlation time of the dye laser

light is expected to be in the subpicosecond region. The angle between the beams 1 and 3 is about 10° in a 10 mm sample cell.

The phase conjugate signal intensity comes out in the direction $\mathbf{k}_4 = \mathbf{k}_1 + \mathbf{k}_2 - \mathbf{k}_3 = -\mathbf{k}_3$, as $\mathbf{k}_1 = -\mathbf{k}_2$ satisfying the phase matching condition for the wavevectors of the interacting electric fields. A beam splitter kept in the path of the beam 3, as shown in the Figure 3.5, separates out the signal beam (4). The output signal intensity is measured as a function of the delay time (τ) of beam \mathbf{I}_3 with respect to beam \mathbf{I}_1 . A fast rise time ($t_r = 1$ ns) photodiode detecting the output signal is connected to a boxcar averager (PARC, M 162) with gated integrator (M 165). The boxcar is triggered with proper trigger pulse from another similar photodiode to synchronize the signal detection.

A normalized plot of the phase conjugate signal intensity versus the delay τ is shown in Figure 3.6. The signal obtained for the Rh B sample with a concentration of 1.75 mole/lit. is symmetric with respect to the delay time and its FWHM calculated using a standard Gaussian fitting procedure is 0.123 ± 0.002 ps. The coherence time calculated from the peak wavelength and the effective spectral width (eqn. 3.12) for a Gaussian spectrum ($\tau_c = \lambda_0^2 / c \delta\lambda_{eff} = 0.128$ ps) matches well with the experimentally measured coherence time of the dye laser pulse. Because the experiment is done in the absorption band of the sample, the signal intensity is very high compared with that obtained using Kerr liquid, CS_2 [45] and its behavior is due to the phase grating formed in the sample. The observed behavior of the signal gives the correlation profile $|\langle g(x) \rangle|^2$ of the incoherent light, where $g(\tau)$ is the autocorrelation function of the incoherent field.

3.4 Interference in complementary domains

The well known fact that interference effects are observable only in the space-time domain when two beams of equal intensity and similar spectral density interfere with their path difference $c\tau$ shorter than the longitudinal coherence length $c\tau_c$ is not

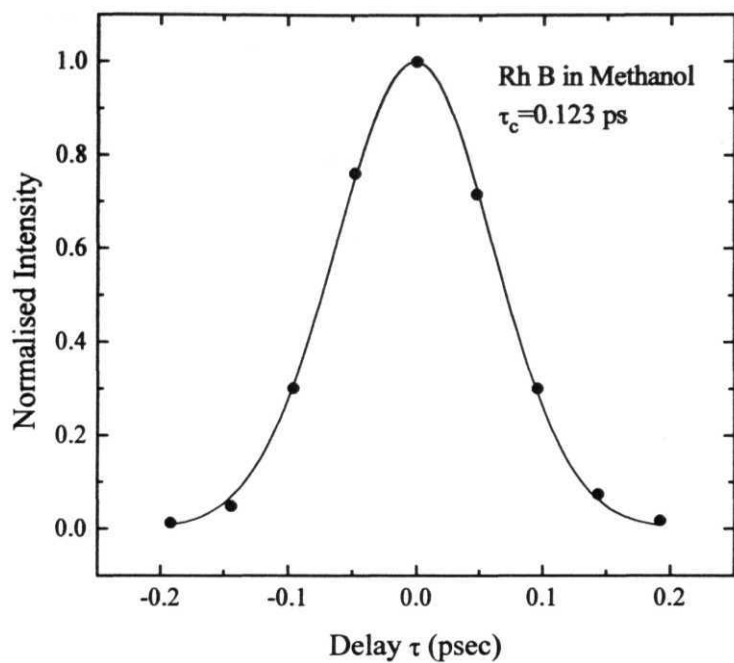


Figure 3.6

Auto correlation profile of the incoherent laser light measured using TDFWM experiment. Dots are experimental points and continuous line is Gaussian fit.

true [20]. When the optical path difference between the two interfering beams \mathbf{ct} is more than the coherence length of the light beam **used**, one does not see interference in the spatial domain. However, if the spectrum of the interfering beams is **monitored**, one observes interference fringe **pattern**, called spectral interferogram [46]. The fringe spacing or the periodicity of the spectral fringes is characteristic of the delay between the two beams and the **fringe** contrast of these spectral fringes gives information about the spectral coherence properties of the interfering beams. Thus interference occurs irrespective of how long or short the optical path difference may be, but the effect is manifested as a periodic spatial variation of the light intensity when $\mathbf{ct} \ll \mathbf{ct_c}$ and as spectral modulations when $\mathbf{ct} \gg \mathbf{ct_c}$.

3.4.1 Theoretical formulation

Let $E(r,t)$ and $E_R(r,t)$, given by **eqns.(3.2)** and (3.6) be the electric field strengths of the two interfering beams which are amplitude divided from a single input beam. Time correlation in stationary optical fields are traditionally characterized by the self coherence function, which is the normalized autocorrelation function of the optical **fields** at a point $P(r)$ arriving at two different times [47]. However, a general treatment is attempted here by considering the interference of the two light beams described by the two complex field amplitudes $\epsilon_1(t)$ and $\epsilon_2(t+\tau)$. The field amplitude at the detector point $P(r)$ is given by

$$e(t) = a\epsilon_1(t) + b\epsilon_2(t + T) \quad (3.13)$$

where x is the time delay between the beams and 'a' and 'b' are pure imaginary numbers which are slowly varying functions of position and **frequency**. Under the assumed conditions of the optical field being stationary and ergodic, the ensemble average of the measured intensity is equal to the corresponding time average and is given by

$$I = \langle \epsilon^*(t)\epsilon(t) \rangle_t$$

$$= |a|^2 \langle \epsilon_1^*(t) \epsilon_1(t) \rangle_t + |b|^2 \langle \epsilon_2^*(t+\tau) \epsilon_2(t+\tau) \rangle_t + [a^* b \langle \epsilon_1^*(t) \epsilon_2(t+\tau) \rangle_t + c.c] \quad (3.14)$$

where, $\langle \dots \rangle_t$ is the time average over the fluctuations of the field amplitudes and c.c is the complex conjugate.

$$\text{i.e., } I = |a|^2 I_1 + |b|^2 I_2 + [a^* b \Gamma_{12}(\tau) + c.c] \quad (3.15)$$

I_1 and I_2 are the time averaged intensities of the light from the two arms of the interferometer. If the third term on right hand side of the above equation does not vanish, the time averaged output intensity is not equal to the sum of the averaged intensities of the two beams reaching the point P(r) of observation after passing through the two arms of the interferometer. It differs from this sum by the presence of the interference term $a^* b \Gamma_{12}(\tau)$. Thus, for non zero value of the cross-correlation function $\Gamma_{12}(\tau)$, the two beam superposition will give rise to an interference effect. $\Gamma_{12}(\tau)$ represents the cross-correlation between the two fields separated by a time difference τ ,

$$\Gamma_{12}(\tau) = \langle \epsilon_1^*(t) \epsilon_2(t+\tau) \rangle \quad (3.16)$$

For interference of quasimonochromatic light beams ($\delta\nu/\nu_0 \ll 1$) with path difference less than the coherence length of the input light beam ($A \ll \lambda_0^2/\delta\lambda$), the autocorrelation function is given by

$$\Gamma_{12}(\tau) \approx \tilde{\Gamma}_{12}(\tau) \exp(-2\pi i \nu_0 \tau) \quad (3.17)$$

where $\Gamma_{12}(\tau)$ is a slowly varying function of time, with a characteristic time scale τ_c . The quantity τ_c is the correlation time i.e., it is the time over which the correlation between the two beams is significant or in other words,

$$\tilde{\Gamma}_{12}(\tau) \cong 0, \text{ if } \tau > \tau_c \quad (3.18)$$

Substituting eqn.(3.17) in (3.15), the interference term I_c is

$$I_e \approx \left| \tilde{\Gamma}_{12}(\tau) \right| \cos(2\pi\nu_0\tau + \theta) \quad (3.19)$$

where θ contains the phase factors coming from both $\Gamma_{12}(\tau)$ and $\mathbf{a}^* \mathbf{b}$. For time delays more than the coherence time of the light beam, the interference term vanishes. Thus, there is no interference possible if the path difference is more than the correlation time and the intensity at the output of the interferometer is just the sum of the intensities of the two input beams.

For light beams, there is an alternate measurable quantity, which is the power spectrum $S(\nu)$ of the beams, which gives the energy per unit frequency interval instead of the total integrated intensity. This is done using a spectrum analyzer such as a Fabry-Perot interferometer or a grating spectrometer or a simple prism.

Fourier transform of the eqn.(3.13), for the interference between complex, frequency dependent field amplitudes $\epsilon_1(\nu)$ and $\epsilon_2(\nu)$ at the point of interference is

$$\epsilon(\nu) = \mathbf{a}(\nu)\epsilon_1(\nu) + \mathbf{b}(\nu)\epsilon_2(\nu)\exp(2\pi i\nu\tau) \quad (3.20)$$

where, τ is the time delay between the interfering beams and $\mathbf{a}(\nu)$ and $\mathbf{b}(\nu)$ are the frequency dependent coefficients which depend on the properties of the beam splitter. The spectrum observed at the output of the interferometer is given by the formula

$$\langle \epsilon^*(\nu_1)\epsilon(\nu_2) \rangle = S(\nu_1)\delta(\nu_1 - \nu_2) \quad (3.21)$$

where $\delta(\nu_1 - \nu_2)$ is the Dirac delta function. Using the above equations, the spectrum at the output of the interferometer is expressed as

$$S(\nu) = |\mathbf{a}|^2 S_1(\nu) + |\mathbf{b}|^2 S_2(\nu) + [\mathbf{a}^* \mathbf{b} S_{12}(\nu) \exp(2\pi i\nu\tau) + \text{c.c.}] \quad (3.22)$$

where $S_{12}(\nu)$ is the cross spectral function between the two beams

$$\langle \epsilon_1^*(\nu_1)\epsilon_2(\nu_2) \rangle = S_{12}(\nu_1)\delta(\nu_1 - \nu_2) \quad (3.23)$$

In our case, both the interfering light beams are derived from a single input broad band source, for which $S_1(\nu) = S_2(\nu) = S_0(\nu)$ and $S_{12}(\nu) = S_0(\nu) \mu_{12}(\nu)$, where $S_0(\nu)$ is the

spectrum of the source and $\mu_{12}(\nu)$ is the complex degree of spectral coherence. It is clear from the above equations that even if the correlation time between the interfering beams is zero, (example, random fluctuation white noise) the spectrum will always have cosine like modulations. Thus, the interference which was apparently lost in the time domain is restored in the frequency domain. The corresponding interference equations (3.15) and (3.22) **define** the interference phenomenon in the complementary time and frequency domains.

3.4.2 Experimental demonstration

A simplified experimental setup using a broad band, temporally incoherent laser light and a dispersion compensated Michelson interferometer (**MI**) to demonstrate the interference phenomenon in the complementary spaces is shown in Figure 3.7. Light from the broad band dye laser is amplitude divided at the front surface coated 50-50 beam splitter. A compensating plate made of the same material as the beam splitter is kept in the arm 1 of the interferometer to take care of the unequal dispersion effects between the two arms. After the two beams traverse the two arms of the interferometer, they are **recombined** at the same beam splitter. Aluminium coated mirrors **M₁** and **M₂** are used to **reflect** the beams back in the same path. The mirror **M₁** is kept **fixed** and the **M₂** is mounted on a linear **translational** stage of movement accuracy $\pm 5 \mu\text{m}$. The path difference when adjusted using the variable delay to within the coherence length of the laser, gives a set of interference fringes on the screen kept after a diverging lens (Figure 3.7 (a)) Measurement of the visibility function from the intensity maximum **I_{max}** and **minimum I_{min}** of the spatial interference fringes shows an exponential decrease with the increase in the path difference between the interfering beams.

As we keep increasing the path difference between the beams from the zero delay position, there is an increase in the number of spatial fringes and a corresponding decrease in their **visibility**. Beyond the coherence length (**l_c \approx 40 μm**) of the laser beam, we have observed the spatial interference fringes vanish slowly with the region

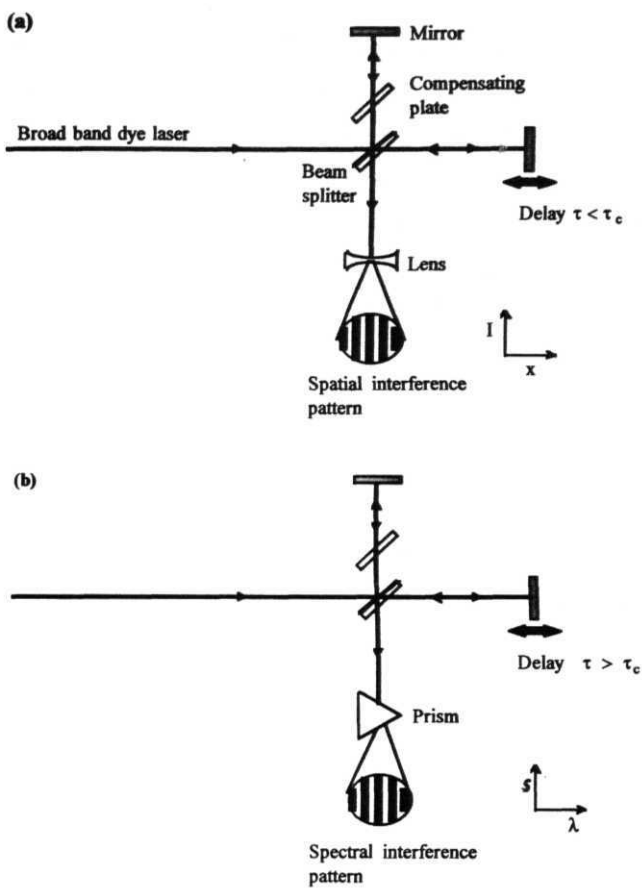


Figure 3.7

Simplified demonstration of the interference phenomenon in the complementary **space-time** and space-frequency domains.

- (a) time difference between the **interfering** beams $<$ correlation time of the source
 (b) time difference $>$ correlation time.

of interference becoming a patch of light without any spatial variation of intensity. At this point, we replace the concave lens with a prism which disperses the light beam into different spectral components and there we see a variation in the spectral intensity similar to the one seen in the spatial domain (Figure 3.7 (b)). This variation in the spectral intensity is called the spectral **interferogram**.

Modulations in the spectra are thus observed for two incoherent nanosecond pulses for separations more than the coherence length or the correlation length of the light beam. These spectral modulations are due to the constructive and destructive interference between the number of different monochromatic components present in the broad band light source for a fixed path difference [11]. Constructive interference occurs for those values of X , for which $X = \Delta/m$, ($m = 1,2,3, \dots$) and destructive interference occurs for $X = \Delta/(m+1/2)$, ($m = 0,1,2,\dots$), where m is the order of interference.

The broad band dye laser pulses are sent into the **MI** (described before) with a path difference more than the coherence length (40 μm) of the light. The pulses after traversing the two arms of the interferometer are **sent** into a 50 cm grating spectrometer (JY, HRS-2) with a maximum resolution of 0.025 nm in the region of the dye spectrum. A **photomultiplier** tube (PMT) at the output of the spectrometer is used to detect the spectrum. As the spectrometer grating is scanned across the spectral range (585 - 610 nm) of the Rh B dye laser, a strip chart recorder (**Packard-611**) connected at the output of the PMT records the spectral modulations.

Figure 3.8 (a) shows the normalized spectrum of the dye laser when one of the arms of the **MI** is closed. It acts as a reference and confirms that the individual laser pulses do not show any spectral modulations. Figures 3.8 (b)-(d) show the spectral modulations for varying path difference between the two arms of the interferometer. These recorded spectra are fitted to the equation

$$S(\nu) = \frac{1}{2} S_0(\nu) [1 + \cos(2\pi\nu\tau)] \quad (3.24)$$

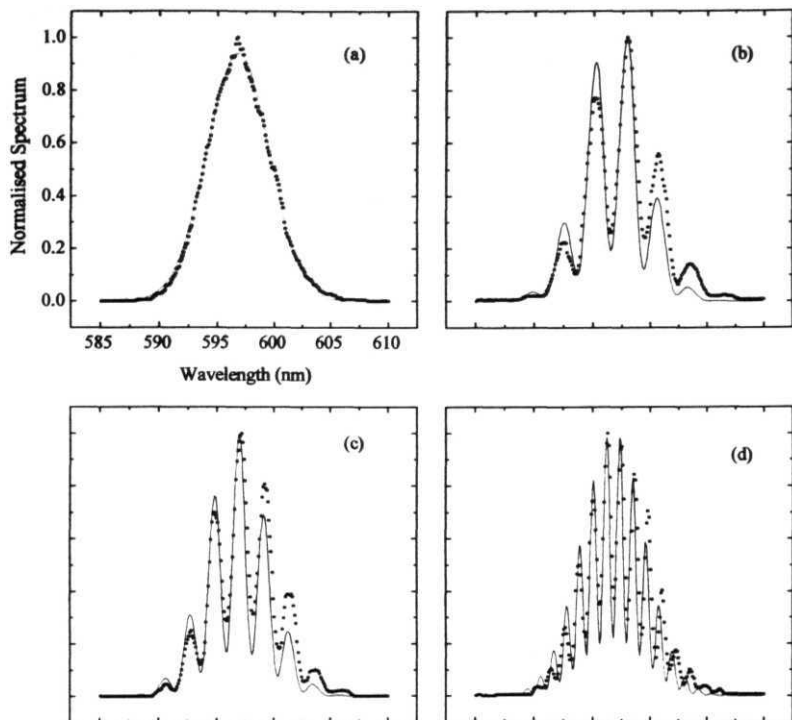


Figure 3.8

Spectral output from the **MI**. Dots are experimental data and continuous curves are the theoretical fit using eqn. (3.24). (a) Dye laser **spectrum**, when one of the arms of the **MI** is **closed**, (b) Path difference $A = 0.12$ **mm**, (c) $A = 0.16$ **mm**, (d) $A = 0.31$ **mm**.

The above equation is simplified from eqn. (3.22) assuming the conditions given along being valid and with $\mu_{12}(\mathbf{v}) = 1$, $|\mathbf{a}|^2 = |\mathbf{b}|^2 = 1/4$ and $\mathbf{a} \cdot \mathbf{b} = 1/2$. With $v = c/\lambda$ and $T = A/c$, the above equation is used to get the exact value of the path difference (A). These values, as indicated in the Figure shows clearly that, the number of spectral fringes increases with an increase in the path difference. The modulations occur within the spectral envelope of the single pulse spectrum and the modulation frequency increases with increasing path difference. The linear dependence of the number of **fringes** 'N' on the path delay T shown in the Figure 3 9, makes it clear that spectral modulations are observed at path delays much longer than the coherence length of the light used. The fitted values of the straight line are, slope = 17.22 ± 0.14 and Y-intercept = 0.79 ± 0.11 . The experimental observation of the spectral fringes with path delay is essentially limited by the band width of the source on the lower limit and by the resolution of the spectrometer in observing the maximum number of fringes.

Now, using the same experimental setup described, we demonstrate the case that the spectral decomposition leads to a **finite** spectral width Δv at every point in the spectrum, and hence the spectral modulations are visible only for a limited interval of time difference [6]. The grating position is kept fixed at some wavelength $\lambda = 595 \text{ nm}$ within the dye laser spectrum. Starting from the zero delay position between the two interfering beams, the output spectral intensity is averaged for 50 pulses each time. As the path delay is increased from this position, we see an oscillatory behavior in the spectral intensity with decreasing amplitude (Figure 3.10). The **functional** form for this kind of a behavior is obtained by integrating the eqn.(3.24) from v to $v + \delta v_{sp}$ over the interval dv to obtain the intensity I_v at a point $P(r)$ in the spectrum.

$$I(v) = \frac{1}{2} I_0(v) \left\{ 1 + \cos \left[2\pi \left(v + \frac{1}{2} \delta v_{sp} \right) \tau \right] \frac{\sin(\pi \delta v_{sp} \tau)}{(\pi \delta v_{sp} \tau)} \right\} \quad (3.25)$$

where $\delta v_{sp} = (c/\lambda^2) \delta \lambda_{sp}$. The experimental data for varying path delay are fitted using the absolute value of the modulation term of the above equation. The overall behavior is that of **sinc-function** envelope with cosine modulations. The fitted constants $A = \pi \delta v_{sp} = 2.454 \pm 0.248$ and $B = 2\pi(v + \delta v_{sp}/2) = 14.489 \pm 0.245$ agree well with the

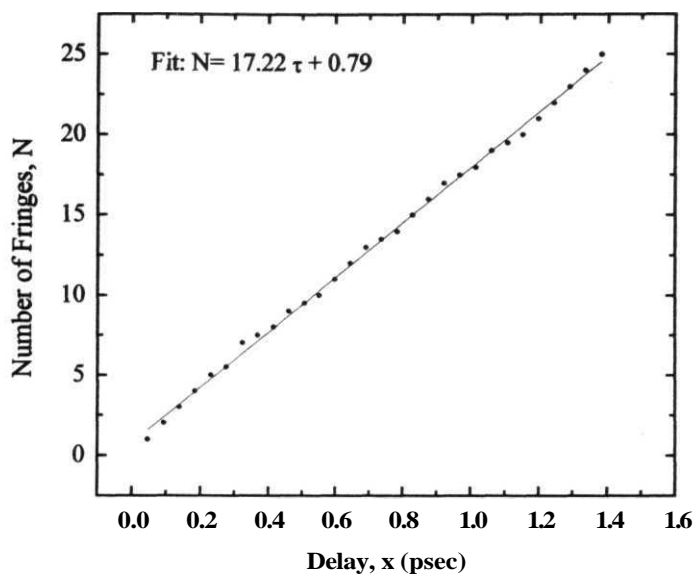


Figure 3.9

Number of spectral fringes(N) Vs path delay(x) of the **ML**.
Dots are experimental points and the straight line is the fit.

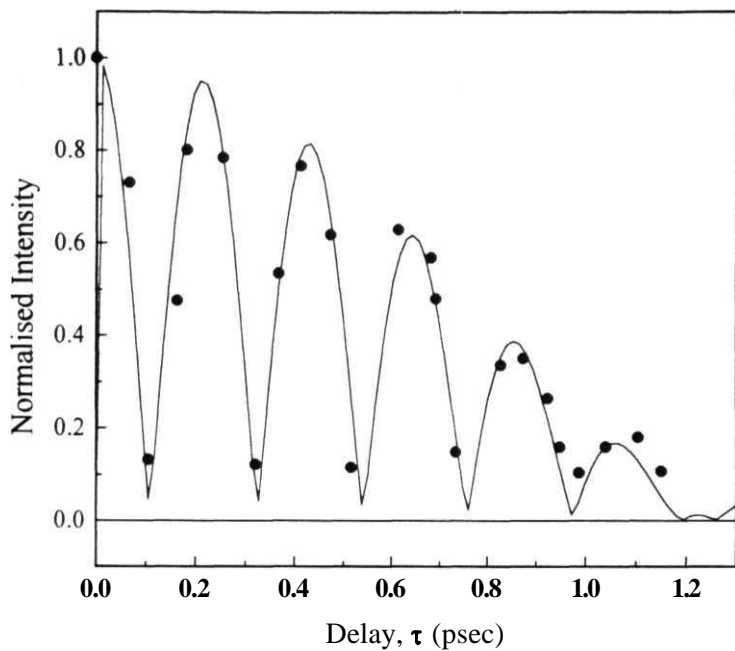


Figure 3.10

Normalized spectral intensity Vs Delay. Dots are experimental data and continuous curve is the fit using the absolute value of the modulation term of the eqn. (3.25).

Fit: $\text{Abs}\{[\sin(AT)/(Ax)]\cos[BT]\}$, $A=2.454$, $B=14.489$.

values calculated using the experimental parameters. With a further increase in the path delay, the oscillatory behavior reappears but, with reduced amplitude corresponding to the second maximum of the **sinc-function**.

References

- [1] G.S. Agarwal, *Found. Phys.* **25**, 219, (1995).
- [2] M..P. Givens, *J. Opt. Soc. Am.* **51**, 1030, (1961).
- [3] L. Mandel, *J Opt Soc Am* **52**, 1335, (1962).
- [4] L. Mandel and E. Wolf, *Rev. Mod. Phys.* **37**, 231, (1965).
- [5] A. Baczynski and G Oster, *J Opt. Soc Am* **55**, 1325, (1965)
- [6] F Heiniger, A Herden and T Tschudi, *Opt Commun.* **48**, 237, (1983).
- [7] C. Delisle and J.M. St-Arnaud, *Can. J Phys.* **48**, 1214, (1970).
- [8] E Wolf, *Phys Rev. Lett* **58**, 2646, (1987).
- [9] M.F. Bocko, D.H. Douglass and R.S Knox, *Phys. Rev. Lett* **58**, 2469, (1987).
- [10] F. Gori, G Guttari, C. Palma and C. Padovani, *Opt. Commun.* **67**, 1, (1988).
- [11] S.L. Chin, V Francois, J.M. Watson and C Delisle, *Appl Opt* **31**, 3383, (1992).
- [12] D.F.V. James and E Wolf, *Phys Lett. A* **157**, 6, (1991).
- [13] M. Santarsiero and F Gori, *Phys. Lett. A* **167**, 123, (1992).
- [14] DF.V. James and E Wolf, *Radio Sci.* **26**, 1239, (1991).
- [15] W E Kock and J.L Stone, *Proc. IRE*, **46**, 499, (1958).
- [16] S A Werner, R Clothier, H Kaiser, H. Rauch and H Wolwitsch, *Phys. Rev. Lett.* **67**, 683, (1991)
- [17] H. Kaiser, R Clothier, S A Werner, H. Rauch and H Wolwitsch, *Phys. Rev. A* **45**, 31,(1992).
- [18] H Rauch, *Phys Lett A* **173**, 240, (1993).

- [19] D **L Jacobson**, S.A. Werner and H. **Rauch**, Phys. Rev. A 49, 3196, (1994).
- [20] **X Y Zou**, T.P. Grayson and **L Mandel**, Phys. Rev. Lett. 69, 3041, (1992).
- [21] C.V. Shank, Rev. Mod. Phys. 47, 649, (1975); R. **Wallenstein**, in Laser **Handbook**, Vol. 3, Edited by M.L. Stith, (North-Holland, 1979); Dye Lasers, Edited by F.P. Schafer (**Springer-Verlag**, Germany, 1990).
- [22] R.L. Fork, C.V. Shank and R.T. **Yen**, Appl Phys. Lett. 41, 223, (1982).
- [23] R.L. Fork, B.I. Greene and C.V Shank, Appl. Phys. Lett 38, 671, (1981).
- [24] M. Maeda, Laser Dyes (Academic Press, NY, 1984).
- [25] F.P. Schafer, Liquid lasers in Laser handbook, Edited by F.T. Areechi and E.O. Schulz-Dubois (North-Holland, 1972), vol. 1.
- [26] U. **Brackmann**, Lambda chrome laser dyes (Lambda Physik, Gottingen, 1986).
- [27] R **C Hilborn**, Am. J Phys. 46, 565, (1978).
- [28] P.P. Sorokin and J.R. Lankard, IBM J. Res. **Developm.** 11, 148, (1967).
- [29] B.H. **Soffer** and B.B. **McFarland**, Appl Phys Lett 10, 266, (1967).
- [30] G. Yamaguchi, F Endo, S Murakawa, S **Okamura** and C. **Yamanaka**, Jpn. J. Appl. Phys. 7, 179,(1968).
- [31] A. **Hnilo** and O.E Martinez, IEEE J. Quant. Electron. 23, 593, (1987); C Jensen in High power dye lasers, vol 65, Edited by F.J. Duarte (Springer series in Optical sciences, 1991).
- [32] O.G. Peterson, Dye lasers in Methods of experimental physics, Edited by **C.L. Tang** (Academic press, 1979), vol. 15A.
- [33] A. Yariv, Quantum electronics, 3rd edition, (John Wiley, NY, 1989), chapter 7.
- [34] R Beach, D DeBeer and S **R Hartmann**, Phys Rev A 32, 3467, (1985).

- [35] **S. Asaka, H Nakatsuka**, M. Fujiwara and M. **Matsuoka**, Phys. Rev. A 29, 2286, (1984).
- [36] H.J. Eichler, **U Klein** and D. **Langhans**, **Appl. Phys** 21, 215, (1980).
- [37] T. Kobayashi, A. **Terasaki**, T. Hattori and K. Kurokawa, Appl. Phys. B 47, 107,(1988).
- [38] Z.Q. **Huang**, Y.J. Xie, **G.L Huang** and **H.S Kwok**, Opt. Lett. 15, 501, (1990).
- [39] **S. Saikam**, T. Kishida, A. Imaoka, K. **Ichikawa**, A. Furasawa and H. **Oasawa**, Opt. Lett. 14,841,(1989).
- [40] PR. Griffiths and J.A. de Haseth, in Fourier transform infrared spectroscopy (Wiley, NY, 1984), Chap. 11.
- [41] H.J. Eichler, P. Gunter and **D.W Pohl**, in Laser induced dynamic gratings (**Springer-Verlag**, 1986).
- [42] MA. Bouchene, A. Debarre, J **C Keller**, J L. Le Gouet and P. Tchenio, J. Opt. Soc. Am. B 9, 281,(1992).
- [43] **A.V Masalov**, in Progress in Optics, Edited by E. Wolf, (Elsevier Science Publishers **B.V.**, 1985), vol. 22.
- [44] K. Kurokawa, T. Hattori and T. Kobayashi, Phys. Rev. A 36, **1298**, (1987).
- [45] **V Nirmal Kumar** and **D Narayana Rao**, **Proc. National laser symposium**, Madras, p-243, (1993).
- [46] L. Lepetit, **G Cheriaux** and **M Joffre**, J. Opt Soc. Am. B 12, 2467, (1995).
- [47] M. Born and E. Wolf, Principles of optics, (**Pergamon**, 1989)

CHAPTER 4

MEASUREMENT OF THE DEGREE OF SPECTRAL COHERENCE

4.1 Introduction

Interference phenomenon, regarded as a manifestation of the correlation between light beams at two or more space-time points is most often used to study the coherence properties of light. The correlation function is obtained from the measurement of the interference fringes formed when light from pairs of space-time separated points in the field are allowed to interfere. This idea was first used in the pioneering work of Michelson in the reconstruction of the image of a distant, incoherent source from the optical correlation function (Michelson stellar interferometer) [1] and was later more formally derived by van Cittert and **Zernike** [2,3]. According to the fundamental relationship stated quantitatively by the van Cittert and Zernike theorem [3], the spatial intensity distribution of an unknown incoherent light source can be reconstructed by taking the Fourier transform of the complex degree of coherence in the far field. Later, a study of the correlation existing in the optical field was more elegantly treated using the theory of partial coherence formulated by Wolf [3,4] and others [5] which gives the statistical description of light in terms of observable quantities. For a better understanding and use of the theory of partial coherence in describing the behavior of optical systems, it is useful to measure the degree of coherence in an arbitrary plane for quasi-monochromatic illumination.

Young's double slit experiment, illuminated by a quasi-monochromatic source was one of the first methods used to measure the absolute value of the complex degree of coherence ($|\gamma_{12}(0)|$) from the measurement of the visibility of the interference fringes. The phase of which can be deduced from the location of the intensity maxima. The formation of interference fringes was later confirmed as a manifestation of the

spatial coherence properties of the light beam [6]. Interpretation of the **Young's** interference experiment based on the **Zernike's** investigations does not exhaust the amount of information that can be deduced from an analysis of the superposition of two light **beams**. For example, the spectral analysis of light in the region of superposition can provide information about the *spectral* coherence properties of the light incident on the double slit [7,8]. From the measurement of the degree of correlation in the space-frequency domain, known as the complex degree of spectral coherence $\mu_{12}(\mathbf{v})$, a clear insight into the spectral coherence properties and concept of cross-spectral purity of light beams is possible.

This chapter highlights the importance of the measurement of the degree of coherence in the space-time and space-frequency domains. An overview of the already existing, extensive research on the different techniques and results on the measurement of the complex degree of coherence in the usual space-time domain is presented **first**. With the recent interest in the effect of the state of coherence of the light **fields** on the spectrum of the interference fringe pattern, different studies are being carried out to understand clearly the physical reason behind the spectral changes. Experimental results are presented here on the systematic measurement of the complex degree of spectral coherence from the spectral analysis of the interference of light beams in Michelson interferometer (**MI**) and Young's double slit (**YDS**) **experiment**. Though different spectral information are obtained from the two experiments, the possibility of using them to recover the amplitude and phase of the spectral degree of coherence from the spectral visibility measurements is demonstrated. The **usefulness** of the measurement of the degree of spectral coherence is emphasized through its applications in the area of synthetic aperture imaging, angular separation of sources, size of a source, intensity distribution across the source, etc.

4.2 Overview of the degree of coherence measurement

A systematic treatment and a precise measurement of the correlation existing between light vibrations has long been the subject of investigation by many workers

[9]. Two pinhole **diffractometer** [10,11] or its variants [2] are some of the earliest experiments done to measure the coherence function. In the method due to **Zernike**, the coherence of the optical field is measured from the fringe visibility by using a Young's two beam interference experiment. The field of interest is sampled by two pinholes and the fringes are viewed at some distance behind the screen. From the measurement of the intensity maximum and the adjacent minimum for a given separation of the two pinholes, the modulus of the degree of coherence is measured and is given by

$$V = |\gamma_{12}(0)| = \frac{I_{\max} - I_{\min}}{I_{\max} + I_{\min}} \quad (4.1)$$

The field is sampled by moving the two pinholes across the field, by varying their separation to give a plot of the modulus of the degree of coherence. Later, the effect of the finite size of the source was taken into consideration and its effect on the coherence was analyzed both qualitatively and experimentally [12-14]. It was also shown theoretically that the fringe visibility decreases with an increase in the spectral **bandwidth**, source size, sampling aperture size and the defocused distance [15].

The experiment of Thompson and Wolf [10] is a variation of the fringe visibility method discussed above. They used a **diffractometer** in the experimental measurement of coherence. Under suitable experimental conditions, the source is assumed incoherent and according to the van **Cittert-Zernike theorem**, it will give rise to correlation between light vibrations at any two points on the surface of a diffracting mask of desired size, shape and distribution placed in the parallel beam between the collimating and focusing lenses. With the usual approximations, the complex degree of coherence is given by the formula

$$\gamma_{12} = |\gamma_{12}| \exp(i\beta_{12}) = \frac{2J_1(v)}{v} \exp(i\varphi) \quad (4.2)$$

$$\text{where, } v = \frac{2\pi\rho_1 d}{\lambda_0 R}, \varphi = 2\pi/\lambda_0 \left(\frac{r_1^2 - r_2^2}{2R} \right)$$

where d is the separation between the two pinholes, ρ_1 is the radius of the pinhole secondary source, R is the distance between the source and the collimating lens, r_1 and r_2 are the distances of the pinholes P_1 and P_2 from the axis and λ_0 is the mean wavelength. The changes in the structure of the interference pattern of partially coherent beams, is investigated as the separation of the pinholes is increased i.e., as the degree of the coherence between the interfering beams is varied. From the maximum and minimum values of the intensity distribution, they have demonstrated a qualitative agreement in the measurement of the degree of coherence between the theoretical results and the experimental observation.

These methods have intrinsic limitations like low light levels due to loss of light at the pinholes, which is not very practical with light sources of low coherence area like thermal light and are inflexible due to a number of masks and pinholes necessary in the experimental setup. Hence, later measurements of coherence used other types of interferometers like the polarization interferometer [16], shearing interferometer [17], reversing wavefront interferometer [18], etc. Polarization interferometers are useful for making correlation measurements when the linear dimensions of the source and the distance between the points are small compared to the distance of the points from the source. A birefringent element like a Wollaston prism or a Savart plate introduced after the plane in which the degree of coherence is to be measured, shears the image of the plane into ordinary and extraordinary beams. A corrected lens forms an image of the plane which interfere and the visibility of the interference pattern gives the modulus of the degree of coherence as a function of the separation between two points in the source.

Also, the disadvantage of the pinhole experiment described above is that the interference pattern is superposed on the diffraction pattern due to a single pinhole. As a result the fringe visibility is not strictly that given by the Michelson's classical definition. The interferometric arrangement presented by Hariharan and Sen [19] is devoid of the above mentioned drawback and has the advantage of sufficient light intensity levels for a graphical presentation of the changes in the fringe pattern with the degree of coherence between the interfering beams. The reversed wavefront

interferometer [20] utilizes a cube-corner prism or a right-angle prism in one of the arms of a Twyman-Green interferometer to demonstrate the variation of the degree of spatial coherence on the equal thickness interference fringes. In the other kind of interferometer for the measurement of the degree of coherence, known as the shearing **interferometer**[17] a cube beam splitter is used to reflect and transmit equal amount of light and a constant shear angle is introduced between them by rotating one of the prisms forming the beamsplitter relative to the other. From the visibility of the interfering sheared wavefronts, the modulus of the degree of coherence is measured as a function of the shear introduced between them.

In most of the methods discussed above, the phase of the correlation function which can be obtained from the measurement of the position of the interference fringes has proved to be far more difficult to measure with accuracy than its modulus, which is related to the visibility of the fringes [3,21]. This leads to the problem of reconstructing the unknown function of spatial distribution of the source irradiance (Optical transfer function) or the spectral distribution of the source (Fourier transform spectroscopy) from the measurement of the modulus alone [22,23]. Considering the reconstruction of the spectral distribution of the source from the temporal autocorrelation function, it is clear that under proper conditions of the time delay $\tau \ll \tau_c$, (coherence time of the light) the phase of the degree of coherence ($\alpha_{12}(\tau)$) can be **simplified** to give the effective phase difference (β_{12}) between the light vibrations at points P_1 and P_2 [3]. The error introduced by such an assumption in the exact measurement of the spectral density of the source is small and its effectiveness has been demonstrated long ago by **Michelson** [1]. Practical methods for determining both the modulus and phase of the degree of spatial coherence using **folded-wavefront** type interferometer are also **available** Kohler and Mandel [23] using such an interferometer, have discussed two methods and their practical feasibility in the spatial reconstruction of the source from the modulus of the correlation function. While the technique proposed by Ohtsuka [24] aims at producing a temporal carrier by imposing sinusoidal phase modulation on the wavefront to get the phase of the complex degree of spatial coherence.

4.3 Effect of the degree of coherence on the radiated spectrum

Spectroscopy until recently is concerned only with two well defined categories of light sources namely incoherent and coherent sources. Highly disordered emission process from thermal sources is considered incoherent and a well stabilized laser generates an highly ordered coherent emission. In a strictly statistical sense, coherent and incoherent sources represent two extreme cases. However, in practice we generally come across sources which are in-between these two extremes, known as partially coherent sources. Spectroscopy of partially coherent sources [25] i.e., sources that are neither completely uncorrelated nor fully correlated has gained renewed interest in the last few years, since the development of the space-frequency description within the frame-work of classical scalar theory of coherence. This new description has led to the elucidation of a number of coherence phenomena and has also predicted a variety of new effects [26].

Spectroscopy, was also based on the implicit assumption that the spectrum of radiation emitted by a source is an intrinsic property of the source and is independent of the location where the spectrum is measured. In other words, as the light propagates through free space, its normalized spectrum remains unchanged. This assumption however was found to be incorrect by Wolf [27]. It was shown that in general, the spectrum of light from an extended source, whether a primary source (set of radiating atoms or molecules) or a secondary source (obtained by passing the radiation from a primary source through an aperture) depends not only on the spectrum of the source but also on some of its statistical properties, characterized by the second-order degree of spectral coherence [7]. Consequently the normalized spectrum of light is in general, not invariant on propagation. This prediction was soon verified experimentally [28] and since then has been demonstrated with the help of many different schemes [29-31][§]

To make the experimental demonstration and discussion on the effect of the degree of coherence on the spectrum of radiation emitted from a source attempted in

[§] Source correlation effects have been demonstrated elegantly in the time domain using the field autocorrelation function by Chopra and others. J Raj, S Raj and S Chopra, Phys Rev A, 47, 4400, (1993).

this chapter complete, few important equations and the conditions which are already derived in the chapter 2 are presented here. The field generated by any realistic optical source will undergo random fluctuations in time which are characterized statistically in terms of different correlation **functions**. Let $\epsilon(\mathbf{r}, \mathbf{t})$ represent the field generated by a fluctuating source. Assuming the fluctuations are statistically stationary, the correlation function of the field at two space-time points is defined by

$$\Gamma(\mathbf{r}_1, \mathbf{r}_2, \tau) = \langle \epsilon^*(\mathbf{r}_1, t) \epsilon(\mathbf{r}_2, t + \tau) \rangle \quad (4.3)$$

which characterizes the correlation in the space-time domain. To analyze the spectral coherence properties of the field, it is convenient to use functions which characterize correlations in the space-frequency domain. The Fourier transform of the eqn.(4.3)

$$W(\mathbf{r}_1, \mathbf{r}_2, \nu) = \int_{-\infty}^{\infty} \Gamma(\mathbf{r}_1, \mathbf{r}_2, \tau) \exp(2\pi i \nu \tau) d\tau \quad (44)$$

is the cross-spectral density of the field. The **cross-spectral** density defined above is itself a correlation function written in terms of the ensemble of random frequency dependent field variables as

$$W(\mathbf{r}_1, \mathbf{r}_2, \nu) = \langle \epsilon^*(\mathbf{r}_1, \nu) \epsilon(\mathbf{r}_2, \nu) \rangle \quad (4.5)$$

where the averaging is done over the ensemble of frequency-dependent **functions**. It is important to note here that the functions $\epsilon(\mathbf{r}, t)$ and $\epsilon(\mathbf{r}, \nu)$ are not Fourier transform of each other for time-stationary fields within the framework of ordinary function **theory**. According to the generalization of the **Wiener-Khintchine** theorem, the spectral density of the field distribution is the diagonal element of the cross-spectral density i.e.,

$$S(\mathbf{r}, \nu) = W(\mathbf{r}, \mathbf{r}, \nu) = \langle \epsilon^*(\mathbf{r}, \nu) \epsilon(\mathbf{r}, \nu) \rangle \quad (46)$$

Consider the field generated by two fluctuating sources located at points \mathbf{P}_1 and \mathbf{P}_2 denoted by vectors \mathbf{r}_1 and \mathbf{r}_2 respectively that are statistically **stationary**. Let $\{\epsilon(\mathbf{r}_1, \nu)\}$ and $\{\epsilon(\mathbf{r}_2, \nu)\}$ be the frequency dependent ensembles that represent the source fluctuations. Let $\{\epsilon(\mathbf{r}, \nu)\}$ be the ensemble that represent the field at an observation

point $P(r)$ generated by the two sources. For **sufficiently** small sources, the realization $\{\epsilon(r, \nu)\}$ may be expressed in the form

$$e(r, \nu) = a(\nu)\epsilon(r_1, \nu) + b(\nu)\epsilon(r_2, \nu) \quad (4.7)$$

where $a(\nu)$ and $b(\nu)$ are the frequency dependent coefficients. The spectrum of the field at the point $P(r)$ is given by

$$S(r, \nu) = \langle \epsilon^*(r, \nu)\epsilon(r, \nu) \rangle \quad (4.8)$$

where the angled brackets denote the ensemble average over the frequency dependent variables. Substituting from eqn.(4.7) into eqn.(4.8), we find that

$$S(r, \nu) = |a|^2 S(r_1, \nu) + |b|^2 S(r_2, \nu) + a^*(\nu)b(\nu)W(r_1, r_2, \nu) + c.c \quad (4.9)$$

where $S(r_1, \nu)$ and $S(r_2, \nu)$ are the spectrum of each of the source distribution as **defined** by eqn.(4.6) and the $W(r_1, r_2, \nu)$ is the **cross-spectral** density of the source fluctuations (eqn.(4.5)) and c.c is the complex conjugate. Assuming the spectrum of each source distribution to be equal i.e.,

$$S(r_1, \nu) = S(r_2, \nu) = S_0(\nu) \quad (4.10)$$

and introducing the degree of spectral coherence at frequency ν , which is a measure of the correlation that exist between the two fluctuating sources to be given by the formula

$$\mu(r_1, r_2, \nu) = \frac{W(r_1, r_2, \nu)}{S_0(\nu)} \quad (4.11)$$

the **field** spectrum given by the eqn.(4.9) is simplified to

$$S(r, \nu) = S_0(\nu) \left[|a|^2 + |b|^2 + a^*(\nu)b(\nu)\mu(r_1, r_2, \nu) + c.c \right] \quad (4.12)$$

To highlight the importance and the role of the complex degree of spectral coherence and the effect it has in modifying the spectrum of the radiation emitted from the two sources at P_1 and P_2 from **an** observation at a point P , we make a further assumption

that **the** two frequency dependent coefficients **a(v)** and **b(v)** are equal. Then the eqn.(4.12) reduces to

$$S(r, v) = 2|a|^2 S_0(v) \left[1 + \text{Re} \left\{ \mu(r_1, r_2, v) \right\} \right] \quad (4.13)$$

where '**Re**' denotes the real **part**. From the above equation, it is clear that in the special cases when $\mu(r_1, r_2, v) \equiv 0$ i.e., when the two sources are mutually completely uncorrelated or when $\mu(r_1, r_2, v) \equiv 1$ when they are mutually completely correlated, the spectrum of the field $S(r, v)$ at the point P will be proportional to the spectrum $S_0(v)$ of the source **fluctuations**. However, in general, the two spectra $S(r, v)$ and $S_0(v)$ will not be proportional to each other, because of the presence of the degree of correlation $\mu(r_1, r_2, v)$ in the eqn.(4.13). Thus it is clear that the field spectrum observed at a point P(r) may differ drastically from the source **spectrum**, the difference depends on the behavior of the correlation coefficient $\mu(r_1, r_2, v)$ as a **function** of frequency and **will** in general be different at different points in space also. This simple derivation shows clearly in a non-trivial way that source correlation can modify the spectrum of **the** emitted field.

The spectral changes for example, may consist of narrowing, broadening, or **shifting** of spectral line or generating several lines from a single broad line etc. Several examples of such spectral changes have been predicted theoretically [32-35] **and** demonstrated experimentally [36-39]. Some of the important work on **these** effects are briefly discussed for completeness sake. Based on the above treatment, Wolf and others [34,35] have predicted and discussed the red shift and blue shift in the spectrum generated by sources with different degrees of correlation between **them**. The first experimental demonstration of the shifts in the spectral lines due to source correlations was made with acoustical sources by Bocko et al [28].

Also, the above discussion of the phenomenon is not restricted to radiation from simple system consisting of two small sources. It is applicable in general to radiation from extended sources, both primary and secondary of various **kind**, such as illuminated apertures [39-41] or illuminated scattering media whose macroscopic

parameters vary randomly in space [42] and time [43-47]. Correlation induced spectral changes with two small apertures illuminated by partially coherent light was first pointed out in a simple demonstration by Mandel [48] in his study on the cross-spectral purity of light beams. Similar, conceptually simple demonstration of the effects of source correlation on the spectra of radiation is achieved in the **Young's** interference experiment with partially coherent **light**, provided the bandwidth of the light incident on the pinholes is sufficiently broad or its degree of spectral coherence varies rapidly enough with frequency over the bandwidth [49,50]. Suitably controlling the degree of spatial coherence of the source, it is possible to produce substantial modifications in the spectra of radiated fields. Indebetouw developed an optical system for synthesizing sources of prescribed coherence properties [40].

In all the above examples of situations leading to the spectral changes, no new frequency component is generated by the correlation mechanism. Source correlations produce either enhancements or reductions in the strengths of the different frequency components contained in the original spectrum and hence the maximum spectral shifts that can be produced are of the order of the effective width of the original spectral line.

4.4 Determination of the degree of coherence from spectral measurements in a Michelson interferometer

Spectral interference fringes produced as a manifestation of the temporal incoherence of spatially coherent light is known for a long time under different names, e.g. **Edser-Butler** fringes [51], channeled spectra [52], etc. The spectral changes arising due to interference between two partially correlated light beams has been studied in the frame work of optical coherence theory only recently [7,8]. It has been predicted that from the spectral analysis of light in the region of superposition in a two beam interference experiment, it is possible to obtain information about the spectral coherence properties of the light fields. Experimental demonstration of the measurement of the degree of spectral coherence utilizing the concept of spectral visibility and spectral correlation was achieved later [53].

4.4.1 Theoretical details

The measurement of the degree of spectral coherence can also be achieved using a Michelson interferometer (**MI**) or a Mach-Zehnder interferometer (**MZI**), where the degree of correlation is varied with the help of the path difference between the interfering beams [54]. Let $\{\epsilon_{in}(\nu)\}$ represent the frequency dependent ensemble [55] of the **field** input into the interferometer, which satisfies all the usual conditions for a random fluctuating field. This beam is amplitude divided by a cube beam splitter into $\{\epsilon_1(\nu)\}$ and $\{\epsilon_2(\nu)\}$ and directed into the two arms of the interferometer. According to the **principle** of conservation of energy and assuming that the beam splitter is **non-absorbing**, the **Stoke's** relationship between the reflectivity 'r' and **transmissivity** 't' can be written as [56]

$$|r|^2 + |t|^2 = 1 \text{ and } r t^* + r^* t = 0 \quad (4.14)$$

The output beam of the interferometer monitored at a point P(r) in the observation plane is equal to the sum of the two fields after passing through the two arms of the interferometer i.e.,

$$\epsilon(\nu) = \epsilon_1(\nu) + \epsilon_2(\nu) \quad (4.15)$$

where $\epsilon_1(\nu)$ and $\epsilon_2(\nu)$ are the fields emerging from the two arms of the **MI** and are related to the frequency dependent input field $\{\epsilon_{in}(\nu)\}$ as

$$\epsilon_1(\nu) = a(\nu)\epsilon_{in}(\nu) \text{ and}$$

$$\epsilon_2(\nu) = b(\nu)\epsilon_{in}(\nu) \quad (4.16)$$

where $a(\nu)$ and $b(\nu)$ are the frequency dependent coefficients, which depend on the properties of the beamsplitter, on the path lengths the two beams travel in the two arms of the **MI** and are given by

$$a(\nu) = r \exp(ikL_1) \text{ and}$$

$$b(\nu) = t \exp(ikL_2) \quad (4.17)$$

where $k = 2\pi\nu/c$ and L_1 and L_2 are the total path lengths the light beams travel in the two arms of the **MI**. Using the eqn.(4.14), the two **frequency** dependent coefficients given by **eqn.(4.17)** can be shown to satisfy the relation

$$|a(\nu) + b(\nu)|^2 = 1 \quad (4.18)$$

The spectrum of the output field is given by

$$S(\nu) = \langle \epsilon^*(\nu) \epsilon(\nu) \rangle \quad (4.19)$$

Using the **eqns.(4.15)**, (4.16) and (4.17), the spectrum of the output field given by eqn.(4.19) can be simplified and written as

$$S(\nu) = |a(\nu)|^2 S_0(\nu) + |b(\nu)|^2 S_0(\nu) + 2a^*(\nu)b(\nu)S_0(\nu)\mu_{12}(\nu) \quad (4.20)$$

where the $S_0(\nu)$ is the input spectrum given by the ensemble average of the input field i.e.,

$$S_0(\nu) = \langle \epsilon_m^*(\nu) \epsilon_m(\nu) \rangle \quad (4.21)$$

and the cross-spectral density of the two interfering beams is given by

$$\langle \epsilon_1^*(\nu) \epsilon_2(\nu) \rangle = \langle \epsilon_2^*(\nu) \epsilon_1(\nu) \rangle \times S_0(\nu)\mu_{12}(\nu) \quad (4.22)$$

Assuming the beamsplitter to be $r/t = 50/50$, the reflectivity and the transmissivity are equal to $|r| = |t| = 1/\sqrt{2}$. Using this value and the eqns.(4.17) and (4.18), it can be shown that

$$|a(\nu)|^2 = |b(\nu)|^2 = |r|^2 |t|^2 = 1/4 \text{ and}$$

$$a^*(\nu)b(\nu) = |r|^2 |t|^2 \exp[ik(L_2 - L_1)] = \left(\frac{1}{4}\right) \exp(ik\Delta) \quad (4.23)$$

where $\Delta = L_2 - L_1$ is the path difference between the **interfering** beams. Substituting the eqns.(4.21), (4.22) and (4.23) into the **eqn.(4.20)**, the spectrum of the output field is given by the expression

$$S(v) = \left(\frac{1}{2}\right) S_0(v) \left[1 + \text{Re}\{\mu_{12}(v)\} \cos(k\Delta) \right] \quad (4.24)$$

where ‘**Re**’ is the real part and $\mu_{12}(v)$ is the complex degree of spectral coherence between the two interfering beams in the **MI** and can be written in terms of the modulus and argument [7] as

$$\mu_{12}(v) = |\mu_{12}(v)| \exp[i\beta_{12}(v)] \quad (4.25)$$

In the above equation, $\beta_{12}(v)$ is the phase of the degree of spectral coherence at frequency v , which is also equal to the phase difference between the amplitude divided light beams and can be assumed to be equal to zero as interfering beams have the same phase. Using this, the eqn.(4.24) is rewritten as

$$S(v) = \left(\frac{1}{2}\right) S_0(v) \left[1 + |\mu_{12}(v)| \cos(k\Delta) \right] \quad (4.26)$$

From the maximum and minimum values of the envelope of the spectral modulations, obtained for path delays $\Delta > l_c$ (coherence length of the light beam), the spectral visibility is deduced to be equal to the modulus of the complex degree of spectral coherence i.e.,

$$V(v) = \frac{S_{\max}(v) - S_{\min}(v)}{S_{\max}(v) + S_{\min}(v)} = |\mu_{12}(v)|$$

$$\text{or } V(\lambda) = \frac{S_{\max}(\lambda) - S_{\min}(\lambda)}{S_{\max}(\lambda) + S_{\min}(\lambda)} = |\mu_{12}(\lambda)|$$

Also, from the eqn.(4.26) it is clear that by recording the output spectral modulations for different path delays Δ and the spectrum of the input beam by closing one of the interferometer arms, the modulus of the complex degree of spectral coherence can be experimentally measured using a **MI**. It is given by

$$|\mu_{12}(v)| \propto \frac{\left[\left(\frac{2S(v)}{S_0(v)} \right) - 1 \right]}{\cos(k\Delta)}$$

From the theoretical analysis developed in the chapter 2, the degree of coherence for a planar, secondary, quasi-homogeneous slit source is equal to the far-zone form of the van **Cittert-Zernike** theorem and is given by eqn.(2.76). Neglecting the effect of the height of the **slit**, it is written as

$$|\mu_{12}(v)| \propto \left(\frac{\sin(kpa)}{kpa} \right)$$

$$\text{or } |\mu_{12}(\lambda)| = A \left[\frac{\sin(B/\lambda)}{(B/\lambda)} \right] \quad (4.29)$$

where, ' k ' = $2\pi/\lambda$ is the **wavenumber** associated with wavelength λ , ' p ' = $(X_1 - X_2)/R$, with $(X_1 - X_2)$ the average distance between the points for which the degree of spectral coherence is calculated, R is its distance from the source, ' a ' is the width of the rectangular slit source, uniformly illuminated by an incoherent, broad band source ' A ' is the constant of proportionality and ' B ' = $2\pi pa$.

4.4.2 Experimental

The experimental setup used for the measurement of the modulus of the degree of spectral coherence is shown in Figure 4.1. A primary broad band source (25 W tungsten **filament** lamp) illuminates uniformly and incoherently an aperture of width 300 μm . The light emerging from this secondary source is **collimated** using a condenser lens of focal length $f = 18$ mm. This is sent into the dispersion compensated **MI**, consisting of a 50-50 cube beam splitter and two aluminium coated mirrors **M₁** and **M₂** in the two **arms**. The mirror **M₂** is mounted on a linear translational stage of movement accuracy ± 5 μm . The beams after passing through the two arms of the **MI** are combined back at the same beamsplitter. The two interfering beams are said to be partially correlated depending on the delay introduced between them. The output beam from the interferometer is focused onto the input slit of a 50 cm grating spectrometer (**JY, HRS-2**). The output of the spectrometer is detected using a PMT which in turn is connected to an ADC data acquisition card in a PC.

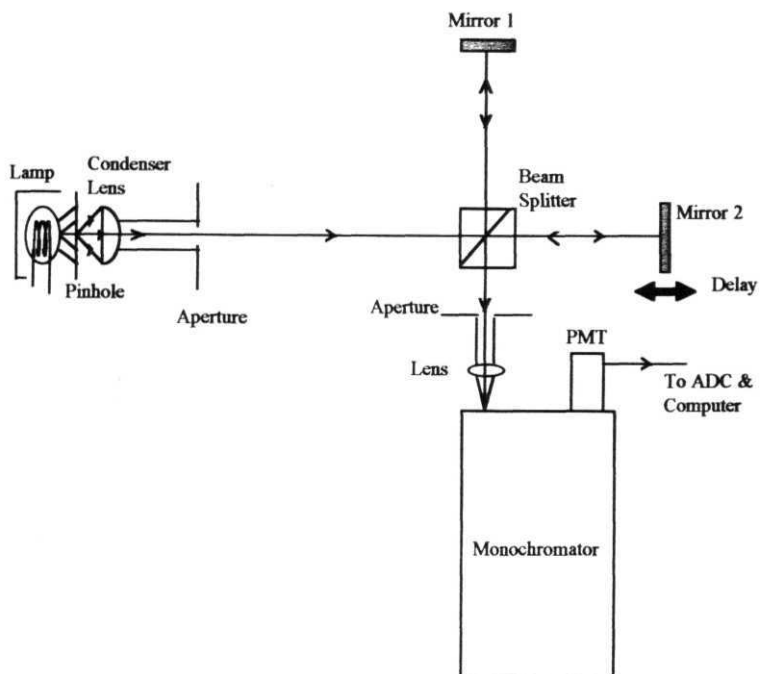


Figure 4.1

Schematic of the Experimental setup used for the measurement of the modulus of the degree of spectral coherence.

Before recording the spectral fringes, it is made sure that the effects relating to the practical construction of the interferometer does not contribute to the measurement of the fringe visibility. By observing visually using a reflection grating, it is ascertained that the spectral fringes formed for different path delays, do not suffer from the defects in the quality and adjustment of the interferometer optical surfaces. The vibration of optical components, leading to a blurring due to the overlapping of the displaced fringe patterns is assumed to be minimum. Parasitic reflections resulting from unwanted reflections is eliminated by using apertures of a **fixed** diameter of 3 mm one each before the light enters the interferometer and before the superposed beam enters the spectrometer, as indicated in the Figure 4 1. Though the spectral response of the PMT and other components of the interferometer are not a constant over the entire visible **region**, the non-uniformity does not affect the results as the measurements of the degree of spectral coherence are made by comparing the appropriately normalized spectral modulations when the two beams interfere, $S(X)$ with the spectrum of the lamp when either one of the arms of the interferometer is closed, $S_0(\lambda)$.

4.4.3 Results and discussion

As it is necessary to have a broad bandwidth for the source to observe appreciable spectral changes because of source correlation effects, we have used a tungsten filament lamp instead of the home built broad band dye laser discussed in the last chapter. The emission bandwidth of the lamp is over the entire visible region from 380 nm to 750 nm. Some of the important constants of the source used in interpreting the experimental results are: the band width of the lamp is $dX > 400$ nm, the emission maximum $\lambda_0 = 533$ nm, the coherence length $c\tau_c < 0.35$ μm and $\delta\lambda/\lambda_0 = 0.75$, which is much larger than the condition for the quasi-monochromatic light source. The spectral modulations recorded for four different path delays between the interfering beams, larger than the coherence length (l_c) of the source are shown in the Figure 4 2. It is clear from the figure that the number of spectral fringes increases with the increase in the path delay (A) between the interfering beams, in accordance with the eqn.(4.26).

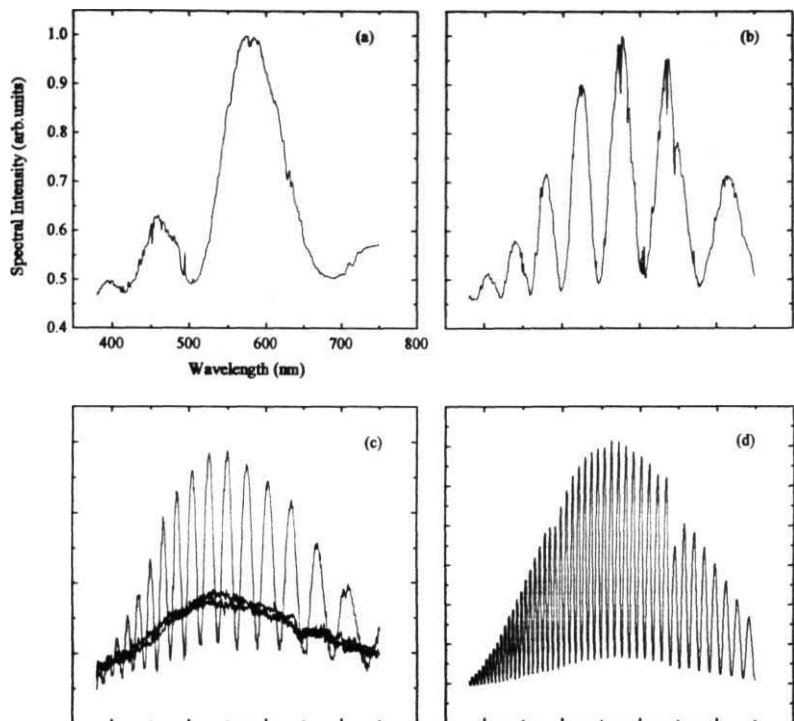


Figure 4.2

White light spectrum and the spectral modulations recorded for different path delays between the interfering beams. (a) $\Delta=0.18\text{E-}5\text{ m}$, (b) $0.5\text{E-}5\text{ m}$, (c) $1.25\text{E-}5\text{ m}$ and the spectra closing the arms of the MI, (d) $\Delta=4.5\text{E-}5\text{ m}$.

In Figure 4.2 (c), the spectrum of the lamp recorded by closing either of the arms of the **MI** are also shown, from which it is clear that the spectral intensity of the two interfering beams are almost equal and the spectral modulations are only because of interference between partially correlated beams. The path delay for each recording is obtained by fitting the spectral fringes to eqn. (4.26) taking an appropriate shape for the spectral profile, $S_0(\lambda)$ with $v = c/X$. The least-square fitting procedure is used in fitting the experimental data and the overall chi-square deviation is about $1E-2$ for all the fittings. It is worth noting here that the experimental results presented in this section are for the interference between partially correlated beams **satisfying** the spectral impurity condition mentioned previously.

Experimentally, the variation in the visibility of the fringes over the visible region and hence the modulus of the degree of spectral coherence can be calculated in two seemingly different ways: (1) the modulus of the degree of spectral coherence as a function of wavelength can be calculated either from **eqn.(4.27)**, by measuring the maximum and minimum of the spectral intensity at different wavelengths or (2) by using the eqn.(4.28), where $S(X)$ with $v = c/X$ is the modulated output spectrum and $S_0(\lambda)$ the input spectrum of the lamp are experimentally recorded and appropriately normalized and A is the path difference between the interfering beams obtained through fitting. Figure 4.3 demonstrates the **applicability** of both these process for the determination of the $|\mu_{12}(\lambda)|$ using the **MI**. From the experimental recording of the spectral modulations for a path delay of about 12.5 μm , the maximum and minimum values of the spectral intensities are determined at different wavelengths. This curve is fitted using the eqn. (4.29) for the experimental parameters of $a = 150 \mu\text{m}$, $X_1 - X_2 = 150 \mu\text{m}$ and $R = 30 \text{ cm}$ with ' k ' = $2\pi/\lambda$. The fitted curve is shown as dashed line in the Figure 4.3 and the value of $|\mu_{12}(\lambda)|$ calculated from the experimental parameters is 0.8568 at $X = 550 \text{ nm}$. Using the appropriately normalized spectral intensities, $|\mu_{12}(\lambda)|\cos(kA)$ is calculated from eqn. (4.28). The experimental data and the fitted curve using the previously determined value for $|\mu_{12}(\lambda)|$ are also given in the Figure 4.3. It is clear from the figure and the value given that the fitted value and the curve

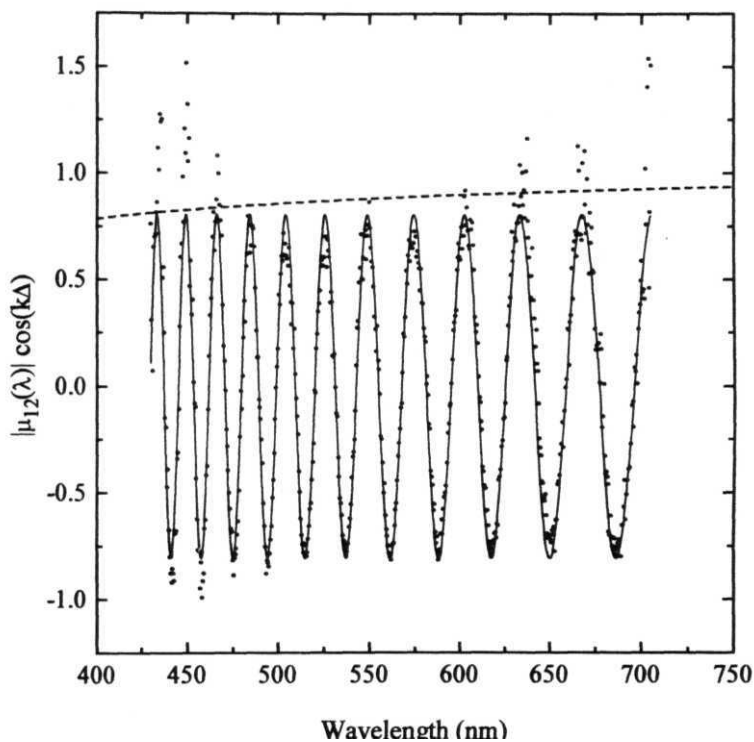


Figure 43

Experimental data (dots) and the theoretical fit (continuous line) using eqn. (4.28) for the real part of the complex degree of spectral coherence. The fitted values are $|\mu_{12}|=0.8083, \Delta=1.2353E-5$. Dashed line is the fit for $|\mu_{12}(\lambda)|$, using eqn. (4.29).

are found to be in close agreement with the value calculated using the experimental parameters and data respectively.

In the **MI**, the variation in the fringe visibility is measured for different widths of the secondary source width of $\rho_1 = 300 \mu\text{m}$, 1 mm and 2 mm for a fixed path delay and spectrometer settings. In all the cases, the fringe visibility calculated at different wavelengths are found to be the same. This is done to make sure that the spectral visibility and spectral correlations in the **MI** does not get affected by an increase in the finite size of the source though the theoretical equations are derived assuming a point source. However, the degree of correlation can be changed either by varying the path delay between the interfering beams or by controlling the resolution of the spectrometer through their slit widths and the speed with which the modulated spectra are recorded. The superposed beam coming out of the interferometer is imaged onto the spectrometer entrance slit with the help of a lens of proper focal length ($f = 20 \text{ cm}$). For the measurement of the visibility of spectral fringes, the entrance slit acts like a secondary source ($\delta x_1 = a$) and the width of the exit slit ($\delta x_2 = X_1 - X_2$) determines the distance between the points for which the degree of spectral coherence is calculated. It is important to note here that when the degree of correlation is measured by varying the path difference between the interfering beams, **R'** is taken as the average distance the beams travel in each arm of the interferometer, which is about 30 cm. This is because, '**R**' is interpreted as the distance the beams travel between the split and the recombination at the same place in the beam splitter. Whereas, when the degree of spectral correlation is measured as a function of the slit width variation of the spectrometer, **R** is then interpreted as the average distance from the source (entrance slit of the spectrometer) to the point where the degree of spectral coherence is measured (exit slit). For the spectrometer used, this distance is about 50 cm.

First, the experiment is done for different path delays between the interfering beams and for a fixed equal input and exit slit widths ($\delta x_1 = \delta x_2 = 5x$) of the spectrometer. The modulus of the degree of spectral coherence $|\mu_{12}(\lambda)|$ is measured from the visibility of the spectral modulations using eqn. (4.27) at different wavelengths. Figure 4.4 gives the experimental data for the variation of the $|\mu_{12}(\lambda)|$

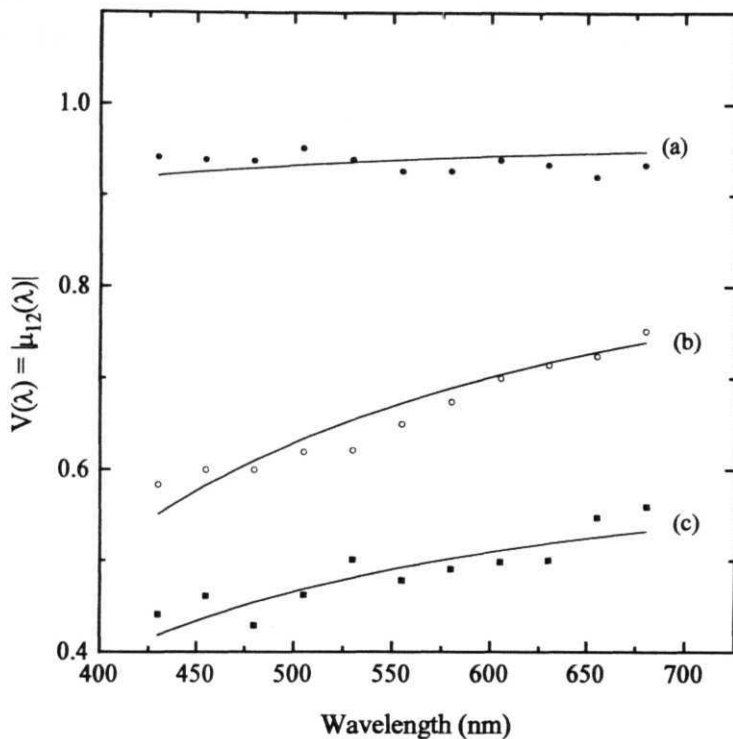


Figure 4.4

Variation of the spectral visibility with wavelength calculated using eqn. (4.27), for a fixed slit width of the spectrometer ($S_x = 100\mu\text{m}$) and different delays between the interfering beams of the MI (a) $A = 28.5\mu\text{m}$, (b) 0.13mm , (c) 0.33mm . The experimental data are fitted to the eqn.(4.29) and the fitted constants are compared with the values calculated from the experimental parameters in Table 42.

as a function of wavelength and the corresponding theoretical fittings for three different path delays ($\Delta \approx 28.5 \text{ } \mu\text{m}$, 0.13 mm and 0.33 mm) and for fixed, equal spectrometer slit widths of $6x = 100 \text{ } \mu\text{m}$. From the behavior of the $|\mu_{12}(\lambda)|$ with X for different path delay between the interfering beams in the **MI**, we conclude that the degree of spectral coherence reduces for larger path delay or for lesser degree of correlation for a particular setting of the experimental conditions, according to the eqn. (4.29). Table 4.1 gives a comparison between the fitted value B' of the width of the **sinc-function** for different delay (using eqn. (4.29)) with the corresponding value calculated using the experimental parameters. The last column in the table gives the reduction in the value of $|\mu_{12}(\lambda)|$ between the fitted and calculated values. This is attributed mainly to the scan speed of the spectrometer which is kept fixed at 20 nm/mm irrespective of the number of fringes available in the entire visible region.

Next, the experiment is done keeping the path difference between the interfering beams fixed and varying the slit width of the spectrometer. Figure 4.5 gives the behavior of $|\mu_{12}(\lambda)|$ for the fixed path delay of 0.33 mm and for three different equal entrance and exit slit widths of 300, 400 and 800 μm . From the figure it is clear that, for a fixed number of **fringes** within the region of interest, an increase in the **slit** widths of the spectrometer results in a decrease in the value of $|\mu_{12}(\lambda)|$. Larger values of the entrance slit width, considered here as the secondary source leads to a reduction in the fringe contrast because of the effect of more incoherent contribution from an increased spatial incoherence. An increase in the exit slit width which determines the distance between the points for which the degree of spectral coherence is **calculated**, reduces the spectral visibility because of the overall reduction in the spectrometer **resolution**. The experimental data of spectral visibility given as a function of X are calculated from the spectral modulations and using the eqn. (4.27). The values obtained by fitting the experimental data to the eqn. (4.29) are compared with the values calculated from the corresponding parameters and are given in the Table 4.2. As before the last column of the table gives the reduction in the degree of spectral coherence between the fitted and calculated values.

Slit width δx (μm)	Path delay A(m)	'A'	Fitted value of	Experimental value $B = 2\pi pa$	Reduction in $ \mu_{12}(\lambda) $
100	2.85E-5	0.967 \pm 0.026	2.295E-7 \pm 1.16E-7	2.094E-7	1.096
	1.29E-4	0.882 \pm 0.048	6.875E-7 \pm 6.01E-8	2.094E-7	3.283
	3.27E-4	0.618 \pm 0.113	6.315E-7 \pm 2.23E-7	2.094E-7	3.015

Table 4.1

Table giving the comparison between the fitted values using the eqn.(4.29) and the values calculated using the experimental parameters for a fixed slit width of the spectrometer and different path delays between the interfering beams of the **MI**. The experimental data and the fitted curves are shown in the Figure 4.4. The last column gives the reduction in the $|\mu_{12}(\lambda)|$ value.

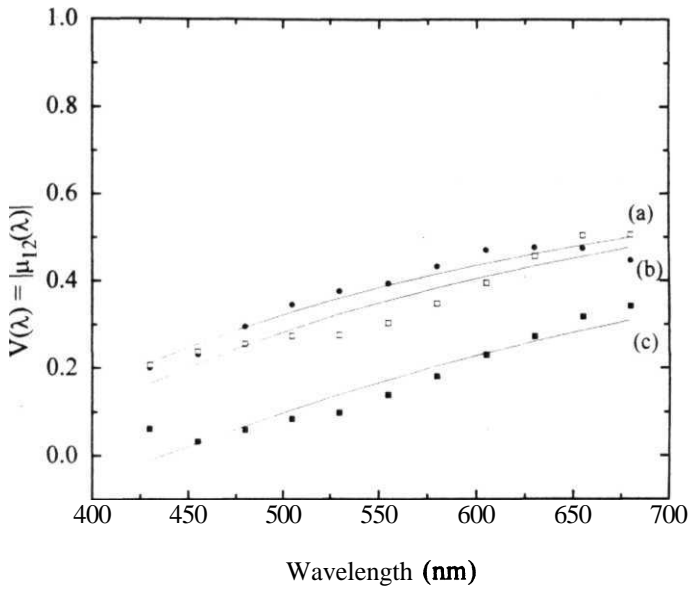


Figure 4.5

Variation of the visibility or the modulus of the degree of spectral coherence with wavelength for a fixed path delay $\Delta=0.33\text{mm}$ of the **M1** and different equal slit widths of the spectrometer (a) $6x=300\text{ }\mu\text{m}$, (b) $400\text{ }\mu\text{m}$ and (c) $800\text{ }\mu\text{m}$. The experimental data (dots) are obtained using the eqn.(4.27) and are fitted to eqn.(4.29) (continuous lines). The fitted values compared with the experimental parameters are given in Table 4.2.

Path delay A(m)	Slit width δx (μm)	'A'	Fitted value of	Experimental value B = $2\pi pa$	Reduction in $ \mu_{12}(\lambda) $
3.27E-4	300	0.761 \pm 0.038	1.034E-6 \pm 3.176E-8	1.131E-6	0.914
	400	0.772 \pm 0.06	1.102E-6 \pm 4.556E-8	2.011E-6	0.548
	800	0.694 \pm 0.068	1.372E-6 \pm 3.739E-8	8.043E-6	0.1706

Table 4.2

Table showing **the** comparison of the fitted constants with the values calculated from **the** experimental parameters for a fixed path delay between the interfering beams of the **MI** and different equal slit widths of the spectrometer. The eqn (4.29) is used for fitting the experimental data, calculated using eqn. (4.27). The corresponding data and curves are shown in the Figure 4 5.

From the Figures 4.4 and 4.5 it is clear that, the modulus of the degree of spectral coherence and hence the degree of spectral correlation between two points in the far-zone is seen to increase for smaller separation between them, with narrower width of the secondary source and for decreasing path difference between the interfering beams. The difference in the values of the constants obtained from the theoretical fittings and the experimental parameters as given in the Tables 4.1 and 4.2 are attributed to the changes in the modulation depth because of the random table vibrations and the speed of the grating movement which is kept constant while recording the modulated **spectra**, irrespective of the path delay or the number of fringes in the region of interest.

4.5 Measurement of the effect of spectral correlation using the Young's double slit experiment

Young's interference experiment is one of the simple and elegant ways to study the spectral coherence properties of light [49,50]. The theoretical investigations and experimental verifications concerning the effects of spatial coherence on the spectra of optical fields has been going on for the last decade. It is now a well established fact that the state of coherence of the radiation incident on the slits can **modify** the spectrum in the region of superposition in a **Young's** double slit experiment. The spectral changes are small for narrow bandwidth of light and / or narrow slit widths, whereas drastic changes can occur with broad bandwidth light incident on wider slits and for larger distance between the secondary source and the double slit . Though the available light intensity will in general be very less for a broad band radiation, the observed spectral changes and hence the variations in the degree of spectral coherence can be quite significant. This leads to the possibility that the correlation function in the plane of the double slit can be determined from the measurement of the power spectra instead of the fringe visibility [53]

The effect of the changes in the spectrum at the center of the **Young's** interference pattern is mainly due to two contributions. The first one is due to the

changes in the source spectrum due to diffraction at the individual slits (this happens even if only one of the slits is open) and the second contribution which is of interest here is due to the interference between the two **beams** and this depends on the state of coherence of the radiation at the two slits. This arises because, the different spectral components of the light beam used have different coherence properties at the double slit and hence their contribution gives rise to spectral changes which is different in comparison to the spectrum when only one of slits is open. It is to be noted here that the spectral changes at the on axis point are not due to the dependence of the fringe period on the temporal delay as in a Michelson interferometer. While such a dependence gives rise to the colored appearance of the interference fringes away from the center with a white light and the spectral composition of the light varies as we analyze each single fringe.

4.5.1 Theoretical details

In the Young's double slit interferometer, let $\{e(n, \nu)\}$ and $\{e(r_2, \nu)\}$ be the ensemble of the frequency dependent realizations of the fields at the two slits $P_1(r_1)$ and $P_2(r_2)$. The area A of the two identical slits are assumed to be sufficiently small so that the amplitude of the field can be taken to be effectively constant across each of them and the angles of incidence and diffraction are near normal. The superposition between the beams from the two slits is observed at a point $P(r)$ in the plane at a distance R from the two slits. Let L_1 and L_2 be the distances from the two slits at $P_1(r_1)$ and $P_2(r_2)$ to the point $P(r)$. The field at this point on the screen is, to a good approximation given by

$$e(r, \nu) = \frac{ikA}{R} \left[e(r_1, \nu) \exp(ikL_1) + e(r_2, \nu) \exp(ikL_2) \right] \quad (4.30)$$

Using the above equation in the eqn (4.19), the output field spectrum at the point $P(r)$ is given by

$$S(\nu) = 2 \left(\frac{kA}{R} \right)^2 S_0(\nu) \left\{ 1 + |\mu_{12}(\nu)| \cos[k\Delta - \beta_{12}(\nu)] \right\} \quad (4.31)$$

where, ' $k' = 2\pi\nu/c$ and A is the path difference between the interfering beams at the point $P(r)$. Equations (4.21), (4.22) and (4.25) and the appropriate conditions are used in simplifying the above equation. Apart from the constant proportionality factor, the above equation implies the following results: (i) for any **fixed** frequency ν , the spectral density at the point $P(r)$ across the observation plane varies sinusoidally with the amplitude and phase of the variation depending on the value of the degree of spectral coherence $\mu_{12}(\nu)$ and (ii) the output spectrum $S(\nu)$ at a fixed point $P(r)$ in the observation plane, differs from the input spectrum $S_0(\nu)$ depending on the degree of spectral coherence of the light at the two slits [50].

For a symmetrical and spatially effectively incoherent illumination of the double slit separated by distance ' b ' which is at a distance ' r ' from the rectangular secondary source of width ' a ', the degree of spectral coherence at the far-zone point, given by eqn.(4.29) can be written as

$$|\mu_{12}(\lambda)| \propto \frac{\sin(\pi ab/\lambda r)}{(\pi ab/\lambda r)} = A \left[\frac{\sin(B/\lambda)}{(B/\lambda)} \right] \quad (432)$$

where, A is the constant of proportionality and $B = (\pi ab/r)$ gives the width of the **sinc-function**. When the spectral density is measured at a point $P(r)$ on the screen which is at a distance ' x ' from the axis of symmetry in the region of **superposition**, assuming that the distance between the double slit and the screen $R \gg x$, and $L_1 \sim L_2 \sim R$, the path difference between the beams at the point $P(r)$ is

$$\Delta = L_1 - L_2 \approx \left(x d / R \right) \quad (433)$$

Two cases of importance here are the effect of spectral correlation at the on-axis and off-axis positions for different input secondary source width and separation between the double slits, as **function** of frequency. For the on-axis point of observation, the path difference A between the interfering beams is zero and so the **eqn.(4.31)** reduces to

$$S(v) = 2 \left(\frac{kA}{R} \right)^2 S_0(v) [1 + \text{Re}\{\mu_{12}(v)\}]$$

$$\text{or } \text{Re}\{\mu_{12}(v)\} \propto \left[\frac{S(v)}{2S_0(v)} - 1 \right] \quad (4.34)$$

where $\text{Re}\{\mu_{12}(v)\}$ is the real part of the complex degree of spectral coherence and is given by

$$\text{Re}\{\mu_{12}(v)\} = |\mu_{12}(v)| \cos[\beta_{12}(v)] \quad (4.35)$$

where $\beta_{12}(v)$ is the phase of $\mu_{12}(v)$.

For an off-axis point of spectral measurement, the eqn.(4.31) can be expanded and written as

$$S(v) = 2 \left(\frac{kA}{R} \right)^2 S_0(v) [1 + \text{Re}\{\mu_{12}(v)\} \cos(k\Delta) + \text{Im}\{\mu_{12}(v)\} \sin(k\Delta)] \quad (4.36)$$

where the real part of the complex degree of spectral coherence is given by eqn.(4.35) and the imaginary part is given by

$$\text{Im}\{\mu_{12}(v)\} = |\mu_{12}(v)| \sin[\beta_{12}(v)] \quad (4.37)$$

Thus, by taking advantage of the path difference between the interfering beams at the point of observation **P**, the entire **function** of the complex degree of spectral coherence $\mu_{12}(v)$ can be **determined**

4.5.2 Experimental

Schematic of the **Young's** double slit experiment used to measure the spectral correlation between two light beams at a point **P** in the observation plane is shown in the Figure 4.6. A 25 W tungsten filament lamp (primary source) whose characteristic values are given in the previous **section**, is used to illuminate a rectangular slit of variable width 'a'. The light beam emerging from this secondary slit source is assumed

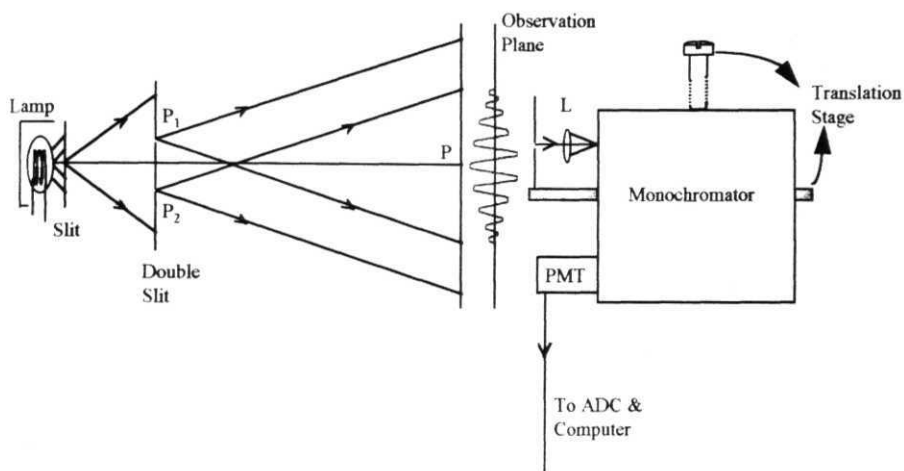


Figure 4.6

Young's double slit experimental setup used for the measurement of the complex degree of spectral coherence.

planar and quasi-homogeneous. In the far-zone of this secondary source, at a distance of $r = 20, 30$ and 50 cm, the double slit with a variable slit width adjustment is kept. A special type of mount designed for this purpose enables a symmetrical adjustment of both the individual slit widths and the separation between the center of the two slits independently. The light beam emerging from the two slits, interfere to produce a fringe pattern on the screen kept at a distance of $R = 50$ cm. One more slit with adjustable width is kept behind the screen to separate the specific fringe to enter the spectrometer. This is then focused onto the input slit of the spectrometer using a proper focal length ($f = 20$ cm) lens. The spectrometer is a 50 cm grating monochromator with a photomultiplier tube PMT fixed at the output slit to measure the spectra of the interfering beams. For all the spectral recordings done in this section, the entrance and exit slit widths of the spectrometer are kept fixed at 100 μm . The output of the PMT is connected to an ADC data acquisition card in a PC. The slit, lens and the spectrometer are mounted on a translational stage to scan the entire fringe system formed at the observation plane.

4.5.3 Results and discussion

In the Young's double slit experiment described here, we measure the effect of partial correlation on the spectrum of the superposed beams capable of forming interference fringes on the screen. The interfering beams in this case are termed spectrally impure, according to the conditions specified in the chapter 2 of this thesis. The superposed spectra $S(\lambda)$ and the spectrum of light from each individual slits $S_0(\lambda)$, closing the other are recorded for two different separation between the double slit ' b ' = 0.1 and 0.09 cm at the on-axis point of observation for a fixed width of the secondary source of ' a ' = 0.01 cm. They are separated by a distance of $r = 30$ cm. From the recordings, it is seen that the individual spectra recorded by closing either one of the slits are the same while the superposed spectrum was different. By using suitably normalized spectra, the real part of the complex degree of spectral coherence between the two partially coherent beams is calculated using the eqn.(4.34), with $\lambda =$

c/v. This experimentally measured behavior of the degree of spectral coherence is **fitted** to the theoretical equation (4.35) with the $|\mu_{12}(\lambda)|$ given by eqn. (4.32). Both the normalized experimental data and the corresponding theoretical fitting are shown in the Figure 4.7. The fitted constants are compared with the values calculated using the experimental parameters are given in the Table 4.3 and the values are found to be in close agreement with each other. The least-square fitting procedure **used**, gives a overall chi-square deviation in the fit of about $5E-2$ for all the fit. Scatter in the experimental data is high because of low light intensity levels and hence noisy spectral recordings.

By increasing the secondary source width '**a**' or by increasing the separation between the double slits '**b**' for a separation of $V = 50$ cm between them, the real part of the spectral degree of coherence at the on-axis point is found to vary drastically as can be seen from the Figures 4.8 and 4.9. The real part of the complex degree of spectral coherence for a fixed value of '**b**' and different values of '**a**' or vice-versa are calculated using the eqn. (4.34) in the same way as mentioned before. The corresponding fitted curves are also shown in the same figure and the fitted constants given in the Table 4.4 are compared with the values calculated using the experimental parameters. Observation of such a large change in $\text{Re}\{\mu_{12}(\lambda)\}$ is possible because of the broadband nature of the source spectrum, within which the degree of spectral coherence changes appreciably. This effect is mainly because of more incoherent contribution in the interfering beams with increasing slit widths affecting the degree of spectral coherence between the interfering beams drastically. This is evident from the increase in the value of the phase factor $P_n(v)$ of the degree of spectral coherence with increase in the slit widths given in the last column of the Table 4.4. In all the above recordings, the distance of the screen from the plane of the double slit is kept fixed at $R = 50$ cm. It has also been demonstrated elsewhere that, using a different source geometry can lead to a rapid variations in the degree of spectral coherence even with a narrower source spectrum [57].

The experimental configuration is now fixed at '**a**' = 0.01 cm, '**b**' = 0.045 cm, '**r**' = 20 cm and $R = 100$ cm so that one gets well separated colored white light

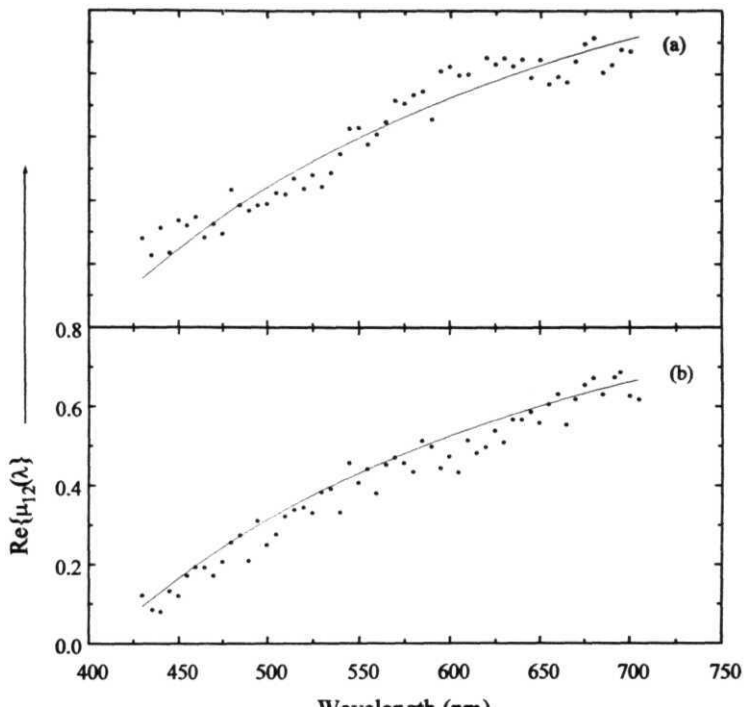


Figure 4.7

On-axis measurement of the real part of the complex degree of spectral coherence as a function of wavelength for two different double slit widths (a) $b=0.1$ cm, (b) 0.09 cm. The experimental data are obtained using eqn.(434) with appropriately normalized spectra. The data are fitted to eqn. (435) with (432) and the fitted constants compared with the experimental values are given in the Table 4.3.

Double slit separation ‘b’ (cm)	A'	B' = ($\pi ab/r$)	C' = $\beta_{12}(\nu)$
0.1	1.296 ± 0.086	1.0E-6 ± 1.361E-8 (1.047E-6)	6.907E-7 ± 3.687E-8
0.09	1.085 ± 0.884	9.987E-7 ± 1.947E-8 (9.425E-7)	6.380E-7 ± 3.687E-8

Table 4.3

Fitted values for the behavior of real part of the complex degree of spectral coherence for a fixed value of the secondary source width of ‘a’ = 0.01 cm and distance between the secondary source and the double slit ‘r’ = 30 cm at the on-axis position. The values given in the brackets are calculated using the experimental parameters. The experimental data and the fitted curves are shown in the Figure 4.7.

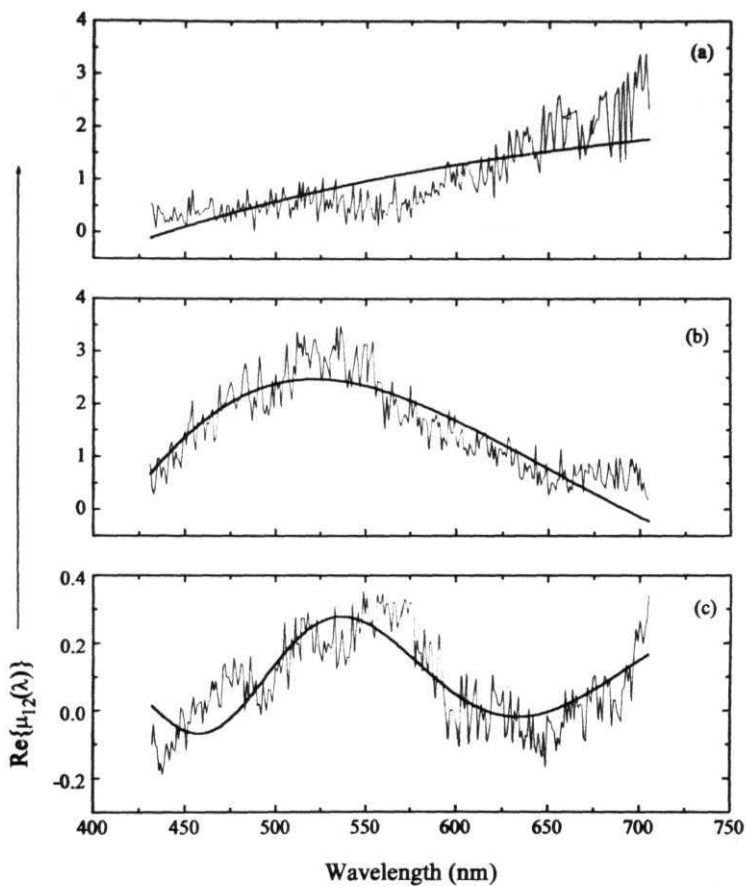


Figure 4.8

Behaviour of the real part of the complex degree of spectral coherence at the on-axis position for a fixed separation between the double slit of $b=0.045$ cm and different widths of the secondary source 'a' **(a)0.006cm,** **(b)0.015** cm and **(c)0.016** cm. The experimental data obtained using the eqn.(4.34) are fitted to the eqns.(4.35) and (4.32).The fitted constants are given in Table 4.4.

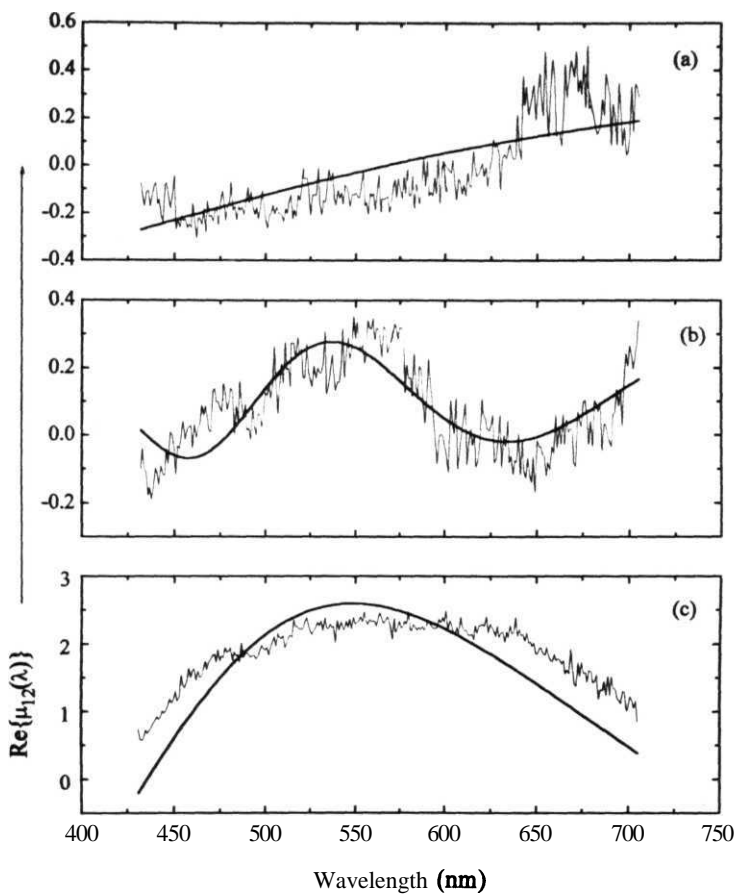


Figure 4.9

Real part of the complex degree of spectral coherence as a function of wavelength at the on-axis position, for a fixed width of the secondary source of $a = 0.016$ cm and different separation of the double slit 'b' (a) 0.038 cm, (b) 0.045 cm and (c) 0.05 cm. The experimental data obtained using the eqn.(4.34) are fitted to the eqns.(4.35) and (4.32) and the fitted constants are given in Table 4.4.

a (cm)	b(cm)	A'	B' = ($\pi ab/r$)	C' = $\beta_{12}(v)$
0.016	0.038	0.654 \pm 0.143	3.675E-7 \pm 2.847E-8 (3.820E-7)	8.899E-7 \pm 2.847E-8
	0.045	2.180 \pm 0.267	4.10E-6 \pm 6.176E-8 (4.524E-7)	6.776E-6 \pm 7.669E-8
	0.05	2.996 \pm 1.146	5.0E-7 \pm 7.993E-7 (5.027E-7)	3.422E-6 \pm 5.059E-8
0.006	0.045	3.205 \pm 0.481	1.540E-7 \pm 3.115E-7 (1.508E-7)	6.912E-7 \pm 3.619E-8
0.015		2.752 \pm 0.168	4.052E-7 \pm 3.307E-8 (4.241E-7)	3.261E-6 \pm 3.940E-8

Table 4.4

Table giving the values of the fitted constants for different width of the secondary source 'a' and separation between the center of the Young's double slit 'b' from the measurement of the $\text{Re}\{\mu_{12}(\lambda)\}$ at the on-axis position. The distances $V = R = 50$ cm. The values given in the brackets are calculated using the experimental parameters. **The** experimental data and the theoretical fit are shown in the Figures 4.8 and 4.9.

interference fringes at the screen. By moving the detection system consisting of the adjustable slit, lens and the spectrometer with the help of a linear translation stage across the colored interference **fringe** pattern, the spectral changes at different off-axis positions as predicted by eqn.(4.36) is demonstrated. According to this equation, the degree of spectral coherence now, has effect from both the real and imaginary contributions from the secondary source and the double slit which leads to a drastic reduction in the fringe visibility and also increase in the number of fringes as a manifestation of the larger temporal delay between the interfering beams reaching the observation point P. It is clear from the Figure 4.10 that as we go away from the axis of symmetry denoted by the distance ' x ', the spectrum changes drastically and the number spectral fringes increases in accordance with the increase in the path difference between the interfering beams reaching that point. There is also a reduction in the total intensity per fringe detected as we move away from the center which makes the recordings noisy. Increasing the slit widths at this point reduces the spectral fringe contrast as expected, because of the increase in the incoherent contribution from the individual slits.

4.6 Space-frequency equivalence and some applications

It is evident from the last two sections that, from a measurement of the spectral distribution in the plane of observation in a Michelson interferometer or Young's double slit experiment, it is possible to determine the degree of spectral coherence $\mu_{12}(\nu)$ of the light beam forming the interference. However, this information can also be deduced by passing the two light beams through filters sharply tuned to the frequency ν or by using a monochromatic light and by measuring the fringe visibility and shift in the position of the fringe maxima in the region of superposition for different path delays between the interfering beams. According to the principle of *space-frequency equivalence* [58], there exists a correspondence between the measurement of the degree of spectral coherence obtained at a fixed frequency ν and for different separations ' b ' of the two slits (or two arms of variable delay in **MI**) and

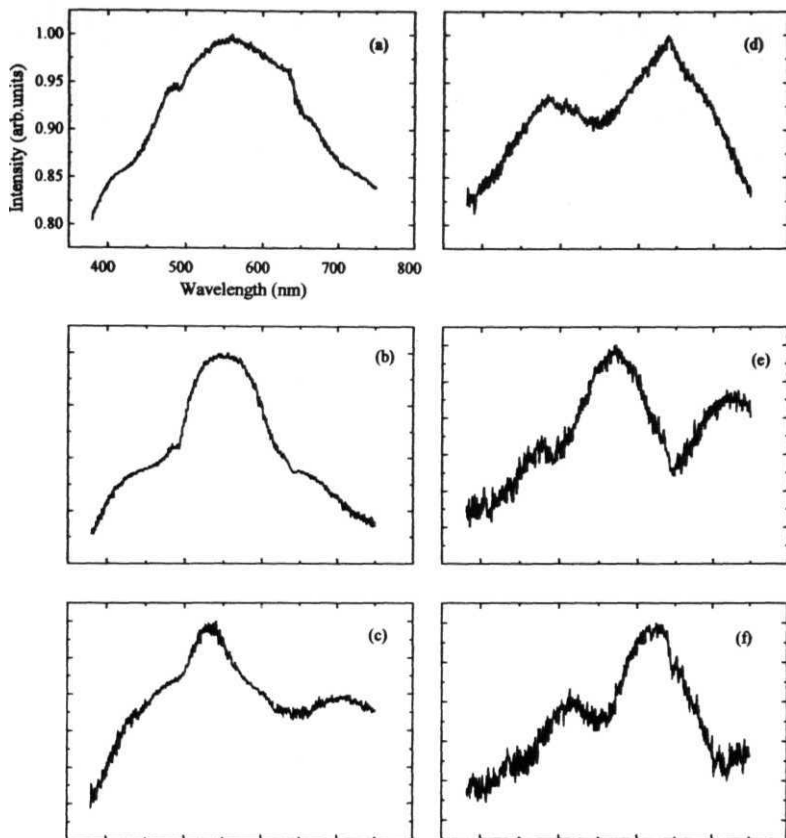


Figure 4.10

Experimental recordings demonstrating the spectral changes in the Young's double slit interference **pattern**, for different off-axis **positions** (a) $x = 0.45$ mm, (b) 0.9 mm, (c) 1.1 mm, (d) 1.35 mm, (e) 1.6 mm, (f) 1.75 mm.

the **frequency** analysis of the radiation from a **fixed** pair of slits (or fixed path delay in **MI**) over the entire bandwidth in a multifrequency correlation system. In other words, the correlation measurement done at a single frequency ν for different values of separation between the interfering beams is equivalent to the measurement over the range of frequencies, obtained for a fixed separation [59]. This principle forms the basis of a technique known as *bandwidth synthesis mapping* in radio astronomy.

Apart from the application of the synthetic aperture imaging technique in the optical region and in radio astronomy, the spectral correlation measurements in both Michelson interferometer and Young's interference experiment are useful in various applications briefed in the following. Using the principle of interferometric equivalence for the scaling law of fields, James and Wolf proposed a method to measure the intensity distribution across the source [59]. This was confirmed later [60] from the experimental measurement of the $\text{Re}\{\mu_{12}(\nu)\}$ in the plane of the double slit over a broad range of frequencies. The single spectral measurement for a fixed separation ' b ' between the slits is related to the Fourier transform of the intensity distribution across the source. Also, from the spectral visibility measurements at off-axis points, which show cosine modulations and from the period of the spectral visibility in the frequency scale, the angular separation between the sources can be measured [61]. In the case of **MI** or a **MZI**, the periodicity of the spectral fringes gives information about the linear displacement [54] between the interfering beams. Recently, it has been demonstrated that the size of the source can be determined by comparing the sum of the source spectra with one of the slits open with the modified power spectrum obtained when both the slits are **open**. From the value of the wavelength where the two spectra intersect, the size of the incoherent source is determined [62].

References

- [1] A A Michelson, *Phil. Mag.* **30**, 1, (1890).
- [2] F. Zernike, *Physica* **5**, 785, (1938).
- [3] M. Born and E. Wolf, *Principles of optics*, (Pergamon, Oxford, 6th edition, 1980), chapter 10.
- [4] E. Wolf, *Proc Roy. Soc. A* **230**, 246, (1955).
- [5] H.H. Hopkins, *J Opt Soc Am.* **47**, 508, (1957).
- [6] L Mandel and E Wolf, *Rev Mod. Phys.* **37**, 231, (1965).
- [7] L Mandel and E Wolf, *J Opt. Soc. Am.* **66**, 529, (1976).
- [8] E. Wolf, *Opt. Lett* **8**, 250, (1983).
- [9] M. Francon and S Mallick, in *Progress in optics*, Edited by E. Wolf, (North-Holland, 1967), Vol 6, B J Thompson, in *Optical transforms*, Edited by H. Lipson, (Academic Press, 1972).
- [10] B.J Thompson and E Wolf, *J. Opt. Soc. Am.* **47**, 895, (1957).
- [11] B J Thompson, *J Opt Soc Am.* **48**, 95, (1958).
- [12] L.R. Baker, *Proc. Phys Soc London B* **66**, 975, (1953)
- [13] B.J. Thompson and R Sudol, *J. Opt. Soc. Am. A* **1**, 598, (1984).
- [14] A.S. Marathay and D.B. Pollock, *J. Opt. Soc. Am. A* **1**, 1057, (1984).
- [15] F T S Yu and Y.W.Zhang, *Appl. Opt.* **25**, 3191, (1986).
- [16] S. Mallick, *Appl. Opt.* **6**, 1403, (1967).
- [17] D.N. Grimes, *Appl Opt* **7**, 1567, (1971)
- [18] M. Bertolotti, M. Carnevale, L. Muzii and D Sette, *Appl. Opt.* **9**, 510, (1970).

- [19] P. Hariharan and D. **Sen**, J. Opt. Soc. Am. 51, **1307**, (1961).
- [20] M.VR.K. **Murty**, J. Opt. Soc Am. 54, **1187**, (1964).
- [21] J. Perina, Coherence of light, (Van Nostrand, London, 1971), chapter 4.
- [22] **D Kohler** and L. Mandel, J. Opt. Soc. Am. **61**, **1589**, (1971).
- [23] D. Kohler and L. Mandel, J. Opt Soc. Am. **63**, **126**, (1973).
- [24] Y. **Ohtsuka**, Opt. Lett. 1, **133**, (1977).
- [25] E. Wolf, in Recent developments in quantum optics, Edited by R. **Ingua** (Plenum, NY, 1993), **369**.
- [26] L. Mandel and E. Wolf, in Optical coherence and Quantum optics, (Cambridge press, 1995), **chapter 5**.
- [27] E. Wolf, Phys Rev. Lett. 56, **1370**, (1986).
- [28] M.F. Bocko, D.H. Douglas and R.S **Knox**, Phys. Rev. Lett. 58, **2649**, (1987).
- [29] G.M. Morris and **D Falkis**, Opt Commun. **62**, **5**, (1987).
- [30] J.T. Foley, Opt Commun. 75, **347**, (1990).
- [31] E. Wolf, in International trends in optics, Edited by J W Goodman, (Academic Press, 1991), **chapter 16**; P.W. Milonni and S. Singh, in Advances in atomic, molecular and optical physics, Edited by **D Bates** and **B Bederson**, (Academic press, 1991), Vol. 28, **chapter 8**.
- [32] E. Wolf, Nature **326**, **363**, (1987).
- [33] E. Wolf, Opt Commun **62**, **12**, (1987).
- [34] E. Wolf, Phys Rev. Lett. 58, **2646**, (1987).
- [35] A. **Gamliel** and E. Wolf, Opt. Commun. 65, **91**, (1988).
- [36] F. Gori, G. Guttari, C. **Palma** and C. Padovani, Opt. Commun. **67**, **1**, (1988).
- [37] **D Falkis** and CM. Morris, Opt Lett **13**, **4**, (1988)

- [38] H.C. Kandpal, J.S. Vaishya and K.C. Joshi, Opt. Commun. 73, 169, (1989).
- [39] **H.C** Kandpal, **J S** Vaishya and **K.C** Joshi, Phys. **Rev A** **41**, 4541, (1990).
- [40] G. **Idebetouw**, J. Mod. Opt. 36, **251**, (1989).
- [41] J.T. **Foley**, J Opt. Soc. Am. A 8, 1099, (1991).
- [42] E. Wolf, J **T** Foley and F. Gori, J Opt. Soc. Am. A 6, **1142**, (1989); *ibid*, J. Opt. Soc. **Am** A 7, **173**, (1990).
- [43] **J.T** Foley and E. Wolf, Phys. Rev. A 40, 588, (1989).
- [44] **E** Wolf, Phys. Rev. Lett. 63, 2220, (1989).
- [45] D.F.V. James, M. **Savedoff** and **E** Wolf, Astrophys J. **359**, 67, (1990).
- [46] **D.F.V.** James and E. Wolf, Phys. Lett. A **146**, 167, (1990).
- [47] **B** Cairns and E. Wolf, J. Opt. Soc. Am. A 8, 1992, (1991).
- [48] L. Mandel, J. Opt. Soc. Am. 51, 1342, (1961).
- [49] D.F.V James and E. Wolf, Opt. Commun. 81, 150, (1991).
- [50] D.F.V James and E. Wolf, Phys. Lett. A **157**, 6, (1991).
- [51] **W.H** Steel, Interferometry, 2nd edition, (Cambridge university press, 1983).
- [52] **F** Heiniger, **A** Herden and **T** Tschudi, Opt. Commun 48, 237, (1983)
- [53] K. Saxena, D.S. Mehta, **H.C** Kandpal, **J S** Vaishya and **K.C** Joshi, Opt. Commun. **111**, 423, (1994); V. Nirmal Kumar and **D** Narayana Rao, to be communicated.
- [54] **G S** Agarwal and **D.F.V. James**, J Mod Opt. 40, 1431, (1993); **D** Narayana Rao and V Nirmal Kumar, J Mod Opt **41**, 1757, (1994); D.S. **Mehta**, H.C. Kandpal, **K** Saxena, **J S** Vaishya and **K.C** Joshi, Opt. Commun. **119**, 352, (1995).
- [55] E. Wolf, J Opt Soc. Am. 72, 343, (1982).

- [56] Z.Y. Ou and L. Mandel, Am. J. Phys. 57, 66, (1989).
- [57] M. Santarsiero and F Gori, Phys. Lett. A **167**, 123, (1992).
- [58] W.E. Kock and J L Stone, **Proc IRE** 46, 499, (1958).
- [59] D.F.V. James and E. Wolf, Radio **Sci** **26**, 1239, (1991).
- [60] H.C Kandpal, J.S Vaishya, K.S. Saxena, D.S Mehta and K.C. Joshi, J. Mod. Opt. 42,455, (1995).
- [61] H.C Kandpal, J S. Vaishya, K.S Saxena, D.S Mehta and K.C Joshi, J. Mod. Opt. **42**, 447, (1995).
- [62] S. Vicalvi, G.S. Spagnolo and M. Santarsiero, Opt. **Commun.** **130**, 241, (1996)

CHAPTER 5

MEASUREMENT OF LINEAR DISPLACEMENT USING SPECTRAL INTERFEROMETRY

5.1 Introduction

Increased interest in the theoretical study and **experimental** investigations of coherence phenomena in the space-frequency domain [1,2] has widened the scope of spectral **interferometry** as a versatile technique in different applications. This is mainly because, many physical phenomena involving the coherence properties of light are more naturally described in the space-frequency domain [3-6] and the number and variety of applications of interferometry in the spectral domain is fast increasing [7]. Wolf [8] and others have demonstrated that the spectrum of radiation emitted from a certain class of sources shows a red shift or a blue shift in the spectral maximum or cosinusoidal modulations of the output spectral intensity [9,10]. These changes in the **field** spectrum of partially coherent sources depend on the source spectrum and its statistical properties, characterized by the second-order degree of spectral coherence [11]. Partially coherent sources which are neither completely uncorrelated nor **fully** correlated, have the uniqueness that the spectrum of light generated under suitable conditions either changes or remains invariant in free space propagation [12]. Polychromatic sources of arbitrary degree of coherence have been experimentally synthesized to demonstrate the effects of source correlation [13]. It has been theoretically predicted and experimentally **verified** that the spectral changes appear pronounced in the case of two beam interference [14], diffraction of stationary and nonstationary wave fields [15,16], interference between two linearly polarized modes of a fibre waveguide [17], **etc**

Absolute position-distance measurement by optical interferometry using either a multiple wavelength [18] or white light source [19] are known for quite some time.

However, because of broad bandwidth of the white light source **used**, usually the group-velocity index must be included in the path length calculations [20] and monochromatic sources suffer from the phase ambiguity problems and there is no information to provide the absolute orders of the interference fringes. For the spectral interferometers operating in the wavelength **domain**, a monochromator is used to scan the wavelength across the source spectrum to provide interference fringes. Alternatively, a dispersing element like a grating and a CCD array detector can also be used in single shot experiments. Because of the controlled bandwidth of the source **spectrum**, the path delay between the interfering beams can be calculated using the simple fitting procedure discussed in this chapter without going through much of complications encountered in the other techniques. Thus from the spectral analysis of light in the region of superposition in a two beam interference experiment, one can get information about the exact path difference or the absolute linear displacement between the interfering beams from the periodicity of the spectral fringes [21,22].

5.2 Spectral modulations in the Mach-Zehnder interferometer

The spectral changes due to different degrees of correlation between the interfering beams, has been investigated for the case of a broad band laser light. This broad band light (details of which are discussed in the chapter 3) satisfies the condition for quasi-monochromatic radiation

$$\text{i.e., } \frac{\delta v}{v_0} = 0.015 \ll 1 \quad (5.1)$$

Different degrees of correlation between the interfering beams can be achieved by introducing a suitable path delay between the interfering beams of the **MZI**. Unequal dispersion between the two arms from the beam splitter material is avoided, as it leads to the characteristics of the spectra at the two output arms of the interferometer different from each **other**. The front surface coated beam splitters (**R/T** = 50/50) in the MZI are arranged in such a way (see Figure 5.1) that material dispersion without any

sample in either of the arms of the interferometer seen by **both the** beams and monitored at the output arms of the interferometer are equal.

The spectral interference law for the superposition of two partially correlated beams has been derived to demonstrate the spectral changes in a broad band light source incident on a Mach-Zehnder interferometer (MZI) [23]. For the broad bandwidth source spectrum used in a two beam interferometer like a MZI, the degree of correlation between the interfering beams can be changed easily by inserting glass slides into one of the arms of the interferometer [21]. After **adjusting** the path difference between the two arms of the interferometer to within the coherence length of the source ($l_c \approx 40 \mu\text{m}$) introduction of a glass slide of sufficient thickness, increases the path difference to more than the coherence length. As a result, spatial interference fringes disappear and then if the spectrum of the output from the interferometer is monitored, spectral fringes are seen. As the modulation frequency of the spectral interference fringes are characteristic of the delay introduced between the two beams, fitting the experimentally recorded spectral interferogram to the theoretically derived spectral interference law, gives the exact value of the linear displacement between the interfering beams. The refractive index of the glass plate used is assumed to be a constant within the bandwidth of the **spectrum**. Though the vibrations and other disturbances do not invalidate the information that can be obtained from the spectral interferogram as it happens in the time domain **interferometry**, an estimation of the amplitude of vibrations from the theoretical **fitting** is tried. The stability of the interferometer **configuration** is improved based on reducing the arm lengths and modifying the dynamically stable Sagnac interferometer to suit our purpose.

Exact measurement of the linear displacement or thickness measurement from the spectral modulations [24-26] is preferred to the usual method of time domain interferometry (also known as Fourier transform spectroscopy) for the following reasons:

In a two beam interferometer illuminated by a **monochromatic** light, the absolute measurement of the optical thickness of samples inserted in one of the interferometer

arms whose thickness is more than half the wavelength of the light used is prevented by the ambiguity of $k\lambda$ (k : integer and λ : wavelength). This can be avoided in some special cases either by moving one of the mirrors of the interferometer [27] or by using two or more beams of different wavelengths to generate a Moire pattern [28]. In the more general time domain **interferometry** using a broad band white light, the output from the interferometer is composed of two out of phase wave trains derived from a single wave train and delayed by the optical path of the sample introduced in one of the arms [25]. Now, the path difference can be determined by analyzing the output using a second interferometer of a variable delay [29-31]. In this case, the main drawbacks [32] are: (1) the signal oscillates very fast, having the periodicity of the mean wavelength of the source as a **function** of the optical path, (2) a large number of fringes must be recorded to obtain high spectral **resolution**, which eliminates the use of single-shot technique like using a CCD array, (3) as most of the information is obtained from the fringe contrast, sophisticated and kinematically stable interferometers with variable path differences are necessary. All these disadvantages can be overcome by using a spectrometer which performs the spectral analysis of the output from the interferometer. Under the condition that the path difference between the interfering beams is more than the coherence length of the source, the output of the spectrometer gives a channelled spectrum, also known as spectral **interferogram**. The frequency of the spectral modulations directly gives information about the optical path because of the sample introduced or the linear displacement between the interfering beams. Also, from the amplitude of the modulations, an estimate of the stability of the interferometer against vibrations and other disturbances can be made.

5.2.1 Theoretical formulation

For the Mach-Zehnder interferometer shown in the Figure 5.1, let r_1, r_2 be the reflectivities and t_1, t_2 the **transmissivities** of the two beam splitters 1 and 2 respectively. The input beam from the broad band dye laser split by the beam splitter 1, goes through the two arms of the interferometer of path lengths L_1 and L_2 and are combined again at the beam splitter 2. Output spectrum of the superposed beams from

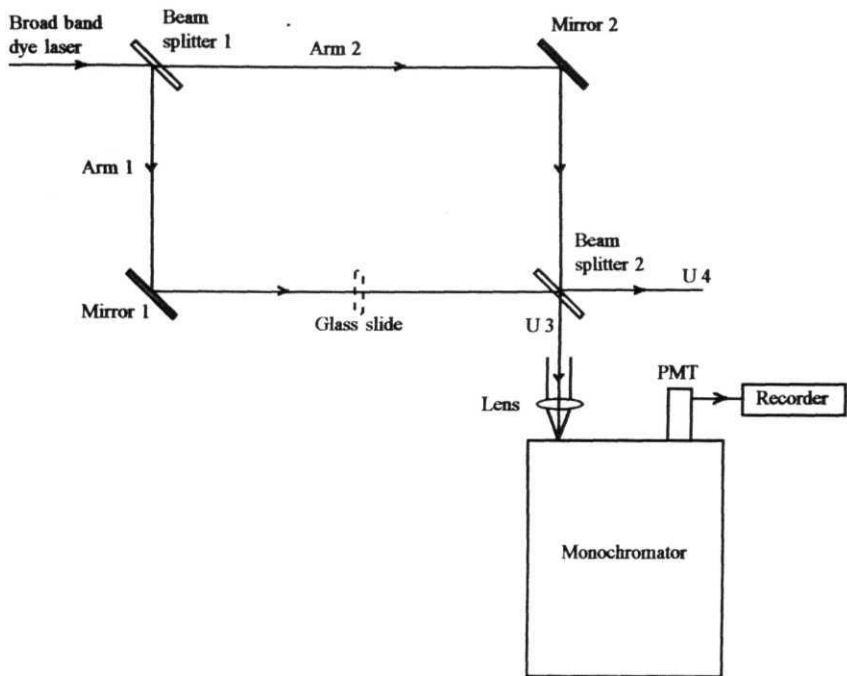


Figure 5.1

Experimental setup for measuring the linear displacement using a **MZI**.

the interferometer at one of the ports (U_3 or U_4) is monitored using a grating spectrometer. For any realistic **source**, the randomly fluctuating source distribution can be described by an appropriate statistical ensemble. Instead of an ensemble of the usual time dependent **realizations**, we can represent the fluctuations in the beams by an ensemble of the frequency dependent realizations introduced by Wolf [33]. Let $\{\epsilon_1(\nu)\}$ and $\{\epsilon_2(\nu)\}$ be the ensembles that represent the source fluctuations at two **fixed** points, assumed to be statistically stationary. The fields of the two frequency dependent ensembles in the two arms of the interferometer are given by

$$\begin{aligned}\epsilon_1(\nu) &= a(\nu)\epsilon_m(\nu) \\ \epsilon_2(\nu) &= b(\nu)\epsilon_m(\nu)\end{aligned}\quad (5.2)$$

where $\epsilon_m(\nu)$ is the input spectrum from the broad band dye laser, $a(\nu)$ and $b(\nu)$ the frequency dependent coefficients which depend on the properties of the beam splitter and the path length taken by the two beams in the two arms of the interferometer, are given by the expressions

$$\begin{aligned}a(\nu) &= r_1 \exp(ikL_1) \\ b(\nu) &= t_1 \exp(ikL_2)\end{aligned}\quad (5.3)$$

where, $k = 2\pi\nu/c$ and r_1 and t_1 are the reflectivity and **transmissivity** of the beam splitter 1. **Using** the principle of conservation of energy for non-absorbing **beam** splitters, the Stokes relations [34] for the reflectivity and transmissivity are written as

$$\begin{aligned}|r|^2 + |t|^2 &= 1 \\ r t^* + r^* t &= 0\end{aligned}\quad (5.4)$$

From the above two equations (5.3) and (5.4), it can be shown that

$$|a(\nu)|^2 + |b(\nu)|^2 = 1 \quad (5.5)$$

The output beam at the two ports of the interferometer (U_3 and U_4) is the sum of the statistical **ensemble** of the fluctuating field from the two arms and is given by

$$\begin{aligned}U_3(\nu) &= r_2 \epsilon_1(\nu) + t_2 \epsilon_2(\nu) \\ U_4(\nu) &= t_1 \epsilon_1(\nu) + r_1 \epsilon_2(\nu)\end{aligned}\quad (56)$$

Assuming the beam splitters to have the same properties i.e., $\mathbf{r}_1 = \mathbf{r}_2 = \mathbf{r}$ and $\mathbf{t}_1 = \mathbf{t}_2 = \mathbf{t}$, the output at both the ports of the interferometer give the same results and we concentrate on the port \mathbf{U}_3 only, for our **further** calculations. Using the **eqns.(5.2)**, (5.3) and (5.6), we get for the output field at the beam splitter 2

$$\mathbf{U}_3(\mathbf{v}) = [\mathbf{r}^2 \exp(ikL_1) + \mathbf{t}^2 \exp(ikL_2)]\mathbf{e}_{in}(\mathbf{v}) \quad (5.7)$$

The spectrum of the output field is given by

$$\mathbf{S}(\mathbf{v}) = \langle \mathbf{U}_3^*(\mathbf{v})\mathbf{U}_3(\mathbf{v}) \rangle \quad (5.8)$$

where the asterisk denotes the complex conjugate and the angular brackets denote the ensemble average over all the frequency dependent variables. On substituting the eqn.(5.7) into eqn.(5.8) and **simplifying**, we get for the output spectrum

$$\mathbf{S}(\mathbf{v}) = \left(\frac{1}{2}\right)\mathbf{S}_0(\mathbf{v}) \left[1 + \cos\left(\frac{2\pi\mathbf{v}\Delta}{c} + \theta\right) \right] \quad (5.9)$$

In deriving the above **equation**, we have taken the real part of the ensemble average, $|\mathbf{r}| = |\mathbf{t}| = 1/\sqrt{2}$, $\langle \mathbf{e}_{in}^*(\mathbf{v})\mathbf{e}_{in}(\mathbf{v}) \rangle = \mathbf{S}_0(\mathbf{v})$, is the spectrum of the input **beam**, $A = L_1 - L_2$ is the path difference between the interfering beams, $\mathbf{t}^2/\mathbf{r}^2 = \exp(i\theta)$ is the additional phase change because of the transmission and reflection **inhomogenities** at the beam splitters and mirrors and which is independent of the path lengths traveled in the two arms. This phase term can be neglected in further calculations for light beams traveling through similar optical components. The real part of the complex degree of spectral coherence $\text{Re}\{\mu_{12}(\mathbf{v})\}$ has been taken = 1 as a consequence of the analysis done in the last chapter.

Equation (5.9) is the interference law for the **MZI** configuration given in the Figure 5.1. We can see from this equation that, when $\Delta/c > \tau_c$ (the correlation time) there will be cosinusoidal modulations in the output spectrum and larger the path difference, more will be the spectral modulations. The dye laser spectrum $\mathbf{S}_0(\mathbf{v})$ obtained by closing one of the arms of the interferometer is fitted to an appropriate envelope function [21]. The spectral modulations obtained for different degrees of

correlation **between** the interfering beams are fitted using eqn.(5.9) to get the exact value of the path difference A.

Limitations The minimum distance Δ_{\min} that can be measured using this technique is limited by the spectral band width $\delta\lambda$ of the dye laser source. A minimum number of atleast two periods of the interference fringe pattern has to be detected to unambiguously calculate Δ_{\min} from the total phase variation $\delta\phi$ across the spectral fringe pattern [19]. The interference phase is then given by

$$\phi = 2\pi v \Delta / c \quad (5.10)$$

and the total phase variation within the spectrum should satisfy the condition,

$$\delta\phi = 2\pi \left(\Delta / c \right) \delta v \geq 2\pi \quad (5.11)$$

$$\text{Where, } 2\pi\delta v = 2\pi c \left(\frac{\delta\lambda}{\lambda_0^2} \right) \quad (5.12)$$

Using the above two equations, the condition for the minimum measurable distance is given by

$$\Delta_{\min} = \left(\frac{\lambda_0^2}{\delta\lambda} \right) \quad (5.13)$$

Where λ_0 is the mean wavelength of the source.

The maximum distance Δ_{\max} that can be measured is **limited** by the spectral resolution ($\delta\lambda_{\text{sp}}$) of the spectrometer. At the resolution limit, atleast three independent samples should be recorded per period of the interference signal [35] to determine the path difference between the interfering beams. The phase difference between the two spectrally resolved fringes is given by condition

$$\delta\phi = 4\pi \left(\Delta / c \right) \delta v_{\text{sp}} \leq 2\pi / 3 \quad (5.14)$$

Using eqn.(5.12) in the above condition, the maximum measurable distance, in terms of the mean wavelength λ_0 and the spectral resolution of the spectrometer $\delta\lambda_{\text{sp}}$ becomes

$$\Delta_{\max} = \left(\frac{\lambda_0^2}{6\delta\lambda_{sp}} \right) \quad (5.15)$$

The spectral resolution of a grating spectrometer, calculated using the standard grating formula is,

$$\frac{\lambda_0}{\delta\lambda_{sp}} = R = \frac{mN}{2} \quad (5.16)$$

Where, m is the diffraction order of the **grating**, N is the number of grooves on the illuminated area of the grating. It is assumed that the true resolving power R of the grating is two times less good than the theoretical resolving power. The grating spectrometer used in our experiments for which the diameter of the illuminated area of the grating is 70 mm having 1200 grooves/mm, working in the first order, the practical resolving power is calculated to be 42,000. For the peak wavelength of the dye laser of $\lambda_0 = 579.5 \text{ nm}$, the spectral resolution limit $\delta\lambda_{sp} \approx 0.014 \text{ nm}$.

5.2.2 Experimental measurement of linear displacement using a broad band laser source

The path difference between the two arms of the **MZI** is first adjusted by moving the beam splitter 2 and one of the mirrors **M₂** so that spatial interference fringes are seen on a screen. At this point, we can say that the difference in the arm lengths are equal to within the coherence length of the source ($l_c \approx 40 \mu\text{m}$). All the optical components of the interferometer are fixed onto the table and from now on, the correlation between the interfering beams is changed by introducing glass slides into one of the arms. As it is experimentally quite difficult to place the beam splitter and the mirror in a MZI to arrive at the exact zero path difference between the two arms, we started with a path difference close to zero and introduced glass slides into the arm 1 of the interferometer. After one glass plate, we could make sure that by introducing more plates into the same **arm**, the path difference between the arms increases without going through the zero path difference. This way, both the absolute

displacement between the interfering beams and the path difference between the beams for two thickness of glass plates introduced can be exactly measured. Thickness of each glass slide, measured manually using a screw gauge is ' t ' $\approx 150 \mu\text{m}$. The refractive index of these **microslides** measured using a white light source and an Abbe **refractometer** is ' n ' = 1.521. These values together correspond to an optical path **of $nt \approx 228 \mu\text{m}$** by introducing one **microslide** into the interferometer arm.

The broad band dye laser used has already been described in detail in the previous chapter 3. The oscillator with a fully reflecting broad band mirror and a glass plate as the cavity elements and a single stage amplifier are pumped by the second harmonic (532 nm) of a Q-switched NdYAG laser. The Rh 6G dye used gives a peak emission wavelength **of $\lambda_0 = 579.5 \text{ nm}$** and the bandwidth (FWHM) obtained by fitting for a Gaussian profile and corrected for the Gaussian random process is $\delta\lambda = 8.7 \text{ nm}$. The spectral resolution of the 50 cm grating monochromator (JY, HRS-2) in the Czerny-Turner configuration is calculated to be $\delta\lambda_{sp} \approx 0.014 \text{ nm}$. From these values and using the eqns(5.13) and (5.15), the maximum and minimum values of the displacement that can be measured using this technique are: $\Delta_{max} \approx 3.7 \text{ mm}$ and $\Delta_{min} \approx 38 \mu\text{m}$. Using a broader spectral width for the source like a tungsten filament lamp or a SLD (super luminescent diode), the measurement range of the interferometer can be **increased**.

First, it is visually confirmed that the number of spectral fringes at the output of the interferometer increase with the number of glass slides introduced in the arm 1 of the **MZI**, by using a reflection type grating and projecting the dispersed interference pattern onto the **wall**. The output beam from one of the arms (U_3) of the interferometer is then passed through the monochromator and the output from the PMT at the exit slit is sent to a chart recorder (Packard **611**) for recording the **spectra**. The recorded spectra are digitized and fed to a PC for data processing. The fringe spacing observed in our experimental recordings of 0.4 to 2.3 nm between consecutive maxima **fall** well within the range of the resolving power of the monochromator (**0.014 nm**). The spectral modulations recorded and digitized with 5 glass slides in the arm 1

of the **MZI** is shown as dots in Figure 5.2 (a). The corresponding path **difference** calculated using values mentioned previously and the formula $(n-1)Nt$, where N is the number of glass slides is 390.75 μm . The recorded spectral modulations are fitted to the eqn. (5.9) with $v = c/\lambda$, using least-square fitting routine written in FORTRAN to get the exact path difference (A). Assuming the refractive index 'n' to be constant over the bandwidth of the spectrum (560 - 580 **nm**), the fitted value for the path difference $A = 403 \mu\text{m}$. The theoretical fit is shown as continuous line in the same Figure 5.2(a). The spectral modulations and the corresponding theoretical fit for three additional glass slides introduced into the same arm are shown in Figure 5.2(b). The path difference calculated from the experimental parameters 234.45 μm is in close agreement with the value obtained from the fit of 240 μm . In both the cases, there is a maximum difference between the experimental and fitted values of the path difference of about 4%. This difference is attributed to the inaccuracy in the manual measurement of thickness of the glass slides and the initial non-zero path **difference** with which we started the experiment. The accuracy of the estimated A values depend on the accuracy with which the theoretical fittings can be carried out.

A comparison of the path difference calculated by fitting the spectral modulations to the theoretically derived eqn. (5.9) with an already known technique is attempted to substantiate our claim that, the technique used here gives values for the path difference with better accuracy. The Fourier transform of the spectral **interferogram** recorded for a particular path delay between the interfering beams gives the spatial interferogram [36] and from the separation of the autocorrelation peaks, the path difference between the two interfering beams can be obtained. The first peak near the origin corresponds to the autocorrelation of the first beam and the distance between the first peak and the second peak gives the optical path difference between the **beams**. The spectral modulations recorded for a fixed path delay between the beams shown in the Figure 5.3 (a) is first fitted to the eqn. (5.9) to get the path difference of $A = 39.838 \mu\text{m}$. The chi-square error involved in the fitting is as low as $1\text{E-}3$ which is evident from the closeness with which the experimental data and the theoretical fit match. Now, taking the fast Fourier transform of the experimental data

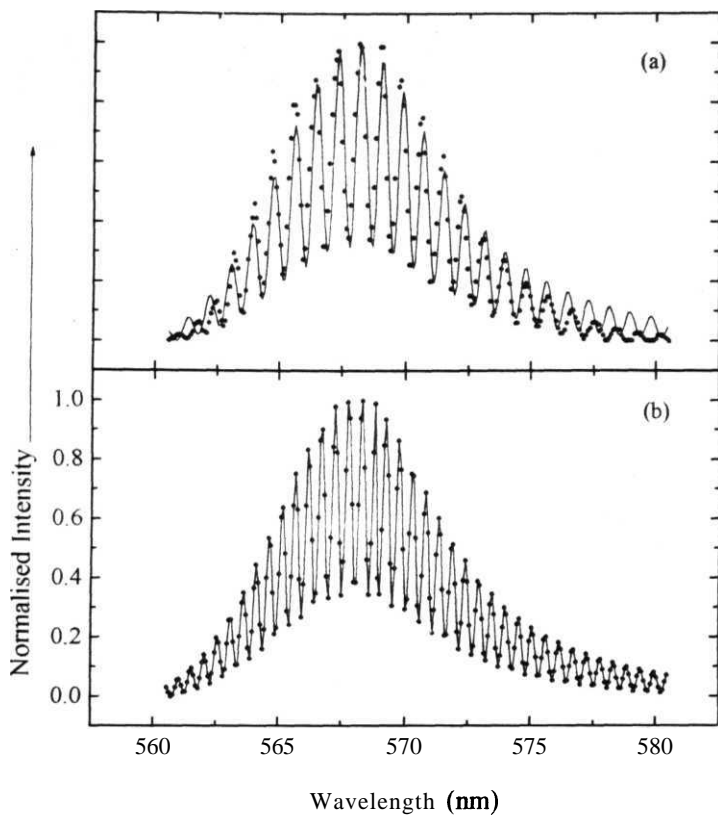


Figure 5.2

Experimental recordings of spectral modulations for two different thickness of glass slides: (a) $\Delta=\Delta_1=403\mu\text{m}$; (b) $\Delta_2=\Delta_1+240\mu\text{m}$. Dots are experimental data and continuous curve is the theoretical fit

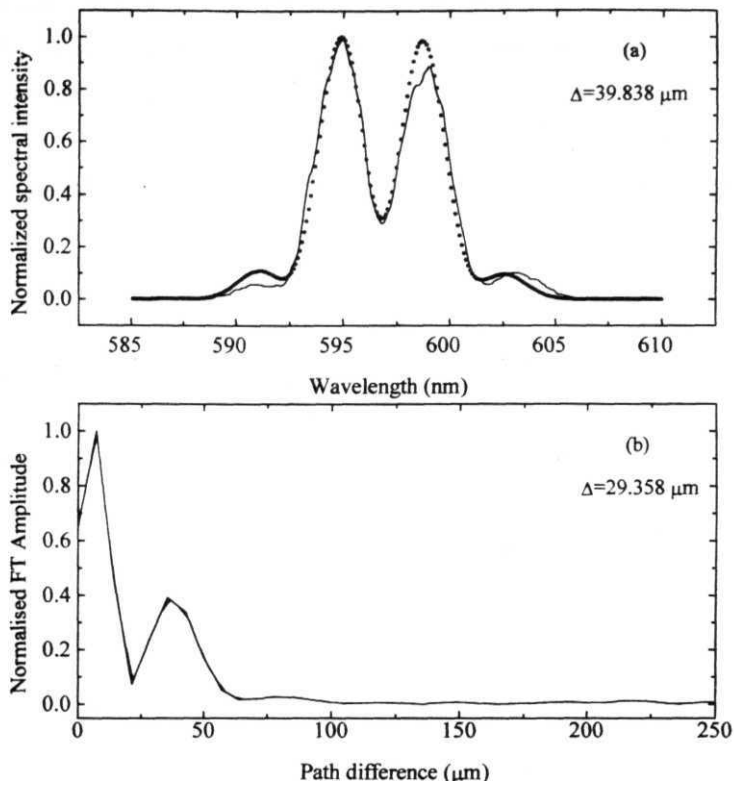


Figure 5.3

Measurement of the linear displacement using two different methods
 (a) Fitting of experimental data using eqn. (5.9) dots are experimental data and continuous line is the fit; (b) fast Fourier transform of the experimental data.

gives two autocorrelation peaks (Figure 5.3 (b)) and from their **separation**, the path difference between the beams is calculated to be 29.358 μm . The difference in the values is due to the resolution of the spatial interferogram which is expected to be less than 10 μm .

5.3 Effect of vibrational stabilization on the spectral interferogram

For any interferometer stability is one of the most important requirement. A study of vibrations and other disturbances which generally spoils the interferometer signal is one of the most useful applications of **interferometry**. The most common disturbances that affect the stability of the interferometer are the air turbulence, thermal drifts, surface vibrations etc. [37]. Because of the instability of the optical components of the interferometer to all these effects, there is no fixed phase relationship between two interfering beams, i.e., under same physical conditions, the **fringe** pattern due to different laser shots are not the same and this results in a poor fringe contrast. Pulsed laser interferometry (**PLI**) has generated considerable interest for probing short time phenomena [38]. One of the advantages of using PLI is that it solves the synchronization problem in detecting weak signals [39]. In a two beam interferometer (for example **MZI**), the two optical beams traverse two separate optical paths before recombining. Though the use of different optical paths is advantageous for various applications [40-42], it does not allow for self compensation of unwanted surface vibrations and the inplane component of the vibrations decreases the fringe contrast.

Vibrations of the interferometer parts relative to each other leads to different effects, depending on the frequency spectrum of the disturbance, their amplitude, the method of determining the path difference and the **measuring** time. Low frequency vibrations i.e., the vibration period smaller or comparable with the measuring time, can be considered as drifts and their influence can be reduced by averaging independent measurements. High frequency vibrations can lead to visibility losses of the interference pattern if the integration time of the detector is greater than the period of

the vibrations. Other disturbances like air turbulence which is quasi-random in character can be offset by averaging independent measurements or working in a perpendicular optical arrangement. Thermal drifts can also influence the whole setup and its effects can be minimized to a large extent by using a CCD camera, which reduces the recording time.

Stabilizing the laser interferometer using electronic devices works well only for cw laser interferometers [43]. The electronic devices compensate for the changes in the optical path caused by vibrational displacements in the optical elements. The conventional Fourier transform interferometers used for displacement or thickness gauge measurements using a monochromatic or a white light source requires kinematic stabilization of the interferometer geometry to a fraction of a wavelength. The complementary technique of spectral **interferometry** however gives spectral interferogram which can be recorded in a single shot mode by photographic method or a using a CCD detector. The small fluctuations in the optical path do not erase the spectral interferogram, although they reduce the fringe contrast if their time scale is shorter than the recording time.

5.3.1 Analysis of vibrations

The experimental recordings of the spectral modulations (Figure 5.2) do not have their minimum going down to zero though the eqn.(5.9) that is used to fit it predicts a zero **minimum**. One of the reasons for this discrepancy is found to be due to the vibrations of the table [21]. Thus, the modulation depth analysis of the spectral fringes gives a quantitative estimate of the amplitude of vibrations and of the reduction in the fringe contrast.

(i) *Effect of arm length:* The effect of vibrations on the interference **fringes** are felt more with longer arm lengths of the interferometer. To verify that the observed reduction in the modulation depth of the spectral **fringes** is due to the vibrations of the **table**, the experiment is carried out for three different arm lengths of the **MZI**: $L \approx L_1$ or $L_2 = 10, 30$ and 50 cm. From the recordings shown in the Figure 5.4, it is clear that

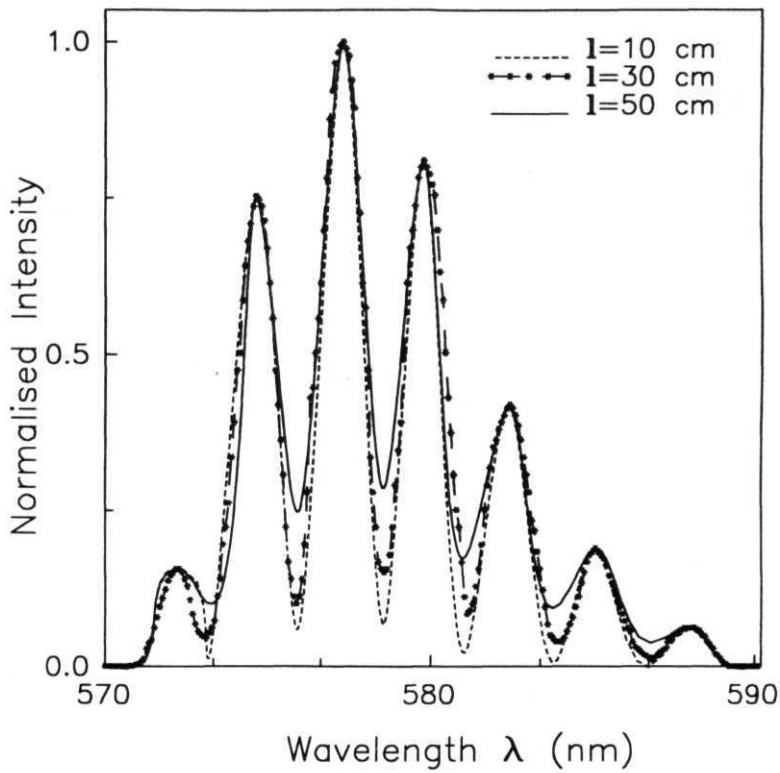


Figure 5.4

Experimental recordings showing the effect of vibrations on the modulation depth for different arm lengths of the MZI.

the modulation depth decreases with increasing arm length. The fringe contrast or the visibility (V) is calculated at a particular wavelength λ using the **Michelsons'** definition

$$V(\lambda) = \frac{S_{\max}(\lambda) - S_{\min}(\lambda)}{S_{\max}(\lambda) + S_{\min}(\lambda)} \quad (5.17)$$

The values, calculated at the peak wavelength of the recordings for the three arm lengths are: $V = 0.9901$ (for $L = 10$ cm), 0.747 (30 cm) and 0.5786 (50 cm). As the effects of the table vibrations are more predominant for longer arm lengths, it is confirmed that the surface vibrations modulate the arm lengths randomly leading to variations in the path difference and hence a reduction in the modulation depth for longer arm lengths. A further improvement is possible by arranging the interferometer on a vibration isolation table. For the simple case when the mirror M_2 suffers a translational shift ($\delta x, \delta y$) because of the vibrations, the extra optical path difference for the **MZI** is given by [37]

$$\Delta_v = |L_1 - L_2 + (\delta x + \delta y)| = |\delta x + \delta y| \quad (5.18)$$

For a purely translational shift, $5x = 6y$ and hence $\Delta_v = 25x$. Introducing this random variations in the path difference due to vibrations and using $v = \frac{c}{\lambda}$ the eqn. (5.9) is modified as

$$S(\lambda) = \left(\frac{1}{2}\right) S_0(\lambda) \left\{ 1 + \cos \left[\frac{2\pi}{\lambda} (\Delta \pm \Delta_v) \right] \right\} \quad (5.19)$$

Taking different amplitude values for Δ_v , the above equation is used to fit the spectral modulations given in the Figure 5.2. From the theoretical fit, the maximum amplitude for the path length change due to random vibrations obtained is $\Delta_v \approx 0.0016$. This indicates the sensitivity of this technique to measure the vibrations of even small amplitudes. When the path difference between the interfering beams A is slightly more than the coherence length giving less number of spectral fringes, the fringes are observed to be quite sensitive to vibrations and air currents because of the changes in the optical path lengths leading to continuous shift in the peaks. Also, while recording

the curves for different arm lengths, precaution is taken to ensure that the beam diameters are the same. By inserting an aperture of diameter $d = 2$ mm before the beam splitter 1 for the arm length of $L = 30$ cm it is seen that the modulation depth increases to 0.769. This increase is attributed to the spatial coherence of the broad band laser light entering the interferometer.

(ii) Modified Sagnac interferometer: Improvements based on the Sagnac interferometer (SI) configuration [44], where the two interfering beams travel along identical path but in opposite directions is also tried to stabilize the interferometer against disturbances. The advantage of the SI is that, any disturbance acts on both the counter propagating beams simultaneously to cancel out the **effect**, making the interference pattern relatively insensitive to vibrations. As it is only the spatial interference pattern we get in a SI, the beams are shifted either in the horizontal plane or vertical plane so that they take different optical paths but are very close to each other. This would essentially lead to the **effect** of any disturbance almost equal on both the interfering beams and thereby increasing its stability compared to the **MZI**. However, the path **difference** between the interfering beams to get spectral modulations of different fringe spacing is achieved by inserting glass slides into one of the shifted beams [45] Based on the derivation of the equation (5 18), the extra path difference because of vibrations of the table for a Sagnac interferometer can be written as

$$\Delta_v = |L_1 - L_2 + 2(\delta y - \delta x)| = 2|\delta y - \delta x| \quad (5.20)$$

Comparing this equation with **eqn (5 18)**, it can be seen that in the **MZI** the overall shift in the interferometer plane is an addition of the linear displacements δx , δy Whereas in the SI because of the counter propagation of the two interfering beams, the effect of the translational shift between the two beams are subtracted. Thus, the overall effect of vibrations on the interference fringes is reduced in the **modified SI** making it less sensitive to vibrations than the **MZI** The spectral modulations recorded for the **modified** rectangular SI **configuration** shown in Figure 5 5 (a) of total path length $L = 30$ cm and a horizontal separation between the interfering beams of '**s**' =

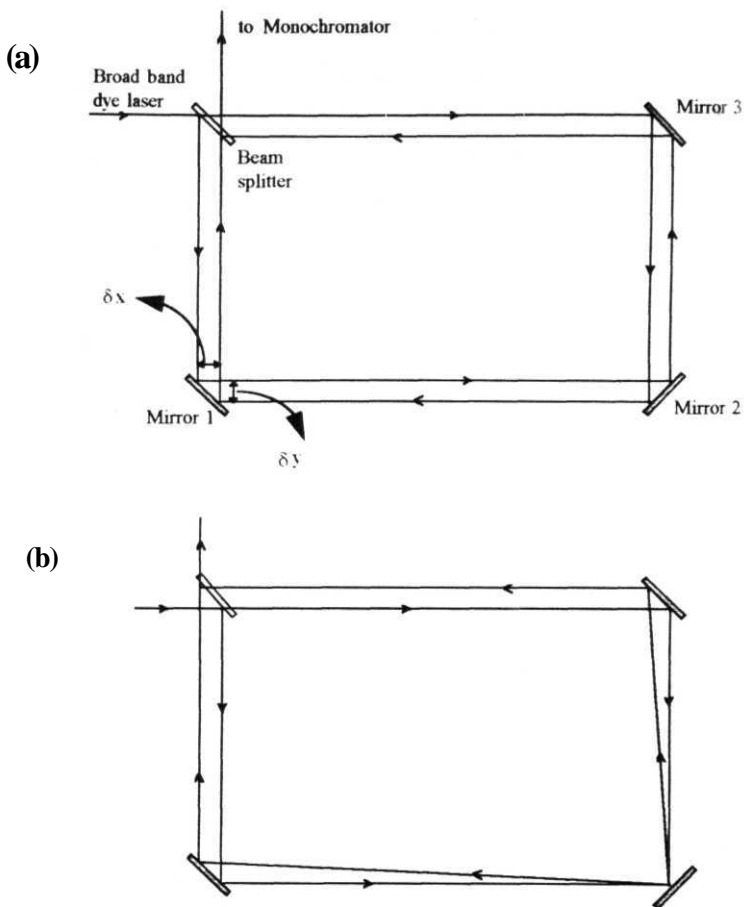


Figure 5.5

Modified SI setup to increase the stability against disturbances
 (a) horizontal shifted square/rectangular modified SI,
 (b) vertical shifted modified SI.

7.5 mm, gives a visibility of 0.816. Decreasing the separation between the beams to 2.5 mm, increases the value of visibility to 0.865. This increase is because, for smaller horizontal separation between the interfering beams, the performance of the modified SI approaches that of the dynamically stable and auto compensating SI. Modifying to a square SI improves the visibility further to 0.912. The effect of vibrations on equal arm lengths will be less than that for unequal arm lengths of the interferometer.

As mentioned before, the effect of air turbulence can be minimized by working in the vertical geometry of the interferometer. Arranging the square SI in the vertical shifted configuration as shown in the Figure 5.5 (b), there is a definite increase in the visibility value of the spectral modulations to 0.952. All these modified SI configurations have a total path length of 30 cm and reducing it will increase the fringe contrast further, as discussed in the section on the effect of arm length. The final plot of the visibility of the spectral fringes for all the different interferometer configurations discussed so far is presented in Figure 5.6. An overall analysis of the results makes it clear that, by proper selection of the interferometer configuration, arm lengths and spatial coherence of the source, one can achieve an almost perfect cosinusoidal modulations as expected from the theoretical equations. It is also made sure that in all the spectral recordings used to get the visibility, the number of fringes within the band width of the recordings is the same making sure that the effect of the amplitude of vibrations estimated, is the same for all interferometer configurations. Even after all modifications and refinements in the interferometer configuration, a perfect visibility of 1 could not be achieved. This could be due to the combined effect from the inhomogenities in the mirrors, beamsplitters and also the complex degree of spectral coherence between the interfering beams and the resolution limit of the spectrometer.

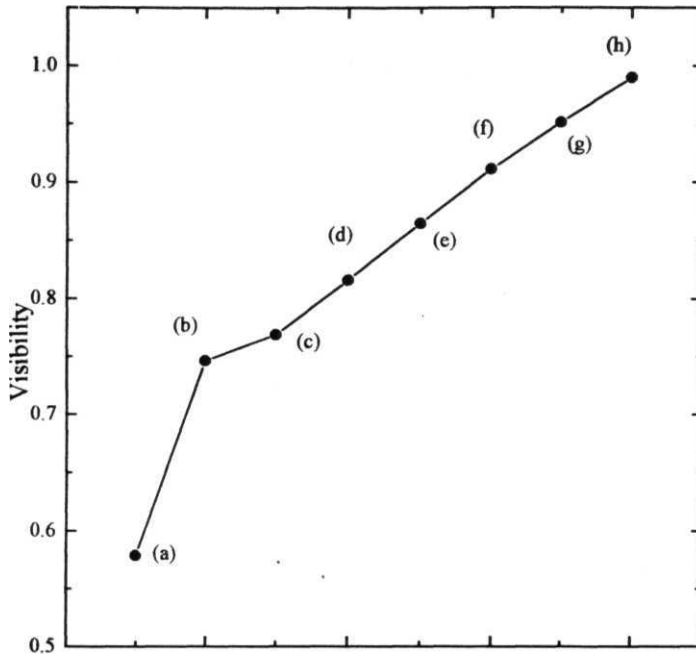


Figure 5.6

Plot of the spectral visibility for different interferometer configurations.

- (a) MZI (l=50cm); (b) MZI (l=30cm), without aperture;
(c) MZI (l=30cm), with aperture; (d) Modified SI (l=30cm, d=7.5mm);
(e) Modified SI (l=30cm, d=2.5mm); (f) Square SI (l=30cm, d=2.5mm);
(g) Vertical shifted SI (l=30cm); (h) MZI (l=10cm).

References

- [1] E. Wolf, in Recent developments in Quantum optics, Edited by R. Ingua,
(Plenum, NY, 1993), p-369.
- [2] L. Mandel and E. Wolf, Optical coherence and Quantum optics, (Cambridge
University Press, 1995), Chapter 4 and 5
- [3] E. Wolf and G.S Agarwal, J. Opt. Soc. Am. A 1, 541, (1984).
- [4] W Wang and E Wolf, J. Mod. Opt 32, 2007, (1992).
- [5] E. Wolf, J.T. Foley and F Gori, J Opt Soc. Am. A 7, 173, (1990).
- [6] W. Wang, R. Simon and E. Wolf, J. Opt. Soc. Am A 9, 287, (1992).
- [7] Refer to section 1.2 and table 1.1 in the chapter 1 and the references given
therein.
- [8] E. Wolf, Phys. Rev. Lett. 58, 2646, (1987).
- [9] A. Gamliel and E Wolf, Opt. Commun. 65, 91, (1988).
- [10] F. Gori, G Guattari and C. Palma, Opt Commun. 67, 1, (1988).
- [11] L Mandel and E. Wolf, J. Opt. Soc. Am. 66, 529, (1976).
- [12] E. Wolf, Phys. Rev Lett 56, 1370, (1986).
- [13] G Indebetouw, J. Mod Opt 36, 251, (1989).
- [14] D F.V James and E. Wolf, Phys Lett. A 157, 6, (1991).
- [15] M. Bertolotti, A Ferrari and L Sereda, J Opt. Soc Am B 12, 1519, (1995).
- [16] M Bertolotti, A Ferrari and L Sereda, J Opt. Soc. Am. B 12, 341, (1995).
- [17] P Hlubina, J. Mod. Opt 43, 1745, (1996).
- [18] C. Polhemus, Appl Opt. 12, 2071, (1973).

- [19] J. Schwider and L. Zhou, Opt. Lett. 19, 995, (1994); U. Schneil, E. Zimmermann and R. Dandliker, Pure Appl. Opt. 4, 643, (1995).
- [20] P. de Groot, **Opt Lett.** 17, 898, **(1992)**.
- [21] D. Narayana Rao and V. **Nirmal** Kumar, J. Mod. Opt. 41, 1757, (1994).
- [22] **D.S Mehta, H.C. Kandpal, K. Saxena, J.S. Vaishya and K.C Joshi, Opt. Commun.** 119, 352, (1995).
- [23] **G S Agarwal** and **D.F.V** James, J. Mod. Opt. 40, 1431, (1993).
- [24] J P. Goedgebuer, A. Lacourt and M. Guignard, Opt. Laser Technol. 10, 193, (1978).
- [25] J.E. Calatroni, **P** Sandoz and G. Tribillon, Appl. Opt. 32, 30, (1993).
- [26] P. Sandoz, **G** Tribillon and H. Perrin, J. Mod. Opt. 43, 701, (1996).
- [27] H. Bouasse and Z. Carriere, Interferences, (Delagrave, Paris, 1923).
- [28] **D.N** Wang, K.T.V. Grattan and **A.W.** Palmer, Opt. Commun. 127, 19, (1996).
- [29] **PA. Flournoy, R.W. McClure and G. Wyntjes, Appl. Opt.** **11**, 1907, **(1972)**.
- [30] A. Kohlhaas, C. **Fromchen** and E. **Brinkmeyer**, J. Lightwave Technol. 9, 1493, (1991).
- [31] T. Li, A. **Wang**, K. Murphy and R. **Claus**, Opt. Lett. 20, 785, (1995).
- [32] L. Lepetit, **G** Cheriaux and M. **Joffre**, **J Opt Soc. Am. B** 12, 2467, (1995).
- [33] **E** Wolf, Opt. Commun. 38, 3, (1981).
- [34] **F.A.** Jenkins and H.E. White, Fundamentals of Optics, (4th **edition**, McGraw Hill, 1981), pp-286-288.
- [35] **W** Demtroder, Laser spectroscopy, Springer series in chemical physics, vol. 5, (**Springer-Verlag**, NY, 1982).

- [36] N. Tan-no, T. **Ichimura**, T. **Funaba**, N. Anndo and Y. **Odagiri**, **Opt. Lett.** **19**, **587**, (1994).
- [37] J. Schwider, in Advanced evaluation techniques in interferometry, in Progress in optics, Edited by E. Wolf, (North-Holland, 1990), vol. 28.
- [38] Y. Li, G. **Eichmann** and R.R. Alfano, **Appl. Opt.** **25**, 209, (1986).
- [39] H. Schmidt, H. **Salzmann** and H. Strohald, **Appl. Opt.** **14**, 2250, (1975).
- [40] **F J Weinberg**, Optics of Flames, (**Butterworth**, London, 1963).
- [41] **V** Grigull and H. Rottenkolber, **J Opt. Soc. Am.** **57**, 149, (1967).
- [42] **D Malacara**, Optical shop testing, (John Wiley, NY, 1978).
- [43] **P** Shajenko and E.L. Greene, **Appl. Opt.** **19**, 1895, (1980); A. Olsson, C.L. Tang and **E.L.** Greene, **Appl. Opt.** **19**, 1897, (1980).
- [44] P. Hariharan, **Appl. Opt.** **14**, 2319, (1975).
- [45] **D** Narayana Rao and **V** Nirmal Kumar, unpublished results, (1994).

CHAPTER 6

SPECTRALLY RESOLVED WHITE LIGHT INTERFEROMETRY FOR SIMULTANEOUS MEASUREMENT OF THE REFRACTIVE INDEX AND THICKNESS.

6.1 Introduction

Study of the interference effects in the space-frequency domain is substantially different from the study in the space-time domain though the basic equations are similar in their form. Recently, there is been an increasing interest in the theoretical and experimental investigations of number of coherence phenomena in the space-frequency domain [1,2]. As has already been amply discussed and demonstrated in the earlier chapters of this thesis, the interference between two amplitude or wavefront divided beams occur irrespective of the path delay between the interfering beams. The effect is manifested as periodic spatial variation of intensity or as spectral variations depending on whether the path difference between them is less or more than the coherence length of the source respectively [3-8]. The spectral interference phenomenon giving rise to spectral modulations for different degrees of correlation between the interfering beams has been studied theoretically [7,9] and verified **experimentally**[8,10]. The periodicity and characteristics of these spectral fringes depend on the way the interfering beams are correlated and on the bandwidth of the source used.

Dispersion measurements are usually done either by measuring the centroid of the interference pattern produced with a Michelson interferometer and a filtered white light source at different wavelengths [11-13] or by measuring the refractive index at different selected monochromatic wavelengths [14,15] and fitting the experimental

data to Cauchy, **Sellmeier** or Conrady equation to obtain the empirical dispersion law over the entire spectral bandwidth [16-19]. However, these methods encounter with difficulty in the realization of high wavelength resolution [20,21] and the phase ambiguity associated with using a monochromatic light source [22]. The method of spectral measurements using a white light interferometry can overcome these difficulties and has advantages mentioned in the previous chapter over the time domain measurements. This technique is capable of high **precision**, high spectral resolution and absolute measurement of the optical constants of the material by making use of the entire bandwidth of the white light source [23-30] for the measurements.

The amplitude and the frequency of the spectral modulations depend on the degree of correlation between the interfering beams, in particular on the absorptive and/or the dispersive nature of the delay introduced between the interfering beams. In this chapter, the effect of normal dispersive material like a glass plate or a polymer film and an absorbing material like dye solution, introduced into one of the arms of a dispersion compensated Michelson interferometer (**MI**) is studied over the entire visible region using the spectral interferometry technique. A detailed description of the experimental setup highlighting the importance of the different parts of the setup and recording of the spectral interference **fringes** with different samples are given. This is followed by a brief note **on** some important theoretical equations necessary for describing the behavior of the spectral interference pattern with a normal dispersive material in one of the arms of the interferometer. The experimental parameters determining the maximum and minimum measurable optical path difference is also given. But as we will demonstrate, our method is not restricted by such conditions and has practically infinite dynamic measurement range. After introducing a glass plate or a coated polymer film into one of the interferometer arms, the variable arm of the **MI** is moved to make the group optical path difference between the interfering beams equal. From the characteristics of the spectral fringe pattern obtained after introducing the transparent normal dispersive material, its optical constants $n(X)$ and '**t**' can be estimated to a very high accuracy of the order of 10^{-5} [31] through theoretical fitting. The versatility of this measurement technique is demonstrated by using materials

having different values for the optical constants and is been found to be practically limitless [32,33]. A single shot, real time, non-destructive measurement of the refractive index of the material over the entire visible region of the spectrum and the simultaneous measurement of its thickness is the highlight of this technique. It has also been proposed as an alternate to the more expensive ellipsometer and other measurement techniques which are tedious and have limited measurement range. Depending on the wavelength at which the group dispersion between the two interfering beams are made equal one can see a stationary fringe denoted by ' λ_g '. This gives an estimate of the variations in the phase difference between the interfering beams around the stationary phase **region**, as a function of the wavelength. Finally, a brief qualitative discussion on the effect of amplitude modulation on the spectral interference fringes because of introducing an absorbing sample into one of the interferometer arms is given. From the changes in the spectral visibility, the absorption of the sample can be calculated.

6.2 Experimental details

6.2.1 White light source

The white light from an ordinary tungsten filament source, **also** known as quasi-thermal or Gaussian light is often categorized as incoherent light. However, the white light remains coherent over temporal delays of the order of its coherence time ($\tau_c \sim$ femtoseconds), the shortness being due to the ultrafast Gaussian statistical fluctuations. In the linear correlation type of experiments with slow detection systems for dispersion measurements presented here, it is not possible to distinguish between the experiments done using a short coherence length femtosecond laser source [34] and an ordinary bulb, getting almost the same information [35,36] with the advantage of simplicity and affordability. Thus a white light source, used in combination with a standard Michelson interferometer has received increased attention as a valuable tool in the study of the dispersive properties of optical materials. The main interest being the measurement of the group-delay dispersion and higher order dispersion as most of

the optical components used in sophisticated femtosecond laser systems are restricted by proper selection of materials.

6.2.2 *Interferometer*

A simple dispersion compensated **Michelson** interferometer is used in our measurements. As the work is done in the frequency domain, where the dispersive effect of material studied is of importance, it becomes necessary to compensate for the unequal material contribution due to optical components other than the sample, like the beam splitter and mirrors. Dispersion compensation between the interfering beams is achieved either by using a cube beam splitter or if a surface coated plate beam splitter is used, a compensating plate of the same material should be kept in the appropriate arm of the MI through which the light beam travels less of the material. One of the mirrors is kept on a linear translation stage and by moving it, optimum number of spectral fringes within the region of interest can be obtained for any arbitrary value of a constant L_0 . The flexibility in selecting the required path difference between the interfering beams, makes it possible to extend the **useful** dynamic measurement range of the technique in measuring different thickness samples. This flexibility is also useful to observe the stationary fringe at any wavelength within the **spectrum**, where the group velocity between the two arms of the interferometer is compensated.

6.2.3 *Samples*

(i) Glass slides: The optical properties of glass are important in many applications from the practical every day use in windows to the more critical lenses for cameras to the recent technological applications in fibres for optical **communications**. There are hundreds of glasses available for use in the visible region. Oxide glasses, free from transition metal oxides and certain other coloring agents are very transparent in the visible, near UV and near **IR** regions of the spectrum. The refractive index of glass varies with wavelength. This variation can be considerable and it is necessary to have accurate information on the variations in the visible, near UV and IR regions for

different applications of glass in optical systems. Moreover, very high tolerance levels required to make good quality optical glass, requires the ability to make precise measurements of the refractive index.

The glass that is used in the experimental study are commercially available microslides and glass plates and are generally used as substrate for coating polymer films. The glass samples are first thoroughly cleaned before making the measurements. The bulk refractive index of these normal dispersive materials are measured by the spectrally resolved interferometric technique using a white light source over the entire visible region. The surface and bulk inhomogenities of the sample are found to affect our measurements and a separate estimate of them can be possible.

(ii) Polymer films: Thin dielectric films have many applications in microelectronics [37], as planar waveguides for processing of optical signals by **modulation**, switching, frequency conversion and in a variety of nonlinear optical devices and applications [38,39]. To make the best use of the thin films for devices, it is necessary to know the specific optical properties of the material like the real (dispersive) and imaginary (absorptive) parts of the refractive index at different wavelength regions, its anisotropy and the film thickness. A variety of techniques are available for the measurement of the refractive index and thickness of thin films [40-43], most of which are destructive techniques and are limited in their effective measurement range.

Depending on the material and the coating mechanism, the refractive index and thickness of the film could vary from place to place. Conventional methods of thin film coatings are vacuum evaporation [44], sputtering [45], ion implantation [46], etc. For coating thin polymer films on a glass substrate, the technique of deposition from liquid solutions is used [47] The method involves slow evaporation of the solvent, followed by heat treatment at slightly higher temperature so that the solvent evaporates completely and at the same time, the sample does not decompose. Such solution deposited films have been used for the thin film light guiding experiments [48] and thin film ring laser systems, when doped with organic compounds like **Rhodamine** 6G laser dyes [49].

The polymer films are coated on a glass substrate of known refractive index (over the entire measurement region) and thickness. First, the glass plates are thoroughly cleaned with soap water and **methanol** and are blown dry with pure nitrogen. Care is taken while preparing the polymer solution. 0.3 **gms** of commercially available polyvinyl alcohol (PVA) is dissolved in 10 ml of distilled water. The solution is gently warmed to make a clear, homogeneous mixture and is poured onto the previously cleaned glass plate after filtering. In spin coating technique, the glass plate with the polymer solution is fixed onto the shaft of an adjustable speed dc motor. By using solutions of different concentration **and/or** by adjusting the speed of the motor, polymer films of different thickness can be coated. In doctor-blade technique, after pouring the polymer solution onto the glass substrate, the plate is fixed on a horizontal platform which has parallel railing with a blade fixed to it. After adjusting the height of the blade and moving it over the sample, excess solution from the glass plate is taken off, leaving a uniform layer of the film. Here, different thickness films are achieved by adjusting the height of the blade. By a proper combination of the solvent and slow evaporation process, it is possible to achieve smooth and uniform films. The coated glass plates are kept in an oven at 40°C for about 2-3 hours to make sure that the solvent is completely removed. Similar procedure is followed to prepare the thin films of polystyrene (PS) dissolved in xylene and polymethyl **meta** acrylate (PMMA) dissolved in toluene. By coating slightly thicker films and with a fast evaporation rate, the coated films can be easily peeled off from the substrate and can be used as free standing films for their optical characterization.

A schematic of the compact experimental setup used for the simultaneous measurement of the refractive index over the entire visible region, $n(\lambda)$ and the thickness 't' of a transparent sample introduced into one of the arms of the Michelson interferometer is shown in the Figure 6.1. The source used is a 25 W tungsten filament lamp (the spatial, temporal and spectral characteristics of this lamp are mentioned in detail in the previous chapters of this thesis). This lamp illuminates a pinhole of diameter $\sim 300 \mu\text{m}$, which acts as the secondary source. Light beam emerging from

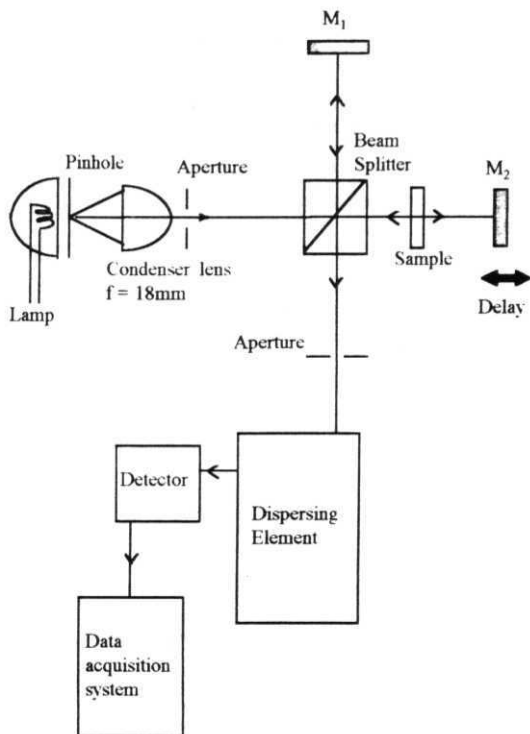


Figure 6.1

Schematic of the compact experimental setup used to measure the refractive index and thickness of transparent materials, using the technique of spectral interferometry.

the pinhole is collimated using a proper lens combination or a condenser lens of focal **length**, $f = 18$ mm. An aperture of about 3 mm diameter kept in the collimated beam uses only the spatially filtered central portion of the **light**, which is verified to have plane **wavefront** using a knife-edge experiment. This beam of light is sent inside a standard, dispersion compensated Michelson interferometer (**MI**). The 50-50 cube beam splitter, amplitude divides the input light beam and sends it into the two arms of the interferometer. The two aluminium coated mirrors **M₁** and **M₂** reflect the two beams back into the same path and they interfere at the same point in the beamsplitter. The beams traverse a total length of **L₁** and **L₂** in the two arms of the **MI**. The mirror **M₁** is kept **fixed**, while the other mirror **M₂** is placed on a linear **translational** stage of movement accuracy ± 5 μ m. A special mount with an aperture of variable diameter is made for the purpose of keeping the sampled area of the material introduced in one of the interferometer arms, fixed. One more aperture of the same diameter is kept at the exit of the interferometer to select only the central part of the superposed beams. Light emerging from the interferometer is imaged onto the entrance slit of a 50 cm grating spectrometer (**JY**, HRS-2) in **Czerny-Turner** optical **configuration**, which is the dispersing element used in our experiment. A **photomultiplier** tube (PMT) is used as the detector at the output of the spectrometer and is connected to an ADC data acquisition card, fixed in a personal computer. The spectral modulations over the entire visible region are recorded by scanning the grating in the spectrometer and by simultaneously collecting the corresponding intensity values through the detection system.

6.3 Theoretical background

Two beams, amplitude divided from a single input light beam, by a 50-50 beams splitter are made to interfere at the same point after they pass through the two arms of the **MI**. Spectral analysis of the interfering beams gives information about the path difference existing between them. **S(r, λ)**, the spectrum at a point P(r) at the input

slit of the spectrometer given by the spectral interference law for the partially coherent beams in the MI (eqn.(4.20)), with $\mathbf{v} = \mathbf{c}/\lambda$ is

$$S(\mathbf{r}, \lambda) = \left\{ \begin{aligned} &|a(\lambda)|^2 S^{(1)}(\mathbf{r}, \lambda) + |b(\lambda)|^2 S^{(2)}(\mathbf{r}, \lambda) \\ &+ 2a^*(\lambda)b(\lambda)\sqrt{S^{(1)}(\mathbf{r}, \lambda)S^{(2)}(\mathbf{r}, \lambda)} \operatorname{Re}[\mu_{12}(\mathbf{r}, \lambda) \exp(i\alpha - 2\pi\Delta/\lambda)] \end{aligned} \right\} \quad (6.1)$$

where, $a(\lambda)$ and $b(\lambda)$ are the wavelength dependent coefficients that depend on the properties of the beam splitter, $S^{(1)}(\mathbf{r}, \lambda)$ and $S^{(2)}(\mathbf{r}, \lambda)$ are the individual spectra of light from the two arms of the interferometer 1 and 2, recorded by closing the other arm, 'Re' is the real part, $\mu_{12}(\mathbf{r}, \lambda)$ is the complex degree of spectral coherence, ' α ' is the phase of the interference term, which is weakly dependent on the wavelength and the dimensions of the source and can be neglected and ' Δ ' is the path difference between the interfering beams. Simplifying the eqn.(6.1) further using eqns. (4.23) and (4.25) we get

$$S(\mathbf{r}, \lambda) = \left(\frac{1}{4} \right) \left\{ S^{(1)}(\mathbf{r}, \lambda) + S^{(2)}(\mathbf{r}, \lambda) + 2\sqrt{S^{(1)}(\mathbf{r}, \lambda)S^{(2)}(\mathbf{r}, \lambda)} |\mu_{12}(\mathbf{r}, \lambda)| \cos\left(\frac{2\pi\Delta}{\lambda} \right) \right\} \quad (6.2)$$

where, the argument $\beta_{12}(\mathbf{r}, \lambda)$ is taken to be zero for interference between same wavefronts in the MI. The visibility of the spectral modulations can be obtained from the above equation to be

$$\begin{aligned} V(\mathbf{r}, \lambda) &= \frac{S_{\max}(\mathbf{r}, \lambda) - S_{\min}(\mathbf{r}, \lambda)}{S_{\max}(\mathbf{r}, \lambda) + S_{\min}(\mathbf{r}, \lambda)} \\ &= \left[\frac{2\sqrt{S^{(1)}(\mathbf{r}, \lambda)S^{(2)}(\mathbf{r}, \lambda)}}{S^{(1)}(\mathbf{r}, \lambda) + S^{(2)}(\mathbf{r}, \lambda)} \right] |\mu_{12}(\mathbf{r}, \lambda)| \end{aligned} \quad (6.3)$$

For a dispersive sample kept in one of the arms of the interferometer, the spectra of the interfering beams are almost equal and reduction in the visibility of the spectral modulations is because of the reflection losses at the sample, spectral coherence properties of the interfering beams and the effect of table vibrations. Whereas an absorbing sample kept in one of the arms reduces the spectral intensity of that beam

depending on the strength and region of absorption of the sample. Hence, according to the eqn (6.3), the visibility of the spectral interference fringes reduces due to interference between beams of unequal spectral intensity, in addition to the above mentioned reasons.

Because of the large bandwidth of the source **used**, the dispersive contribution of the sample introduced in the light path affects the interference fringes as a result of the refractive index change over the entire visible region. Thus the optical path difference between the two interfering beams because of the purely dispersive sample introduced in one of the arms, for each wavelength within the bandwidth of the light can be written as

$$\Delta(\lambda) = n(\lambda)2t - L_0 \quad (6.4)$$

where $n(\lambda)$ is the refractive index of the material introduced in the **interferometer arms**, ' t ' is its thickness and L_0 is an arbitrary path length introduced to get either the stationary fringe point within the region of the spectrum or to get well resolved spectral fringes within the region of observation. The explicit equation form for the refractive index as a function of wavelength for normal dispersive materials like glass and polymers which do not have any absorption in the visible region of the spectrum is given by the **Cauchy's** dispersion relation [50]

$$n(\lambda) = \left[C + \left(\frac{D}{\lambda^2} \right) + \left(\frac{E}{\lambda^4} \right) \right] \quad (6.5)$$

Though Cauchy's dispersion relation holds good satisfactorily for the case of normal dispersive materials and is useful from a practical point of view, fitting of the refractive index data by the improved **Sellmeier** dispersion relation for optically transparent materials can give more accurate results for both glass and **nonglass** materials [16,51]. The five constant Sellmeier equation is written in a simplified form as

$$n(\lambda) = A\lambda^4 + B\lambda^2 + C + \left(\frac{D}{\lambda^2} \right) + \left(\frac{E}{\lambda^4} \right) \quad (6.6)$$

in both the equations (6.5) and (6.6), **A**, B, C, D, and E are the dispersion **constants**, characteristic of the material and which are determined from the fitting process. It is also clear from the equations that the refractive index is a **function** of wavelength λ and using it along with **eqn** (6.4) in eqn.(6.2), one can see that the corresponding spectral modulations show a **variation** in the periodicity of the fringes with λ . The constant **L₀** can be chosen such that the total phase difference or the group dispersion between the two interfering beams becomes zero at some wavelength within the bandwidth of the **spectrum**, where one can see a broad fringe with the periodicity of the fringes changing on either side. Experimentally this is achieved by translating the mirror **M₂** and visually observing the fringes with a grating. From the discussion given in the chapter 5, on the limitations of the technique in measuring the path delays between the interfering beams, the minimum path delay given by **eqn.(5.13)** is

$$\Delta_{\min} = \left(\lambda_0^2 / \delta\lambda \right) \quad (6.7)$$

where λ_0 is the mean wavelength and $\delta\lambda$ is the bandwidth of the source. For the white light source that is used in the experiment, $\lambda_0 = 530 \text{ nm}$ and $\delta\lambda = 194.4 \text{ nm}$, the minimum path delay that can be measured is about **1.4 μm** . The maximum measurable path delay depends on the resolution capability of the spectrometer and is given by eqn.(5.15)

$$\Delta_{\max} = \left(\lambda_0^2 / 6\delta\lambda_{\text{sp}} \right) \quad (6.8)$$

where, $\delta\lambda_{\text{sp}}$ is the maximum resolution limit of the spectrometer used to analyze the spectral fringes. For the 50 cm grating spectrometer used for the experimental measurements, $\delta\lambda_{\text{sp}} = 0.014 \text{ nm}$ and hence the maximum measurable path delay is 3.12 mm. However, these theoretical limitations can be overcome by making use of the arbitrary path delay L_0 introduced in the eqn.(6.4), as will be demonstrated later.

6.4 Results and discussion

6.4.1 Normal dispersive materials

First, the **MI** is aligned with the help of a broad band dye laser (coherence length $\sim 40 \mu\text{m}$) to have spatial interference fringes. By doing this, it is possible to arrange the path difference between the two arms to within an accuracy of $< 40 \mu\text{m}$. After this initial **alignment**, the laser light is replaced by the collimated white light of much shorter coherence length ($0.35 \mu\text{m}$). The appearance of the spectral fringes is visually monitored with the help of a grating (Bausch & **Lomb**, 600 grooves /mm, blazed at 54°) and reducing the path delay between the interfering beams. After getting the white light spectral fringes, recording the spectrum of the lamp by closing either of the interferometer arms in turn and the spectral modulations for an arbitrary path difference between the interfering beams. Without any sample in the interferometer arms it is made sure that the two beams are of almost equal intensity and there is no unequal dispersion between **them**, affecting the periodicity of the fringes. The corresponding experimental recordings are already given in the chapter 4 (Figure 4.2).

(i) $n(X)$ and t of **glass slides**: After the initial exercise of getting the spectral fringes and making sure that the material dispersion are the same in both the arms of the interferometer, a $150 \mu\text{m}$ thick glass slide is introduced into one of the arms of the **MI**. The spectral modulations recorded now shows a clear change in the modulation frequency of the interference fringes right from 380 nm to 750 nm of the **spectrum**, which is a function of the refractive index over the entire visible region and the thickness of the sample. Now, by moving the mirror **M₂** of the interferometer and visually observing the spectral fringes with the help of the grating, the stationary phase point denoted by λ_s is brought to some point at the center of the visible region where the condition

$$\Delta(\lambda) = n(\lambda_s)2t - L_s = 0 \quad (6.9)$$

is satisfied. This stationary phase point corresponds to the wavelength where the group dispersion between the two arms are equaled for an arbitrary value of the constant L_0 . Observation of this position is a test for equal optical paths [52]. The validity of the condition for equal optical paths, $\Delta \approx 0$ for the group paths of light in the two arms of the MI at some wavelength λ_* implies that the phase-time difference x ($=\Delta/c$) is stationary at some wavelength $X = \lambda_*$ i.e., any change of fringe position with X has a stationary value at that wavelength. This position is identified from the recorded spectral fringes by the fact that the regular fringes are normal to the direction of dispersion whereas at the stationary point, the fringe becomes parallel to this direction at the particular wavelength X^* .

To verify the accuracy involved in our study, different thickness and different batch glass slides and plates are introduced into arm 1 of the interferometer. Figure 6.2 shows the spectral recordings for different thickness of the glass plates. The experimental data are fitted to the equation

$$S(\lambda) = \left(\frac{1}{2}\right) S_0(\lambda) \left\{ 1 + V(\lambda) \cos\left(\frac{2\pi\Delta(\lambda)}{\lambda}\right) \right\} \quad (6.10)$$

where $\Delta(\lambda)$ is given by eqn.(6.4) with the dispersion relation eqn.(6.5). The above eqn (6 10) is the simplified form of the eqn (6 2), using eqn (6 3) and assuming that the two interfering beams have equal spectra. An appropriate form for the spectrum of the lamp, $S_0(\lambda)$ is used in the fit. The theoretical fitting is done using the least-square fitting program written using SIMPLEX algorithm in FORTRAN language. From the fit, the values of the thickness and the three dispersion constants of the Cauchy's relation are directly obtained. The refractive index (at $X = 633 \text{ nm}$) and thickness of the different glass samples introduced into the interferometer arm, along with the dispersion constants (C, D, and E), stationary phase point (X^*) and the value of the arbitrary constant L_0 are listed in the Table 6.1. The overall chi-square deviation between the data and the fit is as low as $1E-3$ for our fit, which is evident from the closeness with which the theoretical curve fit the experimental data (Figure 6.4).

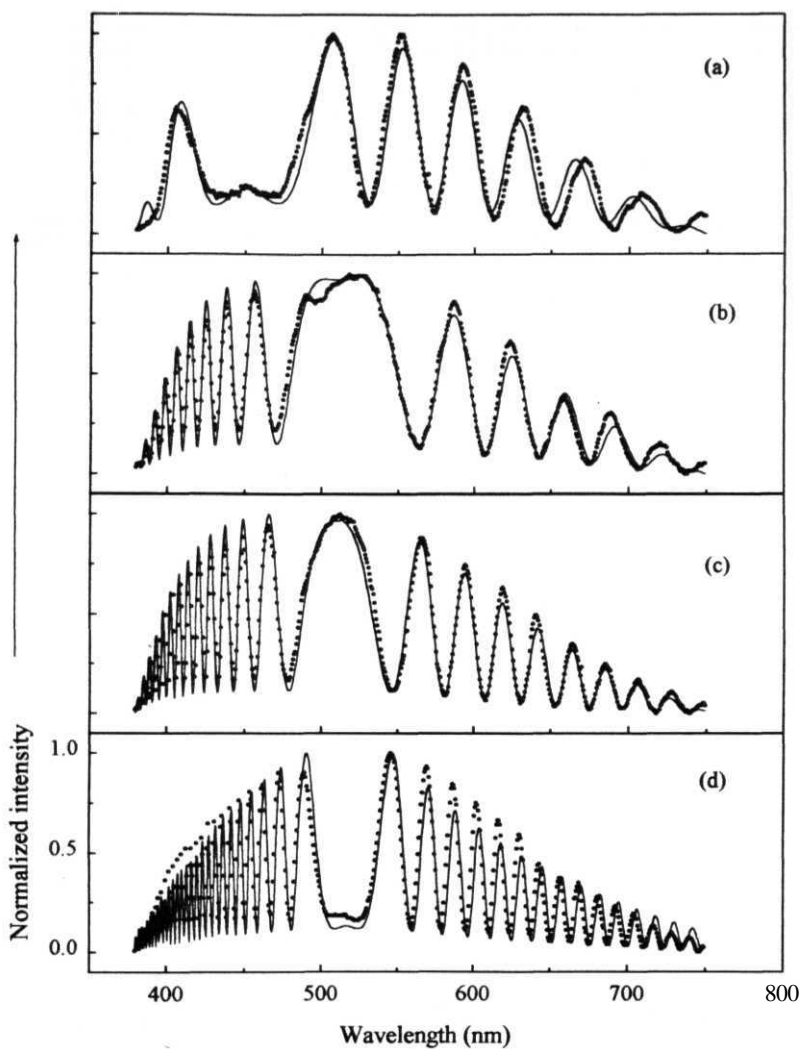


Figure 6.2

Experimental recordings of the spectral modulations (dots) for different thickness glass plates kept in the arm 1 of the **MI** and the corresponding theoretical fit (continuous line) using eqn (6.10). (a) $t=150\ \mu\text{m}$, (b) $300\ \mu\text{m}$, (c) $450\ \mu\text{m}$, (d) $1.5\ \text{mm}$. The fitted constants are given in the Table 6.1.

Experimental parameters and optical constants	Number of glass slides			
	1	2	3	1.5 mm
λ_a (nm)	437.449	518.152	512.68	523.623
L_0 (μm)	236.765	468.466	702.95	2264.199
t (μm)	149.989	299.975	449.973	1443.917
C	1.508523 (1.512002)*	1.508522	1.508538	1.521600
D	2.899964E-15 (2.30996E-15)*	2.899963E-15	2.899979E-15	2.4999964E-15
E	2.85007E-29 (4.950039E-29)*	2.850064E-29	2.85022E-29	-5.207E-29
n (at 633 nm)	1.515938 (1.518075)*	1.515937	1.515953	1.521924

Table 6.1

Table giving the summary of the experimental parameters and material constants obtained from the theoretical fitting. The thickness of each glass slide t * **150 μm** . The values of the fitted constants denoted by asterisk sign are obtained for a separate fit of the corresponding curve.

The value of the dispersion constants of one glass slide calculated over the entire visible region of the spectrum are used to fit the spectral modulations recorded with more number of glass slides of the same material and from **same** batch introduced into the interferometer arm. The experimental recordings and the corresponding theoretical fit are shown in the Figure 6.2 (a-c). It is clear from the figure that the fit is quite good for all the three thickness of the glass slide. A variation in the fifth decimal place ($\pm 1\text{E-}5$) for the fitted constants is found to affect the theoretical fit appreciably. The uniqueness of the $n(\lambda)$ and 't' values are studied by varying $n(\lambda)$ and calculating 't' and **vice-versa**. From this, it is concluded that with our fitting routine an accuracy of $\pm 1\text{E-}5$ in the refractive index $n(\lambda)$ and thickness 't' (in μm) can be achieved. Figure 6.2 (d) shows the experimental data and theoretical fit for a 1.5 mm thick glass plate of a different make.

On a closer inspection, it can be seen from the Figure 6.2 that the theoretical fit matches better with the experimental data in the Figures 6.2 (b) and 6.2 (c) but does not match well with the data in Figure 6.2 (a) especially in the higher wavelength region. Though all the glass slides are from the same **batch**, we could see a difference in the dispersion constant values. A separate fit for the 150 μm glass slide (Figure 6.2 (a)) is tried and the values of the new fit are given in the Table 6 1 marked by '*'. This clearly indicates that the technique is sensitive enough to see a small variation of 0.002 in $n(\lambda)$ at 633 nm between samples of the same batch. Using the dispersion constants obtained from the theoretical fit, the refractive index curve over the entire visible region is generated, as shown in the Figure 6.3 for the two different glass samples used in our experiment.

From the Figures 6.2 (a-d) it can also be seen that the width of the stationary phase region is reduced as the thickness of the glass plate is increased. This variation in the width of the stationary phase region is more clearly seen from the Figure 6.4, where the variations in the modulus of the phase difference $|\phi(\lambda)| = 2\pi\Delta(\lambda)/\lambda$ between the interfering beams is plotted as a **function** of wavelength over the entire visible **region**. The minima for $|\phi(\lambda)|$ are seen to occur at λ_m and the variation of the

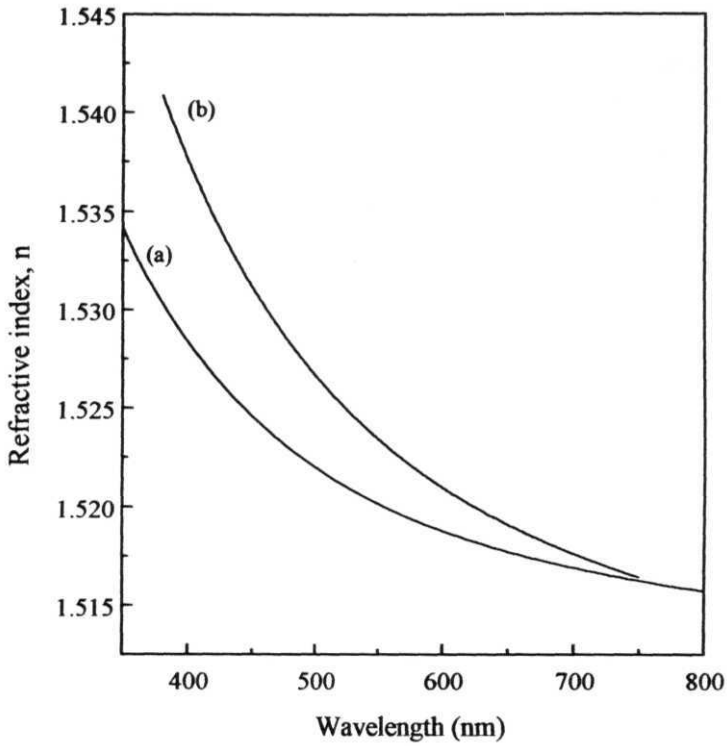


Figure 6.3

Refractive index of the glass plate introduced in the interferometer **arm**, as a function of wavelength generated using the dispersion constants obtained from the theoretical fitting (a) $t = 150$ pm, (b) 1.5 mm.

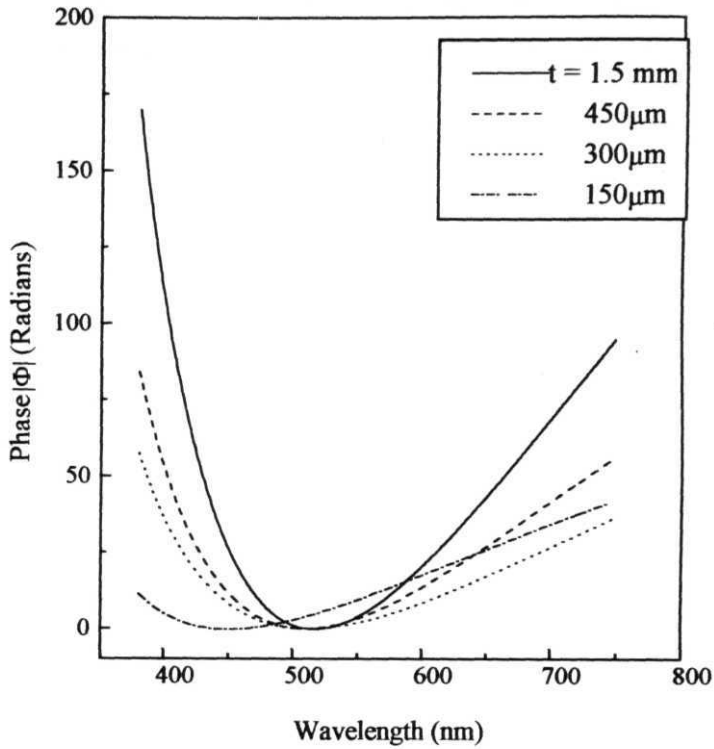


Figure 6.4

Plot of the phase obtained from the spectral modulations for different thickness of the glass plate introduced into the interferometer arm. The minimum in the curve phase point corresponds to the stationary phase point (λ_s).

phase function with wavelength around $\lambda = 0$ is steeper for thicker materials and the variation is much slower for thinner materials. As a result, it can also be concluded that the periodicity of the fringes for a particular λ increases with the thickness of the material.

(ii) $n(\lambda)$ and t of polymer films: After measuring the refractive index over the entire visible region and the thickness of a glass plate using the method described above, the same glass plate is used as the substrate for coating thin polymer films of different material and thickness. Now, without disturbing the interferometer the glass plate is taken out and **reintroduced** after coating it with the PVA polymer film. A special mount designed for this purpose takes care of the fact that we are sampling the same location in the glass plate so that the effect of surface and bulk **inhomogenities** of the substrate can be neglected. Comparison of the modulated spectra recorded with the glass plate alone and after coating with the polymer film as given in Figure 6.5, shows the following interesting features: (1) the stationary phase point (λ_s) is red **shifted**, and (2) there are more number of fringes in the region of observation as a result of the excess path seen in the arm where the sample is introduced, by the light beam passing. The modulated spectrum obtained with the PVA film coated on the glass substrate is fitted with the equation

$$S(\lambda) = \left(\frac{1}{2}\right) S_0(\lambda) \left\{ 1 + V(\lambda) \cos \left(\frac{2\pi [\Delta(\lambda) + \Delta'(\lambda)]}{\lambda} \right) \right\} \quad (6.11)$$

where $\Delta'(\lambda)$ is the extra path difference taken by the light beam with the coated polymer film. While fitting, we have used an improved and more realistic five constant **Sellmeier** dispersion relation (eqn.(6.6)) for both the glass plate and the polymer film to get better accuracy in the calculated optical constants. The values of the dispersion constants, refractive index and thickness of the glass plate and the PVA film calculated from the fitted constants are given in Table 6.2. As before, the accuracy are estimated from the theoretical fit of the experimental data and the values are found to be accurate to $< \pm 0.1 \text{ nm}$ for ' t ' and $\pm 1\text{E-}5$ for $n(\lambda)$. Table 6.2 also gives the values of λ_s for the glass substrate alone and after coating with the PVA film and the visibility of the

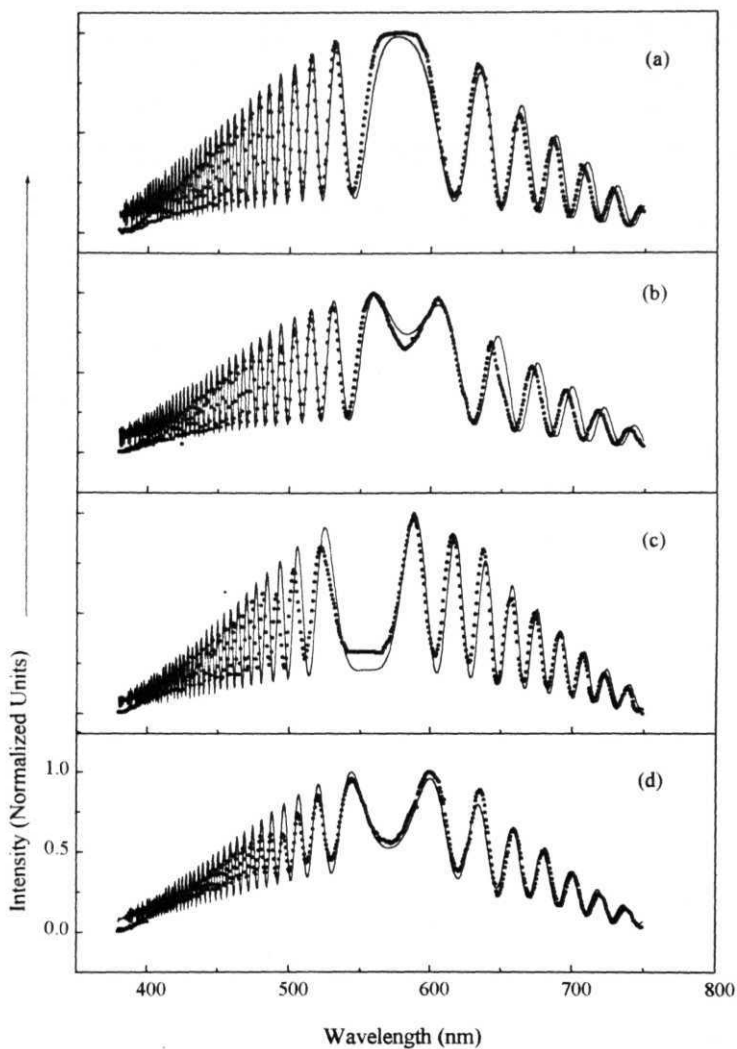


Figure 6.5

Normalized spectral modulations and the corresponding theoretical fit (using eqns (6.10) and (6.11)). Dots are experimental data and the continuous line is theoretical fit (a) glass plate, (b) glass plate+PVA, (c) glass plate, (d) glass plate + PMMA. The fitted constants are given in Table 6.2.

Constants	Glass plate (average)	PVA	PS	PMMA	PF
A	-1.35640E20	-1.37E20	-1.370E20	-1.370E20	9.98649E19
B	4.40640E7	3.6596E7	5.65960E7	5.6596E7	1.00015E7
C	1.51210	1.500991	1.57651	1.483863	1.5005
D	3.23853E-15	2.59450E-15	2.50004E-15	1.81373E-15	3.65049E-15
E	9.99981E-29	9.99998E-31	2.98196E-29	7.98013E-29	1.22549E-29
n (at 633 nm)	1.520793	1.507468	1.582941 (1.587)	1.488891	1.509707
t(m)	9.99981E-4	3.33116E-7	3.23062E-7 (3.237E-7)	1.54365E-6	3.99975E-5
V	0.68	0.60	0.65	0.45	0.025
λ_{a} (nm)	567.624 578.424 551.117	575.079	581.699	572.425	
L_0	1.546076E-3				6.4999E-5 6.9001E-5

Table 6.2

Table giving the experimental parameters and the optical constants obtained from theoretical fitting for the glass substrate and the polymer films. The values given within the brackets are from the ellipsometer measurements.

spectral modulations. The $n(X)$ and ' t ' values are also tabulated for other polymer **films** like PS and PMMA having different thickness depending on the coating mechanism. Substituting the values of the dispersion constants obtained using the theoretical fit, the dispersion curves are generated for all the polymer films and the glass substrate used and are shown in the Figure 6.6.

The estimated value of the refractive index at some fixed wavelength ($X = 633$ **nm**) for the different polymer films are compared with the values available in the literature [42] and are found to agree reasonably well. To compare the accuracy of these results, the ' n ' (at $X = 633$ nm) and ' t ' are measured using an **ellipsometer**. For the measurement, the back surface of the glass plate was properly grounded first to eliminate the reflections from the second surface of the glass plate. The values measured are given in the same Table 6.2, denoted by ' \star '. Approximate value of the thickness of the sample is found before hand from transmission measurements. The ellipsometer study could not give the refractive index and thickness values for the PVA **and** PMMA films as their refractive indices are either close to or lower than the glass substrate.

To demonstrate that the technique developed here, has better flexibility and larger dynamic range for the measurement of the refractive index and thickness, **we** have used commercially available thin polythene films. These films are fixed free standing and unsupported on a mount and placed in one of the arms of the interferometer adjusted to approximately zero path difference. Because the film is thin and the bandwidth of the source is less than the optical path difference introduced by the **material**, there is no significant change observed in the recorded spectrum. This limitation is overcome by moving the mirror to an arbitrary position so that there are sufficient number of fringes within the spectrum. These spectral modulations are fitted using the eqns.(6.10), (6.4) and (6.6) to get the dispersion constants of the free standing polythene film. The experimental data and the corresponding theoretical fit are shown in the Figure 6.7 (a). It can be seen from the figure that the modulation depth of the spectral fringes are less. This is because of the surface and bulk **inhomogenities** of the material, which increases the scattering loss for the light beam

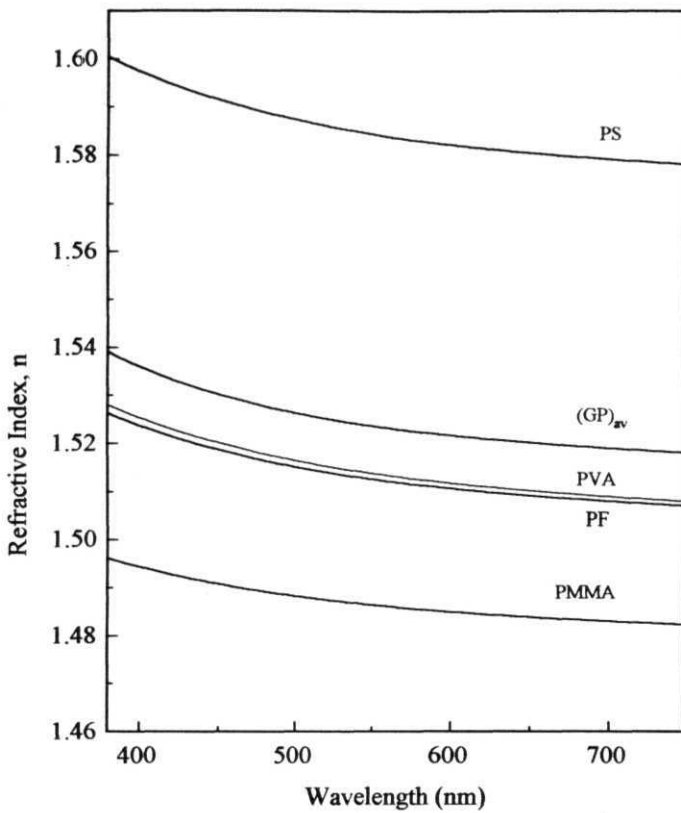


Figure 6.6

Plot of the dispersion curves for different materials placed in the interferometer **arm**, calculated from the fitted constants. PMMA: polymethyl meta acrylate, PF: polythene film, PVA: poly vinyl alcohol, **(GP)_{av}**: average of all glass plates, PS: polystyrene.

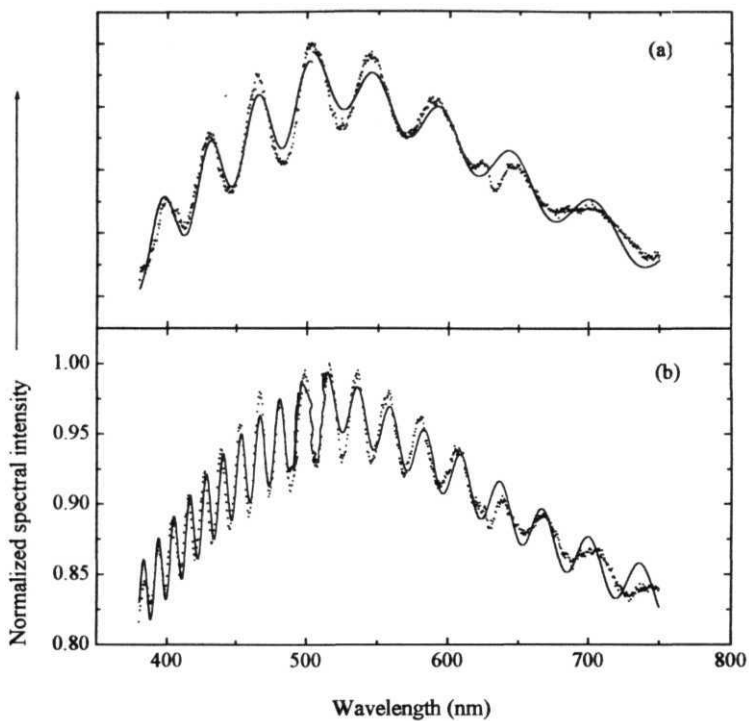


Figure 6.7

Spectral modulations with a bare polymer film in arm 1 of the **MI**. Dots are experimental data and continuous line is the theoretical fit (eqn. (6.10)). The fitted constants given in the Table 6.2, except L_0 are the same for both the fitting.

in the **arm 1**. To confirm that the arbitrary path length introduced in one of the arms of the interferometer via L_0 does not affect the value of the dispersion constants estimated, we repeated the experiment increasing the value of L_0 . The fitted values of the dispersion constants and the thickness are the same as the values obtained for a different value of L_0 and are given in Table 6.2. Figure 6.7 (b) gives the experimental data and the fit for a different value of the arbitrary constant L_0 used to increase the path difference and hence the number of fringes. The refractive index curve for the free standing polythene film, generated using the fitted constants is given in the Figure 6.6.

6.4.2 Absorbing materials

The effect of free propagation on the spectrum due to interference between two partially coherent optical fields and the changes in the periodicity of the spectral modulations due to the introduction of normal dispersive material in one of the arms of a white light spectral interferometer have been discussed in detail in the chapter 3 and this chapter. Recently, there has been some significant theoretical work done regarding the effect of an absorbing medium on the propagation of partially coherent beams [53,54]. The significant result of such a study is that the degree of coherence is found to increase with the propagation of the beam at each frequency of the **radiation**. Here, we discuss the effect of an absorbing medium kept in one of the arms of a **MI**, in reducing the spectral visibility of the interference fringes [27]. The method briefly discussed here, is a novel technique to determine the optical constants (n, k) of the material from the measurement of the spectral interference fringes with an absorbing sample.

The absorbing sample introduced in one of the arms of the interferometer reduces the available spectral intensity of the beam in the absorption region of the material. This spoils the condition of having equal spectral intensity of the two beams to form good contrast interference fringes over the entire region of interest. As a result, there is a decrease in the amplitude of the spectral modulations proportional to

the concentration of the solution and the path length the light beam travels in the material before interfering. If A_0 is the amplitude of the input light which passes through an absorbing cell of length T having a solution of absorption coefficient ' α ' and concentration ' C ', then the amplitude of the light emerging from the cell ' A ' is given by the Beer's law

$$A = A_0 \exp(-\alpha Cl/2) \quad (6.12)$$

As a result of the absorption of one of the beams, the interference fringes appear amplitude modulated. By measuring the decrease in the spectral visibility, the absorption spectrum of the sample can be obtained. Also by increasing the number of fringes within the absorption region, the absorption behavior of the sample can be more closely monitored. This is achieved by moving one of the mirrors M_2 of the MI and this arbitrary constant is included in L_0 while fitting it to the theoretical equation.

Figure 6.8 shows the amplitude modulated spectral fringes with a dilute Rhodamine B (Rh-B) in methanol solution kept in a cell of 1 cm path length in the arm 1 of the MI. The figure also gives the spectra of the two interfering beams recorded by closing the other arm of the interferometer. As can be seen, the absorption of the Rh B dye is asymmetrical in shape which makes our analysis slightly difficult. The neodymium nitrate solution has an approximately Gaussian shaped absorption spectrum and hence is used to demonstrate our technique. In Figure 6.9 (a) the amplitude modulated spectral fringes are shown for a 0.05M solution of Neodymium nitrate in water ($Nd(NO_3)_3 \cdot xH_2O$). The sample is kept in a 1 cm cell in the arm 1 of the MI. By varying the path delay between the interfering beams, different fringe spacing are obtained for the same solution as shown in the Figures 6.9 (b) and (c). This is fitted to a modulated absorption spectrum of the form given in eqn.(6.10) assuming a Gaussian absorption spectrum. From the figure it is also seen that the modulation frequency of the spectral fringes remain a constant and hence it can be concluded that the dispersive contribution within the absorption region is the same and hence the refractive index of the material is taken to be a constant over the region of recording, having a value of about 1.335. The absorption peak of the sample is around 581 nm

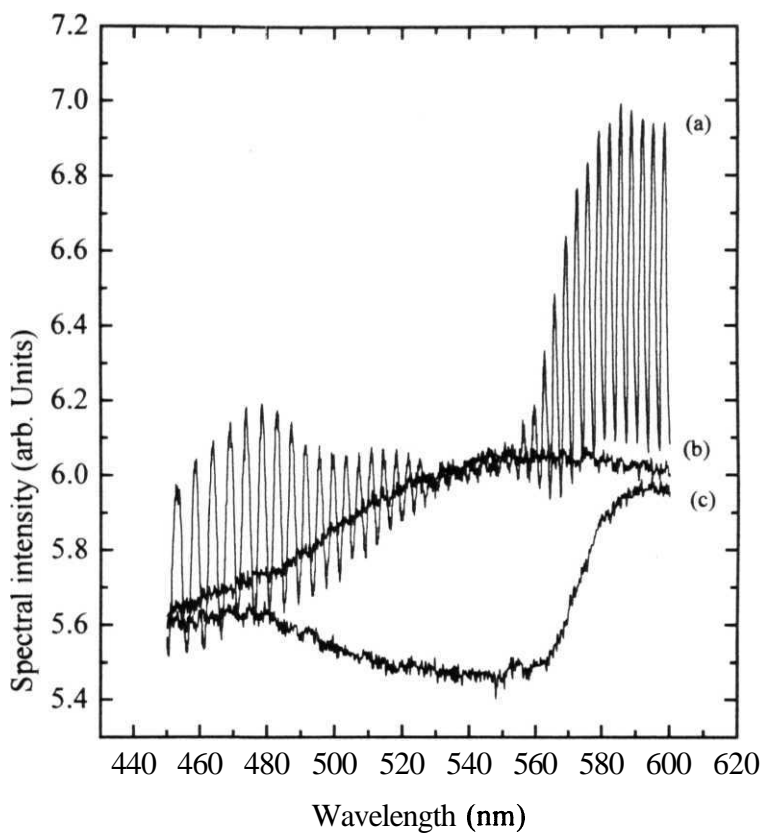


Figure 6.8

Demonstration of amplitude modulation of spectral fringes by keeping dilute RhB solution in one of the arms of the MI. (a) spectral modulations, (b) spectrum of the lamp by closing the sample arm, (c) spectrum, closing the other arm of the interferometer.

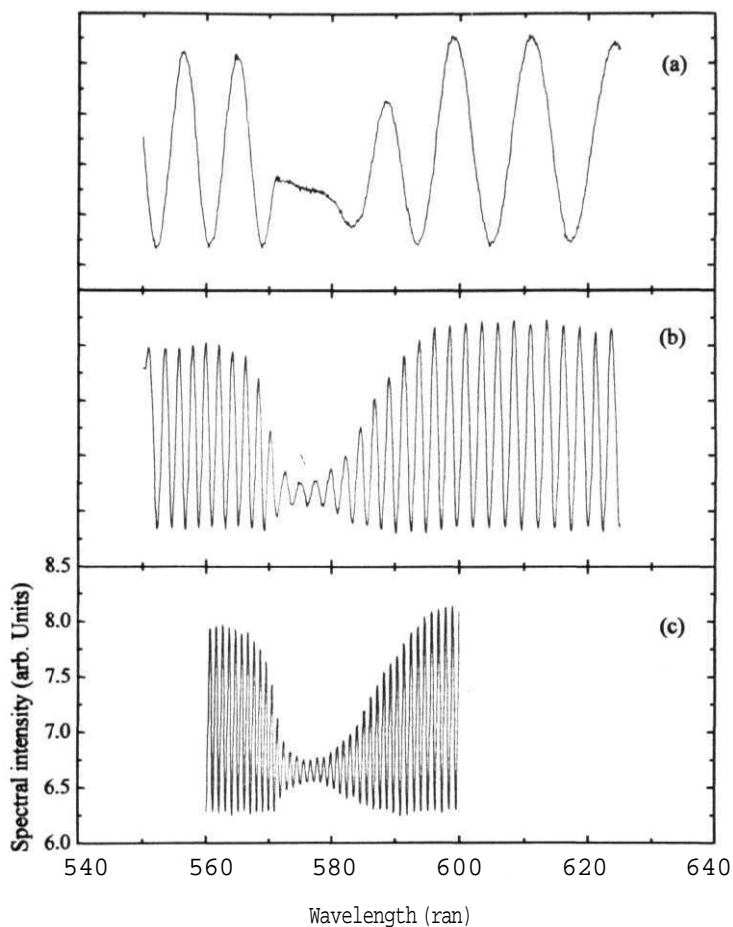


Figure 6.9

Amplitude modulation of the spectral fringes showing the effect of absorption with increasing number of fringes. Sample used is 0.05M solution of Neodymium nitrate in water.

which corresponds to the transition $^4\mathbf{I}_{9/2} \rightarrow ^4\mathbf{G}_{5/2}, ^2\mathbf{G}_{7/2}$ of the Nd. Using the fitting procedure described in the previous sections, the experimental curve is fitted and from the fitting, the absorption curve is calculated. From this the corresponding dispersion is calculated by differentiating the fitted curve and both are shown in the Figure 6 10. The advantage of this technique is that, from a single spectral recording over the entire region of interest, one can get both the dispersive contribution, from the periodicity of the spectral fringes and the absorption contribution from the reduction in the spectral fringe visibility.

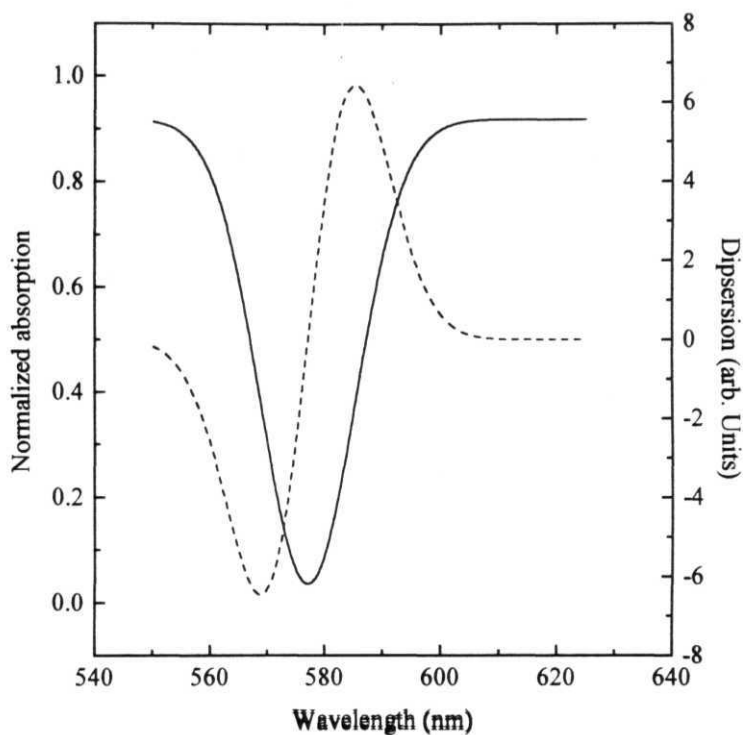


Figure 6.10

The normalized absorption curve (full line) obtained from fitting the amplitude modulated spectral fringes(Fig.6.9(b)) and the corresponding dispersion curve (dashed line) of 0.05M **Neodymium** nitrate in water.

References

- [1] L. Mandel and E. Wolf, in Optical coherence and Quantum optics, (Cambridge press, 1995), chapter 5.
- [2] E. Wolf, in Recent developments in Quantum optics, Edited by R. Ingua, (Plenum press, NY, 1993).
- [3] L. Mandel and E. Wolf, J. Opt. Soc. Am. **66**, 529, (1976).
- [4] E. Wolf, Opt Lett **8**, 250, (1983).
- [5] D.F.V. James and E. Wolf, Opt. Commun. **81**, 150, (1991).
- [6] X.Y. Zou, T.P. Grayson and L. Mandel, Phys. Rev. Lett. **69**, 3041, (1992).
- [7] G.S. Agarwal and D.F.V. James, J. Mod. Opt. **40**, 1431, (1992).
- [8] D. Narayana Rao and V. Nirmal Kumar, J. Mod. Opt. **41**, 1757, (1994).
- [9] D.F.V. James and E. Wolf, Phys. Lett. A **157**, 6, (1991).
- [10] M. Santarsiero and F. Gori, Phys. Lett. A **167**, 123, (1992).
- [11] W.H. Knox, N.M. Pearson, K.D. Li and C.A. Hirlimann, Opt. Lett. **13**, 574, (1988).
- [12] K.D. Li, W.H. Knox and N.M. Pearson, Opt. Lett. **14**, 450, (1989).
- [13] Z. Bor, K. Osvay, B. Racz and G. Szabo, Opt. Commun **78**, 109, (1990).
- [14] L. Malitson, Appl. Opt. **2**, 1103, (1963).
- [15] S. Mitachi and T. Miyashita, Appl. Opt. **22**, 2419, (1983).
- [16] O. Stavroudis and L. Sutton, J. Opt. Soc. Am. **51**, 368, (1961); L. Sutton and O. Stavroudis, J Opt Soc Am. **51**, 901, (1961).
- [17] B J Pernick, Appl Opt. **22**, 1133, (1983).

- [18] E R. **Peck**, *Appl. Opt.* 22, 2906, (1983).
- [19] C.K. **Carniglia**, K.N. Schrader P.A. O'connell and S.R. Tunge, *Appl. Opt.* 28, 2902,(1989).
- [20] K. Naganuma, **K. Mogi** and **H Yamada**, *Opt. Lett.* 15, **393**, (1990)
- [21] K. Naganuma and H. **Yasaka**, *IEEE J Quant. Electron.* 27, 1280, (1991).
- [22] **K. Creath**, in *Progress in Optics*, Edited by E. Wolf, (North-Holland, Amsterdam, 1988), vol **26**
- [23] M. **Tateda**, **N Shibata** and **S Seikai**, *IEEE J Quant Electron.* 17, 404, (1981).
- [24] M. Beck and I. A. **Walmsley**, *Opt. Lett.* 15, 492, (1990).
- [25] C. Sainz, J E. Calatroni and G. Tribillon, *Meas. Sci. Technol.* 1, 356, (1990).
- [26] A L Guerro, C. **Sainz**, H. **Perrin**, R. Castell and J. Calatroni, *Opt. Laser Technol.* 24,333,(1992).
- [27] C. **Sainz**, **P Jourdain**, R. Escalona and J. Calatroni, *Opt. Commun.* **110**, 381, (1994)
- [28] X D Cao and D.D Meyerhofer, *Opt. Lett.* 19, 1837, (1994).
- [29] A P Kovacs, K.Osvay, Zs. Bor and R Szipocs, *Opt Lett.* 20, 788, (1995).
- [30] S **Diddams** and J.C **Diels**, *J Opt. Soc Am. B* 13, 1120,(1996).
- [31] V. **Nirmal Kumar** and D. Narayana Rao, *J. Opt Soc. Am. B* **12**, 1559, (1995).
- [32] V. Nirmal Kumar, **Y Chandrasekar** and **D Narayana Rao**, *Pramana* 47, 163, (1996).
- [33] **V Nirmal Kumar** and D. Narayana Rao, communicated.
- [34] **J Zhou**, **G Taft**, **C.P Huang**, **M.M Murnane** and **H.C Kapteyn**, *Opt. Lett.* 19, **1149**, (1994).
- [35] M. Beck and I A **Walmsley**, *Opt Lett* 15, 492, (1990).

- [36] M. Beck, I. A. **Walmsley** and J D. **Kafka**, IEEE J. Quant. Electron. 27, 2074, (1991).
- [37] L **E** Katz, in VLSI Technology, Edited by S.M. Sze (McGraw Hill, NY, 1982), chapter 3.
- [38] SE. Miller, Bell, Syst. Tech. **J** 48, 2059, (1969).
- [39] PK. **Tien**, R. Ulrich and R **J** **Martin**, Appl. Phys. Lett. 17, 447, (1970).
- [40] R. **Ulrich** and R. Torge, Appl. Opt. 12, 2901, (1973); AC. Adams. DP. Schinke and CD. Capio, J. **Electrochem. Soc.** 126, 1539, (1979).
- [41] **T** Ding and E. **Garmire**, Appl Opt 22, 3177, (1983).
- [42] J D. **Swalen**, M. Tacke, **R** Santo and **J** Fischer, Opt. **Commun.** 18, 387, (1976)
- [43] R.M. **Azzam** and N.M. **Bashara**, Ellipsometry and polarized light, (North-Holland, Amsterdam, 1989).
- [44] PK. Tien, R. Ulrich and R **J** Martin, Appl. Phys. Lett. 14, 291, (1969).
- [45] J **E** **Goell** and S.D. Standley, Bell Syst Tech. J. 48, 3445, (1969).
- [46] E **R** Schineller, **R.P** Flam and **D.W** Wilmot, J Opt Soc Am 58, 1171, (1968).
- [47] R. Ulrich and **H.P** Weber, Appl Opt. **11**, 428, (1972).
- [48] **JH** Harris, R. Schubert and J.N. **Polky**, J Opt. Soc. Am. 60, 1007, (1970).
- [49] **H.P.** Weber and R. Ulrich, Appl. Phys. Lett. 19, 38, (1971).
- [50] FA. Jenkins and **H.E.** White, Fundamentals of optics, (4th edition, McGraw Hill, 1981), chapter 23.
- [51] **B** Tatian, Appl Opt 23, 4477, (1984)

- [52] W.H. Steel, in Progress in optics, Edited by E. Wolf, (North-Holland, Amsterdam, 1966), vol. 5.
- [53] W. Wang and E. Wolf, J. Mod. Opt. 39, 2007, (1992).
- [54] **C Palma, P** De Santis, **G** Cincotti and G. Guttari, **J** Mod. Opt. 42, 1123, (1995).

CHAPTER 7

MEASUREMENT OF THE INSTRUMENT FUNCTION OF A SPECTROMETER

7.1 Introduction

Instrument function is a measure of the intensity distribution in the output plane of a spectroscopic system assuming the input to be an ideal *sharp* isolated spectral line [1]. It is very essential to know, apart from the resolution limit of the spectrometer also the complete instrument function for the measurement of the exact line profile of spectral sources. The resolution properties of a spectral device can be completely determined considering a perfect monochromatic line representation. The instrument function of a spectrometer is defined by its response $\sigma(v-v')$ to a perfectly monochromatic spectral line represented by the Dirac function $\delta(v-v')$. For an apparatus illuminated by a spectral line of spectral energy distribution $S(v)$ (the source function), the spectral energy distribution recorded, $s(v)$ is a convolution of the source function by the instrument function i.e.,

$$s(v) = \int_{-\infty}^{\infty} S(v')\sigma(v-v')dv' \quad (7.1)$$

or this may be written as

$$s(v) = S(v) \otimes \sigma(v), \quad (7.2)$$

where \otimes is the symbol for convolution. Two monochromatic lines are said to be resolved when their frequency separation v_2-v_1 is greater than a certain value δv_p which is of the order of the width ' w ' of the instrument function $\sigma(v)$, where δv_p is the effective limit of resolution. For simplicity in the analysis of results, it is assumed that $\delta v_p = w$ where, for example ' w ' is the full width at half maximum (FWHM) of a

Gaussian curve or the distance between the maximum and the first zero for a **diffraction** curve. The resolving power of the spectrometer is defined by $\mathcal{R} = \nu/\delta\nu_{\text{eff}}$ and the effective resolving power is obtained by taking into account all the characteristics of the device which contribute to the width of the instrument function $\sigma(\nu)$.

Typically, the instrument function remains a constant over a broad range of frequency. Over the spectral region where the instrument function does not change, the spectrometer acts similar to a linear system. If the input varies sinusoidally with frequency, the output is also sinusoidal, but with lesser modulation depth. The ratio of the output to the input modulation is known as the *spectrometer transfer function*, which is the normalized Fourier transform of the instrument function [2,3]. This quantity is analogous to the *optical transfer function* (OTF) of noncoherent imaging systems [4]. The OTF gives a powerful way to evaluate the image performance of an optical system, and it has been applied to lens systems in many ways. Lohmann was the first to apply the concept of OTF to plane grating with different kinds of ruling errors [5]. Depending on the amount of aberrations or the region of spatial frequency considered, the OTF of grating spectrometers have also been evaluated based on the geometrical optics or wave optics treatment [6].

Real spectral apparatus [7] like a spectrometer is not an ideal harmonic analyzer of radiation i.e., the distribution of energy over the spectrum obtained with the help of a spectrometer differs from the ideal distribution. The distortions are due to different reasons. Among them, the important ones are: (i) change with the solid angle of the slits of the spectrometer, (ii) of its dispersion, (iii) of the angular and linear magnification, (iv) of the sensitivity of the radiation detector etc. The slits have to be infinitely narrow in an ideal spectrometer, but for infinitely narrow slits, the throughput of light into the apparatus is very small and it is difficult to work with real measurable quantities. As the limiting resolution for any spectrometer is imposed by its finite slit width, it also leads to distortion of the output spectral distribution. Thus, it becomes important to characterize the spectral instrument for least distorted output spectrum under the actual working conditions.

Although several names are given in the literature to describe the contribution of the function $\sigma(v)$ (defined by eqn. 7.2), in this text we use the general terminology of *instrument function* or its Fourier transform *modulation transfer function* (MTF). The description of the effects of two important distorting factors like the slit width and the resolution limit variations of the plane grating spectrometer are used to characterize the instrument from the observed distribution of illumination assuming vanishingly small effects of other distorting factors. The MTF is also known as the *spectral transfer function* [8] when it is measured for a dispersing system as a function of the slit width of the spectrometer or as *spectral modulation transfer function* [9] when the measurement is made as a function of the number of fringes or the optical path difference of the interferometer used for the measurement.

7.2 Measurement techniques

Increasing interest in the applications of high-resolution spectroscopy and the advances made in the spectroscopic systems makes it necessary to evaluate the performance of the measuring **instruments**. Although the resolving power is used as one single measure of the performance, the instrument function is more useful and provides a more powerful means to analyze the spectrographic details. The instrument function of dispersion spectrometers, which is our prime interest here is determined by the slit image [2]. In a scanning spectrometer, the instrument function is given by the convolution of the slit image and the detector aperture and its full width is equal to the sum of the detector width and input slit image widths. The measurement techniques of the instrument function or the transfer function of a spectroscopic system is **classified** into three methods: 1 The OTF of spectroscopic systems can be measured from the Fourier transform (FT) of the line-spread **function** [10] However, the results can be inaccurate because of the errors involved in determining the line profiles and in computing their Fourier transforms, 2. Autocorrelation method, where the OTF of the spectrometer is calculated by the wave optical method, by defining the OTF as the autocorrelation function of the wavefront aberrations on the pupil of the spectroscopic system [6] and 3 the recently developed sinusoidally modulated spectrum (SMS)

method, where the OTF is measured from the response of the spectroscopic system to the sinusoidal input having different periodicity of the spectral fringes [11,12].

Interferometers can be used as a convenient means for calibration and to study the optical properties of spectrometers [13]. The errors involved in the interferometric frequency calibration of infrared spectrometers are evaluated to be due to the slit width and slit height effects. These effects are manifested as blurring of the interference pattern and shift in the maxima of the interferogram. There is also the spurious spectral resolution problem to be taken care of in the exact analysis of a spectrometer. The periodic spectral detail which is generally lost when the slit width of the spectrometer is widened to a particular value, reappears with further widening of the slits. This behavior can be identified from the appearance of secondary maxima in the spectral transfer function of the spectrometer and was first demonstrated experimentally in the IR region using the interference fringes from a Fabry-Perot etalon

The direct determination of the slit function was achieved by analyzing the spectral distribution at the output of an incoherently illuminated spectrometer by using a scanning Michelson interferometer [14]. From the recorded interferogram, which is the FT of the spectral distribution of the radiation input to the spectrometer $\mathbf{s}(\mathbf{v}-\mathbf{v}_0)$ and the envelope of the interferometer output $\mathbf{F}(\boldsymbol{\sigma})$, the slit scanning function $s(v)$ is calculated. It is important to note that the instrument function of a spectrometer depends on the state of coherence of the input radiation and in most of the spectroscopic analysis, the source radiation is thermal and incoherent. Hence, the instrument function calculated using a laser gives only the values for coherent radiation and is unsuitable for any further data analysis [3].

7.3 Sinusoidally modulated spectra

7.3.1. Fabry-Perot interferometer:

Fabry-Perot interferometers (**FPI**) have been extensively used **for** the measurement of the spectral slit width and hence the limiting spectral modulation frequencies of **monochromators** [15]. Direct measurement of the optical transfer function of spectroscopic systems can be achieved from the measurement of the reduction in amplitude and phase shifts of sinusoidal inputs having various frequencies of the fringes. The principle behind such a technique is the use of FPI as a sinusoidal signal **generator**. The interference fringes produced are equi-spaced in the wavenumber of known amplitude. The separation of adjacent peaks Δ in the spectrum of transmitted light is given by [11]

$$\Delta = \frac{\lambda^2}{2nt(\cos\theta)} \quad (7.3)$$

which can be varied by changing the separation between the plates ' t ' of the interferometer with a medium of constant refractive index ' n ' between the plates and a **fixed** emergent angle θ . The spectrum of the transmitted light can be made approximately sinusoidal with the frequency $1/\Delta$, by adjusting the **finesse** due to **field** angle ' Φ ' or the reflectivity of the two plates R or the roughness of the plates λ/M . The modulus of the OTF is determined from the ratio of the amplitudes of the input sinusoidal spectra and the dispersed output from the spectrometer for different frequencies of the **fringes**. From the attenuation of the fringe **pattern**, information about the spectral slit width and hence the spectral band passed by the spectrometer in any spectral region can be measured. The measurement of the instrument function or its Fourier transform, the MTF is also possible by varying the path difference of the interferometer or by scanning the interference pattern over the frequency range of interest for a fixed fringe spacing from the interferometer and set mechanical slit width of the spectrometer.

The sensitivity of these measurements are limited by the fringe amplitude obtainable from the FP1, which is a function of the reflectivity of the interferometer plates and their alignment [15]. It is possible to improve the accuracy with which the spectral slit widths can be measured by working at higher values for the amplitude of the interference pattern. Moreover, a true sine wave of the interference pattern is achieved only for values of the peak-peak amplitude of less than 30%. At higher values of the amplitude which is achieved by increasing the reflectivity of the interferometer windows, the interference maxima sharpen and the minima broaden leading to unequal fringe spacing. Increasing the reflectivity also leads to multiple reflections from the windows which can give rise to spurious interference patterns and these fringes superimposed on the fundamental fringe pattern can lead to error in the measurements. However, the effect of the harmonics of the fundamental interference is effective only when observed at $\alpha=0$ and are filtered out when determining the spectral slit width at the minimum $a = n$ where, $a (= 2\pi\delta vnt)$ is a function of the fringe spacing. For fixed parameters of the light source used, the fringe spacing A can be varied over a wide range by varying the separation of plates 't' and the finesse by the field angle Φ . But invariably the calculated fringe frequency and the field angle are different from the measured ones. The differences are because of the poor parallelism of the beams and bad focusing of lenses.

7.3.2. Michelson interferometer:

Cosinusoidally modulated spectral fringes of greater flexibility and control can be obtained using a dispersion compensated Michelson interferometer (MI) and a white light source [16]. When the path difference (A) between the interfering beams is more than the coherence length (l_c) of the source, monitoring the spectrum of the source shows interference fringes. A complete schematic of the experimental setup with the source, the MI used to generate the sinusoidally modulated spectra and the spectrometer which is to be calibrated are shown in the Figure 7.1. The source is a 25 W tungsten filament lamp is the white light source used which, after passing through a

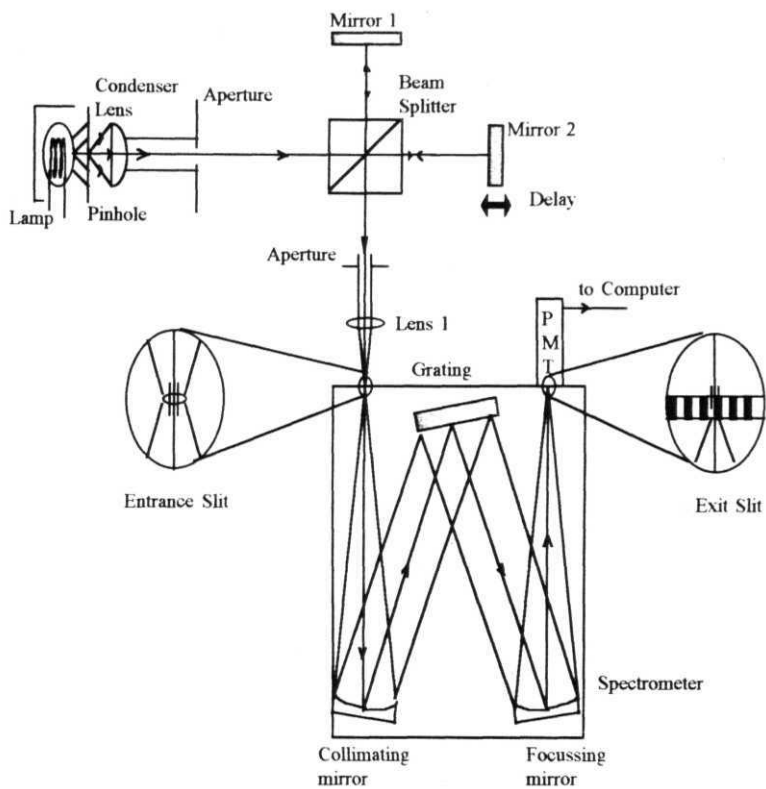


Figure 7.1

Schematic of the experimental setup used to measure the instrument function of a grating spectrometer.

pinhole is collimated using a condenser lens of focal length $f = 18 \text{ mm}$. The Michelson interferometer is compensated for unequal dispersion by using a cube beamsplitter and similar aluminium coated mirrors. The unequal dispersion between the interfering beams arise because of the light beams traveling unequal paths in the material of the different optical components. One of the mirrors M_2 is mounted on a linear translational stage with a movement accuracy of $\pm 5 \text{ }\mu\text{m}$ and the other mirror M_1 is kept fixed. By moving the mirror M_2 , the number of spectral fringes can be varied over a very large range depending on the resolution of the spectrometer to be calibrated. Further details of the MI setup, the recording procedure and the characteristics of the spectral interference fringes were already discussed in detail in the earlier chapters of this thesis.

For the accurate measurement of the modulation transfer function (MTF) and hence the instrument function of a grating spectrometer using the spectral modulations from the MI, the fringe number and the fringe visibility should be known exactly as a function of the path delay between the interfering beams. The first step in calibrating the MI is to count the number of fringes in the entire visible region of the white light spectrum ($\lambda = 380 - 750 \text{ nm}$) for increasing delay between the interfering beams. This measurement is plotted in Figure 7.2 (a). From the figure it is clear that the increase in the number of spectral fringes with path delay is linear. The straight line fitted to the experimental data, gives the values of the slope and Y-intercept to be $m = 1.058\text{E}+6$ and $c = -26.133$ respectively. A path delay of 1 mm between the interfering beams corresponds to the number of fringes $N \approx 1032$. This value is close to that calculated from $N = 1/\Delta = 1000$ fringes. As all our transfer function measurements of the spectrometer are based on the decrease in the visibility of the spectral modulations, the behavior of the spectral visibility with path delay is also an important characteristic of the MI. Figure 7.2 (b) gives the behavior of the spectral visibility calculated from the maximum and minimum of the spectral fringes using the visibility equation defined by

Michelson
$$V = \frac{S_{\max} - S_{\min}}{S_{\max} + S_{\min}}$$
. This value is calculated for different path delays at a

fixed wavelength of $\lambda = 550 \text{ nm}$. The visibility remains almost a constant in the region

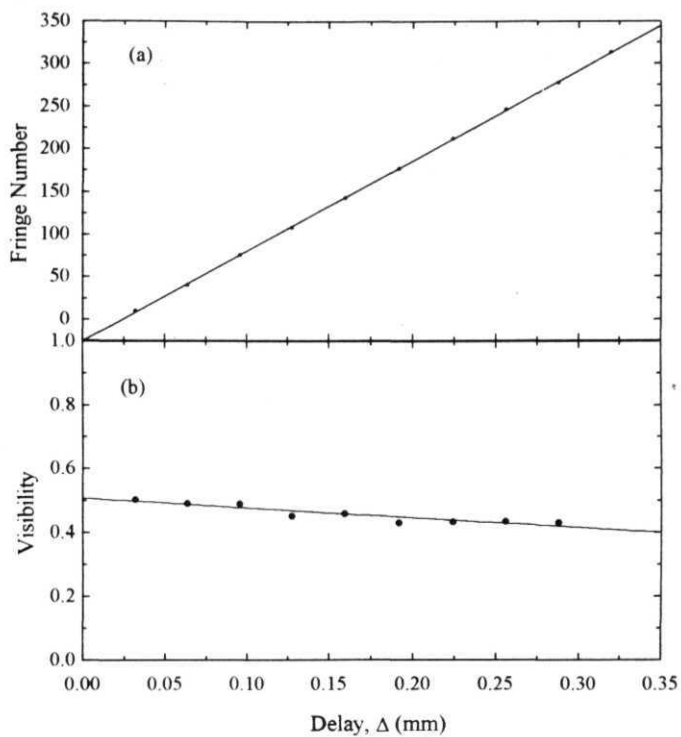


Figure 7.2

Characteristics of the white light fringes from a Michelson interferometer (a) Number of fringes (N) Vs the path delay (Δ)
 Fitted equation: $y = (1058140)\Delta - 26.133$
 (b) Visibility of the fringes (V) Vs the path delay (Δ)

of our **measurement**. Thus it is made sure that whatever decrease observed in the visibility for **various** settings of the interferometer and spectrometer are only because of the effect of the instrument function.

The advantages of using a sinusoidally modulated spectrum produced by a white light Michelson interferometer are: (i) The number of fringes or the periodicity of the spectral fringes can be very easily varied to any value so that the measurement can be made on any spectrometer irrespective of its resolution and at any value of wavelength within the source **spectrum**. (ii) The measurement of the transfer **function** and hence the instrument function of the spectrometer are made from the behavior of contrast or the fringe visibility of the spectral fringes. Moreover, as the spectral modulations have good signal to noise ratio, the reliability of the values evaluated are more and hence this method is far better than the usual Fourier transform **method**, where the TF is evaluated from the line **profiles**.

7.4 Grating spectrometer

The instrument for which the calibration and characterization is sought is a 50 cm grating spectrometer (**JY**, HRS-2) in the symmetric **Czerny-Turner** (C-Z) **configuration**. The entrance slit is located at the focal plane of the lens **L₁** ($f = 20$ cm). The output beam from the **MI** is focused using this lens onto the entrance slit. An aperture of 3 mm diameter is kept before this lens to avoid any stray light from entering the spectrometer. The dimensions of the **collimating** and focusing mirrors in the spectrometer are: focal length = 58.8 cm, height = 8 cm, width = 10.5 cm. The projected slit width and height in the output plane are equal to the corresponding input values because of the unit magnification of the system. The dispersion element is a plane grating (**M** - 29) of dimension **D** = 7 cm **square**. The grating order number is $m = 1$ and has 1200 grooves/mm. The angular dispersion is $(d\theta/d\lambda) = 0.014$ mrad/nm, with the dispersion parallel to the slit width and the spectral element of width $\delta\lambda_{sp}$ is isolated and projected onto the output slit. The dispersing element accepts all the light from the collimating mirror. The angle subtended by the slit on the focused input beam

is $(\delta x/f) = 0.25 \text{ mrad}$ for a 50 μm slit width (6x) and increases to 2.5 **mrad** for a 500 μm slit width. Similarly, the angle (ϕ) subtended by the slit at the **collimating** mirror varies from about 0.1 mrad to 1 mrad depending on the slit width. In terms of the angular dispersion [17],

$$\delta\lambda_{\phi} = \phi' \left(\frac{d\lambda}{d\theta} \right) = \left[\frac{w'}{f' (d\theta/d\lambda)} \right] = w' P$$

where, ϕ' is the angle subtended by the exit slit on the focusing mirror, w' and f are the width and the focal length of the focusing mirror and P is the reciprocal linear dispersion expressed in **nm/mm**. For $P = 1.2 \text{ nm/mm}$, at 550 nm, and 50 μm exit slit width, $\delta\lambda_{\phi} = 0.06 \text{ nm}$ which is more than the resolution limit of the spectrometer of 0.014 nm.

The entrance and exit slit widths of the spectrometer can be adjusted independently of each other to an accuracy of $< \pm 5 \text{ }\mu\text{m}$. For the type of grating used, the width of the spherical aberration spot is 7 μm and no further resolution can be obtained if the slit widths are reduced below this value [18]. However for slit widths between few μm and 50 μm , the instrument function is deformed by widening of the bottom of the curve because of spherical aberration and increase in the curve asymmetry with wavelength because of **coma**. As a result of these considerations, the working widths of the spectrometer slits are selected to be $> 50 \text{ }\mu\text{m}$. Though for maximum resolution, the experiments are done with equal slit widths, **fixing** one slit and varying the other gives a clear picture of the behavior of the effect of the individual slits on the output **spectrum**. It is also known that the widest slit width determines the pass band of the spectrometer.

The stringent restriction on the spectral resolution \mathcal{R} of the grating spectrometer is the **diffraction** of radiation at the **slits**. Assuming that the finite slit width decreases the spectral resolution, the effect of finite slit widths on the spectral modulations can be **estimated**. For the C-Z type spectrometer described, the uncertainty in the angle because of the finite slit width is $\delta\phi = \pm (\delta x/2f)$, where, f is the

focal length of the **spectrometer** Thus the total spectral resolution of the spectrometer is [19]

$$1/\mathcal{R} = 1/\mathcal{R}_g + 1/\mathcal{R}_s = \left[\frac{d \cos \varphi_1}{D} \right] + \left(\frac{\delta x_f}{f} \right) \left[\left(\frac{d}{\lambda^2} \right) \cos^2 \left(\frac{\varphi_2}{2} \right) - \left(\frac{1}{4} \right) \right]^{1/2}$$

where, \mathcal{R}_g and \mathcal{R}_s are the contributions to the resolution from the grating and the slits, φ_1 and φ_2 are the angles of the incident and diffracted beams and other symbols have the usual meanings, already **defined** If the slit widths are reduced to values less than certain limit, the diffraction losses at the slits increases drastically. This limit can be approximately evaluated from the equation

$$(\delta x_{\min}/\lambda) = (2f/D) \approx 16.8$$

to be $\delta x_{\min} \approx 9 \mu\text{m}$ at $\lambda = 550 \text{ nm}$

This minimum slit width and the effective width of the grating together determine practically the maximum spectral resolution \mathcal{R}_{\max} of the grating spectrometer independent of the quality of the sources and detectors used:

$$1/\mathcal{R}_{\max} = \left(\frac{d}{D} \right) \left[2 \cos \varphi_1 + \cos(\varphi_2 - \varphi_1) \right]$$

7.5 Modulation transfer function of the spectrometer

The spectral interference law for the Michelson interferometer (**MI**) which is used to generate the sinusoidally modulated spectra (SMS) of **variable** fringe spacing is given by the spectral density distribution at the input plane of the spectrometer as [16]

$$S(\nu) = \left(\frac{1}{2} \right) S_0(\nu) \left[1 + \text{Re}\{\mu_{12}(\nu)\} \cos(2\pi\nu\tau + \theta) \right] \quad (7.4)$$

where $S_0(\nu)$ is the spectral density of the input **beam**, $\text{Re}\{\mu_{12}(\nu)\}$ is the real part of the complex degree of spectral coherence which is taken to be unity based on the analysis in the chapter 4 for spatially coherent beams and τ is the time delay between the two interfering **beams** If A is the path difference between the two beams, then $x = A/c$ and

0 is a phase factor introduced to take care of the phase of $\mu_{12}(\nu)$ and the phase due to the reflection and transmission coefficients at the **beam splitter**, which is a constant and can be neglected. Thus for a white light source of continuous spectral density, the integrated irradiance at the input of the spectrometer is,

$$\int S(\nu) d\nu = \left(\frac{1}{2}\right) \int S_0(\nu) [1 + \cos(2\pi\nu\tau)] d\nu \quad (7.5)$$

For constructive interference, $\nu = m/\tau$ ($m = 1, 2, 3, \dots$ is an integer). The periodicity of the spectral fringes is $5\nu = 1/\tau$ and the fringe order number ' m ' counted from the zero path delay is the optical path difference, which is given by $m = \nu_0\tau = \nu_0/\delta\nu$ in terms of the central frequency ν_0 . Let $S(\nu)$ be the input spectral density distribution and $\sigma(\nu-\nu')$ be the instrument function which is a function of the separation between the frequency of interest ν' and the setting frequency of the spectrometer ν . Now we assume two conditions: first, the condition of **isoplanatism** which means that the instrument function does not change in form within the spectral region of interest and second, the linear superposition condition means that the spectral density distribution in the output plane is a linear **superposition** of the instrument function for each spectral component. Under the validity of the above two conditions, the spectral density distribution at the output plane of the spectrometer is expressed by the convolution integral,

$$s(\nu) = \int S(\nu') \sigma(\nu - \nu') d\nu' \quad (7.6)$$

The Fourier transform of this equation is $s(\tau) = S(\tau) \sigma(\tau)$, where $\sigma(\tau)$ is the Fourier transform of the slit function and is known as modulation transfer function (MTF) of the spectrometer. The Fourier transform of the individual quantities are **defined** as

$$\begin{aligned} s(\tau) &= \int s(\nu) \exp(2\pi i \nu \tau) d\nu, \\ S(\tau) &= \int S(\nu) \exp(2\pi i \nu \tau) d\nu, \\ \sigma(\tau) &= \int \sigma(\nu) \exp(2\pi i \nu \tau) d\nu. \end{aligned} \quad (7.7)$$

The MTF defined by

$$\sigma(\tau) = s(\tau) / S(\tau) \quad (7.8)$$

is the ratio of the Fourier transform of the output spectrogram to the input modulated spectrum and is a function of the delay time x . If the dimension of the path delay between the interfering beams expressed in terms of the path difference $A (= \tau c)$ is cm, then the variable that is used to express the TF has its dimension as cm^{-1} (a spatial - frequency function). The function $\sigma(0)$ obtained from the integrated spectral intensity at the input and output planes $S(0)$ and $s(0)$ for delay $\tau = 0$ can be normalized according to

$$\sigma(0) = \int \sigma(v) dv = 1 \quad (7.9)$$

The measurement of the spectral visibility, $V(x)$ as a function of the path delay at a particular frequency v is equivalent to the measurement of the **MTF**, $\sigma(\tau)$ which is the Fourier transform of the slit function $\sigma(v-v')$ [20]. This equivalence can be demonstrated by considering the equations (7.5) and (7.6). Substituting the spectral density distribution given by eqn.(7.5) in the convolution integral (eqn.(7.6)), we obtain for the spectrogram at the output plane

$$\begin{aligned} s(v) &= \left(\frac{1}{2}\right) \int \left\{ S_0(v') [1 + \cos(2\pi v' \tau)] \right\} \sigma(v - v') dv' \\ &= \left(\frac{1}{2}\right) \int S_0(v') \sigma(v - v') dv' + \left(\frac{1}{2}\right) \int S_0(v') \cos(2\pi v' \tau) \sigma(v - v') dv' \end{aligned} \quad (7.10)$$

The first term in the above equation which is the spectrum of the input beam is a constant $= \left(\frac{1}{2}\right) S_0(v)$ and acts like a dc bias in the output. The second term is the **interferogram** of the slit function. This can be simplified using the shift theorem of Fourier transform and is written as

$$s'(\tau) = \left(\frac{1}{2}\right) S_0(v) [\sigma_s(\tau) \cos(2\pi v \tau) - \sigma_a \sin(2\pi v \tau)] \quad (7.11)$$

where, a , and a , are the Fourier transforms of the symmetric and antisymmetric parts of the slit function $\sigma(v-v')$. The eqn. (7.11) can also be written as

$$s'(\tau) = \left(\frac{1}{2}\right) S_0(v) \sigma_0(\tau) \cos[2\pi v\tau - \phi(\tau)] \quad (7.12)$$

$$\text{with } \sigma_0^2 = \sigma_s^2 + \sigma_a^2 \text{ and } \tan \phi = -\sigma_a / \sigma_s$$

Thus using the eqn. (7.12), the eqn.(7.10) can be written as

$$s(v) = \left(\frac{1}{2}\right) S_0(v) \{1 + |\sigma_0(\tau)| \cos[2\pi v\tau - \phi(\tau)]\} \quad (7.13)$$

This is the equation for the spectral interferogram of the SMS at the output plane of the spectrometer. Assuming the slit function to be symmetric, the phase $\phi(\tau)$ in the above equation is equal to zero and the spectral interferogram consists only of the MTF, $\sigma_0(\tau)$ modulated by equi spaced spectral fringes.

By using the concept of spectral visibility [21], the contrast of the spectral interferogram is given by

$$V = \frac{s_{\max}(v) - s_{\min}(v)}{s_{\max}(v) + s_{\min}(v)} \quad (7.14)$$

where $s_{\max}(v)$ and $s_{\min}(v)$ are the extreme values measured from the experimentally recorded spectral interferogram at a particular value of the frequency v . Knowing that the spectral visibility V remains a constant (Fig. 7.2 (b)) for the time delays used in the experiment, the maximum and minimum values of the spectral densities are given by

$$\begin{aligned} s_{\max}(v) &= \left(\frac{1}{2}\right) S_0(v) [1 + |\sigma_0(\tau)|], \text{ for } 2\pi v\tau - \phi(\tau) = 2n\pi \text{ where, } n \text{ is an integer} \\ s_{\min}(v) &= \left(\frac{1}{2}\right) S_0(v) [1 - |\sigma_0(\tau)|], \text{ for } 2\pi v\tau - \phi(\tau) = (2n+1)\pi \end{aligned} \quad (7.15)$$

Using the above two equations in eqn. (7.14), the visibility is simplified to be

$$V = |\sigma_0(\tau)|$$

Thus the visibility of the spectral interferogram of the SMS is equivalent to the modulation transfer function of the spectrometer. The curves of the MTF are obtained from the measurements of visibility of the spectral interferogram by varying either the

path delay $A (= xc)$ between the interfering beams of the **MI** or the entrance or exit slit widths (δx_1 or δx_2) of the spectrometer.

Spectrometer is a device used to analyze or separate light according to **frequency** ν or wavelength $X (=c/\nu)$ of the input radiation. In the visualization of spectral modulations between the interfering fields, an ideal spectrometer should completely separate every single frequency component ν . Then the spectral modulations are visible for any value **of** the delay τ between the interfering beams however long it be. But a real instrument performs spectral decomposition with a finite spectral width $\delta \nu_{sp}$, which depends on the resolution of the spectrometer. As a result, spectral modulations are visible only for a limited interval of delay τ . To demonstrate this and to get the **functional** form for the modulation transfer **function**, the **eqn.(7.13)** is integrated between $\nu-d\nu/2$ to $\nu+d\nu/2$ over the interval $d\nu$:

$$\int_{\nu-d\nu/2}^{\nu+d\nu/2} s(\nu') d\nu' = \left(\frac{1}{2}\right) \int_{\nu-d\nu/2}^{\nu+d\nu/2} S_0(\nu') \{1 + |\sigma_0(\tau)| \cos(2\pi\nu'\tau)\} d\nu' \quad (7.17)$$

This gives the distribution of the spectral band passed by the spectrometer of finite width $d\nu = \delta \nu_{sp}$ at a frequency ν and delay x to be

$$s(\nu, \delta \nu_{sp}, \tau) = \left(\frac{1}{2}\right) S_0(\nu) \left\{ 1 + |\sigma_0(\tau)| \frac{\sin(\pi \delta \nu_{sp} \tau)}{(\pi \delta \nu_{sp} \tau)} \cos(2\pi \nu \tau) \right\} \quad (7.18)$$

Comparing the above equation with the **eqn.(7.13)**, we see that because of the limited resolution of the spectrometer, the visibility or the MTF, $\sigma_0(\tau)$ is modified to

$$\sigma_0(\nu, \delta \nu_{sp}, \tau) = |\sigma_0(\tau)| \sin(\pi \delta \nu_{sp} \tau) \quad (7.19)$$

This gives a quantitative determination of the MTF observed by the detector as a **function** of the path delay τ at any fixed value of frequency ν . Continuously varying the path delay x between the interferometer arms, for fixed frequency and equal slit widths of the spectrometer gives a decrease in the fringe visibility with increase in the fringe number according to the above equation.

If the entrance slit is illuminated with incoherent radiation as is the case in most of the spectroscopic applications, the slit function is a convolution of the illumination distribution in the plane of the entrance slit and the shape of the exit slit and the MTF is the product of the corresponding transfer functions. For narrow slit widths, the MTF is given by

$$\sigma_0(v, \delta v_{sp}, \tau) = |\sigma_0(\tau)| \sin c^2(\pi \delta v_{sp} \tau) \quad (7.20)$$

A correspondence between the spectral widths of the spectrometer and the actual slit widths is derived using the grating equation to be

$$\delta x / \delta \lambda_{sp} = m \mathcal{R} / d \cos \theta \quad (7.21)$$

where, $\delta \lambda_{sp} = \lambda^2 \delta v_{sp} / c$, 'm' is the grating order (1), \mathcal{R} is the resolution of the spectrometer (42,000), 'd' is the grating spacing (0.833 μm), δx is the actual slit width of the spectrometer and θ is the diffraction angle (0°).

From the above two equations (7.20) and (7.21), it is clear that the exact mathematical form of the MTF and hence the slit function of the spectrometer are determined by the diffraction at the grating which means, as a function of the wavelength λ , the geometry of the exit slit, light distribution at the slits and aberrations of the optical system.

However, there is an alternate method for the measurement of the spectral slit width of the spectrometer [15]. Here, the interferometer path delay T is kept fixed to give a known number of spectral **fringes**. Fringe visibility is recorded for different unequal widths of the entrance and exit slits to study the behavior of the effect of each slit keeping the other fixed. In this case, the slit function and the MTF are determined by the factors apart from those mentioned in the previous **paragraph**, also by the geometry and illumination of the entrance and exit slits. Here again the behavior is governed by the **eqn.(7.19)** for fixed entrance slit and varying exit slit whereas it is given by the square of it (eqn.(7.20)) for fixed exit slit and varying entrance slit. From

this the spectral slit width and the instrument function can be calculated by taking the IFT of the MTF (eqn.(7.8)).

7.6 Results and discussion

The instrument function or its FT, the modulation transfer function of dispersion spectrometers is determined mainly by the slit image. In a scanning spectrometer, the instrument function is a convolution of the entrance slit image and the detector slit. In the geometrical regime, rectangular source and detector aperture gives a triangular rectangular or trapezoidal instrument function depending on whether their widths are equal or unequal. The full width of the instrument function is the sum of the detector width and the input slit image width and for a given sum, throughput is maximized if the two widths are equal ($\delta x_1 = \delta x_2 = \lambda_0$), in which case the instrument function is triangular [15]. With separate slit controls existing on the spectrometer, the widest slit determines the pass band ($\delta \lambda_{sp}$). The instrument function is trapezoidal for unequal slit widths ($\delta x_1 > \delta x_2 > \lambda_0$) and is rectangular in form for the condition ($\delta x_1 = \delta x_2 \gg \lambda_0$), where λ_0 is the mean wavelength.

7.6.1 Variation with path delay:

The Michelson interferometer giving sinusoidal modulations of different periodicity is used to determine the modulus of the MTF of the grating spectrometer at different equal entrance and exit slit widths. Figure 7.3 gives the experimentally measured curves of the MTF as a function of the path difference A (in mm). For every setting of the path delay, the MTF is determined from the visibility of the spectral modulations recorded by scanning the spectrometer around $\lambda_0 = 550 \text{ nm}$. For narrow, equal entrance and exit slit widths ($\delta x = 50, 100 \text{ } \mu\text{m} > XQ$) of the spectrometer, the MTF data recorded for different path delays are shown in the Figure 7.3 (a), (b). As the instrument function is expected to be a triangular function for narrow slit widths, the experimental data are fitted according to the IFT of the triangular function, which

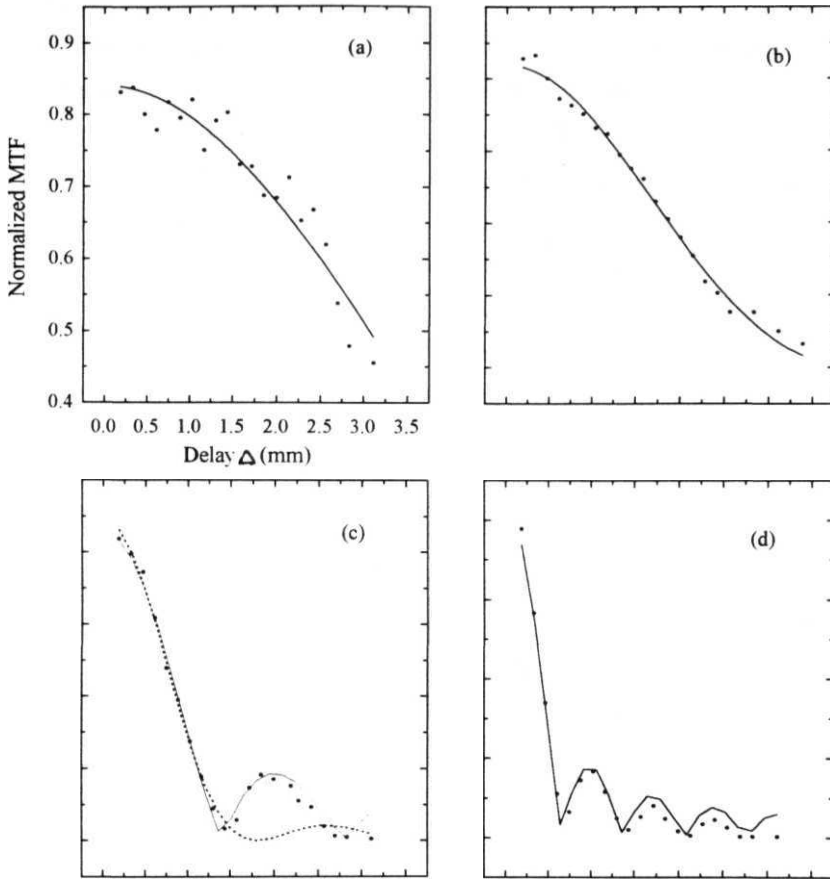


Figure 7.3

Variation of the modulation transfer function (MTF) as a function of the path delay between the interfering beams in the **MI**, for different equal values of the equal entrance and exit slit widths. (a) $\delta x_1 = \delta x_2 = 50 \mu\text{m}$, (b) $100 \mu\text{m}$, (c) $200 \mu\text{m}$, (d) $400 \mu\text{m}$. Dots are experimental data and continuous lines are theoretical fit using eqn.(7.20) for (a) and (b) and eqn.(7.19) for (c) and (d) Dotted line in (c) are for theoretical fit using the eqn (7.20).

is a **sinc²** function given by eqn. (7.20). The values of the fitted constants $A = |\sigma_0(\tau)|$, and $B = (\pi\delta v_p/c)$ which are the amplitude and width of the function respectively, for these slit widths is given in **Table-7.1**. From the fitted values, the full widths of the instrument function (δv_p) can be calculated. Also tabulated for comparison are the full widths of the instrument function (B) calculated from the **IFT** of the MTF data and the values calculated using eqn. (7.21) for the experimental parameters. The values of the widths calculated from the IFT and the experimental parameters match closely with the corresponding fitted values for narrow slit widths. However, the small difference in the values is because of the fact that at narrow slit widths, the effect of optical aberrations make significant contribution and the curves do not resemble exact triangular slit function. The errors due to possible defocusing should also be taken into consideration in explaining the differences.

As the slit widths are made wider to $5x = 200$ and $400 \text{ } \mu\text{m} \gg \lambda_0$, the MTF no longer could be fitted to the **sinc² functions** (as indicated by dotted line in the Figure 7.3 (c)). This is because for wider slits of equal widths, the slit function takes a rectangular form, which is the IFT of sine-function given by eqn. (7.19). Thus, the theoretical fits are done using eqn. (7.19) to the experimental data for wider slit widths and are shown in the Figure 7.3 (c) and (d) and the fitted values are given in the Table 7.1, marked with the asterisk symbol '*'. It can be seen from the Table 7.1 that the fitted values of the width are found to match closely with the width calculated from the EFT. The widths calculated using the eqn. (7.21) and the experimental parameters do not take into consideration the effects due to wider slits and hence there is a large difference in its value compared to the values of the width obtained from the fittings and from the IFT. In all the theoretical fittings, the overall chi-square deviation from the experimental values are as low as **1E-3**.

When the slit widths are made more wider ($5x = 200, 400 \text{ } \mu\text{m}$), an interesting observation from the experimental recordings is that one sees lobes of minima and maxima corresponding to spurious resolution of the spectrometer **coming** into effect (Figure 7.3 (e), (d)). From the figures it is also clear that as the slit width becomes large, the values of the MTF decreases more rapidly and the cutoff path difference

Slit width ‘ δx ’ (μm)	Fitted parameters		Calculated width ‘ B ’	
	$A = \sigma_0(\tau) $	$B = (\pi\delta v_{\varphi}/c)$	Using eqn.(7.21)	From EFT
50	0.840 ± 0.012	395.72 ± 14.14	323.55	319.63
100	0.838 ± 0.01	767.75 ± 10.34	647.10	723.57
200	0.893 ± 0.016	1734.14 ± 29.17	1294.20	2710.89
	$0.858 \pm 0.015^*$	$2224.0 \pm 23.43^*$		
400	$0.837 \pm 0.029^*$	$4538.8 \pm 60.28^*$	2588.39	4875.26

Table 7.1

Fitted values of the MTF plotted as a **function** of the path delay between the interfering beams of the **MI**, for different equal entrance and exit slit widths (Fig. 7.3), using eqn. (7.20). ‘**A**’ is the amplitude and ‘**B**’ is the width of the MTF. The fitted constant ‘**B**’ is compared with that calculated using eqn. (7.21) and the experimental parameters and the width of the **IFT** of the experimental data. Values indicated by ‘*’ are for the **fit** using eqn. (7.19).

corresponding to the first minimum of the function also **decreases**. This can be explained using the q -parameter introduced by Mielenz [22]. Accordingly, when $q = \left(\delta x D / 2 \lambda f \right) > 1$, the width of the line spread function or the fringe width is almost equal to the geometrical image of the entrance slit and we see a minimum in the **MTF**. For $\delta x = 50 \text{ }\mu\text{m}$, $D = 70 \text{ mm}$, $\lambda = 550 \text{ nm}$ and $f = 50 \text{ cm}$, ' q ' is equal to 6.36 and the value is more for wider slit widths and hence there is a rapid decrease in the behavior of the MTF.

The spectral slit width ($\delta \nu_{\text{sp}}$) in the spatial frequency domain which is **defined** as the frequency difference between two points at which the energy through the exit slit is half its maximum value is a quantity used to describe the output intensity distribution of a spectrometer. This is determined by knowing the number of fringes at the place where the MTF goes through the first **minimum**. This is also equal to the resolving power of the spectrometer for that particular **setting**. The values of the path delay at the first minimum obtained from the Figures 7.3 (a)-(d), the corresponding number of fringes and the slit widths are listed in the Table 7.2. From the value of the path difference Δ_{min} , the corresponding number of spectral fringes (N_0) (Figure 7.2 (a)) and the fringe width ($\delta \lambda_{\text{sp}}$) considering the whole bandwidth of the input white light spectrum (370 nm) are obtained. The spectral slit widths are calculated by using $\delta \nu_{\text{sp}} = \delta \lambda_{\text{sp}} / \lambda_0^2$ at $\lambda_0 = 550 \text{ nm}$ and are listed in the last column of the Table 7.2. The value of the spectral slit width for the narrowest slit width of $50 \text{ }\mu\text{m}$ used, is 1.5 cm^{-1} . This is larger than the theoretical resolution limit of the spectrometer of 0.4 cm^{-1} , which is calculated assuming a parallel beam of light filling the entire **grating**. By taking into consideration, the effect of geometrical aberration of the spectrometer [17], the practical resolution limit is calculated to be about 0.9 cm^{-1} . This limit can be achieved experimentally by working at slit widths smaller than $50 \text{ }\mu\text{m}$ but more than the diffraction limit of $7 \text{ }\mu\text{m}$ ($\delta x_1 = \delta x_2 \rightarrow \lambda_0$) for the spectrometer. Thus, from the measurement of the path difference at which the fringe visibility goes to minimum, the resolution limit for a particular setting can be calculated and also the ambiguity in the

Slit width 'Sx' (μm)	Path delay Δ_{\min} (m)	Number of fringes N_0	Fringe width $\delta\lambda_{\text{ap}} = 370 \text{ nm}/N_0$	Spectral slit width (cm^{-1})
50	7.88E-3	8312	0.45	1.5
100	4.04E-3	4249	0.87	2.9
200	1.82E-3 1.39E-3*	1900 1445*	1.95 2.56*	64 8.5*
400	7.0E-4	715	5.17	18.8

Table 7.2

Table giving the values of the path delay Δ_{\min} , where the MTF goes to the first minimum, corresponding number of fringes (N_0) in the entire spectral region, the fringe width ($\delta\lambda_{\text{ap}}$) and spectral slit width ($\delta\nu_{\text{ap}}$). The values are obtained from the theoretical fitting shown in the Fig 7.3. For 200 μm slit width, two values are given to show that the instrument function is close to the rectangular form (denoted by the asterisk symbol ‘*’) instead of the triangular function.

exact measurement of the spectral slit width due to **spurious** lobes, for larger slit widths can be **avoided**

7.6.2 Variation with the slit widths:

The actual measurement of the resolving power of a spectrometer is fully **described** by taking into account the finite size of the slit widths [23] and so it becomes essential to know the behavior of the individual slits on the SMS generated by the **MI**. This is an alternate method for the measurement of the spectral slit width discussed in the last **section**. Here, for a fixed path delay (A) between the interfering beams, either the exit slit width (δx_2) or the entrance slit width (δx_1) is varied keeping the other slit width fixed. As described before, the visibility or the MTF of the spectral fringes are measured for different settings of the interferometer path delay and the spectrometer slit **widths**. The spectral slit width calculated from the theoretical fitting are compared with the values calculated from the **IFT** of the experimental data.

Figure 7.4 gives the behavior of the MTF as a function of the exit slit width (δx_2) for a fixed entrance slit width of $\delta x_1 = 50 \text{ } \mu\text{m}$ and for different path delays (A) recorded as mentioned before around $\lambda_0 = 550 \text{ nm}$. As the exit slit width is increased from $50 \text{ } \mu\text{m}$ to $500 \text{ } \mu\text{m}$, the behavior of the curves is expected to resemble the convolution of two rectangular slits of unequal widths which is the FT of a trapezoidal function. The functional form of the **trapezoidal** distribution can be written as

$$\sigma_0(v, \delta v_{sp}, \tau) = \left| \sigma_0(\tau) \right| \left(\frac{\sin(\pi \delta v_{sp} \tau)}{(\pi \delta v_{sp} \tau)} \right) \left(\frac{\sin(\pi \delta v_{sp} \tau - y)}{(\pi \delta v_{sp} \tau - y)} \right) \quad (7.22)$$

for the case $\delta x_2 > \delta x_1 > \lambda_0$ where, y is a function of the constant difference between the slits. When $y = (\pi \delta v_{sp} \tau)$, one gets FT of a rectangular function (eqn. (7.19)) and when $y = 0$, its a triangular function (eqn. (7.20)). However, the EFT of the experimental data resemble more closely the rectangular function and hence it was decided to fit all the curves using the **sinc-function** given by eqn. (7.19). The fitted values along with the fitting errors for different path delays are given in the Table 7-3. From the Figure

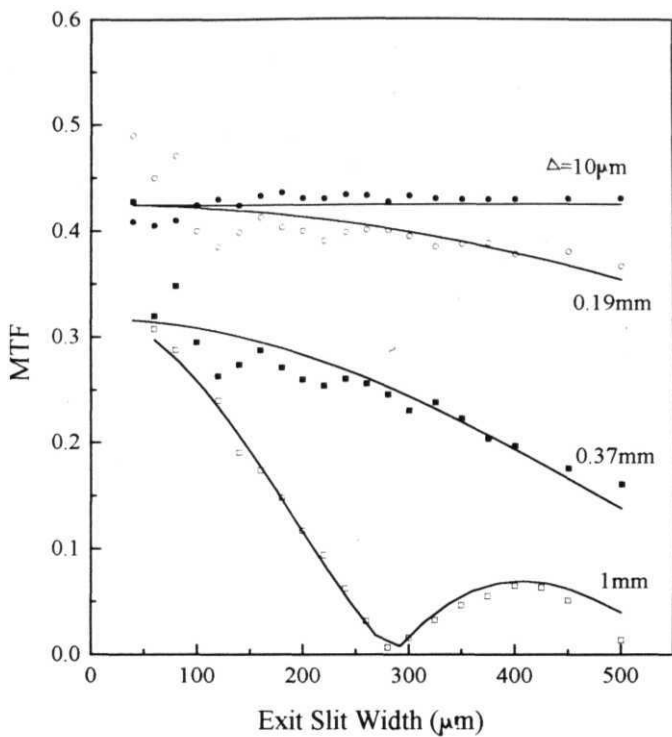


Figure 7.4

Variation of the modulation transfer function (MTF) as a function of the exit slit width (δx_{\perp}) for different fixed path delays (Δ) between interfering beams of the MI. The entrance slit width is kept fixed at $50\mu\text{m}$. The experimental data shown by different symbols are fitted using eqn.(7.19) and the fitted values are given in the Table 7.3.

Path delay A (m)	Fitted constants	
	$A = \sigma_0(\tau) $	$B = A(m)$
10E-6	$0.529 \pm 7.83E-3$	$9.981E-6 + 0.98$
0.19E-3	$0.426 \pm 8.2E-3$	$0.207E-3 \pm 0.02$
0.37E-3	$0.397 \pm 1.43E-2$	$0.41E-3 \pm 0.029$
1.0E-3	$0.401 \pm 7.35E-3$	$1.106E-3 \pm 0.012$

Table 7.3

Fitted values of the amplitude (A) and the width (B) of the MTF plotted as a **function** of the exit slit width for different path delays between the interfering beams of the **MI** (Fig. 7.4). The entrance slit width is kept fixed at 50 urn Equation (7.19) is used for the fitting the experimental data.

7.4 it is seen that when the path delay between the interfering beams is $10\text{ }\mu\text{m}$, the change in the MTF with increasing exit slit width is less and is almost a **constant**. As the path delay is increased to higher values, the number of **fringes** within the entire spectrum are more and the visibility of the spectral fringes decreases for increasing slit width, as the detector starts to see more than just one bright fringe at a time during the **scan**. For $A = 1\text{ mm}$, the visibility of the spectral modulations is almost zero at a value of the exit slit width of $\delta x_2 = 284\text{ }\mu\text{m}$. This is the value at which the detector sees exactly one bright and one dark **fringe** and hence the integrated intensity goes to a **minimum**. As the spectrometer slit width is further widened, the **periodic** spectral modulation detail which was lost returns back giving rise to a secondary maximum. Spurious spectral resolution can occur because of the appearance of the secondary maxima in the MTF. The limiting spectral resolution of the spectrometer ($\delta\lambda_{\text{sp}}$) obtained in three different ways are tabulated in the Table 7-4. From the **fitted** value of the experimental data, the path difference is obtained from which the number of fringes and hence the limiting spectral width of the **fringes** is calculated, as mentioned before. This value is compared with the spectral width obtained from the experimentally measured path difference and from the extrapolated value of the slit widths where the **fringe** visibility goes to a minimum (δx_{min}) and the focal length of the spectrometer ($f = 58.8\text{ cm}$) and the grating spacing ($d = 0.833\text{ }\mu\text{m}$).

For a fixed path delay of $A = 1\text{ mm}$, the exit slit width is varied continuously from $50\text{ }\mu\text{m}$ to $500\text{ }\mu\text{m}$ each time calculating the visibility from the recorded spectral modulations around 550 nm for different fixed entrance slit widths. The experimental data and the corresponding theoretical fitting are shown in the Figure 7.5. The curves are fitted to the **sinc-function** form given by eqn. (7.19). The fitted amplitudes (A) and the widths (B) are listed in the Table 7-5. The observed decrease in the spectral fringe contrast with increase in the entrance slit width is a direct manifestation of the effects of spatial coherence of the **light**. As a result of **increasing** the entrance slit width of the spectrometer, the light throughput and hence the incoherent contribution into the

	Path delay A(m)	Number of fringes N	Slit width δx_{\min} for minimum visibility	Spectral slit width $\delta \lambda_{\text{sp}}$ (nm)
From experiment	0.19E-3	175		2.114
	0.37E-3	365		1.014
	1.0E-3	1032		0.36
From fitting	0.207E-3	193		1.917
	0.41E-3	408		0.907
	1.11E-3	1144		0.323
From theory			214E-5	3.03
			105E-5	1.488
			284E-6	0.402

Table 7.4

Comparison of the spectral slit widths calculated for the variation of MTF with exit slit width (Fig. 7.4). Number of fringes is calculated using $N = (1058140)\Delta - 26.133$ (Fig. 7.2 (a)) and $\delta \lambda_{\text{sp}} = (\delta x_{\min} d)/f$, where 'd' is the grating spacing = 0.833 μm and 'f' is the focal length of the spherical mirrors of the spectrometer = 58.8 cm.

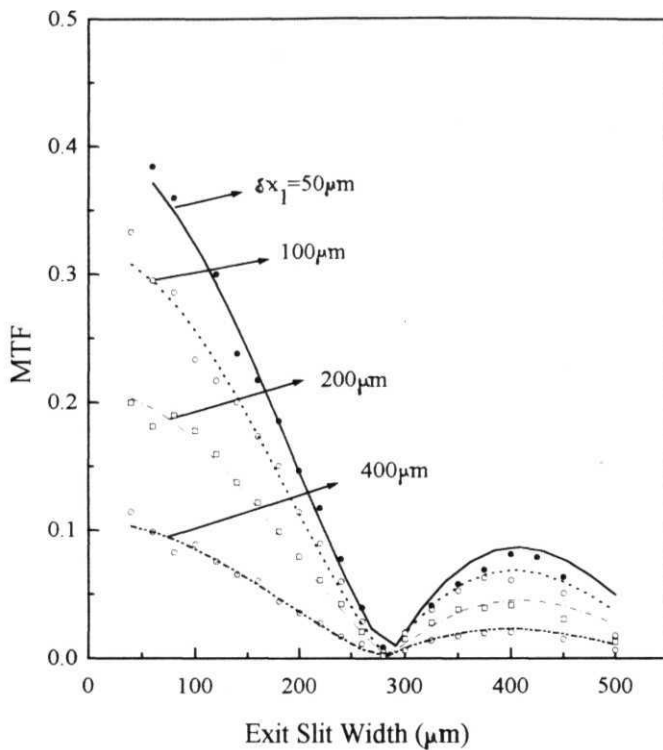


Figure 7.5

Variation of the MTF as a function of the exit slit width δx_2 for a fixed path delay of $\Delta = 1$ mm and different entrance slit widths. The experimental data shown by different symbols are fitted using eqn.(7.19) (continuous lines) and the fitted values are given in Table 7.5.

Entrance slit width δx_1 (urn)	Fitted parameters	
	$A = \sigma_0(\tau) $	$B = A(m)$
50	$0.401 \pm 7.35E-3$	$1.106E-3 \pm 0.012$
100	$0.318 \pm 5.43E-3$	$1.117E-3 \pm 0.022$
200	$0.211 \pm 3.19E-3$	$1.104E-3 \pm 0.012$
400	$0.107 \pm 2.19E-3$	$1.134E-3 \pm 0.016$

Table 7.5

Fitted values for the amplitude (A) and width (B) of the variation of the MTF with exit slit width (Fig. 7.5) using the equation (7.19). The path delay (A) between the interfering beams of the MI is kept fixed at 1 mm and the entrance slit width δx_1 is varied for each recording.

spectral **fringes** are **more**. Also, the size of the image of the entrance slit as seen by the exit slit is more and hence there is a reduction in the contrast of the fringes

The MTF for the **variation** of the entrance slit width for different fixed exit slit widths can be considered as the convolution of the Fourier transforms of two rectangular slits of unequal widths which is a trapezoidal function (eqn. (7.22)) but can be approximated to a **sinc²-function** of the form given by **eqn (7.20)** for small variations. For a fixed path delay of 1 mm between the interfering beams of the **MI**, the number of fringes in the entire spectral region is fixed. The spectral visibility data which gives the modulation transfer function of the spectrometer is plotted as **a** function of the varying entrance slit width (Figure 7.6). As the exit slit width is increased from 50 μm to 400 μm , there is a decrease in the contrast of the fringes due to a decrease in the resolution of the spectrometer. From the fitted values given in the Table 7-6, the widths of the entrance slit function are obtained. These values are compared with the values obtained from the widths calculated by taking the inverse Fourier transform (**IFT**) of the experimental data and are also tabulated in the Table 7-6. The scatter in the experimental data for narrower slit widths are high because of the low light intensity levels input into the spectrometer and the effects of **optical** aberrations, which are predominant at smaller slit widths. It can be seen from the Table 7.6 that the width of the instrument function remains almost a constant for different exit slit widths, which only means that the entrance slit width variation does not have much of an effect on the width of the instrument function or its resolution except for a decrease in the fringe contrast.

In Figure 7.7, the variation of the MTF with the entrance slit width for a fixed exit slit width **of** 50 μm and vice-versa are shown for a fixed path delay of 1 mm along with the corresponding theoretical fits. From the behavior of the MTF, with respect to the slit widths of the spectrometer, the respective instrument function behavior and the limiting spectral slit widths are obtained by taking the IFT of the experimental data [24]. The modulus and the phase behavior of the instrument function are shown in the Figures 7.8 and 7.9 for the variation of MTF with the entrance and exit slit widths respectively, keeping the other slit fixed at 50 μm width. The value of the spectral slit

Exit slit width δx_2 (urn)	Fitted parameters $A = \sigma_0(\tau) $ $B \text{ (cm}^{-1}\text{)}$		Width of the instrument function from IFT (cm ¹)
50	$0.244 \pm 8\text{E-}3$	21.30 ± 0.92	20.40
100	$0.245 \pm 2.8\text{E-}3$	18.31 ± 0.33	18.21
200	$0.111 \pm 1.5\text{E-}3$	18.53 ± 0.38	18.21
400	$0.059 \pm 1\text{E-}3$	19.13 ± 0.48	18.59

Table 7.6

Fitted values of the MTF plotted as a function of the variation of the entrance slit widths (6x1) for different fixed exit slit widths (δx_2). The path delay between the interfering beams of the **MI** is fixed at $A = 1 \text{ mm}$. From the theoretical fitting using **eqn (7.20)**, the amplitude (A) and the width (B) are **obtained**. The IFT of the experimental data are calculated using standard fast Fourier transform routines from which the **half** width at half maximum of the instrument function is measured.

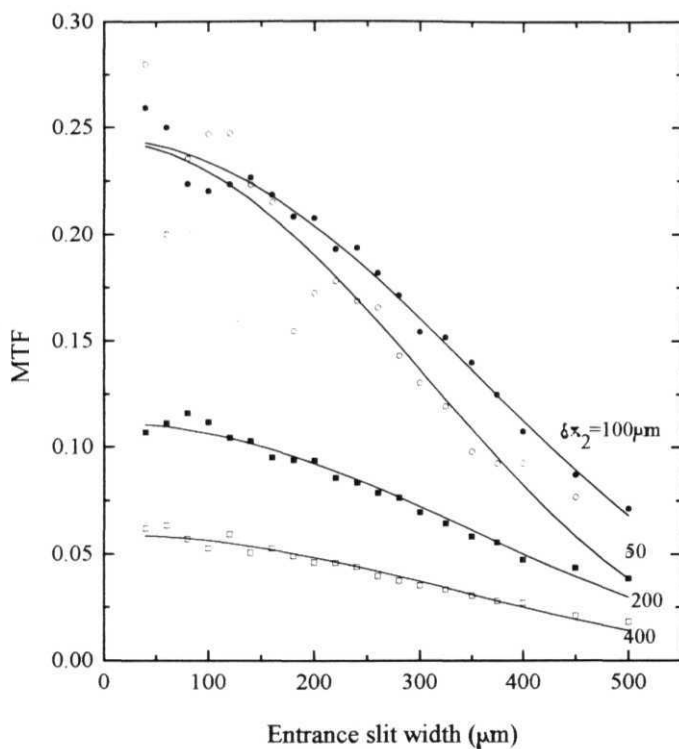


Figure 7.6

Variation of the MTF as a function of the entrance slit width δx for different fixed exit slit width (δx_2). The path delay of the MI is kept fixed at 1mm. Experimental data are represented by different symbols and are fitted using eqn.(7.20). The fitted values are given in Table 7.6.

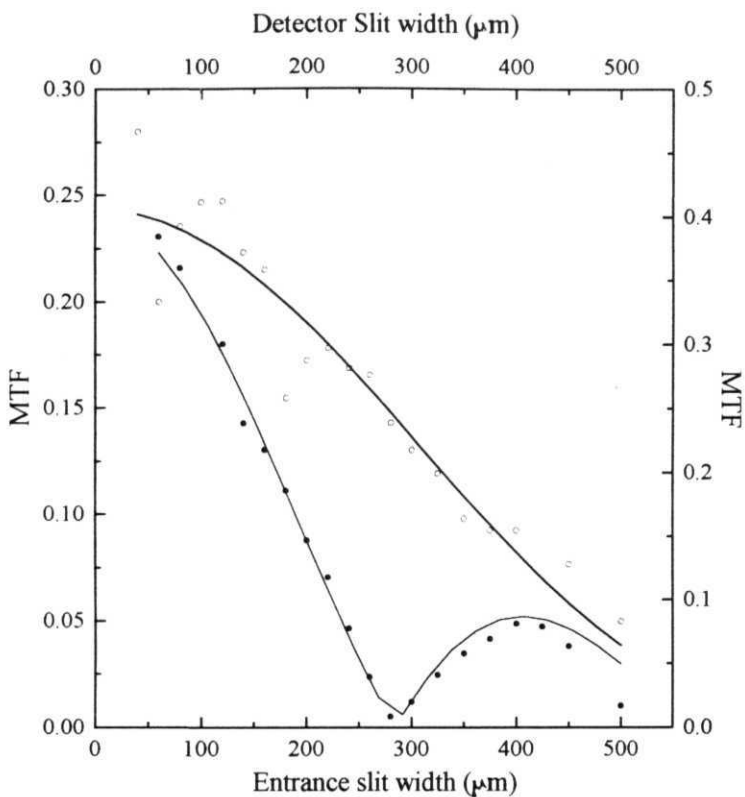


Figure 7.7

Behavior of the MTF for the variation in the entrance slit width (open circles) and exit slit widths (closed circles). The path delay of the **MI** is fixed at **1mm**. The fixed slit width is **50μm** for both the **curves**. The theoretical fits (continuous line) are using eqns.(7.20) and (7.19) for the entrance and exit slit width variations respectively.

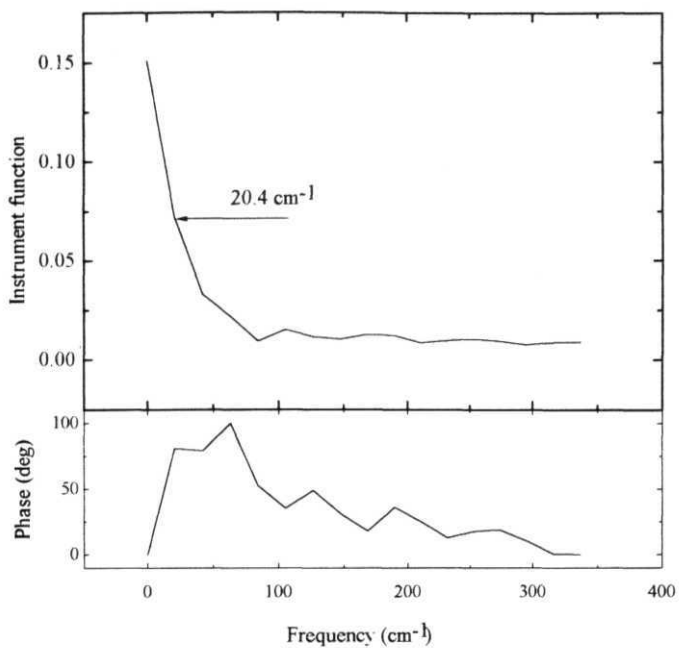


Figure 7.8

Inverse Fourier transform (IFT) of the MTF variation with entrance slit width gives the corresponding instrument function of spectral slit width indicated in the figure. Both the modulus and the phase are used in correcting blurred spectrum [11].

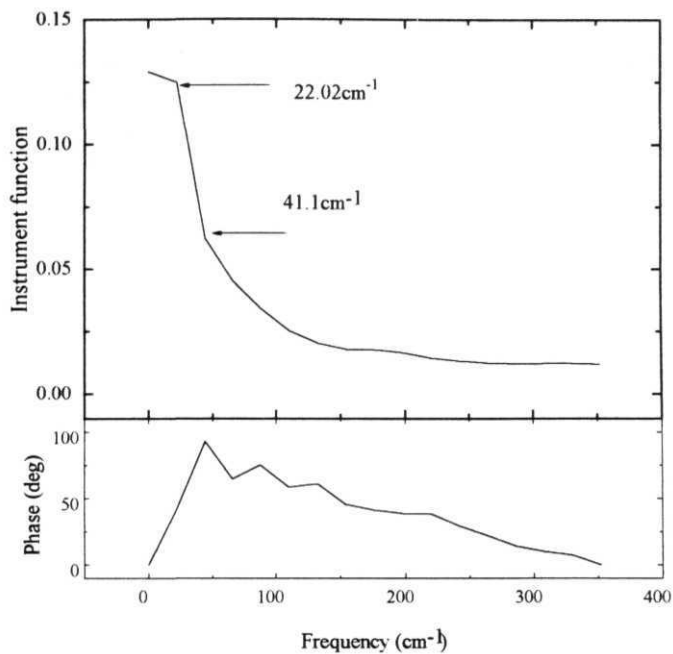


Figure 7.9

Modulus and phase of the instrument function obtained by taking the EFT for the variation of the MTF with the exit slit width of the spectrometer. The form of the curve gives the corresponding instrument **function**, from which spectral slit width can be calculated and the value is indicated in the figure.

width calculated for the triangular function variation of the entrance slit is 20.4 cm^{-1} . The **IFT** for the exit slit variation is not exactly a rectangular function, as expected. The instrument **function** looks close to a trapezoidal function with a slightly broader **base**. This difference is attributed to the finiteness of the entrance slit **width**. The spectral slit width calculated from the half width at half maximum is 19.08 cm^{-1} after subtracting the constant difference between the entrance and exit slits (eqn. (7.22))

The measurement of the MTF and hence the instrument function of a spectrometer can be used to correct the blurred spectrum and are found to be better than the spectrum corrected using the optical transfer function obtained from the FT of line profiles [12]. From a complete description of the dispersion grating spectrometer in terms of the modulation transfer function (MTF), the limiting resolution of the spectrometer and spectral slit widths are **obtained**

References

- [1] P. Jacquinot, **Rep Prog Phys.** 23, 267, (1960); G.W. Stroke, Diffraction gratings, in Handbook of physics, 29, 426, (1967)
- [2] D.S. Goodman, Basic optical instruments, in Methods of experimental physics, vol 25, Ed by D. Malacara, (Academic Press, 1988).
- [3] K Iizuka, Engineering optics, Springer series in optical sciences, (Springer-Verlag, Berlin, 1985), vol 35, chapter 10
- [4] K.R. Barnes, The optical transfer function, (Adam Hilger, 1971).
- [5] A. Lohmann, Opt. Acta, **6**, 175, (1959).
- [6] T. Katayama and A Takahashi, **Japn J. Appl. Phys** 9, 1509, (1970).
- [7] S.G Rautian, **Sov. Phys USEPKHI**, 66, 245, (1958).
- [8] J.E. Stewart, **Appl. Opt** 4, 609, (1965)
- [9] J.E Stewart, **Appl Opt** 6, 1523, (1967)
- [10] K. Gotto and S. Morozumi, **Appl. Opt.** 10, 764, (1971)
- [11] H Kanamori and K. Kozima, in Applications of holography and optical data processing, Ed. by E. Marom, A. A. Friesem and E Wiener-Avnear, (Pergamon Press, 1977).
- [12] K. Kozima, H. Kanamori and O Matsuda, **Japn. J. Appl. Phys.** 17, 1271, (1978).
- [13] S. Brodersen, **J Opt Soc Am.** 46, 255, (1956).
- [14] H. Sakai and G. Vanasse, **J. Opt Soc. Am.** 56, 357, (1966).
- [15] V.J Coates and H. Hansdroff, **J. Opt. Soc. Am.** 45, 425, (1955).

- [16] V. **Nirmal** Kumar and D. Narayana Rao, **J Opt Soc Am B** **12**, 1559, (1995),
Refer also to the previous chapters of this thesis.
- [17] D.J. Schroeder, **Diffraction** grating instruments, in *Methods of Experimental Physics*, Ed. by N. Carleton, (Academic Press, 1974).
- [18] Instruction manual of **HRS-2**, JY Grating monochromator.
- [19] F. Kneubuhl, **Appl. Opt.** **8**, 505, (1969)
- [20] H. **Fujiwara**, **J Opt Soc Am** **71**, 238, (1981).
- [21] L. Mandel and E. Wolf, **J Opt Soc Am** **66**, 529, (1976).
- [22] **K.D. Mielenz**, **J. Opt Soc Am.** **57**, 66, (1967).
- [23] S. Brodersen, **J Opt Soc Am** **44**, 22, (1954)
- [24] V. Nirmal Kumar and D. Narayana Rao, submitted to *Appl. Opt.*